MAX-PLANCK-INSTITUT
FÜR CHEMISCHE PHYSIK FESTER STOFFE

TECHNISCHE
UNIVERSITÄT
DRESDEN

Investigation of Electronic and Magnetic Response in Topological Semimetals

Dissertation

zur Erlangung des akademischen Grades

Doctor of Philosophy

(Ph. D.)

vorgelegt

dem Bereich Mathematik und Naturwissenschaften
der Technischen Universität Dresden

von

M. Sc. Sukriti Singh

Geboren am 18.05.1995 in Ballia, India

Eingereicht am:

Die Dissertation wurde in der Zeit vom Februar 2019 bis zum August 2022
am Max-Planck-Institut für chemische Physik fester Stoffe in Dresden
angefertigt.

Gutachter: Prof. Dr. Claudia Felser
Gutachter: Prof. Dr. Hans-Henning Klauss

List of publications

1) <u>Sukriti Singh</u>, Vicky Süß, Marcus Schmidt, Claudia Felser, and Chandra Shekhar, **Strong correlation between mobility and magnetoresistance in Weyl and Dirac semimetals**, *J. Phys. Mater.* **3**, 024003 (2020).

2) <u>Sukriti Singh</u>, Jonathan Noky, Shaileyee Bhattacharya, Praveen Vir, Yan Sun, Nitesh Kumar, Claudia Felser, and Chandra Shekhar, **Anisotropic nodal-line-derived large anomalous Hall conductivity in ZrMnP and HfMnP**, *Adv. Mater.* **33**, 2104126 (2021).

3) <u>Sukriti Singh</u>, Nitesh Kumar, Subhajit Roychowdhury, Chandra Shekhar and Claudia Felser, **Anisotropic large diamagnetism in Dirac semimetals $ZrTe_5$ and $HfTe_5$**, *J. Phys.: Condens. Matter*. **34**, 225802 (2022).

4) <u>Sukriti Singh</u>, Ana García Page, Jonathan Noky, Subhajit Roychowdhury, Maia G. Vergniory, Horst Borrmann, Chandra Shekhar, H.-H. Klauss, and Claudia Felser, **Anomalous Hall effect in ferromagnetic Weyl semimetals NiMnSb and PtMnSb**, *to be submitted*

---

5) Subhajit Roychowdhury, <u>Sukriti Singh</u>, Satya N Guin, Nitesh Kumar, Tirthankar Chakraborty, Walter Schnelle, Horst Borrmann, Chandra Shekhar, and Claudia Felser, **Giant topological Hall effect in the noncollinear phase of two-dimensional antiferromagnetic topological insulator $MnBi_4Te_7$**, *Chem. Mater.* **33**, 8343 (2021).

6) Subhajit Roychowdhury, Kartik Samanta, <u>Sukriti Singh</u>, Chandra Shekhar, Walter Schnelle, Maia G. Vergniory, and Claudia Felser, **Flat band induced giant anomalous Hall effect in an antiferromagnetic kagome spin-ice,** *to be submitted*

Contributions

- Prof. Dr. Claudia Felser, Dr. Chandra Shekhar, and Prof. Dr. Hans Henning Klauss supervised this PhD thesis.

- Ana García-Page, Dr. Jonathan Noky, Dr. Kartik Samanta, Dr. Maia G.Vergniory, and Dr. Yan Sun carried out the electronic structure calculations.

- Dr. Walter Schnelle, Dr. Nitesh Kumar, and Dr. Subhajit Roychowdhury helped with the interpretation of the magnetic and transport data.

- Dr. Kaustuv Manna provided me with samples of CoSi, PdGa, PtGa, AlPt, RhSi, and Ni doped RhSi. Dr. Nitesh Kumar provided me with samples of $MoTe_2$, WTe_2, LaSb, LaBi, and Cd_3As_2. Marcus Schmidt and Vicky Süβ helped me providing the samples $TaTe_2$, NbP, NbAs, TaP, TaAs, and $NbAs_2$ for the study of diamagnetism in topological semimetals.

- Dr. Horst Borrmann carried out the single crystal XRD measurements on $PtGa_5$.

- Silvia Kostmann carried out the metallographic polishing and light microscopy investigations on $MnPt_2Sn_3$.

- Monika Eckert and Ulrich Burkhardt helped in performing the WDXS experiments on $MnPt_2Sn_3$.

Acknowledgments

Countless credible people, with whom I've discussed and worked over the last few years, has contributed significantly to the research works contained in this thesis. The most important thing is to express my gratitude to Prof. Dr. Claudia Felser for giving me an opportunity to join her research group, which was kind of a dream coming true for me as I used to read her research articles during my masters, without being aware that someday I could get the opportunity to work under her supervision. I am very grateful for her guidance and support during my time here at MPI-CPfS. It was thanks to her open-ended approach to projects and her willingness to listen without judgment that I was able to expand both personally and professionally throughout my time with her. I'm especially glad for the opportunity she provided me to speak at international schools and conferences and interact with the researchers from around the world. I am also thankful to Prof. Hans Henning Klauss for his constant guidance and fruitful discussions.

Dr. Chandra Shekhar, my study group leader, deserves all my gratitude for his patience in teaching me the ropes of their trade on a daily basis. I learned a lot from him about how to conduct research in a relaxed manner while also having fun, and to never be afraid to ask questions and try new things. I'd want to express my gratitude to Dr. Subhajit Roychowdhury, for his daily conversation and for providing me with fresh perspectives on my work and also helping me to go through all phases of ups and downs. Many thanks to Rebeca and Narayan for all of the brief physics discussions and for always listening to me and keeping me going when I needed it most. I would also like to thanks my colleagues Dr. Nitesh Kumar for his help in knowing the laboratory and Dr. Kaustuv Manna for teaching me experimental technicalities. It would not have been possible without theoretical group especially Dr. Yan Sun, Dr. Maia G. Vergniory, Dr. Jonathan Noky, Dr, Kartik Samanta and Ana and who always helped me in supporting my experimental data. I am thankful to Dr. Gerhard Fecher for his fruitful discussions. I would also like to thank Walter Schnelle and Gudrun Auffermann for always helping me in the laboratory and for the discussions.

I would like to thanks other people in my group for being very helpful, and spending their time to help me in laboratory.

I would like to thanks especially my family and friends for always supporting me and believing in me.

Contents

List of figures

List of tables

1. Introduction

Numerous advancements and benefits of the digital age have been made possible by the advent of quantum computers, which is the result of a countless effort of researchers. The rate at which tasks are completed has significantly picked up, while at the same time, the size of these devices is continuing shrinking. When it became clear that even the silicon industry would soon reach its point of saturation, those in the research community became aware of the need to look for an alternative solution [1]. And if we are talking about boosting the speed of computers and reducing the amount of storage space they occupy, there is yet another significant obstacle to overcome in terms of the conservation of energy. Researchers should be working on a solution right now because we are in the midst of a significant energy crisis, and this would be the best time for them to do so. It would be in their best interest to look into ways to reduce their energy consumption, given that we are already aware of how vital it is to pursue such avenues of inquiry.

We are certain that the investigation of topological materials can make a contribution to the solution of a good deal of these issues, and we are very optimistic about this prospect (Figure 1.1). It is anticipated that perhaps up to 24 % of all materials will have some topological features [2]. As a consequence of this, the range of possible applications can be increased due to the wide variety of materials that are available. Over the course of the last decade, the expansion of the field of research that focuses on condensed matter physics has directly caused a sea change in the field as a direct result of the growth of materials [3]. These topological materials have the potential to bring scientists one step closer to discovering practical applications for unusual phases. Some of these applications include having the potential to revolutionize electronics and catalysis. These topological materials provide researchers with additional hope to find a solution for the energy crisis. Additionally, prior to the development of applications, it is necessary to identify materials that are suitable for these applications and to study the physical phenomena that are associated with these materials. There are a variety of topological materials that are currently being reexamined for use in improved thermoelectric devices, improved catalytic processes, and various spintronic devices. At the same time, researchers are also looking into new materials which can be used for technical applications in these fields.
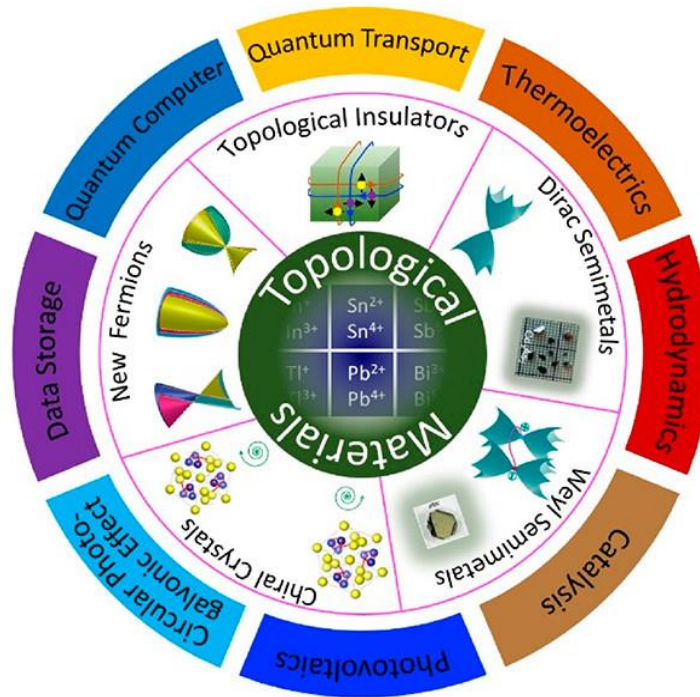
Figure 1.1: Overview of topological materials. Topological quantum materials with their possible fields of application. [Adapted from the ref. 3]

With this motivation of PhD thesis, several topological semimetals were synthesized to investigate their electronic and magnetic response, and the search for new topological materials with intriguing physical properties were also sought.

1.1 Organization of thesis

This thesis is structured in 7 major chapters. In chapter 2, principle and theoretical background of topology in materials have been established to create a better understanding of the aspects used in further chapters. Based on the theory of topological electronic band structure, the classification of topological materials has been discussed, which include Dirac semimetals (DSMs), Weyl semimetals (WSMs), Nodal line semimetals, and multifold fermionic semimetals. Unusual transport of such topological semimetals has been also discussed in this chapter explaining basics of anomalous Hall effect (AHE), anomalous diamagnetism, quantum oscillations, and extremely large magnetoresistance (MR) and mobility. A comprehensive list of references is provided at the end of the thesis.

Chapter 3 describes the experimental techniques used to grow high quality single crystals of topological materials and study their transport and magnetic response. As discussed above how magnetic topological materials are important for spintronic applications, there is a need to look for room temperature ferromagnets with the topological features exhibiting large anomalous Hall conductivity (AHC) and anomalous Hall angle (AHA), as these parameters are more reliable in terms of being used for further

technological applications. Also, there are huge category of materials known and investigated earlier, but their many physical phenomena were not understood clearly, and thus they need to be studied to create a better understanding. With this motivation it was decided to revisit materials from two major families including transition metal pnictides and Heuslers exhibiting room temperature ferromagnetic property in chapter 4. In this chapter, electro-magnetic transports of ZrMnP and HfMnP is discussed in section 4A, where these compounds exhibit topological nodal lines near Fermi energy (E_F). And these nodal lines are gapped under spin-orbit coupling (SOC) effect further resulting in large AHC and AHA. While in section 4B, NiMnSb and PtMnSb has been discussed, as these materials were never explored for their topological features and it turns that they have accidental Weyl nodes near E_F.

Compounds can be fascinating as many phenomena got better understanding after the introduction of topology. While for some phenomena, the researchers developed a better understanding earlier, but some were overlooked in topological materials. Diamagnetism in non-magnetic topological materials is one of them. Chapter 5 explains some of non-magnetic topological semimetals to understand the reason behind large diamagnetism. To understand this in such large class of semimetals is rather difficult and thus $ZrTe_5$ and $HfTe_5$ is used as an example to understand as they have simple band structure. Both the compounds are classified as DSMs and show very large diamagnetism due to enhanced orbital diamagnetism from interband effects of linearly dispersed Dirac bands near the E_F.

Condensed matter research in general and material science in particular are driven by the hunt for novel materials with potential applications. Examination of previously known phases with undiscovered topological transport are described in the preceding chapters. The results presented in chapter 6 are focused on the search for novel materials with novel topological properties. The origin of high MR and high mobility from the previously known topological materials was understood, and employed the criterion in new compounds, expecting the similar behavior. In a simple rule, the probability of finding topology near to E_F is more in semimetals since both valence and conduction bands are close to the E_F. It is virtue to measure electro-magnetic transport of new semimetals that have not been examined previously, which fit in our previous knowledge. In chapter 6, electronic and magnetic response of $PtGa_5$ is discussed. $PtGa_5$ is an interesting compound as it shows extremely large MR and extremely high mobility along with Shubnikov-de Haas (SdH) oscillations. The electro-magnetic response, and the electronic band structure of $PtGa_5$ have been discussed, indicating it to be strong topological insulator (TI).

As discussed above, search of new topological materials is always one of the virtues for the researchers in condensed matter physics. In chapter 7, a completely new material from Mn-Pt-Sn family is discussed, from which $Mn_{1.4}PtSn$ is well known for antiskyrmions. The new material is $MnPt_2Sn_3$, which is interesting for a topological view and shows striking physical properties. The magnetic ground state of $MnPt_2Sn_3$ is antiferromagnet (AFM), and exhibits AHC despite of being AFM nature.

2. Fundamentals

To provide better comprehend base for the thesis, this chapter gives a background information, which are essential. The information offered here is mostly covered from the following references:

- Topological Phases of Matter; Roderic Moessner, Joel E. Moore; Cambridge (2021)
- Magnetism and Magnetic Materials; J. M. D. Coey; Cambridge (2009)
- Magnetic Oscillations in Metals; D. Shoenberg; Cambridge (2009)

2.1. Topological state of matter

Bridging of high energy physics and condensed matter physics provides exchange of knowledge about spontaneous symmetry breaking and phase transition. Such insights have helped physicists and material scientists for understanding of many phenomena. As a result, the topological phases of matter have arisen as an intriguing new subject of research in the condensed matter physics community in 21st century and quantum Hall effect (QHE) is known to be first topological phenomena [4]. In following years, a theoretical prediction of a potential insulating 2D state known as a quantum anomalous Hall insulator was discovered by Thouless, Haldane, and other researchers [5,6]. However, until Kane and Mele [7], and Fu and Kane [8] identified a class of 2D nonmagnetic spin Hall insulators [9,10] whose Bloch states are topologically twisted in a certain situation, and at that time, the particular research area didn't really begin to take off. Both types of states were introduced as a topological state of matter and later it was introduced as topological insulators (TIs) [11-15]. When it came to a broader range of symmetry classifications, the notion of TIs was quickly expanded in the "weak" and the "strong" TIs. This led to the development of topological crystalline insulators [16,17]; topological semimetals [18-21]; and other various topological phases [11]. These quantum materials have attracted substantial attention owing to their nontrivial electronic band structures that offer the potential for revolutionary device applications. In the topological materials database, different types of band twisting give rise to various types of topology, which capture more than 20% compounds of the Inorganic crystal structure database (ICSD) [2,22-24]. A nontrivial band topology appears when band inversion occurs in momentum space; that is, the conduction band is below the valence band with respect to their natural order. This inversion may occur in several manners, and the corresponding wave function of each band twists and induces a finite Berry phase [25,26]

that is associated with the Berry curvature (BC) [27]. The degeneracy of band touching in momentum space determines the classification of the topological materials [19]. Among them, semimetals are particularly interesting as their topology can even appear close to the Fermi energy (E_F), which directly influences their physical properties. This field has attracted considerable attention in condensed matter physics and material science in recent years and show many interesting physical properties, including extremely large magnetoresistance (MR) [28-36], high mobility [32,34,37,38], chiral anomaly [37,39-42], anomalous Hall effect (AHE) [43-49], 3D-QHE [50-52], anomalous Nernst effect (ANE) [25,39,49,53-57], large Seebeck coefficients [58] and many others interesting phenomena [59-63].

2.2. Classification of topological materials

From the research progress of recent decades, the topological materials can be classified depending on the types of band crossing. It is known that a strong spin-orbit coupling (SOC) causes band inversion, which results nontrivial surface states in TIs [64]. These gapless surface states within the bulk energy gap of a TI are unique and differ from trivial surface states [15,65,66]. The spin and momentum of these surface states are typically locked up and perpendicular to each other, and follow the Dirac dispersion relation in momentum space. In a 3D-TI, bands cross linearly and the crossing point is protected by time-reversal symmetry (TRS). To further classify topological materials in subcategory, degeneracy of crossing points and symmetry protection are taken into consideration. The crossing point is two and four degenerate points for Weyl semimetals (WSMs) and Dirac semimetals (DSMs), respectively, in which Dirac and Weyl fermions behave as quasiparticles. However, the classification of topological material does not end here. In recent years, a large variety of topological materials goes beyond the Weyl and Dirac. Some examples are double Weyl semimetals, triple point Fermion metals, and many others. In this section, various topological semimetal phases of matter have been discussed which include, DSM, WSM, nodal line semimetal (NLSM) and chiral multifold semimetal (CMSM) (Figure 2.1); more details can be found in these references [3,11,18,19,42,67,68]. After breaking TRS, the Dirac node splits into two Weyl nodes and consequently, DSM converts in WSM. The material with TRS and inversion symmetry (IS) breaking is a possible candidate of WSM with appearance of minimum one and two pairs of Weyl points, respectively. Examples of materials for all these classifications can be seen in chapter 5. These materials are intriguing because of the topology of the band structure that imparts a variety of unusual physical properties.

2.2.1. Weyl semimetals

From Herring's research in 1930s [69], it has been known that there are instances of degeneracies that are not protected by symmetry. Herring referred to them as "accidental degeneracies", as they are not present because of symmetry rather, he concluded that they are robust, which means that the degeneracy is not affected by the perturbations or defects. The Hamiltonian that describes the bands near the degenerate point has the same form as the one introduced in 1929 by Weyl [70],

$$H(k) = \chi_c \, c \, p \cdot \sigma \,. \tag{2.1}$$

Such degenerate points are now referred to as Weyl nodes/points. Here, c represents the speed of light, p is the momentum, χ_c is chirality which defines the handedness (particle direction parallel to spin or anti-parallel to spin) and σ is the Pauli spin matrix.
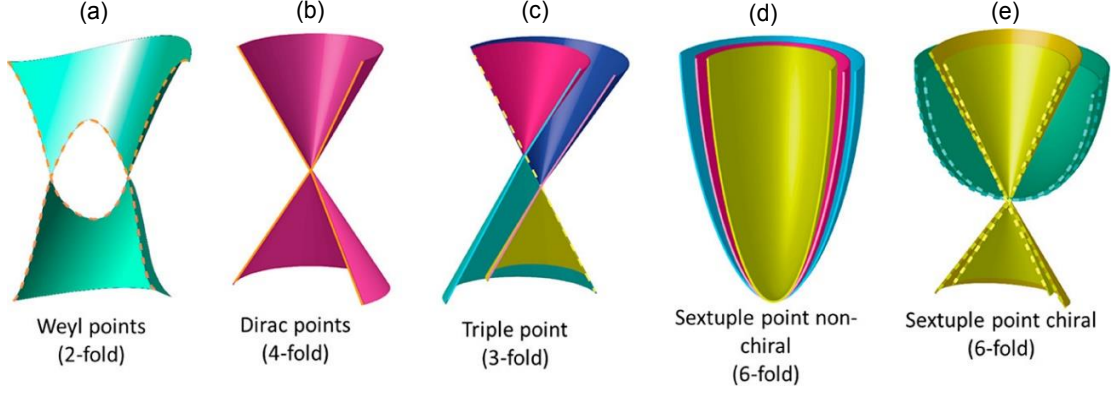
Figure 2.1: Schematic representation of different topological semimetals. **(a)** Weyl semimetal **(b)** Dirac semimetal **(c)**, **(d)**, & **(e)** multifold fermionic semimetals. [Adapted from the ref. 3]

In WSMs, the conduction band and valence band cross each other at discrete points called as Weyl nodes, and they disperse linearly in momentum space (Figure 2.1(a)). Chirality of Weyl nodes are analogous to magnetic monopoles with opposite sign of chirality. In momentum space (*k*-space), these two chiral charges of opposite chirality are connected by a topological surface state in constant energy contour known as Fermi arcs. In compounds, a symmetry element is a crucial symmetry operation in determining the circumstances for band touching. In particular, WSMs do not have a global band gap due to touching of the valence band and conduction bands in bulk, and thus any topological variant over the entire Brillouin zone (BZ) does not change. However, individual Weyl node corresponds to the topological number/chirality ±1, which is Chern number defined as integral of BC over *k*-space that encloses a Weyl node. Weyl nodes always appear in pairs either breaking of TRS and IS or both, and are doubly degenerate. Their existence does not rely on crystalline symmetry.

Even though the concept of Weyl nodes has been around for a while, it took a long time to be realized experimentally. The first real material for the experimental realization is family of TaAs [19,42,71] that has a non-centrosymmetric crystal structure (*i.e.* IS breaking). On the other hand, the material can also be magnetic in order to break the TRS; the ferromagnetic materials, such as $Co_3Sn_2S_2$, [72] Co_2MnGa, [53,73] and many others. WSMs can be classified further as type I or type II [19], depending on the tilt (asymmetric dispersion) of Weyl cones. When the Weyl cones are tilted, materials are known as type II WSMs, with examples being WTe_2 [31] and its sister compound $MoTe_2$

[74], however when the Weyl cones are linearly dispersed in all three directions without tilting, materials are referred to as type I WSMs.

2.2.2. Dirac semimetals

In general, the touching point of conduction bands and valence bands is 4-fold degenerate. In nontrivial case, these bands are linearly dispersed around the touching point, forming a bulk Dirac cone (Figure 2.1(b)), which fit in the criteria of DSMs [75]. The crossing point is known as Dirac point/node, and numerous families of such compounds have been discovered [67,76-78]. Since both TRS and IS are preserved and linear crossing between two bands is present with 2-fold degeneracy of each band. Therefore, each Dirac node can be assumed as pair of degenerate Weyl nodes of opposite chiralities. The Hamiltonian for DSMs can be written as: [11]

$$H(k) = \begin{bmatrix} \vartheta_f k \sigma & m \\ m & -\vartheta_f k \sigma \end{bmatrix}, \qquad (2.2)$$

which describes two Weyl nodes located at the same points in k-space with opposite chirality. The mass term, m in the Hamiltonian defines the massive Dirac system in which a gap opens up at Dirac node, but when this mass term is zero, the band crossing takes places at the node with 4-fold degeneracy. Usually, the 4-fold degeneracy is lifted to 2-fold degeneracy if the symmetries are broken. To avoid this, one must rely on additional symmetries which includes rotational symmetries or non-symmorphoic symmetries like screw rotation or glide planes. In the following chapter many DSMs have been discussed, which includes $ZrTe_5$ and $HfTe_5$ [50,62,79,80] classified as a massive DSM and other closes the gap at a node e.g. Cd_3As_2 [81-83], $Bi_{0.96}Sb_{0.04}$ [84,85] and more.

2.2.3. Nodal line semimetals

Depending on the dimension of the nodes crossing, it may cross along 1 D line in k-space or a closed curve and such compounds are known as nodal-line compounds [20,21]. Such crossing of lines can extend further and runs across the BZ, or in closed loop or a chain consisting of several loops inside the BZ called as nodal chain. The distinct feature of nodal line semimetals is that instead of fermi arcs, the nodal line is accompanied by a weakly dispersive surface state, projecting the nodal line onto the respective surface. Due to their special shape, they are called as drum head-like Fermi surface (FS) [86]. NLSMs has two different classifications, based on the protection of topological surface state by symmetry. These nodal lines are gapless until they are protected by symmetry either TRS or IS. In many materials, the nodal lines are usually protected by mirror symmetry, and when this symmetry is broken, these nodal lines are gapped out. However, such nodal lines are stable and protected even after the inclusion of SOC in a non-centrosymmetric structure. The compounds like CaAgAs [87], $TlTaSe_2$ [88] are examples of NLSMs, in which the nodal lines are protected even after introducing SOC. In the following chapters , NLSMs ZrMnP and HfMnP have been discussed in detail, where inclusion of the SOC

results in gapped nodal lines, exhibiting a very large anomalous Hall conductivity (AHC) [44].

2.2.4. Chiral semimetals

In chiral topological materials with multiple chiral crystal structures, a recent new class of gapless electronic excitations develops. In their crystal structure, the atoms are arranged in the shape of a spiral staircase, in which symmetry-enforced multifold band crossings at the high symmetric locations of the BZ are protected by the unique crystalline symmetry [89,90]. The famous chiral crystals are CoSi [91,92], RhSi [93,94], and AlPt [95] from the space group of 198, which exhibit multifold crossings at the BZs corner point R and zone center point Γ. The 6-fold and 4-fold degenerate points are at R and Γ, respectively. The 6-fold points are located at the variations corner, connecting the Fermi arc and extending over the entire BZ. In this regard, the longest length of Fermi arc exists in the chiral compound and it has a topological charge (Chern number) of 4 for the particular space group of 198 compounds. A change in the handedness of a chiral structure, i.e., from left-handed to right-handed chiral and vice-versa, similarly alters the corresponding Fermi arc velocities because the multifold fermions are strongly bound and protected by the crystalline symmetry. Numerous unusual phenomena, including the chiral magnetic effect, the quantized circular photo galvanic effect, and other optoelectronic phenomena are produced by the multifold crossing in chiral semimetals crystals.

2.3. Magnetic and non-magnetic topological semimetals

Topological materials can be magnetic or non-magnetic. In magnetic topological materials, TRS is already broken, which is one of the essential conditions for DSMs turning to WSMs. In magnetic materials, the magnetism and topology are entangled, and depending on the applied magnetic field direction, symmetries break, the degeneracy is lifted and a nontrivial gap is opened [40,48,49,53]. In such materials where SOC is inevitably present, the Berry phase contribution comes into account, thus enhancing many transport properties like anomalous Hall conductivity (AHC), anomalous Nernst conductivity (ANC), and many more. While in non-magnetic topological semimetals, topology comes from the present crystal symmetries. The presence of non-trivial topological states in non-magnetic topological semimetals results in many exotic physical phenomena as discussed in the next sections below.

2.4. Characteristics of magnetic topological semimetals

One of the main scientific goals of the current era is the design of energy-efficient and dissipation-free electronics. The magnetic topological materials represent a class of compounds whose properties are strongly influenced by the topology of electronic wavefunctions coupled with their spin configuration. Such materials with their novel topological features and usage of magnetic spins for spintronic applications such as quantum computing, hard disk drives, data storage, etc., can serve as an ideal foundation

to construct ultra-fast electronic devices. Because of the diverging BCs around the nodal points, several anomalous transport phenomena, including AHE and ANE, can be observed. Tuning topological bands by the use of external perturbations (such as pressure, magnetic field, etc.), the BC distribution can be tuned, allowing for the realization of a variety of unusual phenomena such as the huge topological Hall effect [96,97], gravitational anomaly [98,99] and chiral magnetic effect [100].

2.4.1. Anomalous Hall effect

Interaction between electricity and magnetism results in the fascinating phenomenon known as the Hall effect. In 1879, Edwin H. Hall [101] made the discovery that the charge carriers migrate and create potential on one side of the conductor when it is placed in a magnetic field. When magnetic field B is applied perpendicularly to the current flow I, the charge carrier deflects due to the Lorentz force acting on them, which results in an additional transverse voltage develops across the material, this is called Hall effect. Later he realized that in ferromagnetic iron (Hall, 1881) this effect is 10 times larger. This stronger effect in ferromagnetic conductors, discovered by Hall was known as the AHE.

AHE is one of the important family members of Hall effects which usually arises due to the presence of ferromagnetic properties in a material. In such materials, in addition to the linear relation between Hall resistivity and magnetic field, additional transverse momentum is gained by the charge carriers due to spontaneous ferromagnetic polarization. Moreover, the Hall resistivity curve resembles the magnetization curve, and its magnitude is affected by temperature. As mentioned above, Hall resistivity, ρ_{yx} in ferromagnets can be defined as $\rho_{yx} = \rho_{OHE} + \rho_{AHE}$ [101,102]. The first term is ordinary Hall contribution ρ_{OHE} (Figure 2.2(a)) from Lorentz force while the second term is anomalous Hall contribution, ρ_{AHE} (Figure 2.2(b)) which is a non-zero value for magnetic materials even though magnetic field is absent. Hall conductivity, σ_{xy} can be derived from Hall resistivity, ρ_{yx} and longitudinal resistivity ρ_{xx} using the relation

$$\sigma_{xy} = \frac{\rho_{yx}}{\rho_{yx}^2 + \rho_{xx}^2}.$$

(2.3)

From the σ_{xy} vs. B curve, the AHC (σ_{xy}^A) can be estimated. AHC can be both intrinsic and extrinsic contributions from different mechanisms. Figure 2.3 depicts the three basic mechanisms that were postulated to explain the contributions in AHC, which are namely intrinsic deflection, side jump, and skew scattering. The intrinsic contribution originates from anomalous velocity perpendicular to the field which further arises due to the interband coherence induced by an external electric field. And this anomalous velocity is related to BC of non-trivial electronic states. However, the extrinsic contributions arise from the skew scattering and side-jump effect, which originated due to the interactions between electrons and impurities. In side jump scattering, the electrons are deflected in the opposite direction while approaching or leaving an impurity by the opposite electric field.

However, the skew scattering is caused by the asymmetric scattering of electrons on an impurity due to spin-orbit interaction.
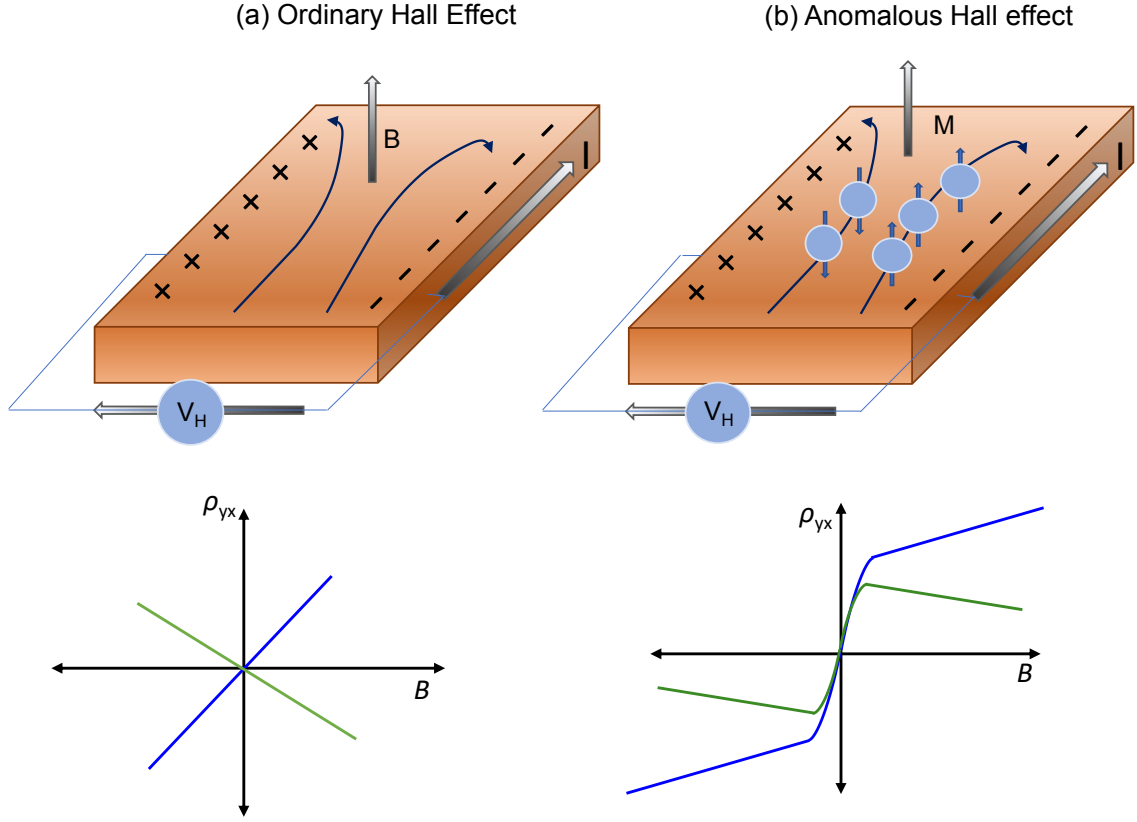
Figure 2.2: Schematic for ordinary and anomalous Hall effects. Top panel: **(a)** ordinary Hall effect, where longitudinal current under magnetic field results in transverse voltage due to Lorentz force acting on charge carriers and **(b)** Anomalous Hall effect, where electron with majority and minority spin have different anomalous velocity leads to unbalanced charge carrier concentration resulting transverse voltage. Bottom panel: shows sketch of the field-dependent Hall resistivity curve, $\rho_{yx}(B)$, for respective Hall effects. Different colors illustrate materials with different dominant charge carrier, where green and blue color signifies electron and hole as majority charge carriers.

From the recent discovery of relation between electron motion (anomalous Hall velocity) and BC, there has been a resurgence of interest in AHE driven by BC. And this relation sums AHC as integration of BC for all the occupied states in momentum space [49]. To define all these three contributions empirically, the temperature-dependent ρ_{yx}^{A}, can be expressed as

$$\rho_{yx}^{A}(T) = \alpha\rho_{xx0} + \beta\rho_{xx0}^{2} + \gamma\rho_{xx}^{2}(T), \tag{2.4}$$

where ρ_{xx0} is the residual longitudinal resistivity. The first and second terms represent the extrinsic contributions from the skew scattering and the side-jump, respectively, whereas the third term denotes the intrinsic contribution. To extract the intrinsic contribution from the above relation, a linear fit is done on the plot of ρ_{yx}^A as a function of ρ_{xx}^2 at different temperatures. The slope (γ) of the linear fit directly provides the estimation of the intrinsic value of AHC. These aspects of AHE will be used in chapter 4.
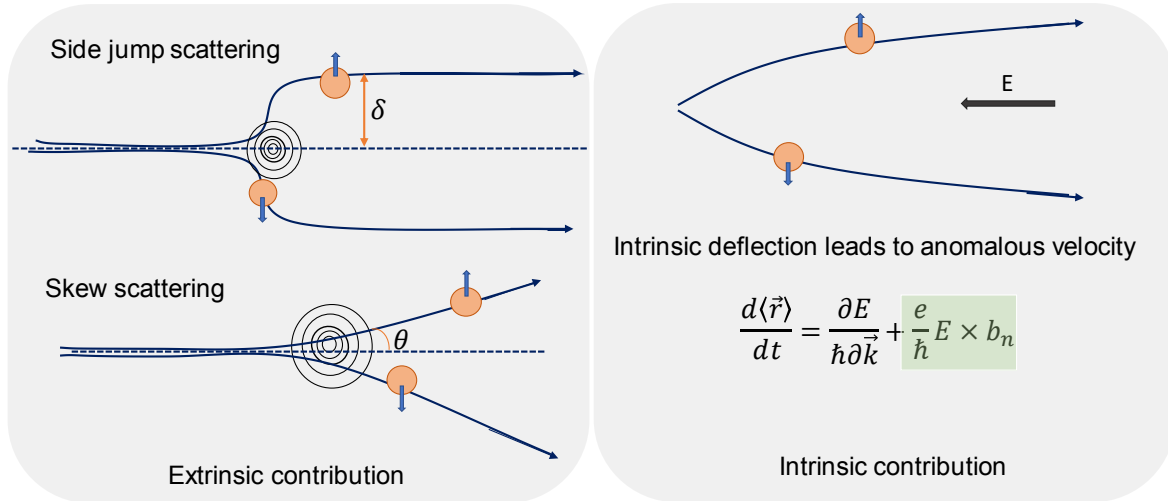
Figure 2.3: Different mechanisms involved in AHE. Schematics to illustrate different mechanism involved in AHE. [Adapted from the ref. 101]

2.5. Characteristics of non-magnetic topological semimetals

Tremendous new electrical properties have been accomplished by topological semimetals. Topologically protected states like topological Fermi arcs and drumhead surface states are robust, which makes them more interesting. Various spectroscopy measurements have directly emphasized these surface states. Peculiar quantum cyclotron orbits known as Weyl orbits resulting from the Fermi arc have been mapped by quantum oscillations. Low-energy excitations of the electron in the topological semimetals are extremely robust against crystalline disorder and defects due to the linear dispersion and spin (pseudospin) momentum locking, resulting in exceptionally high carrier mobility. On application of magnetic field, such charge carriers localize easily and exhibit non-saturating MR [31,32,103]. These localizations are more effective when the compound has charge carrier compensation between electrons and holes. Recently, large diamagnetism is also observed in many non-magnetic topological materials arising due to interband effects from the linear dispersive bands.

2.5.1. Magnetoresistance and mobility

An external magnetic field has a significant impact on electron transport, especially in the topological semimetals. Extremely large MR and high mobilities are the signature of DSMs and WSMs, which can be accredited to the massless fermions present in linearly dispersed bands together with non-trivial surface states, wherein back scattering is restricted [28,29,31,32]. MR is defined as the extent of resistance changes on applying a magnetic field. In this section, MR and mobility will be discussed, which will be helpful for chapter 6.

MR is usually calculated as the change in resistance (resistivity) under the field and is normalized by the zero-field resistance (resistivity) [104-106], i.e.,

$$\text{MR} = \frac{R(B)-R(0)}{R(0)} \quad \text{or MR} = \frac{\rho(B)-\rho(0)}{\rho(0)}. \tag{2.5}$$

Due to the close proximity of the valence band maximum and conduction band minimum in semimetals to the E_F and the low energy requirements to excite the charge carriers. As a result, the changes are easily detectable in the physical properties and are sensitive to even slight perturbations.

As we know, the resistance and mean free path of metal are inversely proportional. In presence of magnetic field, when electrons complete a considerable portion of a cyclotron orbit before being scattered, the curtailment of the mean free path in the current direction causes a change in resistance. When $\omega_c \tau \geq 1$, where τ is the time between scattering events and ω_c is cyclotron frequency, MR associated with the cyclotron motion enhances significantly. With respect to an applied magnetic field, MR usually exhibits a quadratic behavior [107] but it varies linearly in some of the topological materials [30,103,108]. If we consider a single band free electron model with spherical FS, MR is zero as it depends on interband scattering. Thus, we observe very small MR in metals, while in semimetals where massless fermions resulting in very large mobility show a large MR [32,35,36]. Normally in the semimetals, electron and hole both charge carriers are present, and due to charge carrier compensation results in such large MR [109,110]. Reports, however, also claim that some topological semimetals do not achieve charge carrier compensation. And the possible explanation is that the backscattering is suppressed by some mechanisms linked to nontrivial band topology, nevertheless, at high magnetic fields this is significantly enhanced. A strong correlation between extremely large MR and high mobility due to linearly dispersed Dirac/Weyl cones may offer some hints for a deeper understanding of the huge MR [38].

Along with a large MR, topological semimetals also exhibit high mobility. The mobility refers to the velocity acquired by the charge carrier in a unit of electric field. Mobility (μ) and conductivity (σ) are connected by the formula

$$\sigma = nq\mu \ , \tag{2.6}$$

where n and q are carrier density and charge, respectively [111]. The Hall coefficient, R_H for a single-band system can be written as $1/nq$, and thus one can relate the μ and R_H by $\mu = \sigma \cdot R_H$. The field dependence of Hall resistivity ρ_{yx}, however, departs from linearity in multiple-band systems [29,32,35]. In this scenario, the mobility and the carrier density cannot be computed directly as for a single-band system because the R_H, defined as $\partial\rho_{yx}/\partial B$, becomes field dependent. The multiple-band model which assumes that the contributions of different bands to the conductivity are additive, is a frequently used method for studying the transport parameters. In this case, two band model is more suitable to extract the values of n and μ.

Among the topological materials, there is comparatively a smaller number of compounds, which show linear MR. Due to charge carrier compensation, the majority of compounds have MR that deviates from linearity and exhibits parabolic behavior. For example, the type II Weyl semimetals unavoidably possess the Fermi level through a tilted Weyl cone and simultaneously form electron and hole bands and serve as a prime illustration of parabolic MR [29,31]. Regardless of MR behavior, disorder or inhomogeneity are two additional causes of mobility fluctuations that apply to a variety of materials. The search for new topological materials with large MR and mobility is required and will be discussed in more detail in chapter 6.

2.5.2. Quantum oscillations

Various physical quantities capture the information about FS geometry. Such quantities depend on universal constants (e, h, m, or c), and other parameters like temperature, magnetic field, crystal orientation, etc. These measured quantities help in extracting the information about electronic band structure, which is described by the geometry of the FS. Measuring such physical quantities at low temperature and high magnetic field require high quality material in single crystal form to eliminate the scattering effect. Another condition $\omega_c\tau \gtrsim 1$ needs to be fulfilled i.e. charge carriers complete the orbit without getting scattered. This condition can be achieved either by a larger relaxation time, τ or by applying a very high magnetic field. The former is rather easy (to prepare clean crystal), while the latter is hard (to produce very high magnetic field in a normal laboratory). Keeping these two quantities in mind, one might expect to see quantum oscillations.

Study of these quantities are important to understand the geometry of the FS as this will help us further to understand many other transport phenomena as they depend on its geometry. The quantities which show this oscillatory effect in resistance are known as Shubnikov–de Haas (SdH) effect, in magnetization/magnetic torque is known as de Haas–van Alphen (dHvA) effect. In 1930, Shubnikov and de Hass discovered oscillations in field dependent electrical resistivity of Bi [112,113], which led to the discovery of quantum oscillation in magnetization and torque, later in 1932 [114-116]. The theory of quantum oscillation for non-relativistic fermions is well described in earlier textbooks by D.

14

Shoenberg [112] and the literatures [82,117-119]. In this section, the key aspects of SdH effect will be discussed, which will be helpful for chapter 6.

It is very well known that when we apply the magnetic field perpendicular to an 2D electron gas system, the motions of electrons are constrained, and in classically, they are forced to move in cyclotron orbits with frequency

$$\omega_c = \frac{eB}{m^*} . \tag{2.7}$$

While in the quantum picture, electrons occupy quantized energy eigenvalues and this quantization of cyclotron motion of electrons under fields is called as the Landau quantization of the energy states. The quantized energy eigenvalues for non-relativistic fermions with a parabolic dispersion (Figure 2.4) can be written as:

$$E(k, v) = \frac{\hbar^2 k^2}{2m^*} + \hbar\omega_c \left(v + \frac{1}{2}\right), \tag{2.8}$$

where, m^* is effective mass of electrons, ω_c is cyclotron frequency, and v is the index of Landau level (LL). The energy of LLs is equally spaced by $\hbar\omega_c$. In case of relativistic fermion with linear dispersion (Figure 2.4) like in DSMs and WSMs, the LLs are not equally spaced as energy eigenvalues does not linearly depend on LL index,

$$E(v) = \vartheta_f \sin(v) \sqrt{2e\hbar Bv}, \tag{2.9}$$

where ϑ_f is Fermi velocity.

For 3D systems, these LLs form concentric cylindrical tubes as shown in Figure 2.4. When the magnetic field is increased, these tubes start to expand and leave the FS, and the resulting effect appears in the measuring physical quantity, here is resistance. Leaving effect of Landau tubes is periodic in $1/B$ and the corresponding frequency is related to the geometry of the FS and dehined by Onsager relation:

$$F = \left(\frac{\hbar}{2\pi e}\right) A, \tag{2.10}$$

where A is the extremal area of the FS perpendicular to the magnetic field. In other words, the total energy of occupied states undergoes an anomaly (it turns out to be a cusp in the variation of as $\partial E/\partial B$) and thus we expect oscillation of energy, which certainly leads to the periodic oscillations in physical quantities. The amplitude of oscillations can be described by Lifshitz Kosevich formula [112,117] and is directly proportional to the frequency and the decay of amplitude or thermal damping factor as:

$$R_T = \frac{14.69 m^* T\left(\frac{1}{B}\right)}{\sinh\left(14.69 \frac{m^* T}{B}\right)} \tag{2.11}$$
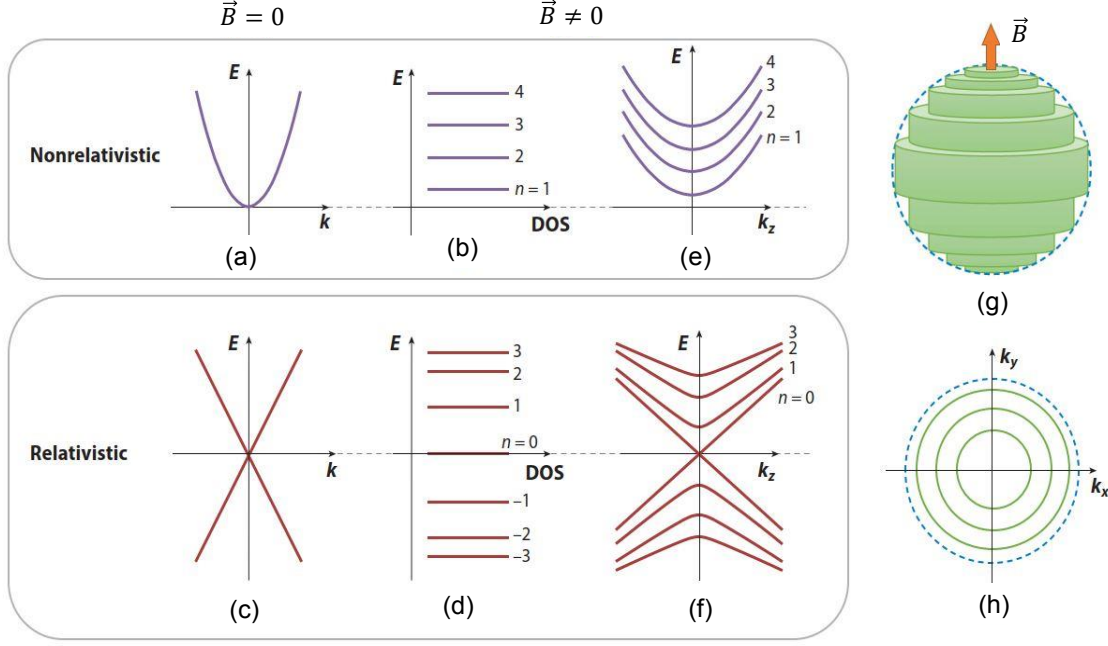
Figure 2.4: Schematic of formation of Landau level. Schematics of energy-momentum dispersions with field along *z*-direction for **(a)** parabolic dispersion (nonrelativistic) and **(c)** linear dispersion (relativistic electrons). The corresponding LLs for 2D system for **(b)** nonrelativistic and **(d)** relativistic electrons. Similar LLs for 3D system for **(e)** nonrelativistic and **(f)** relativistic electrons **(g)** Landau tubes intersecting a 3D spherical FS. **(h)** Landau rings within a 2D-FS. [Adapted from the ref. 63]

Analysis of Shubnikov-de Haas oscillations

To get the amplitude of the oscillations, the measured resistance is fitted by a polynomial and subtracted from it. The frequency of oscillation *F*, is obtained by taking fast Fourier transform (FFT) of oscillatory part, which is ideally a delta function for sine or cosine functions. Other important parameters like effective mass, quantum relaxation time, quantum mobility, Dingle temperature, Berry phase etc. can be obtained from the analysis of LK formula. For the effective mass, m^* for corresponding frequency, a fitting (using equation 2.11) is performed on temperature dependence of oscillation amplitude of that frequency, wherein field is averaged over $1/B$. From Onsager relation (equation 2.10), one can easily extract the area of enclosed FS, which is further related to Fermi wave vector k_F via $A = \pi k_F^2$, assuming a spherical FS. One can also easily extract the Fermi velocity ϑ_F using the relation:

$$m^* = \frac{\hbar k}{\vartheta_F} \tag{2.12}$$

16

2.5.3. Diamagnetism

Material that exhibit negative magnetization is usually referred to as diamagnetic material. Even though magnetic atoms are absent in these materials, itinerant electrons respond differently to an applied magnetic field, i.e. they produce a magnetic moment/force to oppose the applied field. To describe the magnetization of these itinerant electrons, a simple electron model (3D Fermi gas) is taken into consideration. Usually, in 3D Fermi gas, magnetization exhibits paramagnetic response from Pauli-spin paramagnetism and Van-Vleck paramagnetism, and diamagnetic response from Larmor diamagnetism and Landau diamagnetism, wherein the paramagnetic response dominates and is approximately three times larger than Landau diamagnetic response [120]. However, Landau (orbital) diamagnetic response can dominate over paramagnetic response, depending on the origins. In this section, diamagnetism in linearly dispersed systems will be discussed which will be helpful for chapter 5.

To describe a linearly dispersed band (DSMs), a 4×4 Hamiltonian (conduction and valence with spin degrees of freedom) in $k \cdot p$ representation is used, which is also known as Wolff Hamiltonian [121]. This Hamiltonian was used to describe the large diamagnetism in Bi. For simplicity, an isotropic system in k-space is taken into consideration and thus ignoring the spatial anisotropy of velocity. Hamiltonian for a single electron with SOC is described as:

$$\mathcal{H} = \frac{p^2}{2m} + V + \frac{\nabla^2 V}{8m^2 c^2} + \frac{1}{4m^2 c^2} p \cdot (\sigma \times \nabla V) , \qquad (2.13)$$

where σ is Pauli spin matrix, V is crystal potential, and the last term signifies the spin-orbit interaction. For isotropic case, this Hamiltonian transform to

$$\mathcal{H} = \begin{pmatrix} \Delta & i\gamma' k \cdot \sigma \\ -i\gamma' k \cdot \sigma & -\Delta \end{pmatrix}, \qquad (2.14)$$

where 2Δ is the band gap and γ' is the velocity operator, and these two quantities are characteristics of each material (material specific). Wolff Hamiltonian holds true for systems where:

(i)   The time-reversal and parity symmetries are conserved.
(ii) Conduction and valence bands are isolated from the other bands.
(iii) The band gap is much smaller than the other energy scales.
(iv) The spin–orbit interaction is strong.

As mentioned above that there are 4 contributions, out of which only three are major contributions in diamagnetic susceptibility, one as Pauli paramagnetism, second as Van-Vleck paramagnetism and third is the orbital diamagnetic part, which is enhanced due to interband effects. For example, a reasonably high value of diamagnetism in Bi was explained by the enhancement of orbital diamagnetism [122], where the interband effect dominates in the presence of strong SOC [123]. Thus, we will focus on the orbital susceptibility term (which is exact for Bloch electrons), defined as [121,124,125]

$$\chi = \frac{\hbar^2 e^2}{2c^2} k_B T \sum \text{Tr} \left[G_{\vartheta_y} G_{\vartheta_x} G_{\vartheta_y} G_{\vartheta_x} \right] , \tag{2.15}$$

where G is the thermal Green's function, and ϑ_x and ϑ_y is the velocity operator along the x and, y-directions. Solving the orbital susceptibility term for Dirac electrons simplifies to

$$\chi = \frac{e^2 |\gamma'|}{6c^2 \pi^2} K^{II} \tag{2.16}$$

where K^{II} is known as thermodynamic contribution which is defined as:

$$K^{II} = \left[-2 \ln \left(\frac{2E_c}{|\mu_k| + \sqrt{\mu_k^2 + \Delta^2}} \right) \right] , \quad (|\mu_k| > \Delta) \tag{2.17}$$

$$K^{II} = \left[-2 \ln \left(\frac{2E_c}{\Delta} \right) \right] , \quad (|\mu_k| < \Delta) \tag{2.18}$$

K^{II} terms tell us the significance of the position of chemical potential as K^{II} value reaches its peak if chemical potential, μ_k lies within the band gap. Orbital susceptibility can be further simplified to

$$\chi = \frac{e^2 \vartheta_f}{\pi^2 \hbar} ln \left(\frac{2E_c}{\Delta} \right) \tag{2.19}$$

where e is the elementary charge, $\hbar$ is reduced Planck constant, E_c is cutoff energy, ϑ_f is Fermi velocity and Δ is gap [126]. Interestingly, the orbital susceptibility only depends on ϑ_f and Δ, if interband effects are taken into consideration [125,126]. Figure 2.5 shows the behavior of orbital susceptibility with different band structures [127], illustrating the enhancement of orbital susceptibility when chemical potential lies between the Dirac/Weyl gap in case of topological materials. Interband transition is more feasible if the band gap is small, thus enhancing the orbital diamagnetism. The diamagnetism has recently been studied in various semimetals including topological semimetals like graphene [128], Bi [114,121,122,129], TaAs [130,131], Sr_3PbO [132], and $Bi_{1-x}Sb_x$, where orbital diamagnetism is responsible for such large diamagnetism [84,121,128,130-132]. The SOC is one of the main tuning parameters and is unavoidably present in the topological semimetals in which a large orbital diamagnetism can be expected.
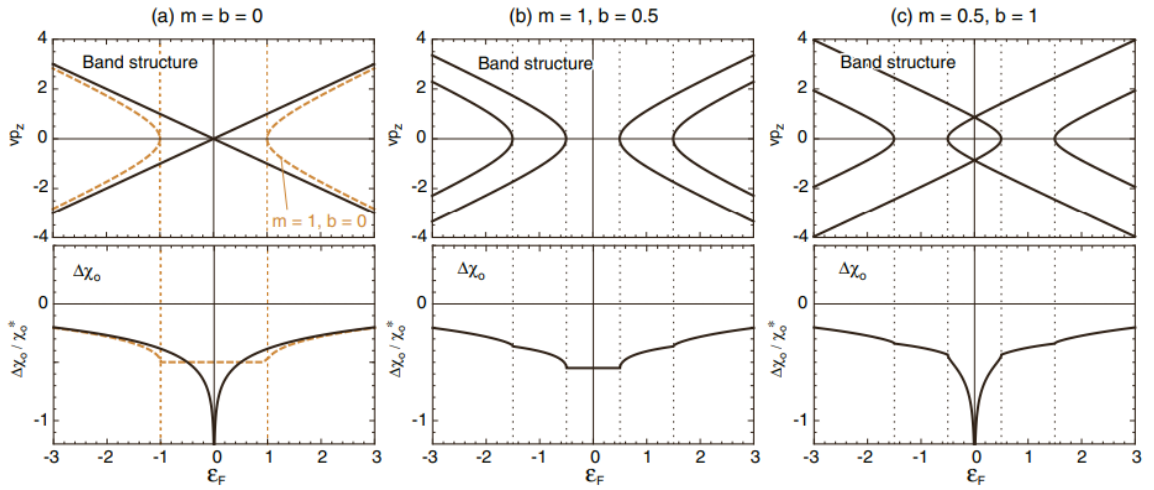
Figure 2.5: Fermi energy dependent magnetic susceptibility for trivial and non-trivial compounds. Top panel: Magnetic susceptibility, χ for **(a)** Dirac semimetals, ($m = b = 0$) and **(b)** the semiconducting case ($m = 1$, $b = 0.5$) and **(c)** the Weyl semimetal case ($m = 0.5$, $b = 1$). Bottom panel: the behavior of corresponding orbital susceptibility, $\Delta\chi_o$ against the E_F. [Adapted from the ref. 127]

3. Experimental techniques

In this chapter, we discuss the various experimental methods, which are usually used for crystal growth and the various techniques employed to characterize and measure property of all the prepared crystals.

3.1. Crystal growth techniques

One of the most important variables impact in the development of topological research is the availability of high-quality single crystals. In a single piece of material, single crystals are unbroken three-dimensional arrays of atoms with their repeating structure [105]. Single crystals need a lot of time and effort to grow, which is justified by their importance in comparison to polycrystalline counterparts [133]. Many types of experimental measurements require only single crystals. This is true not only for measuring the tensor characteristics, but also for the elimination of effects produced by grain boundaries [134,135] in polycrystalline samples. They also allow for the detection of any anisotropic physical properties originating to crystal structure along various crystallographic axes. Single crystals are especially useful for characterizing topological materials using various transport and spectroscopic techniques because of aforementioned benefits. Metal-flux, chemical vapor transport (CVT), Bridgman, optical/laser floating zone (OFZ/LFZ), and Czochralski methods are popular and useful for growing single crystals of a number of topological materials among the various available crystal growth techniques [136]. The procedure to be used is determined by a number of criteria, including volatility, thermodynamic stability, doping amount, and final crystal size. The next section discusses the various techniques available in our laboratory, which are used to grow in single crystal form of the compounds. Various measurement techniques have been utilized to study the structure, magnetic and electronic properties of these prepared materials. These techniques are described below.

3.1.1. Metal flux method

Single crystals can be grown from a solution using a metal flux that can dissolve constituent elements at relatively low temperatures [137,138]. When employing the metal flux method to grow single crystals, constituent elements are dissolved in a suitable low-melting metal flux to obtain a supersaturated solution at high temperature, which then results in single crystals with the necessary compositions after controlled cooling [139,140]. This approach can be used to generate single crystals of a variety of compounds, ranging from intermetallic Heusler compounds to more ionic oxides, chalcogenides, and pnictides [141]. Bismuth, antimony, selenium, tellurium, tin, gallium, aluminum and indium are the most common metal flux as they have very low melting point. The reactant materials are dissolved by the molten flux, which forms a homogenous solution. Nucleation of crystals begins when the liquid exceeds its saturation limit during the cooling, and growth of crystals continues till the melting point of the flux. Excess flux is eliminated by simple decanting or high-temperature centrifugation or dissolving in acid. Figure 3.1 illustrates a typical setup for the flux growth approach. The self-flux approach is used when the flux itself offers at least one of the elements in the required composition. An external flux is used in cases where we don't have any constituent which can be used as flux. NiMnSb and PtMnSb are grown using bismuth as external flux (details discussed in chapter 4B). Shapes and orientation of crystals depend on the favoring symmetry and bonding anisotropies which results in wires, ribbons, or polygons [142]. One of the major drawbacks of the flux
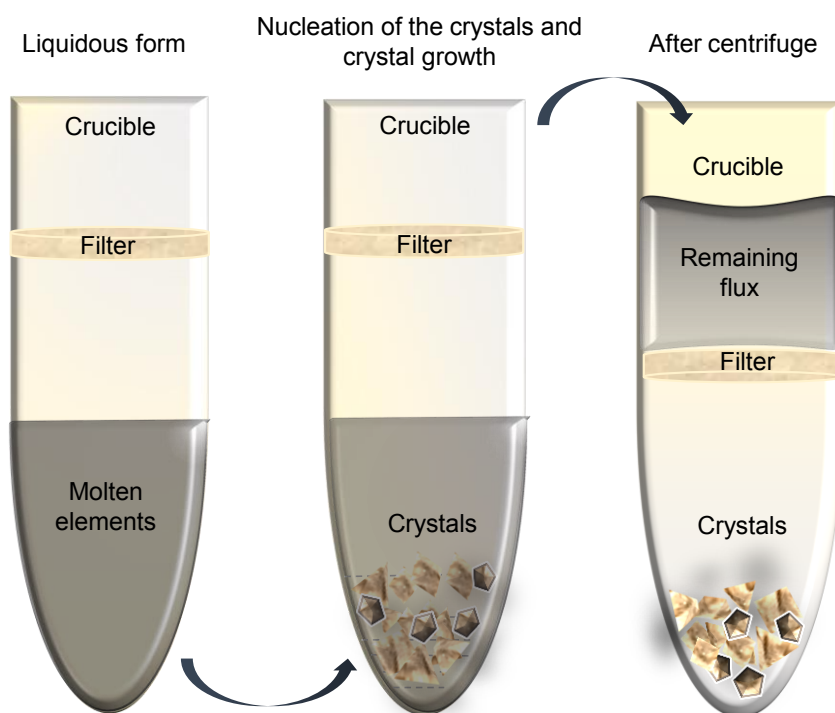
Figure 3.1: Schematic of flux growth. A typical setup for flux growth, wherein whole composition is in liquid state. Once nucleation starts, and then the growth of crystals continues. The flux is removed by centrifugation and crystals are separated from flux.

method is that metal fluxes frequently form inclusions in crystals, which are sometimes difficult to remove.

3.1.2. Chemical vapor transport

Chemical vapour transport (CVT) is a process in which a condensed phase, often a solid, is volatilized and deposited elsewhere in the form of crystals in the presence of a gaseous reactant (transport agent) [143]. Halogens and halogen compounds are common transport agents. A two-zone furnace (source T_2 and sink T_1), as well as the reactant and transport agent, are all contained in one ampoule. To maintain a temperature gradient, the reaction mixture is placed in a horizontal tube furnace with two independent heating zones (see Figure 3.2). The powder source end of the tube and the sink end, where crystal deposition takes place, are kept at different temperatures, with a continuous temperature gradient providing a conduit for gaseous species diffusion [144,145]. Growth temperature, transport direction, mass transport rate, transport agent selection, and reaction free energy are some of the characteristics that must be optimized for a successful CVT growth [146]. Convection and diffusion are the two mechanisms that govern transportation. The source and sink temperatures must be adjusted based on the free energy of the reaction between the species. An exothermic reaction shows movement from the cold to the hot zone, while an endothermic reaction indicates the opposite. Also, no transfer occurs if the reaction between the species is highly exothermic or endothermic. Most of the time, the vapor pressures of the reaction components are too low to transport them at operating temperatures without the assistance of a transport agent; thus, a transport agent is needed. The halogen-based transport agent (Cl_2, Br_2, I_2, HCl, HBr, HI, and metal halides) reacts with the starting material and volatilizes it. The imposed temperature gradient aids mass transport of gaseous species across the tube for redeposition as single crystals.
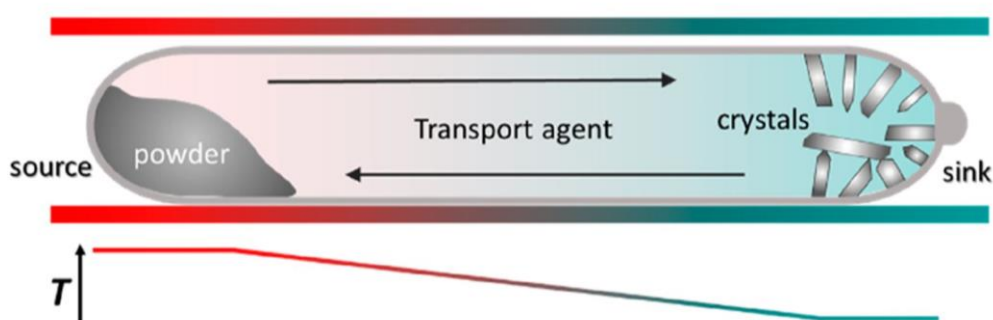
Figure 3.2: Schematic of CVT growth. CVT method wherein a source material (precursor) and transport agent put in a finite temperature gradient [Adapted from the ref. 3].

23

The success story of the topological semimetals especially Weyl semimetals has largely depended on high-quality single crystals grown through CVT. The CVT method was used to get single crystals of the many Weyl and Dirac semimetals, namely NbP, NbAs, TaP and TaAs, ZrTe$_5$ and HfTe$_5$ [38,50,52,68,131,147]. In fact, these chemicals disintegrate at extremely high temperatures before transitioning to the liquid state, the CVT approach is an obvious choice for producing single crystals of them. As a result, procedures like the Bridgman and OFZ techniques are ruled out. Furthermore, there has been limited success using the flux method to grow large, high-quality phosphides and arsenides.

3.1.3. Bridgman method

For producing single crystals of thermodynamically stable substances, high-temperature techniques are ideal. The Bridgman approach is appropriate for congruently melting compounds and materials that do not go through phase transitions between their melting point and room temperature in this situation [141]. The chemical compositions of the solid and the melt are the same when a substance is congruently melted. The process is popular because it creates quickly long crystals, and is relatively simple to use [53,148,149]. A typical Bridgman furnace set-up is shown in Figure 3.3. A temperature gradient is necessary in the furnace, which can be created by either a single heating zone or two independent heating zones. In a crucible with a pointed conical bottom [150], a polycrystalline compound is loaded as shown in Figure 3.3. A sharp temperature gradient is created by heating the material above its melting temperature. The crucible is then progressively translated into the furnace's cool zone at a constant translation velocity. The seed initiates crystal development at the interface of solid and liquid when the temperature at the bottom of the crucible falls below the solidification temperature. The entire melt transforms into a solid single-crystalline ingot after the crucible passes through the cold zone. The Bridgman technique can be used in a vertical (vertical Bridgman technique) or horizontal (horizontal Bridgman technique) [150,151]. These two arrangements have similar working principles. The crystals produced horizontally, have a good crystalline quality (low dislocation density) because they are exposed to less stress due to the free surface at the top of the melt to expand throughout the growth phase. The vertical Bridgman setup present in our laboratory is shown in Figure 3.3.
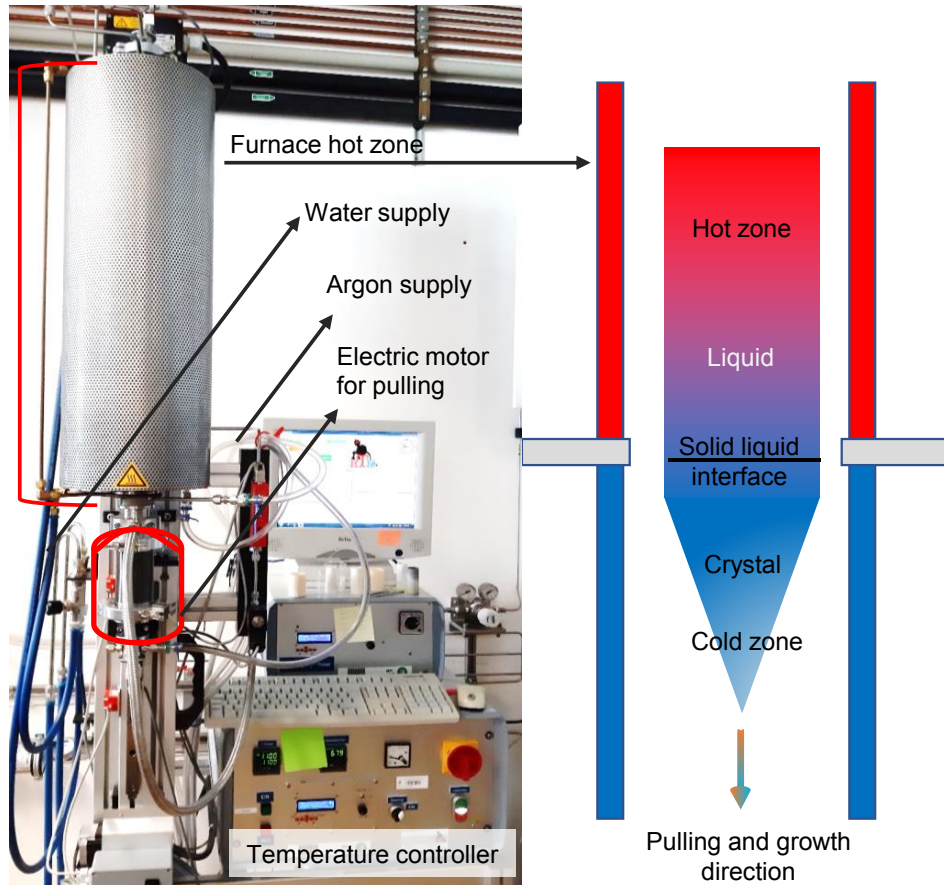
Figure 3.3: Image of used Bridgman furnace and schematic of growth process.
Image of Bridgman setup from HTM Reetz GmbH in our laboratory with internal
schematic of loading and growth mechanism of sample.

3.1.4. Floating zone

The floating zone technique is a crucible free method that avoids the contaminations
during the single crystal growth [152-154]. We employ both laser and optical   furnaces
procured from Crystal Systems Inc., Japan. Depending on the heating source, the
maximum temperature can be reached to 2600 ºC. Utilizing various flexible parameters
e.g. temperature, growth rate, shaft rotation, pressure etc., the required phase for crystal
growth can easily be tuned and achieved [153,155,156]. For growing crystals using
floating zone techniques, we prepare first polycrystalline rod which is further used as feed
and seed rods in growth process. To prepare such rod, we melt the required elements
according to their stoichiometric ratio in arc melting furnace to prepare ingots, which are
then melted further in levitation melting facility.

3.1.4. (a) Arc melting

The chamber with a copper hearth, the vacuum pump (turbo pump), the water, and the electrical power supply are the four main sections of the arc melting furnace. There are four grooves in the hearth. The copper hearth is cleaned with alcohol and brush in the first step. To prevent oxidation, one of the grooves is loaded with Ti, which acts as an oxygen getter. The remaining three grooves are loaded with weighted materials, mainly in form of granules and foils. The system is then emptied and filled with Ar three times. The chamber was then filled with Ar before the power and water supplies were turned on. The copper stages are cooled using the water supply. The tungsten tip is lowered to touch the copper stage which generates arc, then moved uniformly throughout the entire area containing the elements. First Ti is melted several times to minimize the residual oxygen. To obtain a homogenous ingot, the molten ingots are rotated over and remelted several times. The electric power supply is turned off after the ingots were melted, and the water supply was turned off after the ingots were cooled. The melted ingots were removed from the chamber. Temperatures of up to 3000°C can be achieved and the polycrystalline ingot is obtained using this approach.
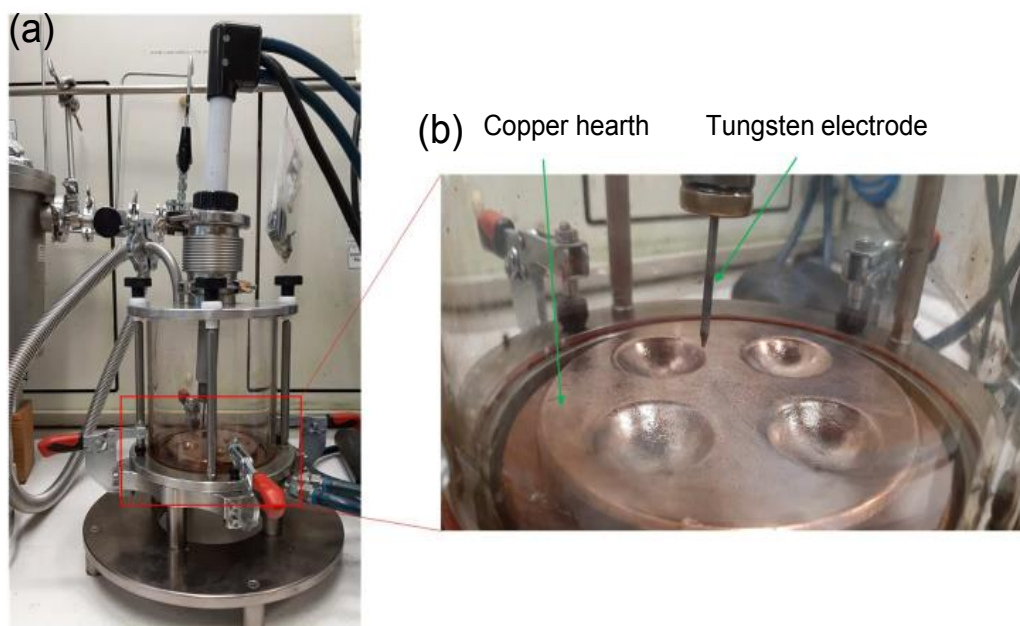
Figure 3.4: Used arc-melting setup. (a) Laboratory customized arc melter in laboratory of MPI-CPfS. **(b)** Copper hearth where raw elements are kept for melting.

3.1.4. (b) Levitation melting facility

The levitation melting facility is a multifunctional apparatus for alloying and casting of sensitive metallic rods using a levitated melt in a cold crucible. Avoidance of contamination by non-metallic inclusions is often crucial for the production of castings and feed rods of susceptible inter-metallic compounds. These inclusions are usually oxide phases which are often formed by reactions between the metallic melt, the crucible material and/or the surrounding atmosphere. Therefore, a method to prevent this contamination is the levitation melting method. A powerful high frequency generator (40 kW to 60 kW, up to 100 kHz) induces strong eddy currents in the metallic sample in a copper crucible [157]. Emerging repulsive magnetic fields cause electrodynamic suspension and magnetic levitation of the sample above the crucible. While the material melts due to resistive heating, the crucible is actively cooled and remains at low temperatures. A fast-moving water-cooled coquille stick is used to pull casting rods out of the levitated melt into a copper tube recipient as shown in Figure 3.5.
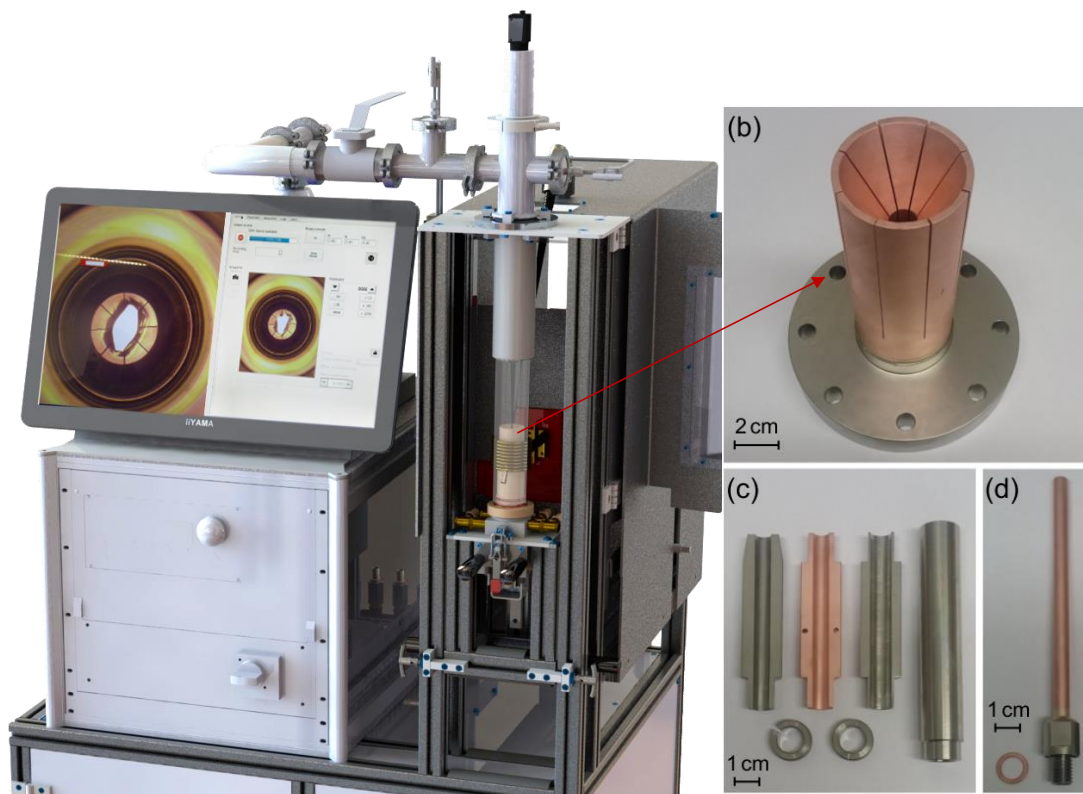
Figure 3.5: Casting rod setup for LFZ growth. (a) Levitation melting setup, **(b)** Copper crucible where ingots are placed and **(c)** different diameter crucible used to prepare rod of different diameters [Adapted from the ref. [157].

Thereafter, the sample material is in a "shell" of its own composition and does not come into contact with the wall of the crucible. The resulting rods have diameters of 5-8 mm and a length of approx. 10 cm, depending on the used crucible. Furthermore, the melting can be carried out under high vacuum up to 10^{-5} mbar or within an inert gas flow atmosphere. The vacuum is generated by a pumping unit with integrated turbo pump. The alternating electromagnetic field ensures a thorough mixing of different components in the levitated melt. The cold crucible is adjustable in the z-axis relative to the coil for an easy installation and removal of the crucible. The generator and the coil have a separate cooling circuit to prevent overheating. A high-resolution CCD (Charge coupled device) camera ensures the visual observation of the process, whereat the sample temperature is measured permanently with a two-color pyrometer. All system parameters are controllable via a comfortable GUI (graphical user interface) and processed by a PLC (programmable logic controller) unit. The levitation melting facility device enables the user to carry out several processes like cleaning metallic precursors by casting, pre-alloy materials and to cast the final material shaped as a rod for crystal growth. Induction melting was used to create rod of the NiMnSb sample analyzed in this thesis.

3.1.4. (c) Laser floating zone

The laser floating-zone (LFZ) is a very powerful and highly efficient technique to grow high-quality single crystals of various metal oxides as well as intermetallic compounds [158-161]. This is a crucible-free method where crystals are grown from the melt, for both conducting and non-conducting materials as shown by sketch diagrams in Figure 3.6. It has usually five 200-600 W lasers with wavelength between 900 and 980 nm. The geometry and power of the laser beams which impact the growth of different sample materials, rod diameters. The width and height of the beam can be modified easily and independently of each other [162-164]. The composition and pressure of the process atmosphere can be adjusted and controlled precisely with independent mass flow controllers for each gas and an easily automated pressure regulator. This set-up allows the user to control the elements diffusion between melt and atmosphere to a certain grade and to rule the growth of materials, which are difficult or impossible to produce at low gas pressures due to the higher volatility of their elements or a meta-stable nature of the desired crystal phase.
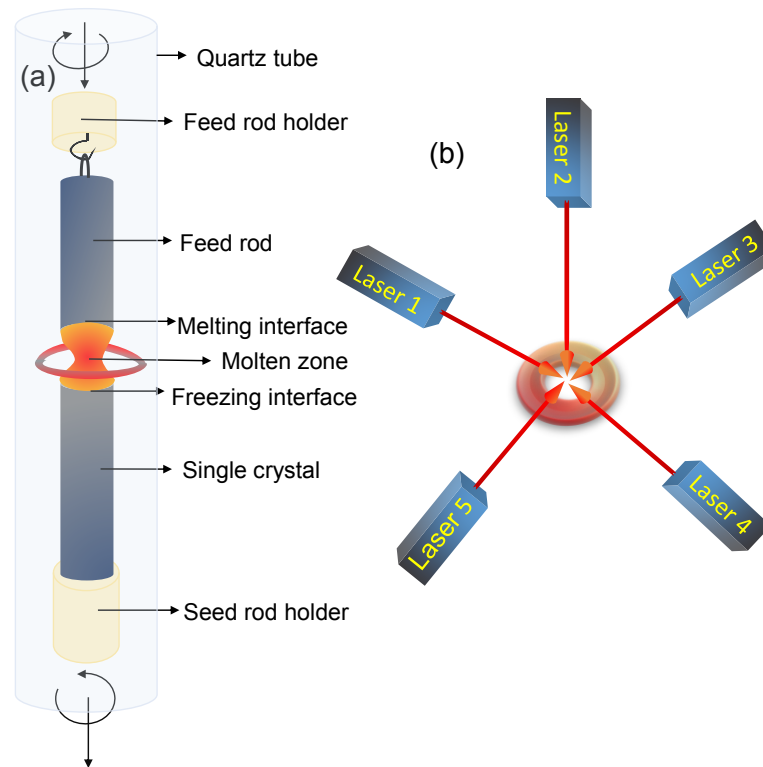
Figure 3.6: Schematic diagram of LFZ method. (a) Schematic illustration of crystal growth in LFZ, **(b)**top-view schematic illustration of an LFZ system with five laser diodes, enabling for an even distribution of irradiation intensity on the raw materials periphery [Adapted from the ref. 163].

The vacuum turbo pump is connected directly to the process chamber using short and wide-diameter pipes. This ensures good vacuum inside the process chamber below 10^{-5} mbar. A lot of processes require an inert atmosphere with a low partial pressure of oxygen in order to perform ultra-clean growths. Optional gas cleaning system removes oxygen traces out of argon reliably down to 10-12 ppm residual O_2 concentration. Furthermore, the temperature of the floating zone as well as of the feed and seed rods can be measured with high-quality bi-color pyrometer or monitored by a high-resolution IR-camera. The furnace is equipped with precise linear and rotation feed through systems for synchronous or independent rotations with up to 130 rpm and linear pulling with rate starting from 0.1 mm h^{-1}. A fast gear is implemented for rod set-up. High-pressure drives are magnetically coupled and completely capsuled without pressurized bearings. Depending on the choice, the feed rod is made of either the same target compound or different to grow the single crystal. A seed rod, which can be polycrystalline or single crystal, is used. After setting a reasonable value of power, a molten zone is formed and held between the seed and feed rods by the material surface tension [160]. After stabilization, the molten zone is moved along the length of the feed rod to grow the single crystal. The growth rate can be up to 300 mm h^{-1}, and the maximum temperature that can be reached is up to 2200 °C. The rotation of the upper and lower shafts can be independently controlled between 5 and 100 rpm, while the total length of the grown crystal can be as long as 150 mm. The stability of the

molten zone is monitored by visualizing the growth through an attached CCD camera. The crystals can be grown under different atmospheres such as O_2, Ar, and air with the maximum pressure up to 10 bar. A magnetic sealing helps to maintain the high-quality atmospheric state in high-vacuum as well as high pressure conditions. System present in our laboratory (Figure 3.7) contains 5 independent laser beam and each has power of 200 W (total 1000 W) from crystal systems corporation, Japan. We have grown NiMnSb using this system for larger crystals.
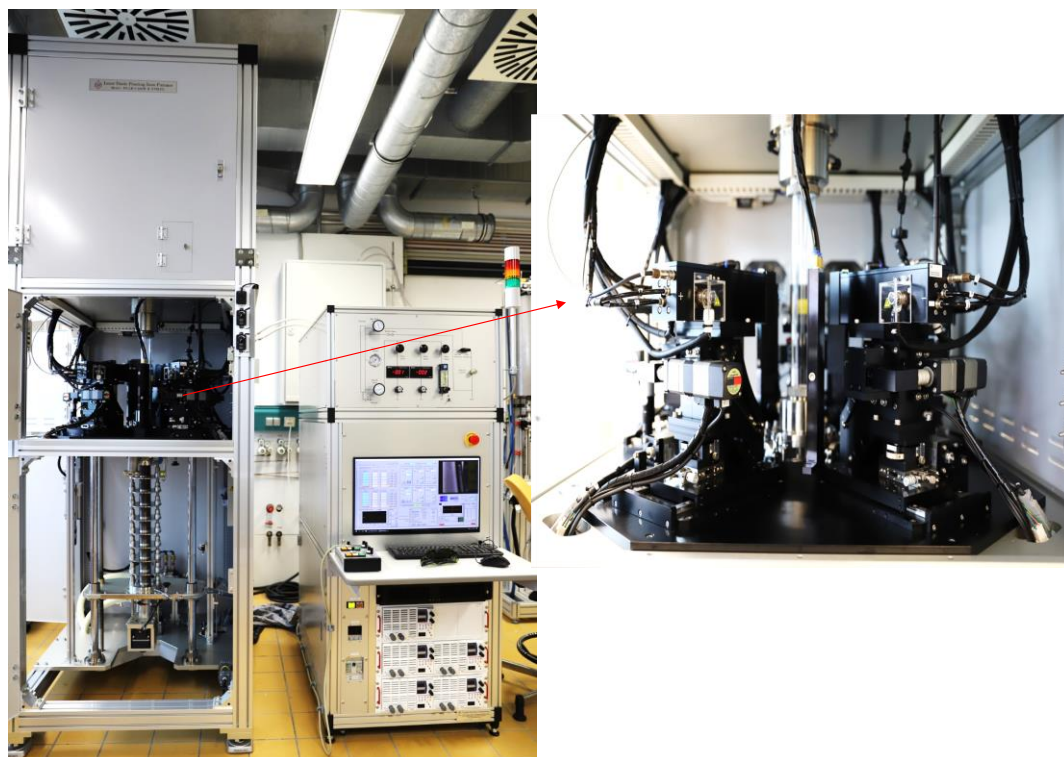
Figure 3.7: Used setup of LFZ. Setup present in our laboratory, where 5 lasers are used to melt sample for single crystal growth.

3.2. Chemical characterization

3.2.1. Energy dispersive X-ray spectroscopy

Scanning electron microscopy (SEM) in the backscattering electron mode (BSE) and polarized light microscopy were both used to detect the number of phases and confirm the compositions of single crystals that had been grown. For this purpose, the SEM of FEI Quanta 200 in the MPI-CPfS laboratory was used. The composition for single crystals is computed by the software Genesis 4000. To get more accurate compositions, the values were averaged over a large number of points. Inductively coupled plasma optical emission spectroscopy (ICP-OES) was used to figure out the total composition of single crystal. This

method was chosen because it was more accurate than wavelength-dispersive X-ray spectroscopy (WDXS) and especially energy dispersive X-ray spectroscopy (EDXS) in the case of $MnPt_2Sn_3$.

3.2.2. Single-crystal X-ray diffraction

X-ray diffraction investigations were employed for structural characterization. A quick, non-destructive method to determine a materials exact crystal structure, including information on atomic locations, lattice parameters, bond angles, and bond lengths, is single-crystal XRD. Single-crystal XRD data were collected by a Rigaku AFC7 diffractometer with Mo K_α radiation and a Saturn 724 $^+$ CCD detector was used.

3.2.3. X-rays Laue diffraction

Laue method is mainly used to determine the orientation of a large single crystal. In this method, the sample is stationary and white radiation of X-rays is used. Such a beam contains a broad range of wavelengths, which cover majority crystallographic planes and satisfy the condition of Bragg's Law [105]. The radiation from the target element molybdenum is used in this method. Laue method can give preliminary information about the symmetry of the crystals. As an example of cubic crystals, the collected pattern for [111] is 3-fold and is 4-fold for [100] [165]. After recording patterns, analyses are done with the help of orient express software.

3.3. Physical properties measurements

3.3.1. Magnetic measurements

All the magnetic measurements were performed in a superconducting quantum interference device (SQUID) magnetometer [166] (MPMS-3) from Quantum Design Inc. The temperature range of measurements was 1.8-400 K in standard option and 300-1000 K in the oven mode option. The magnetic field range of the measurements was −7 to +7 T.

3.3.2. Electrical transport measurements

All the electrical transport measurements were done in physical property measurement system (PPMS) from Quantum Design Inc. Physical properties such as Hall resistivity and longitudinal resistivity of the compounds were measured in a five-probe or four-probe option. The standard temperature range is 1.8 K to 400 K and the applied field was +9 T to −9 T.

Small misalignment of the contacts can lead to a magnetoresistive component in the measured Hall signal and vice versa. To account for such misalignment effects, the asymmetric contributions for the longitudinal resistivity and for the Hall resistivity were calculated from the following equations:

$$\rho_{xy}^{asy}(H,T) = \frac{1}{2}\left[\rho_{xy}(+H,T) + \rho_{xy}(-H,T)\right] \tag{3.1}$$

$$\rho_{xx}^{asy}(H,T) = \frac{1}{2}[\rho_{xx}(+H,T) - \rho_{xx}(-H,T)] \tag{3.2}$$

To get actual value of $\rho_{xy}(H,T)$, the $\rho_{xy}^{asy}(H,T)$ part was subtracted from the measured $\rho_{xy}(H,T)$ for each field direction. A similar procedure was also performed to get actual value of $\rho_{xx}(H,T)$. Notably, the same procedure was applied for both field-sweep as well as temperature-sweep measurements. For example, two sweeps of the temperature dependent Hall effect were collected. One with positive magnetic field, the other with negative and subsequently these data were symmetrized.

4. Anomalous Hall conductivity in room temperature ferromagnets

Hall effect is one of the oldest discoveries, which are deeply used in modern science, the arising Hall voltage is in linear proportional to the applied magnetic field but this rule breaks in case of magnetic material. The quantum version of Hall effect- QHE creates a bridge between geometry and topology. These two quantities are connected through a notion of BCs in various systems, for example, TIs, superconductors and semimetals with topological Dirac, Weyl and beyond the Dirac-Weyl fermion excitations. One of the important emergent features of magnetic topological semimetals is the AHE and its dissipationless nature makes it appealing for applications. AHE is basically an transport phenomenon in ferromagnets which is a consequence of breaking of TRS and spin orbit interaction[101]. TRS is broken as result of appearance of spontaneous magnetization which influences the motion of electrons, giving rise to an addition contribution in term of AHE together with the ordinary Hall signal. The AHE results a non-zero value even in the absence of magnetic field. This was first observed in ferromagnetic materials and was first explained by Karplus and Luttinger years ago [167]. AHE has two major mechanisms involved, one is extrinsic which is result of spin-impurity scatterings (skew and side jump), while on the other hand is the intrinsic mechanism which originates from BC related to topology of electronic bands [102]. BC is an equivalent of magnetic field in the momentum space, originating to the electronic entanglement between the valence and conduction bands. Since researchers discovered a relation between electron motion (anomalous Hall velocity) and Berry phase, there has been a resurgence of interest in AHE driven by BC in recent years. And this relation sums AHC as integration of BC for all the occupied states in momentum space [49]. This sum over a nodal-line or across the topological nodes are usually high for topological semimetals.

4A. Nodal line derived large anomalous Hall conductivity in ZrMnP and HfMnP

4A.1. Preface

Topological materials have attracted substantial attention owing to their nontrivial electronic band structures that offer the potential for revolutionary device applications. A nontrivial band topology appears when the band inversion occurs in k-space; *i.e.*, the conduction band is below the valence band with respect to their natural order. This inversion may occur in several manners, and the corresponding wave function of each band twists and induces a finite Berry phase that is associated with the BC. In addition to the accidental touching of bands at a node, they may also form a line, and such compounds are known as topological nodal-line compounds. In absence of magnetic field, the nodal lines are protected by mirror symmetry, [20,107,168-172] giving rise to a drum head-like topological surface state [20,168-170]. In ferromagnets, all bands are usually singly degenerate but in the presence of mirror planes, they may be doubly degenerate in the form of a Dirac nodal line. In such materials, the magnetism and topology are entangled, and depending on the applied magnetic field direction, the degeneracy of the nodal-line is lifted and a nontrivial gap is opened [49,173]. The BC sum over such gapped lines is enhanced significantly. The BC that is associated with nontrivial bands as a source of AHC has recently been recognized in various compounds; for example, the chiral antiferromagnets Mn_3Sn [174] and Mn_3Ge, [175] kagome lattice ferromagnet $Co_3Sn_2S_2$, [176] and nodal-line ferromagnets Co_2MnZ (Z = Ga, Al) [40,173,177] and MnAlGe [178]. The presence of nodal lines has been revealed experimentally by spectroscopy [178,179]. Among these, Co_2MnZ has exhibited the record AHC value of 1600 to 2000 $\Omega^{-1}cm^{-1}$ at 2 K and many more compounds from the same family are awaiting experimental realization, which suggests the crucial roles of mirror planes [49]. Apart from the nontrivial band topology, an important factor for the occurrence of large AHC is SOC. We observed AHC of 2000 $\Omega^{-1}cm^{-1}$ for ZrMnP and 2840 $\Omega^{-1}cm^{-1}$ for HfMnP. In this work, our approach was to study the AHC in a system with large SOC and that contained ample mirror planes in the crystal structures.

Previously only magnetization was focused and reported by Lamichhane et al. The a- and c-axes were the easy and hard axes for the magnetic moments, respectively, resulting in large magnetic anisotropy [180]. The measured values of the saturation magnetization at 2 K were 1.8 μ_B f.u.$^{-1}$ for ZrMnP and 2.0 μ_B f.u. $^{-1}$ for HfMnP. However, magneto-transport of the both compounds were still not investigated. Our first-principles calculations revealed that these compounds possess Dirac nodal-lines at different energies, which are protected by the various mirror planes. Therefore, the presence of these topological states can result a peculiar magneto-transport of the topological materials. In this chapter, the techniques employed to grow the single crystals and to study their magnetic and magneto-electrical properties have been discussed.

The texts and figures are taken from the following publication-

Sukriti Singh, Jonathan Noky, Shaileyee Bhattacharya, Praveen Vir, Yan Sun, Nitesh Kumar, Claudia Felser, and Chandra Shekhar, **Anisotropic nodal-line-derived large anomalous Hall conductivity in ZrMnP and HfMnP**, *Adv. Mater.*, **33**, 2104126 (2021).

4A.2. Growth and crystal structure

Crystal growth

The single crystals of ZrMnP and HfMnP were grown by the self-flux method, similar to that reported by Lamichhane et. al. [180]. The flux composition of Mn-P is the eutectic point ratio as shown in Figure 4A.1. Initially, Mn chips (99.99%) were cleaned by placement in an evacuated quartz tube, heated to 1000 °C at a rate of 200 °C h^{-1}, and maintained for 24 h before switching off the furnace. Shiny silver Mn pieces were obtained, which were subsequently ground into powder. For the single crystal growth, grounded Mn powder, P lumps (99.999%), and small pieces of Zr/Hf from their foils (99.8%) were used in a (Zr/Hf)$_{1.25}$Mn$_{85.9}$P$_{12.85}$ stoichiometry ratio and placed in the dried alumina crucibles. Thereafter, the crucibles were sealed in a quartz tube with 5 mbar partial pressure of argon. The entire reaction mixture was placed in a box-furnace and heated in two steps: first to 250 °C at a rate of 50 °C h^{-1} and maintained for 3 h, and subsequently to 1180 °C at the same heating rate. At 1180 °C, the reaction was maintained for 12 h for homogeneity. Slow cooling to 1025 °C was conducted over 180 h, at which time the additional flux was removed with centrifugation. Silver needle-shaped single crystals were obtained from the above temperature profile. The crystals of both the compounds were stable in air and moisture.
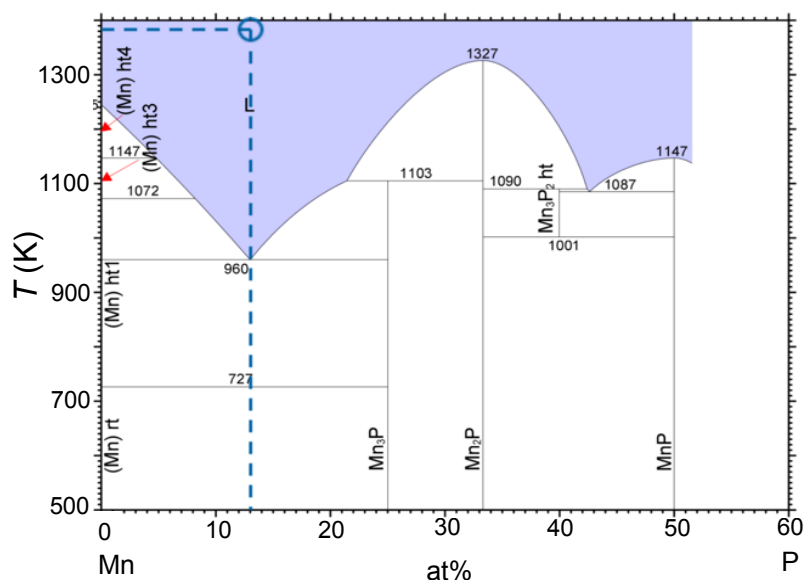
Figure 4A.1: Phase diagram of Mn-P. Phase diagram of Mn-P in which dotted line (eutectic composition) is used for the crystal growth. [Adopted from Springer Materials].

Chemical characterization and crystal structure

Elemental analysis for these compounds were done by EDXS analyzer which further confirmed that the composition of the compounds was close to 1:1:1. Before measuring structural and direction-dependent physical properties, the directions of the crystals were analyzed by the Laue diffraction method. The single crystallinity of the as-grown crystal was evaluated by white-beam backscattering Laue XRD.

The crystals of ZrMnP and HfMnP grew in a needle shape along the *b*-axis with well-defined facets, as demonstrated by the Laue X-ray diffraction (Figure 4A.2(b)). Well defined rectangular facets are [101] direction which is examined by Laue diffractometer and diffraction patterns are shown in Figure 4A.2(b). This figure shows the Laue diffraction patterns together with the superimposed simulated patterns along [101].
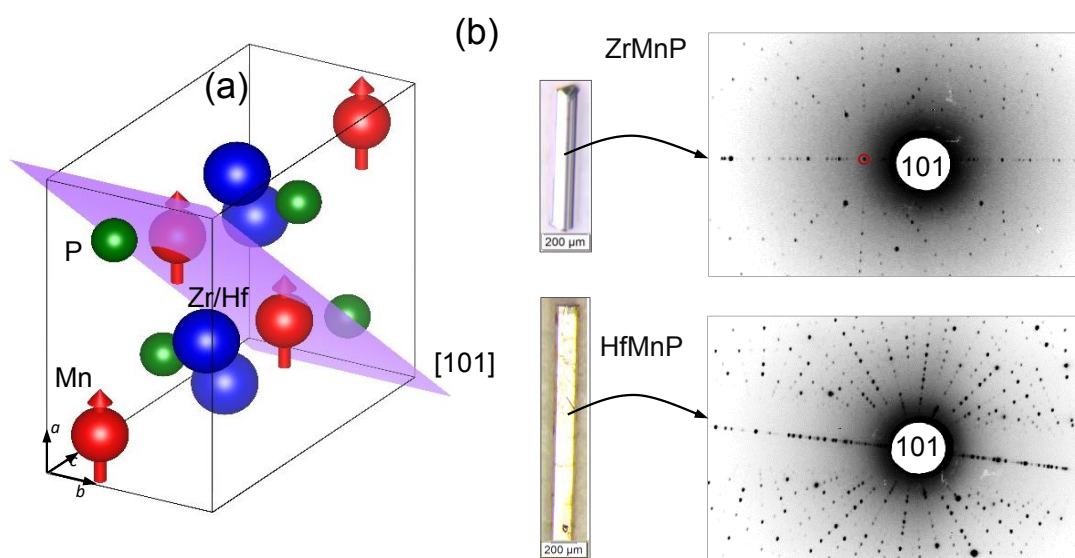
Figure 4A.2: Crystal structure, crystal image and Laue pattern of ZrMnP and HfMnP. (a) Orthorhombic unit cell of compounds with space group *Pnma*. The highlighted (101) is one of the mirror planes. **(b)** [100] facet of as-grown crystals and their corresponding Laue patterns, where the needle direction is [010].

ZrMnP and HfMnP are particularly important compounds, which crystallize in a TiNiSi-type orthorhombic structure with space group (SG) *Pnma* (No. 62) (Figure 4A.2(a)). Single-crystal X-ray analyses demonstrated the lattice parameters to be $a = 3.64$ Å, $b = 6.45$ Å, and $c = 7.53$ Å for ZrMnP and $a = 3.61$ Å, $b = 6.38$ Å, and $c = 7.47$ Å for HfMnP.

4A.3. Magnetization

Transition metal pnictides are of significant interest as they both possess a high ferromagnetic T_C above room temperature and large magnetic anisotropy. Both ZrMnP and HfMnP are ferromagnets and their observed T_C values were 320 and 370 K, respectively (Figure 4A.3(a)). Only the Mn atoms contributed to the magnetism (as indicated in Figure 4A.2(a)).

A magnetic transition from the ferromagnetic to paramagnetic state was observed in the temperature-dependent magnetic measurements with a magnetic field $B = 1$ T along [100], as illustrated in Figure 4A.3(a). The ZrMnP exhibited a relatively higher T_C (370 K) than that of HfMnP (320 K), which was consistent with the resistivity measurements shown in next section. Figure 4A.3 depicts the temperature dependent magnetization and field dependent magnetization of ZrMnP and HfMnP. Figure 4A.3(b) shows the anisotropy present in ZrMnP and HfMnP. The linear extrapolation from the high field region of the easy axis [100] field dependent magnetization curve to zero field determines saturation magnetization M_S. ZrMnP has a slightly greater M_S of 1.8 μ_B f.u.$^{-1}$ at 2 K than HfMnP of 1.6 μ_B f.u.$^{-1}$ at 2 K. To estimate the anisotropy field between the hard axis [001] and the easy axis [100], an extrapolation of tangents from the linear region of field dependent magnetization curves is done. For ZrMnP, the anisotropy field for the [001] axis was determined to be 4.6 T while for HfMnP, it was determined to be 10 T. Figure 4A.4 shows field dependent magnetization of ZrMnP and HfMnP along easy axis [100] and hard axis [001] measured at various temperatures in range of 2-400 K. As, temperature approaches Curie temperature, we see decrease in saturation magnetization, and above Curie temperature, magnetization curve becomes linear indicating loss of ferromagnetic behavior. It is also noteworthy that neither ZrMnP nor HfMnP shows a significant coercivity.
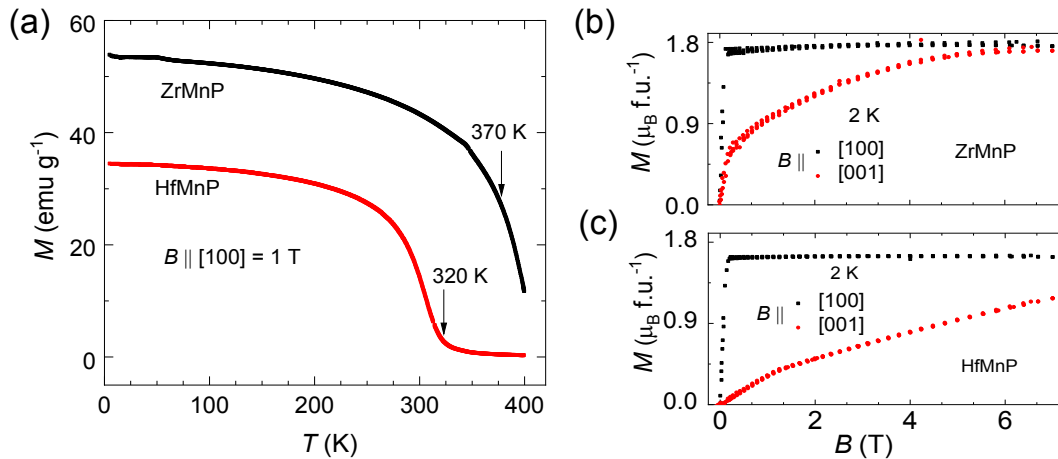
Figure 4A.3: Magnetic properties of ZrMnP and HfMnP. (a) Temperature dependent magnetization of ZrMnP and HfMnP with applied magnetic field of 1 T along *a*-axis, where arrow indicate the Curie temperature T_C. **(b)** Field dependent magnetization with applied field along easy axis (*a*-axis) and hard axis (*c*- axis)
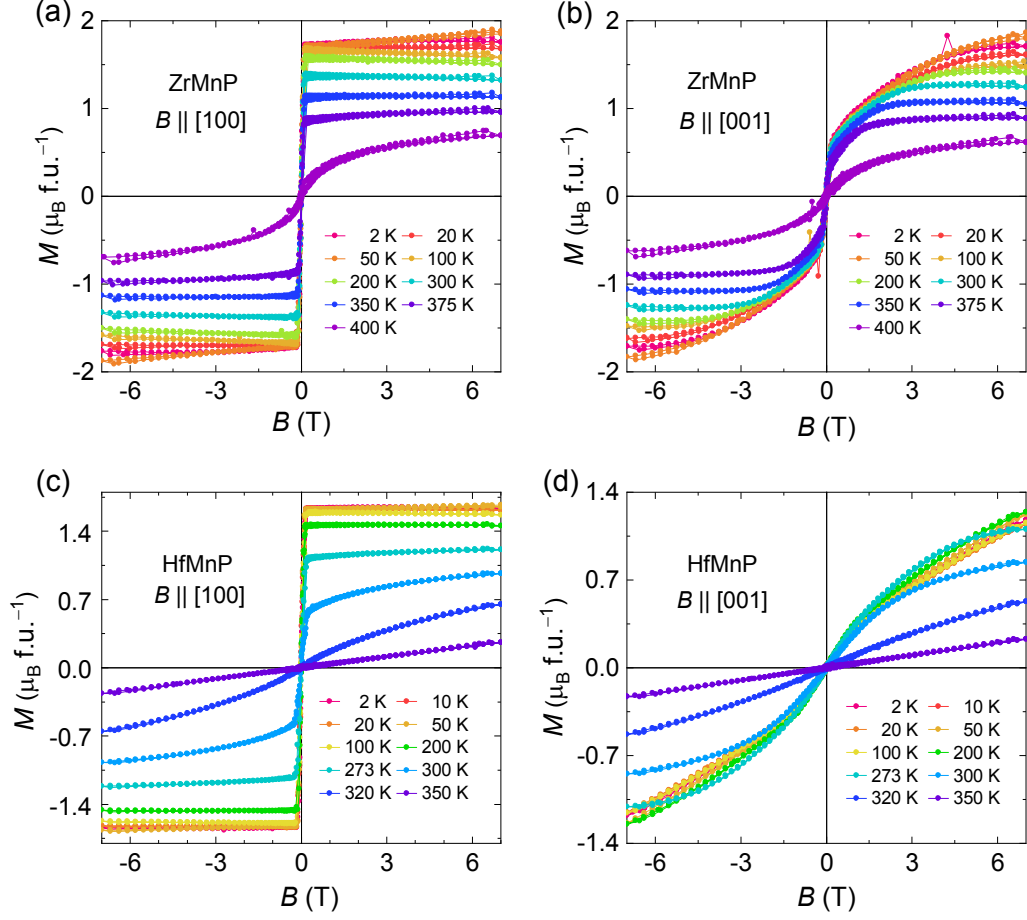
Figure 4A.4: Magnetization in ZrMnP and HfMnP. Field dependent magnetization measured at different temperatures with applied field along **(a)** & **(c)** a-axis, **(b)** & **(d)** c-axis for ZrMnP and HfMnP, respectively.

4A.4. Magneto-transport of ZrMnP and HfMnP

Temperature-dependent resistivity

The zero-field longitudinal resistivity ρ_{yy} (Figure 4A.5) of both compounds increases as the temperature is increased, indicating metallic behavior. For the current $I \parallel [010]$, the value of ρ_{yy} at 2 K was 3.4×10^{-5} Ω cm for ZrMnP and 2.9×10^{-5} Ω cm for HfMnP. Both compounds exhibited similar values of the residual resistivity ratio [RRR = ρ_{yy} (300 K)/ ρ_{yy} (2 K)], which was 5.5, reflecting high quality of the crystals. The kinks in their respective resistivity measurements corresponded to the magnetic transition. Throughout this chapter, the a-, b-, and c-axes of the compounds are equivalent to the x-, y-, and z-directions in the measurements, respectively. Figure 4A.6 depicts transverse magneto-resistivity measured with applied magnetic field along [101] at various temperature in range the of 2-400 K, where negative slope is seen in both compounds. This indicates negative

magnetoresistance due to the reduced spin disorder scattering with the applied magnetic field.
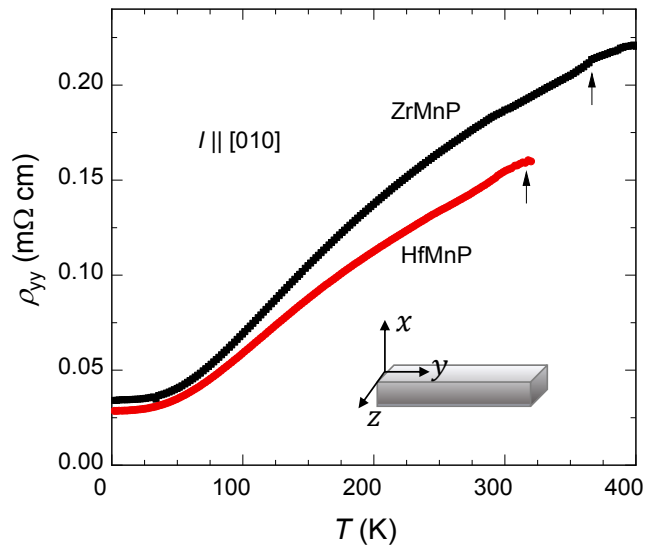
Figure 4A.5: Temperature-dependent longitudinal resistivity. ρ_{yy} along [010], indicating a metallic character with the kinks (indicated by arrows) corresponding to the ferromagnetic transition temperature (T_C) of the compounds.
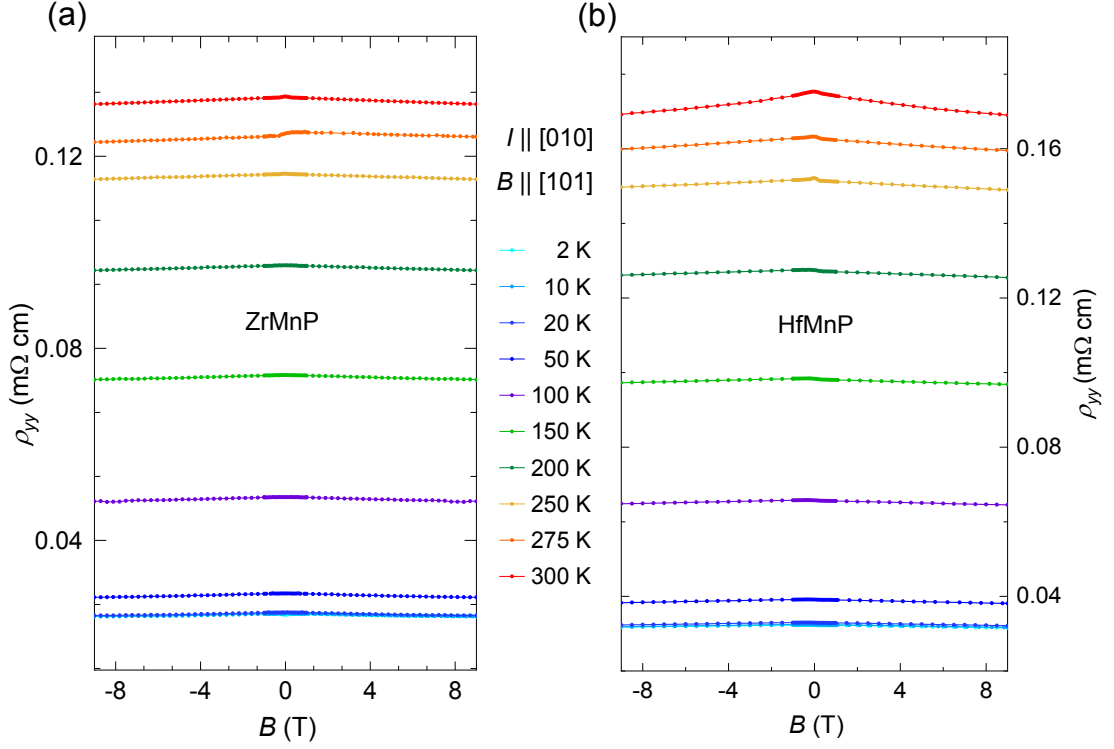
Figure 4A.6: Field-dependent transverse magneto-resistivity. ρ_{yy} along [010] with applied field along [101] **(a)** ZrMnP **(b)** HfMnP, where negative slope in transverse magneto- resistivity indicate suppression of spin disorder scattering.

Hall effect measurements

So far, only magnetization was reported for ZrMnP and HfMnP by Lamichhane et al [180]. Magnetic compound with topological surface states can lead to exciting transport properties and thus magneto-transport study of both the compounds were examined and discussed in this section.

As illustrated in Figure 4A.2, the grown crystals of both compounds had a needle shape, which provided the opportunity to perform Hall measurements without any additional work of cutting the crystals in a Hall bar. The flux crystals grow with a preferred growth orientation along [101], and thus we have performed transport measurement with applied magnetic field in direction [101]. We further polished the surface to obtain easy axis [100], and performed measurements with applied magnetic field in direction [100]. The magnetic field-dependent Hall resistivity ρ_{yx} was measured at various temperatures in the range of −9 to +9 T. For better representation, data are shown in the range of −2 to +2 T.
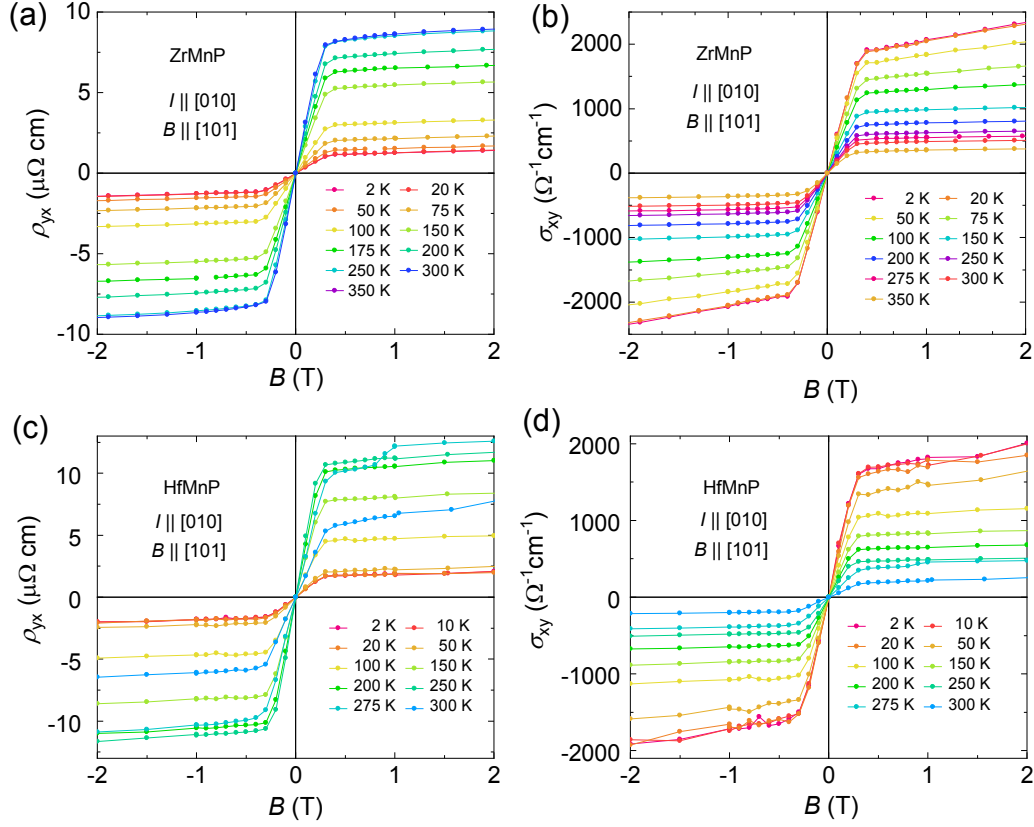
Figure 4A.7: Hall resistivity and conductivity of ZrMnP and HfMnP along [101]. Hall resistivity ρ_{yx} and conductivity σ_{xy} of ZrMnP and HfMnP when field $B \parallel [101]$ and current $I \parallel b$ in the field range of ± 2 T. The first-row panels for ZrMnP: **(a)** field-dependent measured ρ_{yx} at several temperatures and **(b)** corresponding calculated σ_{xy} using equation 2.3. The same measurements are provided in the second-row panels **(c)** & **(d)** for HfMnP.

Applied magnetic field along [101]

The observed behavior of ρ_{yx} is presented in Figures 4A.7 (a) & (b), where the current was passed along the *b*-axis and the magnetic field was applied along the [101] direction; that is, preferred orientation while growth. In ZrMnP, the sign of the observed Hall resistivity data suggests that holes are the majority of charge carriers, and this is same for HfMnP as well. But this change when we measure in different direction as shown in next section.
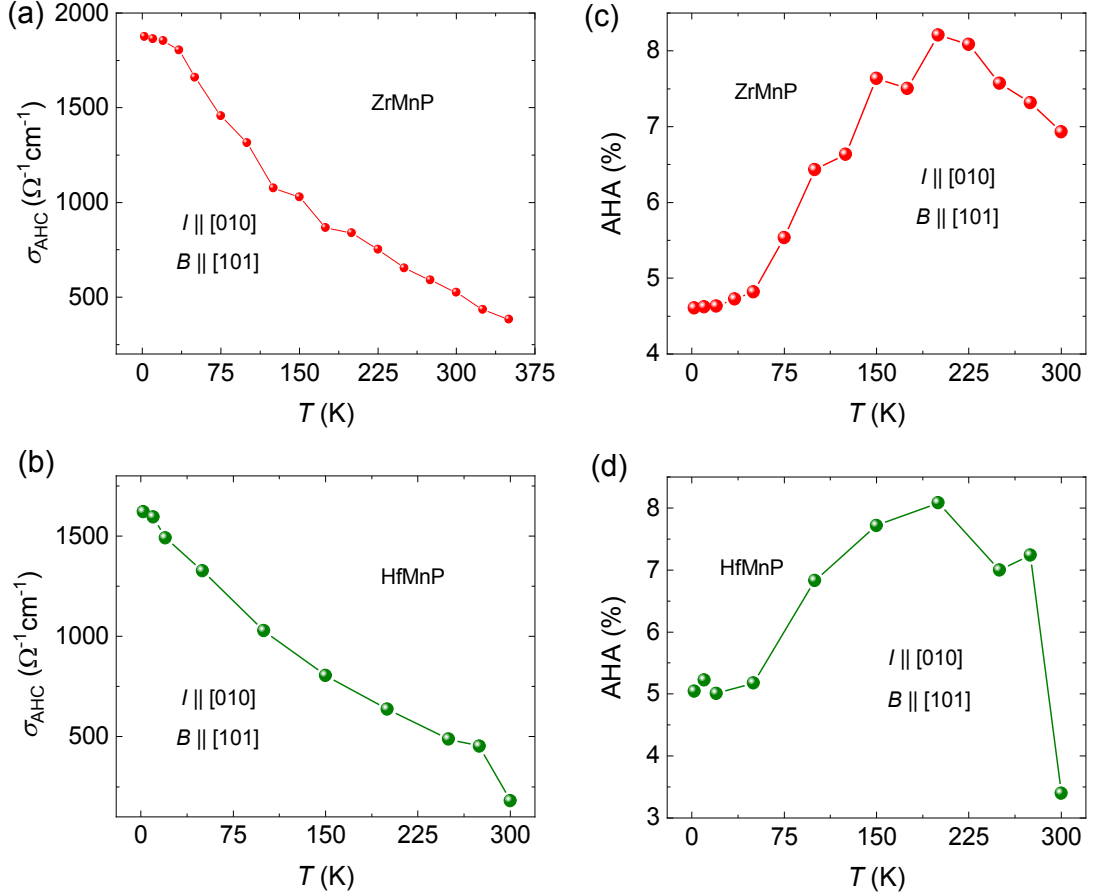
Figure 4A.8: AHC and AHA for ZrMnP and HfMnP. (a) & **(b)** Temperature dependent AHC for ZrMnP and HfMnP, respectively **(c)** & **(d)**Temperature-dependence measured AHA for ZrMnP and HfMnP, respectively, where AHA is defined as the ratio σ_{AHC}/σ_{yy}.

An anomaly is observed in the ρ_{yx} measurements, which is attributed to the anomalous Hall effect (AHE) that normally appears in metallic ferromagnets; that is, a sharp increase at a lower field, followed by saturation with a further increase in the field. Moreover, it exhibits a resemblance with the magnetization curve; however, its saturation value decreases with a decrease in the temperature. The measured ρ_{yx} in ferromagnets is usually defined as a combination of two terms: $\rho_{yx}(T) = \rho_{OHE}(T) + \rho_{AHE}(T)$, where ρ_{OHE} is the contribution from the ordinary Hall effect that arises from the Lorentz force acting on the charge carriers, whereas ρ_{AHE} is the anomalous Hall contribution, which is unique to magnetic samples as discussed in section 2.4.1 [101]. The value of ρ_{AHE} at 2 K is 1.03 μΩ cm for ZrMnP and 1.75 μΩ cm for HfMnP (Figures 4A.7(a) & (c)), which indicates an increasing trend, and reaches 8.3 μΩ cm and 10.5 μΩ cm, respectively, at 300 K. The ρ_{AHE} value at a fixed temperature was estimated by interpolating the high field value of ρ_{yx} to the zero-field as the y-intercept. Similarly, the AHC σ_{AHC} was estimated from the Hall conductivity as the y-intercept. The σ_{AHC} at 2 K is 1740 Ω^{-1}cm^{-1} for ZrMnP and 1585

$\Omega^{-1}\text{cm}^{-1}$ for HfMnP which is observable up to their transition temperature (Figures 4A.8(a) & (b)). Temperature dependent AHC and Anomalous Hall angle (AHA) is shown in Figure 4.8. The AHA defines the ratio of the AHC to the longitudinal conductivity σ_{yy} at the zero-field: AHA = σ_{AHC}/σ_{yy} ($B = 0$). The AHA exhibits a linearly increasing trend with an increase in the temperature, but decreases further after peaking at approximately 200 K.

Applied magnetic field along [100]

Figures 4A.9 (a) & (d), illustrate measured Hall resistivity for ZrMnP and HfMnP where the current was passed along the *b*-axis and the magnetic field was applied along the *a*-axis that is, easy axis. The sign of the measured Hall resistivity data for the ZrMnP indicates that the holes constituted the majority of the charge carriers, whereas in the case of HfMnP, the majority of charge carriers were electrons. These findings are in good agreement with the numerical results from the density functional theory (DFT) calculations presented in next section "First principle calculations". A hole pocket exists around the *U*-point in the first Brillouin zone, which cuts the E_F for ZrMnP but not for HfMnP. The value of ρ_{AHE} at 2 K is 2.5 $\mu\Omega$ cm for ZrMnP and 2.3 $\mu\Omega$ cm for HfMnP (Figures 4A.9(a) & (d)), which indicates an increasing trend, and reaches 17.2 $\mu\Omega$ cm and 16 $\mu\Omega$ cm, respectively, at 250 K. The σ_{AHC} at 2 K is 2000 $\Omega^{-1}\text{cm}^{-1}$ for ZrMnP and 2840 $\Omega^{-1}\text{cm}^{-1}$ for HfMnP (Figures 4A.9(b) & (e)), which is observable up to their transition temperature (Figures 4A.9 (c) & (f)).
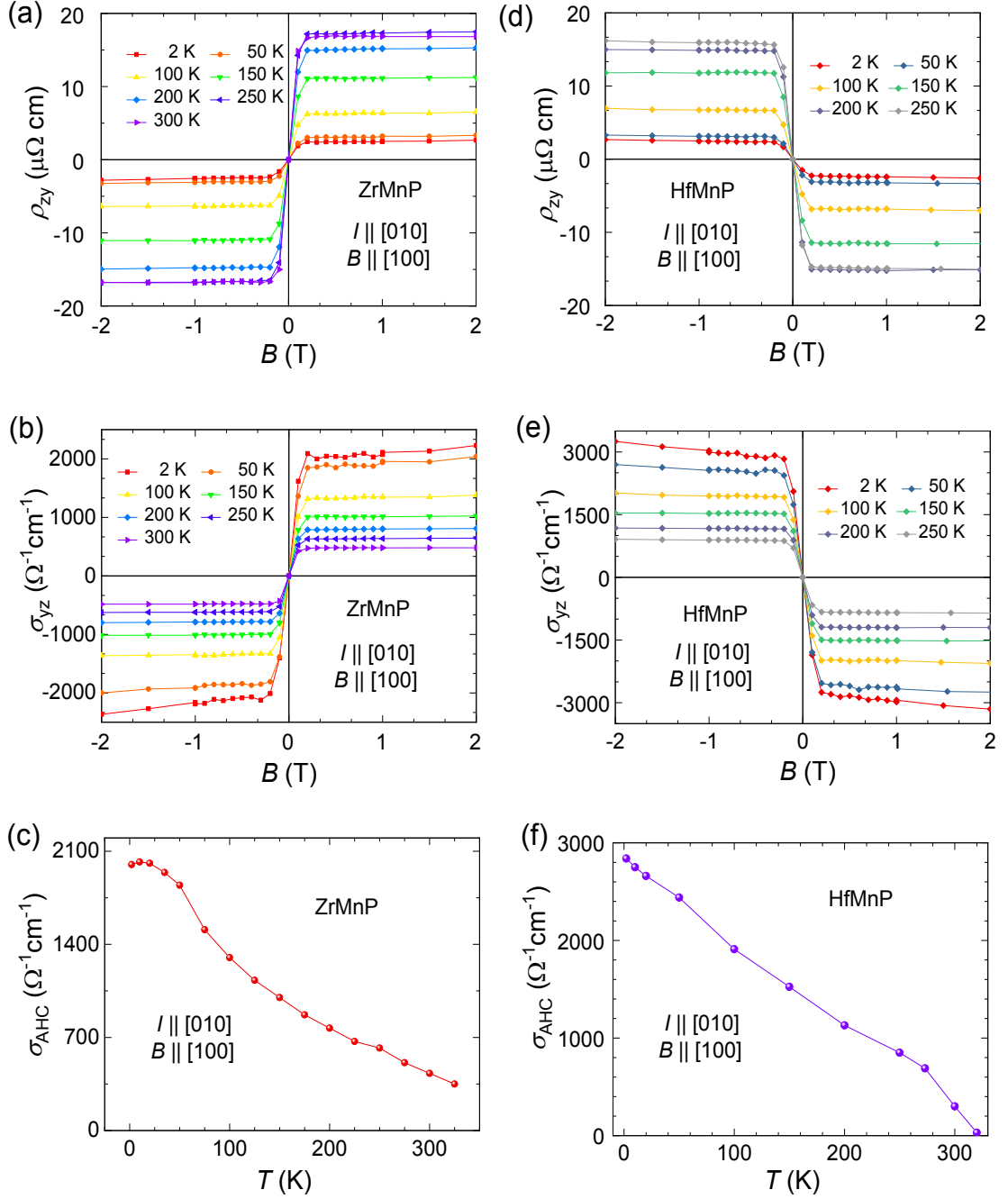
Figure 4A.9: Hall resistivity and conductivity of ZrMnP and HfMnP along [100].
Hall resistivity ρ_{zy} and conductivity σ_{yz} of ZrMnP and HfMnP when field $B \parallel a$ and current $I \parallel b$ in the field range of ± 2 T. The left-column panels for ZrMnP: **(a)** field-dependent measured ρ_{zy} at several temperatures and **(b)** corresponding calculated σ_{yz} and **(c)** temperature-dependent extracted σ_{AHC}. The same measurements are provided in the right-column panels **(d)** to **(f)** for HfMnP.

Estimation of Berry curvature contribution

The total σ_{AHC} has both intrinsic and extrinsic contributions from different mechanisms. The intrinsic contribution originates from the electronic band structure (the BC), whereas the extrinsic contribution arises from the skew scattering or side-jump effect. To define these contributions empirically, the temperature-dependent estimated $\rho_{\text{yx}}^{\text{A}}$ can be expressed as $\rho_{\text{yx}}^{\text{A}}(T) = \alpha\rho_{\text{xx0}} + \beta\rho_{\text{xx0}}^2 + \gamma\rho_{\text{xx}}^2(T)$, where ρ_{xx0} is the residual longitudinal resistivity [101]. The first and second terms represent the extrinsic contributions from the skew scattering and side-jump, respectively, whereas the final term denotes the intrinsic contribution from the BC that is associated with nontrivial bands. To extract the intrinsic contribution, we plotted $\rho_{\text{zy}}^{\text{A}}$ as a function of ρ_{yy}^2 at different temperatures. The slope γ of the straight line directly provides the estimation of the intrinsic value of AHC, which is approximately 900 $\Omega^{-1}\text{cm}^{-1}$ for ZrMnP and 1400 $\Omega^{-1}\text{cm}^{-1}$ for HfMnP (Figure 4A.10(a)). It can be observed that the $\rho_{\text{zy}}^{\text{A}}$ vs. ρ_{yy}^2 plot down-turns slightly with an increasing temperature. The origin of such deviation is not very clear and it has also been observed in other compounds [173,176,178,181,182]. However, the shifting of the chemical potential with the temperature is the most typical and persuasive explanation, whereby the AHC is constant only through the SOC gap [26]. In compounds that possess a large BC-induced AHC, a large AHA is also expected. The AHA exhibits a linearly increasing trend with an increase in the temperature, but decreases further after peaking at approximately 150 K. This is because as T_{C} is approached, the anomalous behavior begins to diminish as the material starts to lose its ferromagnetic property. The ZrMnP and HfMnP exhibit very high AHA values of 10.2% and 13.6%, respectively (Figures 4A.10(b)). These values are sufficiently high to maintain the present compounds among the various ferromagnetic nodal line compounds [173,176,178,181]. Notably, the ZrMnP and HfMnP had the highest AHC values to the best of our knowledge as well as relatively high AHA values.
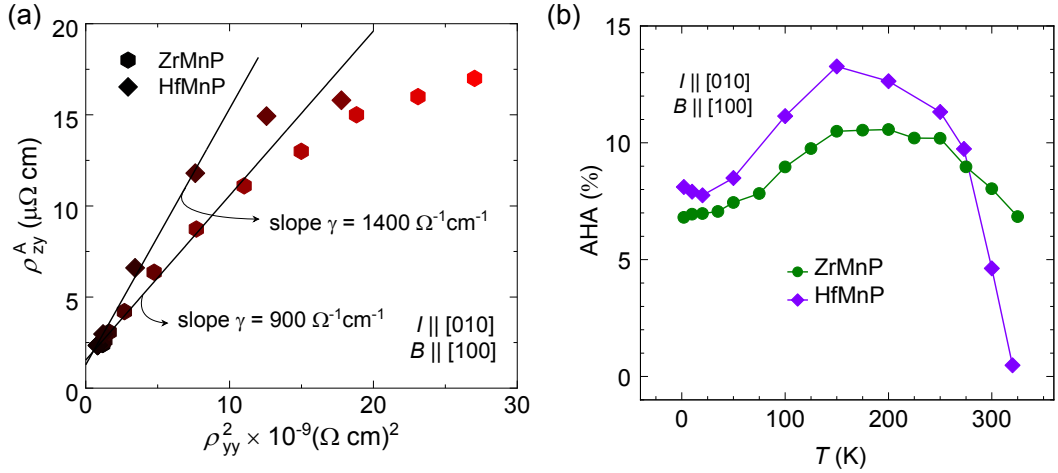
Figure 4A.10: Unified scaling law for AHC and variation of AHA with temperature.
(a) Plot of AHE vs. ρ_{yy}^2 at various temperatures, where the linear slope indicates the intrinsic AHC value. Refer to the text for the deviation from the linearity at the higher end. **(b)** Temperature-dependence measured AHA for ZrMnP and HfMnP, where AHA is defined as the ratio $\sigma_{\text{AHC}}/\sigma_{yy}$.

4A.5. First principle calculations

For the theoretical investigations, we employed *ab initio* calculations based on DFT, as implemented in VASP [183]. This code uses plane waves and pseudopotentials as a basis set. The exchange-correlation potential was used in the generalized gradient approximation [184]. The k mesh used for the integration over the Brillouin zone was $7 \times 13 \times 7$. For calculations with a denser k mesh, Wannier functions were extracted from the DFT results using the Wannier90 package [185]. Using these Wannier functions, we constructed a tight-binding Hamiltonian H, which was used to evaluate the BC Ω in the system as follows [5,26,101]:

$$\Omega = \sum_{m \neq n} \frac{\left\langle n \left| \frac{\partial H}{\partial k_i} \right| m \right\rangle \left\langle m \left| \frac{\partial H}{\partial k_j} \right| n \right\rangle - (i \leftrightarrow j)}{(E_n - E_m)^2},$$ (4A.1)

where $|n\rangle E_n$ are the eigenstates and -energies of H. On this basis, the AHC was calculated as follows [26,101] :

$$\sigma_{xy} = \frac{e^2}{\hbar} \sum_n \int \frac{d^3k}{(2\pi)^3} \Omega_{xy}^z f_n,$$ (4A.1)

where f_n is the Fermi distribution function. The k mesh for the integration over the BZ in this step was selected as $301 \times 301 \times 301$ to ensure converged results.

After measuring the AHC values, we applied the tight-binding method to understand the origin of the AHC. The calculated band structures for the ZrMnP and HfMnP are presented in Figures 4A.11(a) and (b), respectively. Except a tiny band along *Γ-Y* (black line)*,* only those bands (green lines) appear at the E_F, which contribute to the

47

nodal-lines. Such bands primarily dominate in electrical transport. There are three mutually perpendicular mirror planes for the particular SG symmetry *Pnma*. Our calculations without SOC reveal several nodal loops that are located in the band structure, which are enforced by these mirror planes (Figure 4A.11(c)). By considering the SOC and magnetization direction along the *a*-axis as in the experiments, the magnetic moments are not compatible with the mirror symmetry at $y = 0$ [49,173]. In this scenario, the nodal lines are no longer protected and the degeneracy is lifted (Figure 4A.11 (d)). This, in turn, creates strong BC contributions along the former nodal lines, as illustrated in Figure 4A.11(e), which directly contributes to the intrinsic part of the AHC. The calculated intrinsic parts of the AHC are ~1000 Ω^{-1}cm^{-1} for ZrMnP and ~1500 Ω^{-1}cm^{-1} for HfMnP, which are in excellent agreement with the intrinsic parts of the experimental values. As these values are remarkably high, the studied compounds are interesting cases among the known nodal-line compounds.
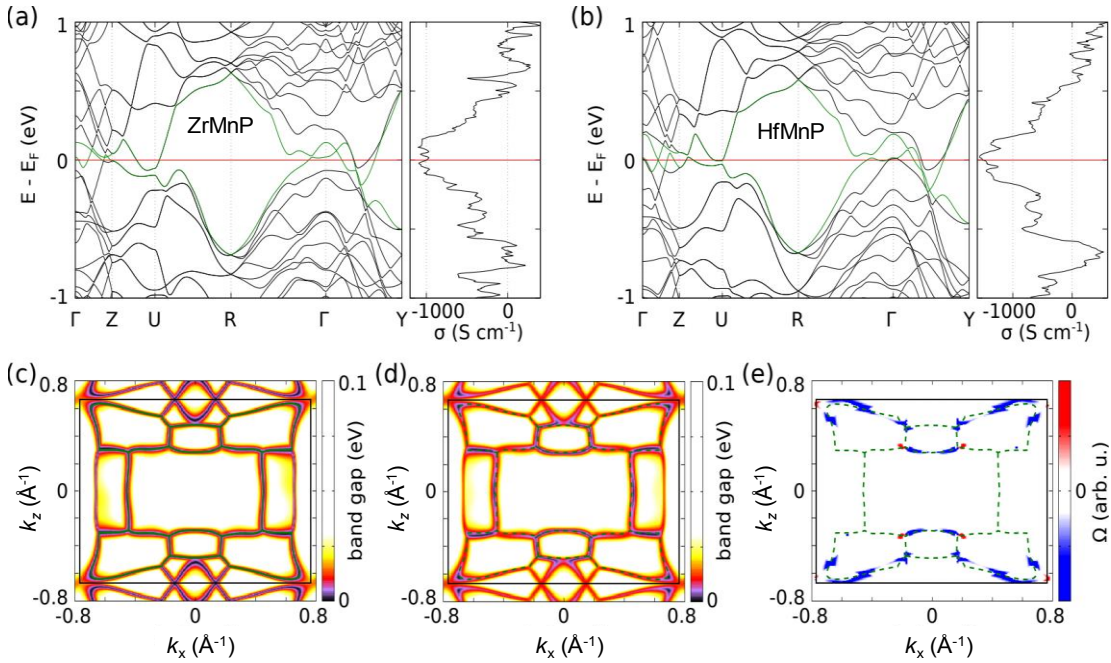
Figure 4A.11: Band structure, AHC, and BC of ZrMnP and HfMnP. (a) Band structure and AHC of ZrMnP. **(b)** Band structure and AHC of HfMnP. In both (a) and (b), the bands (green lines) which contribute to forming nodal-lines **(c)** Bandgap of bands marked in green of HfMnP in (b) in $y = 0$ plane without SOC. Several closed loops are visible (green lines). **(d)** $y = 0$ plane with SOC and magnetization along the *a*-axis, with gapped nodal lines (dashed green lines). **(e)** BC Ω, at E_F in the $y = 0$ plane. The large contributions are located around the gapped nodal lines (dashed green lines). Similar results to those in (c–e) are also expected for ZrMnP.

Among the AHC values that were measured in different directions, the highest value was observed when $B \parallel a$. In this scenario, all nodal lines corresponding to the mirror plane at $y = 0$ has their degeneracy lifted and the nontrivial gap is opened, whereas the other nodal lines remain degenerate. As this gap is larger for HfMnP, we observed a larger AHC for HfMnP than for ZrMnP. Our previous study indicated that the number of mirror planes present in the compound plays a crucial role in the manipulation of the AHC [10]. This was demonstrated by using the simple example of two different space groups that possessed different numbers of mirror planes. SG 225 contains three mutually perpendicular mirror planes at $x = 0$, $y = 0$, and $z = 0$, whereas these planes are absent in SG 216. Consequently, the compounds that are associated with SG 225 exhibit larger AHC values compared to SG 216. Moreover, the location of the nodal line is an important factor. Naturally, the nodal line structure can only contribute to the transport if it is located at E_F. In these two cases, the number of mirror planes is related to the crystal structure, whereas the location is material specific. Our present investigation suggests that compound selection aimed at a high intrinsic value of AHC can be achieved by the tuning of the mirror symmetry that is inevitably present in various achiral space groups.

4A.6 Summary and outlook

We have demonstrated the AHE in ferromagnetic ZrMnP and HfMnP. The crystal structure of these compounds comprises numerous mirror planes, which result in gapped nodal-line states in the band structure under the SOC effect. Among the various nodal lines, several lie at the E_F, making these compounds unique compared to other known nodal-line compounds. These nodal lines are directly responsible for high AHC values owing to the accumulation of large BCs. Various advantages are offered by the present selection of compounds, such as a large ferromagnetic transition temperature, one of the largest ever intrinsic AHC values, a significantly large AHA, and the scope to observe the SOC effect on the AHC value. Our investigations provide various opportunities for tuning the AHC as well as searching for more compounds with higher numbers of mirror planes in their crystal structures.

4B. Anomalous Hall conductivity in Weyl semimetals NiMnSb and PtMnSb

4B.1. Preface

Heusler family is very broad and exists in both full and half Heusler structures. Various ferromagnetic full Heusler candidates have been investigated in quest of BC driven AHE. Co and Fe based full Heusler compounds like Co_2MnGa [48], Co_2MnAl [40], Fe_2NiGa, Fe_2CoAl, [55] and many more have been thoroughly investigated recently [46,73]. While ferromagnetic half Heusler compounds are overlooked. For exceptionally large BC driven AHE, few antiferromagnetic half Heusler RPtBi (R= Gd, Nd, Tb, Ho) compounds have been identified [45,47,186]. Candidates for half Heusler half-metallic ferromagnets are rare and have been disregarded. It is critical from a fundamental standpoint of view to understand the origin of AHE in the half Heusler ferromagnetic family. Theoretically many ferromagnetic half Heusler compounds have been predicted, while only a few of them exist [187-195]. NiMnSb and PtMnSb are well known room temperature ferromagnets and has been explored in almost all possible experimental techniques to study their electronic and magnetic properties [148,194-202]. NiMnSb was the first candidate for half metallicity discovered by Groot in 1983 [203]. While PtMnSb is well known for its very large optical Kerr effect [204]. NiMnSb and PtMnSb still remain attractions for nonvolatile mass storage memory, and various spintronic applications due to their characteristics like room temperature ferromagnets, spin torque, [200] and large spin polarization [198,205]. Since there has been a lack of study of half Heusler ferromagnets from topological perspective, it is important to investigate the very well know room temperature ferromagnets NiMnSb and PtMnSb. First principle calculations show that NiMnSb and PtMnSb both have band inversion which results into Weyl nodes near the E_F. Anomalous transport behavior of half metallic NiMnSb and nearly half metallic PtMnSb have been reported. These half Heusler compounds exhibit very high T_C above the room temperature *i.e.* 660 K (NiMnSb) and 560 K (PtMnSb).

In this chapter, the techniques employed to grow such single crystals of NiMnSb and PtMnSb and to study their magnetic and electrical properties have been discussed. NiMnSb crystals were also grown using the LFZ technique in order to produce larger crystals for future Nernst measurement. These experiments are presented in sections 4B.3 and 4B.4. The magnetic properties are examined by means of magnetization and Hall effect measurements on the single crystals of NiMnSb and PtMnSb. The structural analysis is discussed in detail in section 4B.2. Magnetization measurements reveal that both the systems are soft magnets and anisotropic behavior present is almost negligible which is discussed in section 4B.3. Magneto-electrical transport measurements show the presence of AHE in the system (section 4B.4).

4B.2. Growth and crystal structure

Crystal growth

Flux growth method:

The flux-growth method was used to grow single crystals of NiMnSb and PtMnSb utilizing Bi as a flux. The multiple attempts were carried out utilizing Sb as a (self) flux, but crystals were not produced. After repeated failures, the only alternative was to use secondary flux, which succeeded for growing NiMnSb and PtMnSb crystals. Initially, highly purified Mn (99.999%), Pt (Ni) (99.999%), Sb (99.99%), and Bi (99.999%) were cut into small pieces and weighed in a 1:1:1:10 molar ratio, resulting in a total weight of 15 g. This stoichiometric amount was placed in an alumina crucible altogether. The alumina crucible was then sealed in a quartz tube at an argon pressure of 3 mbar. The quartz ampoule was placed in a box furnace and heated to 800 °C (1000 °C) at a rate of 100 °C h^{-1}. For homogeneity, the whole content was kept at this temperature for 24 hours. The furnace temperature was slowly cooled to 400 °C (600 °C), at a rate of 2 °C h^{-1}, for the crystal growth. At 400 °C (600 °C), the extra flux was removed by centrifugation. From this procedure, silvery single crystals of 1-2 mm in size were obtained. Several crystals were separated for further characterizations. Flux inclusion is always a possibility in crystals formed using the flux method. The composition of NiMnSb and PtMnSb crystals was determined using SEM and an EDXS analyzer. In these analyses, any trace of flux inclusion was not found.

Laser floating zone technique:

To grow crystals of intermetallic compounds using the Bridgman or LFZ methods, the polycrystalline sample must first be prepared. NiMnSb was also grown by LFZ technique. Highly purified Mn (99.999%), Ni (99.999%), and Sb (99.99%) pieces weighed in a 1:1:1 molar ratio, resulting in a total weight of 5 g. Three polycrystalline ingots were prepared in an arc melting furnace each of 5 g. Due to its high vapor pressure, Mn tends to evaporate, hence an additional 2 mg g^{-1} of Mn was added to the mixture to compensate for Mn loss during the melting. All of the elements were melted into one another. After that, the NiMnSb ingot was flipped and remelted. To increase the homogeneity, the technique was performed three times. These polycrystalline ingots were used to prepare the rod using levitating induction melting where 10 cm rod was prepared. Rod was cut into two pieces of 2 cm and 8 cm, which were further used as seed and feed rods to grow single crystals, respectively. The rotation of the upper and lower shafts was kept at 20 rpm, and the growth rate was maintained 1mm h^{-1} over the whole period of growth.

In the flux method, the preferred growth orientation of crystals is along [111], and thus performed the transport measurement with applied magnetic field in direction [111]. On the other hand, NiMnSb which has been grown by LFZ, the crystals were oriented along [110] and performed all measurements with an applied magnetic field along [110], while for flux crystals all measurements has been performed and shown in sections 4B.3 and 4B.4 with applied magnetic field along [111] which is the preferred growth direction.

Table 4B.1: Composition obtained from EDXS analysis for NiMnSb

Elements	Wt %	At %
Ni	24.64	32.70
Mn	24.49	34.73
Sb	50.87	32.56
Total	100	99.99

Table 4B.2: Composition obtained from EDXS analysis for PtMnSb

Elements	Wt %	At %
Pt	57.01	37.98
Mn	30.57	32.64
Sb	12.42	29.39
Total	100	100.01
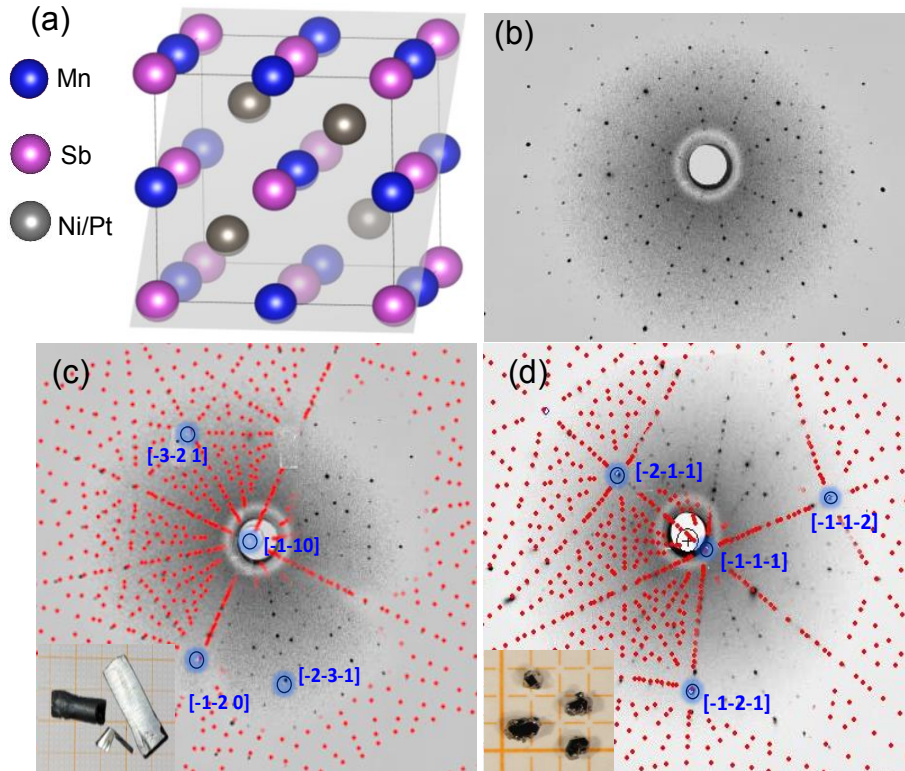
Figure 4B.1: Crystal structure, crystal image and Laue pattern of NiMnSb and PtMnSb. (a) Schematic crystal structure of half Heusler which crystallize in MgAgAs type structure $C1_b$ in space group F-43m (216). **(b)** Laue pattern observed in diffractometer for NiMnSb. **(c)**, **(d)** Fitting done on Laue pattern obtained to orient the crystal along [110] for NiMnSb and [111] for PtMnSb, respectively. Respective inset shows images of crystal grown.

Crystal structure

Elemental analysis for these compounds was done by EDXS analyzer which further confirmed that the composition of the compounds was close to 1:1:1. The average taken of several points scan on the samples of NiMnSb and PtMnSb are shown in tables 4B.1 and 4B.2.

NiMnSb and PtMnSb are half Heusler compounds which crystallizes in non-centrosymmetric cubic structure of MgAgAs type ($C1_b$) space group F-43m (216), with three interpenetrating *fcc* lattices each occupied by Ni (Pt), Mn and Sb atoms as shown in Figure 4B.1(a). The Heusler $C1_b$ structure consists of the Zinc blende structure with the additional occupation of (½, ½, ½) site. Wyckoff positions occupied by each atom are 4a (0,0,0), 4b (½, ½, ½) and 4c (¼, ¼, ¼). Diffraction patterns were collected as a preliminary step to evaluate the crystallinity of single crystals. Then, by rotating the crystal three-dimensionally, reflections were obtained from single crystal XRD. The Laue X-ray diffraction was used to orient the crystals for physical property measurements. In Figure

4B.1(b), the Laue pattern obtained from the single crystal of NiMnSb and the fitted Laue patterns to orient the crystals along [110] is shown in Figure 4B.1(c) for NiMnSb-lr while for PtMnSb facets of single crystals are along [111] shown in Figure 4B.1(d). Along [110] direction two-fold symmetry is present which is clearly visible in Figure 4B.1(c), while along [111] three-fold symmetry is present (Figure 4B.1(d)). Respective insets show the images of crystal grown by laser and flux. The flux and laser grown NiMnSb crystals are named as NiMnSb-fx and NiMnSb-lr, respectively, in further measurements.

4B.3. Magnetization

NiMnSb

Figures 4B.2(a) & (c) show temperature dependence magnetization measured at an applied magnetic field of 10 mT and 100 mT along [110] and [111] for NiMnSb-lr and NiMnSb-fx, respectively. NiMnSb exhibits very large T_C, which is 660 K for NiMnSb-lr and 645 K for NiMnSb-fx. To determine more accurate T_C, first order derivative of magnetization (dM/dT) is taken, which shows a peak at T_C as shown in the inset of Figures 4B.2(a) & (c). Field dependent isothermal magnetization curve measured at various temperatures in range of applied magnetic field of +7 to – 7 T along [110] is shown in Figures 4B.2(b) & (d) for NiMnSb-lr and NiMnSb-fx, respectively. This curve represents a typical ferromagnetic behavior up to 600 K and the saturation magnetization is 3.95 μ_B f.u.$^{-1}$ at 2 K for NiMnSb-lr and NiMnSb-fx as depicted in Figures 4B.2(b) & (d). As temperature increases, we see a decrease in saturation magnetization, and as it approaches T_C, saturation in magnetization is achieved at relatively higher field, while above T_C there is no saturation in magnetization till the measured field of 7 T as compounds lose its magnetic property above T_C.
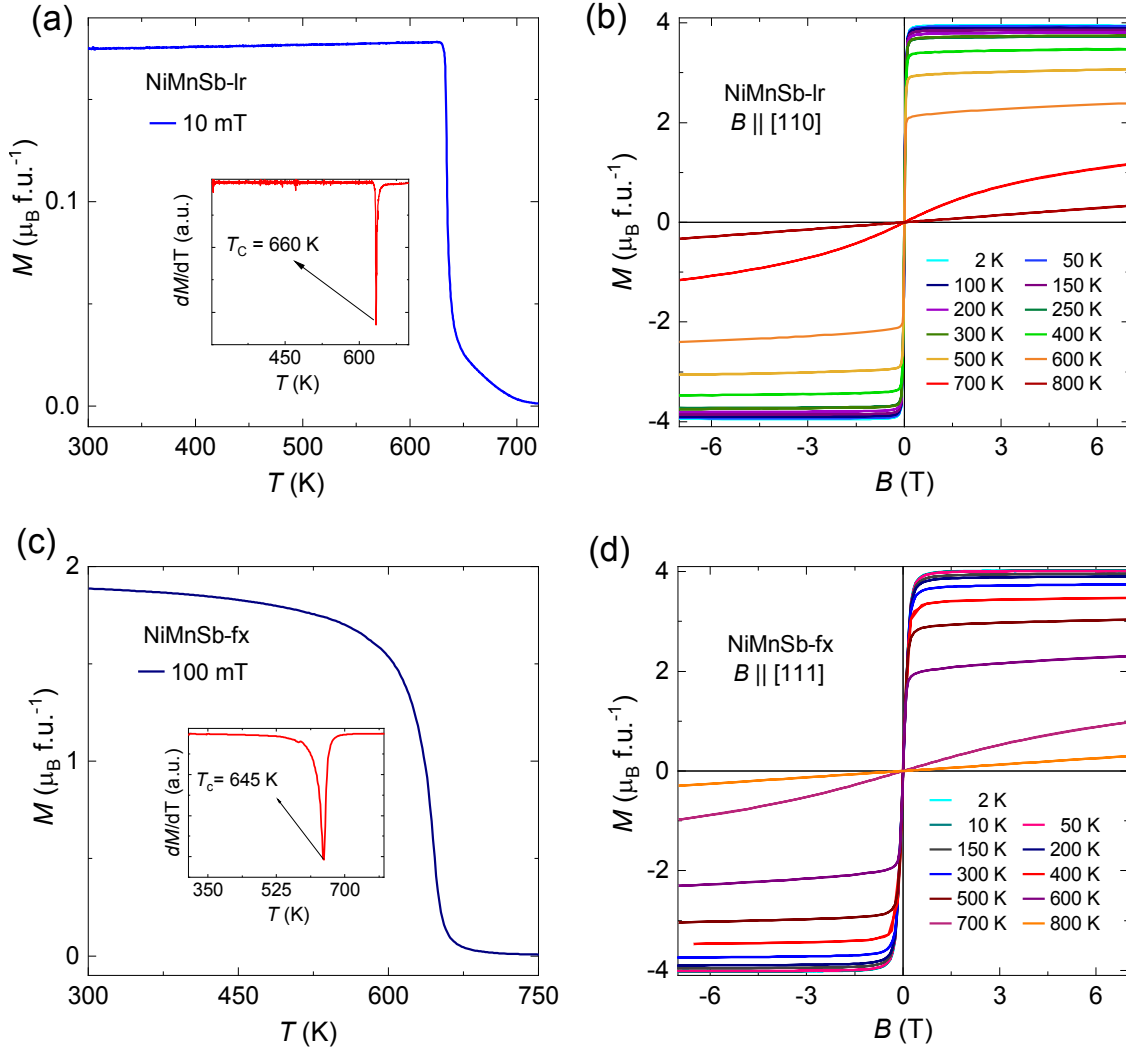
Figure 4B.2: Magnetization of NiMnSb-lr and NiMnSb-fx. (a) & **(c)** Temperature dependent magnetization curve measured at an applied magnetic field of 10 mT and 100 mT shows T_C of 660 K and 645 K for NiMnSb-lr and NiMnSb-fx, respectively. First order derivative is taken to find more accurate T_C, which is shown in inset. **(b)** & **(d)** Isothermal magnetization curve measured with magnetic field applied parallel to (110) and (111) direction for NiMnSb-lr and NiMnSb-fx, respectively.

PtMnSb

Figure 4B.3(a) shows temperature dependence magnetization for a PtMnSb crystal grown by flux technique and measured at 10 mT applied field along [111], which is the preferred crystal growth orientation. PtMnSb exhibits a very high T_C of 560 K, which is slightly lower than NiMnSb. To obtain a more precise T_C, the first order derivative of magnetization (dM/dT) is calculated, which displays a peak at 560 K, indicating the T_C of the observed sample (see inset of Figure 4B.3(a)). Field dependent magnetization (isothermal magnetization) was measured at different temperatures in the range of –7 to +7 T applied magnetic field along [111]. Figure 4B.3(b) shows that the saturation magnetization of NiMnSb is 4.12 μ_B f.u.$^{-1}$ at 2 K. We see a decrease in M_S as temperature rises, and as it approaches T_C, saturation is achieved at a relatively higher field.
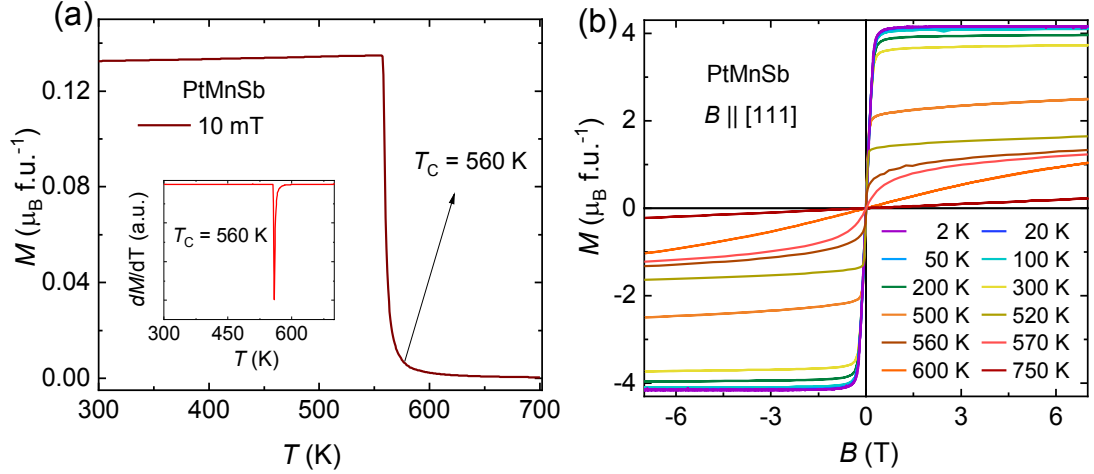
Figure 4B.3: Magnetization of PtMnSb (a) Temperature dependent magnetization curve measured at applied magnetic field of 10 mT shows very high T_C of 560 K for PtMnSb. First order derivative is taken to find more accurate T_C, which is shown in inset. **(b)** Isothermal magnetization curve measured with magnetic field applied parallel to [111].

4B.4. Magneto-transport

All the transport measurements were carried out in a commercial physical properties measurement system (PPMS, Quantum Design) for a field up to ±9 T in the temperature range of 2 to 300 K.

Resistivity of NiMnSb

Laser floating zone crystal

A crystal was cut into a rectangular bar using a wire saw cutter for the Hall bar setup with edges in directions [100] and [110]. The dimension of the sample was $2.64 \times 0.75 \times 0.48$ mm^3. The four-probe transport measurements were performed with configurations $B \parallel$ [110]; $I \parallel$ [100], where applied current and frequency were 8 mA and 57 Hz, respectively, in the electrical transport option (ETO). Same parameters were used for all crystals of NiMnSb and PtMnSb. The Hall resistivity and MR are performed in the four-probe geometry. These contacts were made by using silver paint with 25 μm diameter Pt wire.

Figure 4B.4(a) shows temperature dependent longitudinal resistivity of NiMnSb-lr. The value of RRR is 1.5. However, Figure 4B.4(b) shows transverse MR for NiMnSb measured by changing the magnetic field from $+9$ to -9 T at various temperatures in the range of 2-300 K. We see a positive MR reaching a value of 3.3 % at low temperature (2 K), while at high temperature it becomes negative and reaches to -0.7 % at 300 K, due to suppression of the spin disorder scattering. We see a slight difference in longitudinal resistivity in NiMnSb crystals grown by different techniques, the broad feature in resistivity of NiMnSb-lr is observed previously as well and is claimed due to rich in Mn [148]. We observe negative MR over all temperatures in NiMnSb-fx, while in the case of NiMnSb-lr we observe positive MR and then negative MR at high temperatures, which depends on crystal quality, where spin disorder scattering is suppressed in one even at low temperatures while in other it is suppressed only at high temperatures.

Flux crystal

Figure 4B.4(c) shows temperature dependent zero field longitudinal resistivity of NiMnSb-fx. The dimension of the measured sample was $1.12 \times 0.37 \times 0.12$ mm^3. The resistivity decreases with decreasing the temperature, which indicates that the compound is metallic in nature. The values of resistivity at 300 K and 2 K are 62 μΩ cm and 40 μΩ cm, respectively, giving a RRR of 1.5 (RRR = R_{300K}/R_{2K}). The resistivity was also measured by changing magnetic field from $+9$ to -9 T applied along [111] at various temperature in between 2-300 K and applied field and current are in perpendicular geometry. The data were symmetrized to remove the contribution of Hall signal at each temperature. Figure 4B.4(d) shows calculated MR from resistivity for NiMnSb. We see a negative MR of very small value of 0.8%. Negative MR is usually seen in magnetic compounds as an applied magnetic field suppress the spin disorder scattering. The MR is calculated using the formula 2.5.

58
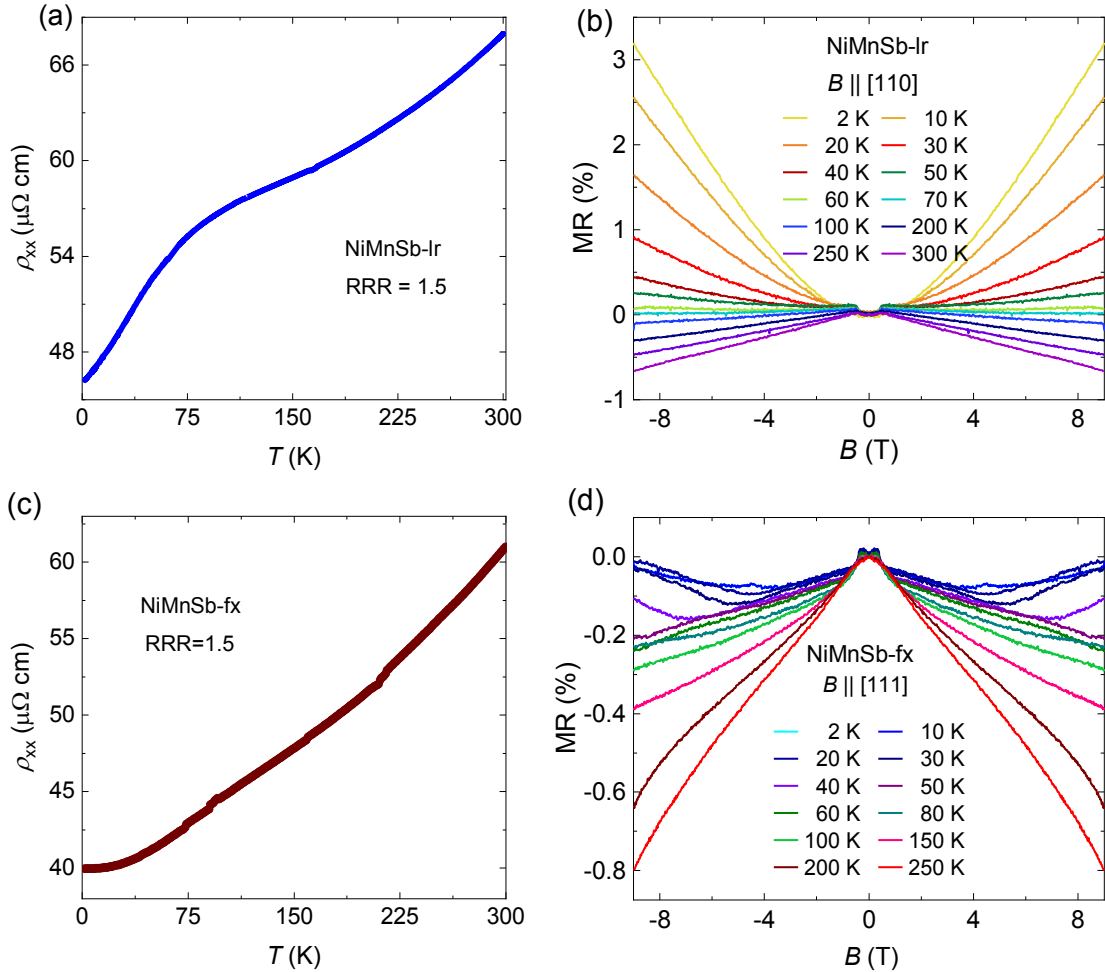
Figure 4B.4: Resistivity behavior of NiMnSb. **(a)** & **(c)** Show temperature dependent zero field longitudinal resistivity ρ_{xx} measured for NiMnSb with RRR of 1.5. **(b)** & **(d)** Show MR measured in range of field from −9 T to +9 T for NiMnSb-lr and NiMnSb-fx, respectively.

Resistivity of PtMnSb

The four-probe geometry was used to perform electrical transport measurements on PtMnSb. The dimension of the measured sample was $1.23 \times 0.22 \times 0.37$ mm^3. Figure 4B.5(a) shows temperature dependent longitudinal resistivity of PtMnSb where we observe decrease in resistivity with decrease in temperature which indicates metallic behavior of the sample. In case of NiMnSb value of RRR is 1.5, while for PtMnSb is almost seven times larger than NiMnSb and is 11.8. The RRR value of PtMnSb is rather large as in magnetic compounds we do not see such large RRR values, which illustrates very high-quality single crystal with less scattering due to disorder present in the compound. Figure 4B.5(b) shows MR for measured by changing magnetic field from +9 to −9 T at various temperatures in between 2-300 K. We see a positive MR reaching a value of 4.3 % at low temperature (2 K), while at high temperature it becomes negative and reaches to −2.4% at

300 K, which is usually seen in magnetic compounds as applied magnetic field suppresses the spin disorder scattering.
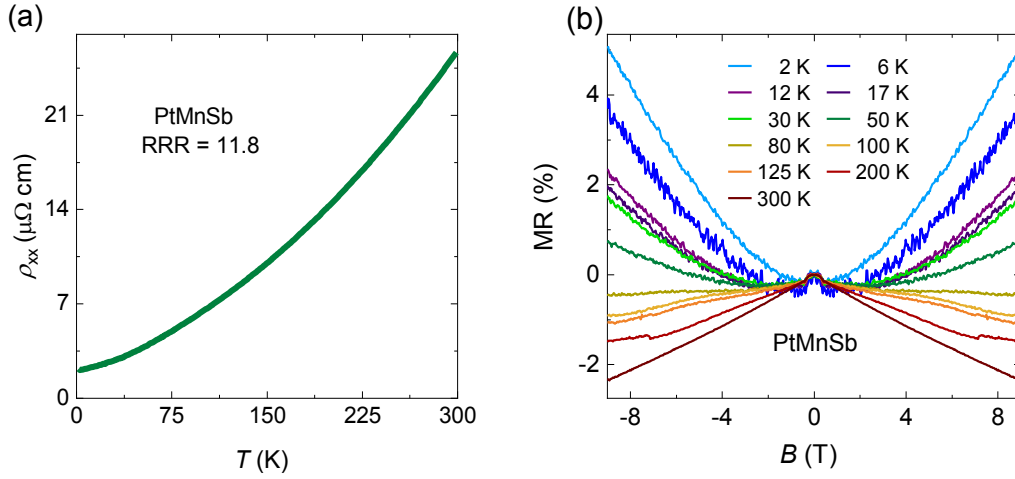
Figure 4B.5: Resistivity behavior of PtMnSb. (a) Shows temperature dependent zero field longitudinal resistivity ρ_{xx} for PtMnSb with RRR of 11.8. **(b)** Estimated MR at various temperatures in range of field from -9 T to $+9$ T.

Hall effect measurements

NiMnSb and PtMnSb are two well-known room-temperature half Heusler ferromagnets, and both compounds have been the subject of intensive investigations including electrical and magnetic properties. However, their topological property was never studied before. As a result, single crystals were grown to investigate the electrical transport property in term of AHE and its correlation with topology of the compounds. Hall resistivity for PtMnSb and NiMnSb is measured using the four-probe setup by changing magnetic field from -9 to $+9$ T at various temperature in between 2-300 K. For better representation, data is shown in the range of -4 to $+4$ T.

NiMnSb Hall effect

Figure 4B.6(a) shows Hall resistivity, ρ_{yx} measured for NiMnSb-lr with applied field along [110] in the temperature range 2 K to 300 K. In ferromagnetic materials, ρ_{xy} is usually written as $\rho_{yx} = \mu_0(R_0 H + R_S M)$, where R_0 and R_S are the ordinary and anomalous Hall coefficients, μ_0 is the vacuum permeability, and H and M are the magnetic field and the magnetization, respectively. Hall effect has two contributions as represented in the formula above, first term is ordinary Hall effect which arises due to Lorentz force on charge carriers when magnetic field is applied, while second term is known as AHE which is unique to magnetic samples explained in more detail in chapter 2. In NiMnSb, the ordinary contribution in Hall effect is large at low temperature, which decreases as temperature

increases. This decrease in coefficient of ordinary Hall effect becomes almost constant after reaching 100 K, this temperature is also consistent where MR changes sign.

The Hall coefficient R_0 for NiMnSb increases to a magnitude higher as we approach low temperature can be seen in figure 4B.7(a) and is calculated from the slope of Hall resistivity at high field. The value of R_0 at room temperature is 1.4×10^4 cm^3 C^{-1} while it reaches 26×10^4 cm^3 C^{-1} at 2 K. The sign of R_0 depicts the type of majority charge carrier involved in transport, which in the instance of NiMnSb is holes. The Hall resistivity measured for NiMnSb is very small at high temperature in range of nΩ cm. The value of ρ_{yx} reaches 728 nΩ cm at 300 K, while this increases almost to an order higher to 2.8 μΩ cm at 2 K measured at 9 T. Figure 4B.6(b) shows extracted anomalous Hall resistivity with magnetic field measured in range of +9 T to −9 T, which is deduced by subtracting ordinary Hall contribution. In this case, the ordinary Hall contribution is eliminated using linear fit in high magnetic field region. Figure 4B.6(c) illustrates the extraction of intrinsic contribution and dominance of intrinsic term which is evaluated from relation of $\rho_{yx}^A \propto \rho_{xx}^2(T)$, which is explained in details in chapter 2. As discussed in chapter 4A for estimation of BC, a linear fit was done on plot of ρ_{yx}^A as a function of ρ_{xx}^2 at different temperatures. The slope of the straight line directly provides the estimation of experimental intrinsic contribution of AHC, which is approximately 1.35×10^2 Ω^{-1}cm^{-1} as shown in Figure 4B.6(c). Figures 4B.6(d) & (e) show Hall conductivity σ_{xy} and AHC σ_{xy}^A with magnetic field, which is calculated using formula 2.3. AHC is evaluated from reduced anomalous Hall resistivity using formula 2.3. The value of AHC is approximately 90 Ω^{-1}cm^{-1} at 300 K and reaches 1.8×10^2 Ω^{-1}cm^{-1} at 2 K. AHC reaches a constant value of 90 Ω^{-1}cm^{-1} after 75 K. Figure 4B.6(f) shows temperature dependence of $|\sigma_{xy}^A|$, where we see that the value of σ_{xy}^A drops almost by half when temperature reaches 70 K and becomes almost constant till room temperature.

Figure 4B.6: Anomalous Hall resistivity and conductivity of NiMnSb-lr. (a) Field dependent Hall resistivity measured with applied magnetic field along [110]. **(b)** Reduced anomalous Hall resistivity as a function of magnetic field is obtained by subtracting ordinary Hall resistivity. **(c)** Plot of ρ_{yx}^A vs ρ_{xx}^2 to extract the intrinsic contribution. **(d)** Hall conductivity, σ_{xy} as function of magnetic field. **(e)** AHC, σ_{xy}^A as function of magnetic field. **(f)** Temperature dependent AHC.
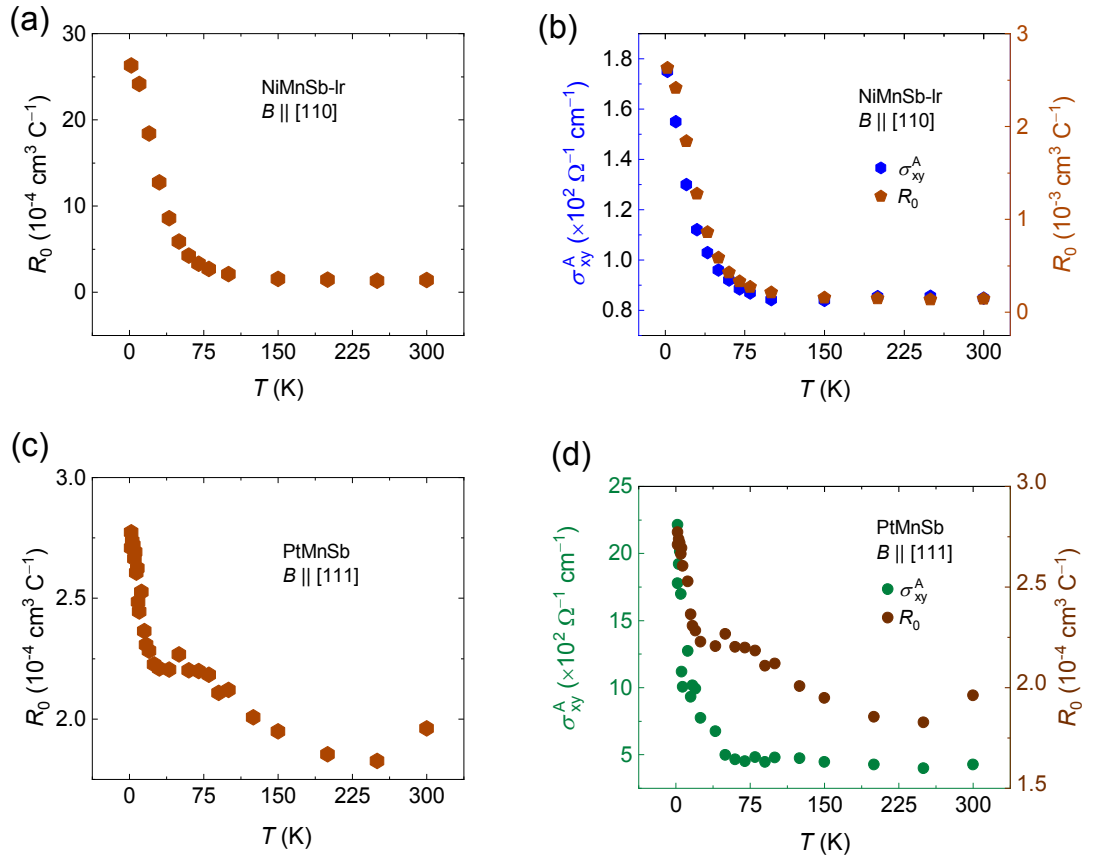
Figure 4B.7: Hall coefficient, and AHC of NiMnSb and PtMnSb. (a), **(c)** Temperature dependence of Hall coefficient R_0; **(b)**, **(d)** AHC and R_0 with temperature of NiMnSb-lr and PtMnSb, respectively.
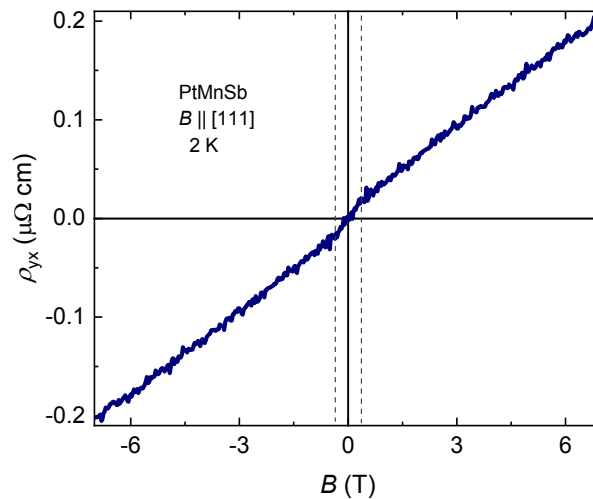
Figure 4B.8: Hall resistivity of PtMnSb at 2K. Hall resistivity of PtMnSb measured at 2 K, where dashed line shows change in slope of Hall resistivity ρ_{yx}.

PtMnSb Hall effect

In case of PtMnSb, the transport behavior is almost similar to NiMnSb. Figure 4B.8 shows transport properties measured with field along crystallographic axis [111] which is preferred orientation during crystal growth. Crystals were polished along [111] direction and cut into rectangular bar for Hall measurements using wire saw cutter. The value of Hall resistivity is of order of nΩ cm shown in Figure 4B. 8(a), the value reaches 320 nΩ cm at an applied magnetic field of 4 T at 300 K and it drops to 94 nΩ cm at 2 K. Since, the value of Hall resistivity is really small, a very careful measurement was needed as it was difficult to see anomalous behavior in the Hall resistivity. The parameters like applied current, and frequency were calibrated, as at very high temperatures the Hall voltage connections were broken at current higher than 8mA.

In case of PtMnSb, the sign of Hall resistivity indicates that majority charge carrier is holes as the slope is positive. At low temperature, the ordinary Hall contribution dominates extensively and thus it seems that anomalous Hall contribution is absent. But if we look closer of 2 K Hall resistivity data shown in Figure 4B.8, a clear slope change is visible at 0.3 T, which indicates the presence of anomalous Hall contribution. Figure 4B.9(b) shows anomalous Hall resistivity obtained by subtracting the linear fit at high magnetic field as discussed in previous section. Figures 4B.9(d) & (e) show field dependent σ_{xy}^A at low temperatures and at high temperatures. AHC σ_{xy}^A reaches 2214 Ω^{-1}cm^{-1} at 2 K and drops to 450 Ω^{-1}cm^{-1} at 70 K, which is 0.125 times of T_C. And the value of σ_{xy}^A at 300 K is 427 Ω^{-1}cm^{-1}, which illustrates that σ_{xy}^A remains almost constant after 70 K similar to NiMnSb. Hall coefficient for PtMnSb shown in Figure 4B.9(c) does not change largely as in case of NiMnSb, reason for which is not very clear. Though, a drop is observed in σ_{xy}^A and R_0 shown in Figure 4B.7(d) are at the same temperature. To extract BC induced AHC value, a linear fit is done (details in chapter 2) on plot of ρ_{yx}^A vs ρ_{xx}^2, shown in Figure 4B.9(c) and the value of intrinsic contribution is 410 Ω^{-1}cm^{-1}, which is 91% of total σ_{xy}^A at 300 K. The Hall coefficient R_0 for PtMnSb can be seen in Figures 4B.7(b) & (d). Temperature dependence AHC is shown in Figure 4B.9(f), where exponential drop is seen similar to NiMnSb. The value of R_0 at room temperature is 2.0×10^4 cm^3 C^{-1} which reaches 2.7×10^4 cm^3 C^{-1} at 2 K. The value of R_0 does not change significantly as in case of NiMnSb even though the ordinary contribution is large at low temperatures.
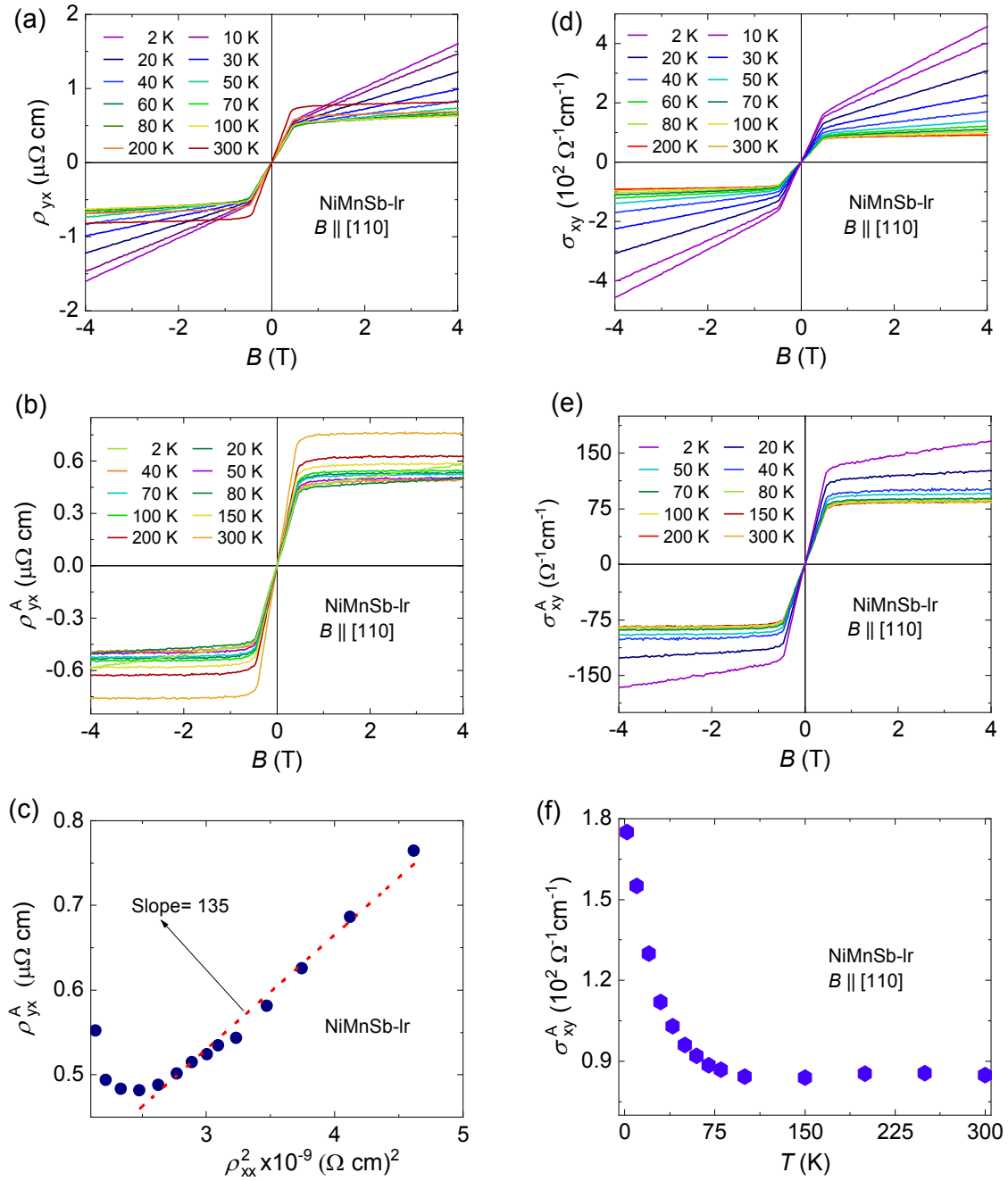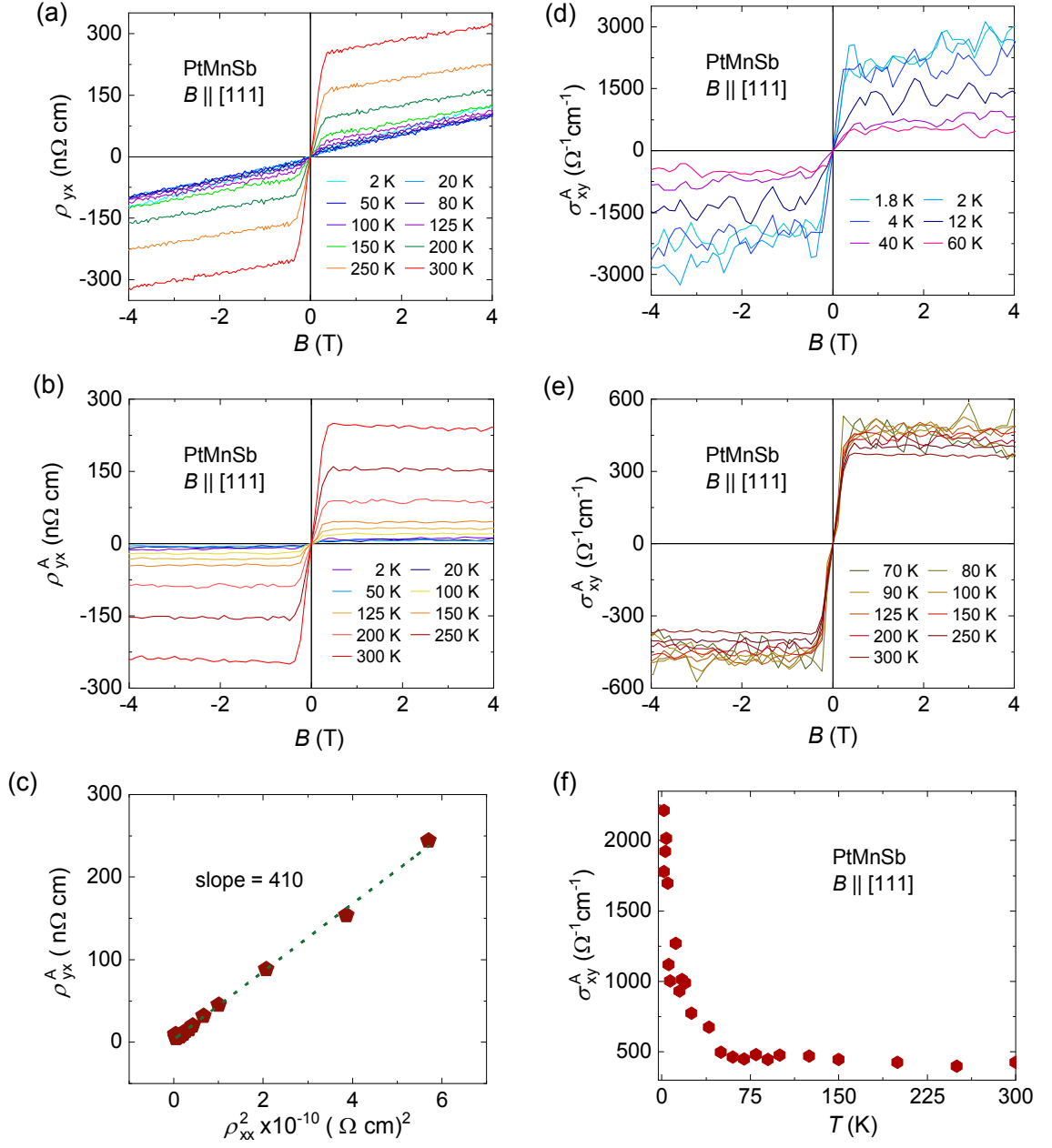
Figure 4B.9: Anomalous Hall resistivity and conductivity of PtMnSb. (a) Field dependent Hall resistivity measured with applied magnetic field along [111]. **(b)** reduced anomalous Hall resistivity as a function of magnetic field is obtained by subtracting ordinary Hall resistivity. **(c)** Plot of ρ_{yx}^{A} vs ρ_{xx}^{2} to extract the intrinsic contribution, where linear fit gives the intrinsic contribution. **(d) & (e)** AHC as function of magnetic field at low and high temperatures. **(f)** Temperature dependent AHC.

The mobility and charge carrier concentration of NiMnSb and PtMnSb are shown in Figure 4B.10, where carrier concentration of both compounds are of order of magnitude 10^{22} cm^{-3}. The mobility of NiMnSb is 43 cm^2 V^{-1}s^{-1} while for PtMnSb is lager and of value of 130 cm^2 V^{-1}s^{-1}. The order of magntiude of charge carrier concentration indicates the metallic range.
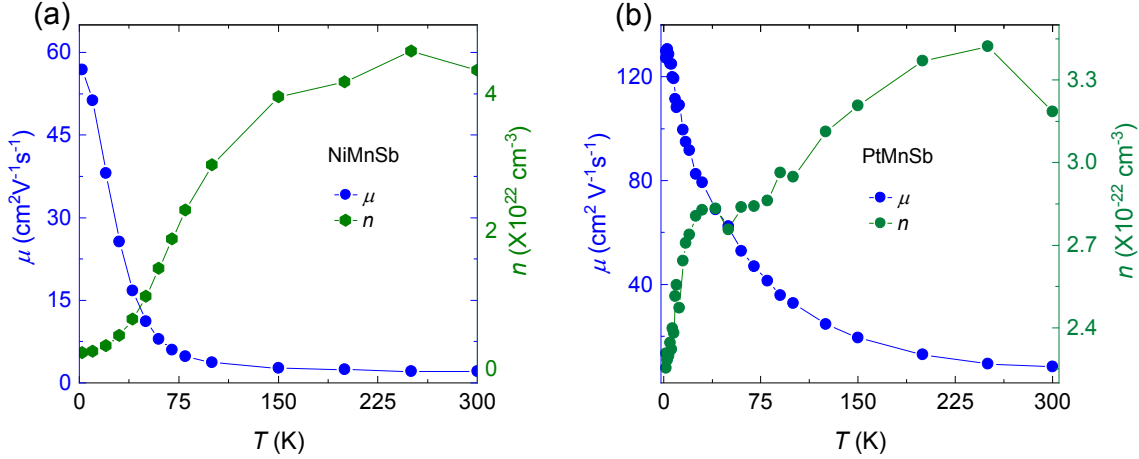
Figure 4B.10: Temperature dependent mobility and carrier density of NiMnSb and PtMnSb. Temperature dependent mobility and carrier concentration for **(a)** NiMnSb and **(b)** PtMnSb.

NiMnSb (flux crystal) Hall effect

In case of NiMnSb-fx, the transport behavior is shown in Figure 4B.11 measured with field along [111], which is the preferred orientation during the crystal growth. The grown crystal of NiMnSb using flux methods are small of size 1mm grown with triangular facet of [111]. Using a wire saw cutter, crystal was polished in [111] and cut into a rectangular bar for Hall measurements. Figure 4B. 11(a) shows magneto resistivity ρ_{xx}, measured with field applied along [111]. The value of ρ_{xx} measured at applied field of 9 T is 32 $\mu\Omega$ cm at 2 K, which reaches to 53 $\mu\Omega$ cm measured at 300 K. Hall resistivity ρ_{yx} measured in range of −9 T to +9 T shown in Figure 4B.11(b), is slightly different from NiMnSb-lr as it is clearly observed that ordinary Hall contribution is small as compared to Figure 4B.6. The value of Hall resistivity is also an order of magnitude smaller to NiMnSb-lr. Anomalous Hall resistivity is deduced from subtracting ordinary contribution and is shown in Figure 4B.11(c), and the range of ρ_{yx}^A is same as NiMnSb-lr. The estimation of intrinsic contribution from BC in NiMnSb-fx is 1.1×10^2 Ω^{-1}cm^{-1} shown in Figure 4B.11(e) and in NiMnSb-lr is 1.35×10^2 Ω^{-1}cm^{-1}, which is almost same. And this gives us clear indication that evaluation of intrinsic contribution is correct as there might be possibilities of difference in defects and disorder present in crystals grown by different methods, despite of which the value of σ_{xy}^A does not differ much. Figure 4B.11(d) shows σ_{xy}^A with applied

magnetic field, which is calculated using formula 2.3, where the value of σ_{xy}^A reaches 190 $\Omega^{-1}cm^{-1}$ measured at 2 K and drops to 165 $\Omega^{-1}cm^{-1}$ at 300 K. Temperature dependent AHC σ_{xy}^A is shown in Figure 4B.11(f), where a gradual decrease in σ_{xy}^A is seen, rather than an exponential reduction as seen in NiMnSb-lr and PtMnSb crystal. In case of NiMnSb-fx shown in Figure 4B.11(f), the decrease in value of σ_{xy}^A is only 18% from 1.8 K to 300 K, while in case of NiMnSb-lr crystal this drop was almost by 60%.
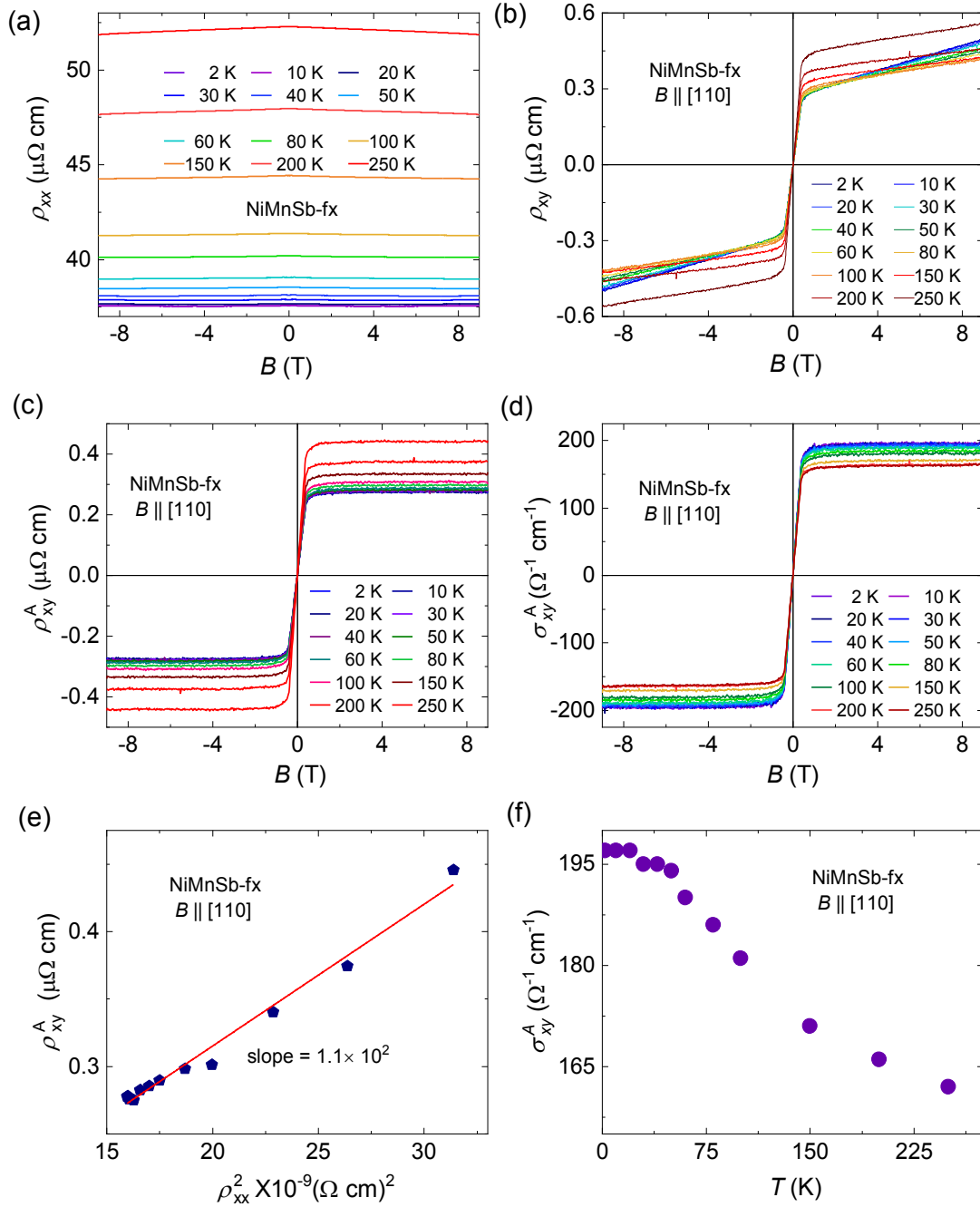
Figure 4B.11 Anomalous Hall resistivity and conductivity of NiMnSb-fx. (a) MR of NiMnSb-fx measured at various temperatures in the range of 2-300 K shows negative MR. **(b)** Field dependent Hall resistivity. **(c)** Reduced anomalous Hall resistivity with field deduced by subtracting ordinary Hall effect. **(d)** Estimated AHC. **(e)** A linear fit on plot of anomalous Hall resistivity and longitudinal resistivity, where slope gives contribution from BC (110 $\Omega^{-1}cm^{-1}$ in present case). **(f)** Temperature dependence AHC.

4B.5. First principle calculations

For the theoretical investigations, we employed *ab initio* calculations based on DFT, as implemented in VASP. This code uses plane waves and pseudopotentials as a basis set. The exchange-correlation potential was used in the generalized gradient approximation. The k mesh used for the integration over the Brillouin zone was $7 \times 13 \times 7$. For calculations with a denser k mesh, Wannier functions were extracted from the DFT results using the Wannier 90 package [26,184, 185]. Using these Wannier functions, a tight-binding Hamiltonian H was constructed, which was used to evaluate the BC Ω in the system using equation 4A.1, and the AHC was calculated using equation 4A.1. The k mesh for the integration over the BZ in this step was selected as $301 \times 301 \times 301$ to ensure converged results.

After measuring the AHC values, we applied the tight-binding method to understand the origin of the AHC. The calculated band structures for the NiMnSb and PtMnSb are presented in Figures 4B. 12(a) & (c), respectively.

The BC can be seen as a correction to the single-band description on materials, since it represents the residual interaction between adjacent bands. When two bands cross non-trivially, topological structures such as Weyl nodes (1D) or nodal lines (2D) appear, leading to finite total BC in the material. If these crossings take place near the E_F, the transport properties of the material are deeply affected, such as the AHE measured in this work. On the other hand, the net BC of the material is finite only under certain circumstances, such as SOC combined with TRS breaking. Therefore, the band structure of the compounds which relies in the crystal symmetries is the origin of the BC. Thereby, the band structure of both NiMnSb and PtMnSb have been obtained (Figures 4B.12 (a & c), respectively) in the high-symmetry line *X-W-L- Γ -X-K-U*. In both compounds, the spin-down channel forms a gapped state, although for the latter material the E_F is located slightly below that gap. The half-metallic and almost half-metallic behavior of NiMnSb and PtMnSb, respectively, can be seen in Figures 4B.12 (a) & (b). In the latter case, a spin-down pocket at Γ appears at E_F, reducing the spin-up polarization of the compound. The spin-up bands close that gap with a strong dispersion. In both compounds, the AHC is a product of the SOC combined with magnetism enabling a non-vanishing net BC to appear. This can be directly seen in Figure 4B.12. The hybridization of bands from different spin channels when the SOC is included (Figures 4B.12(a) & (c)), leads to finite AHE (Figures 4B.12 (b) & (d)).

It is important to note, that the calculated AHC in NiMnSb is rather constant in an energy window from −0.5 to 0.5 eV around the E_F, which allows for a straight-forward comparison with the experimental results. As mentioned above, both values agree very well irrespective of the synthesis procedure. However, for PtMnSb, the AHC is very much energy dependent around the E_F, making a comparison rather difficult.

In more detailed calculations, we also find topological features in the electronic band structures of the two compounds. In particular, a pair of Weyl nodes at a distance

-170 meV below the E_F has been detected in the NiMnSb, originating a small bump in the AHC curve (Figure 4B.12(b)). Nevertheless, these Weyl nodes are very close to each other, less than a distance 0.01 Å, and as a result, it has very little influence on the AHC [41]. On the other hand, for the PtMnSb two pairs of Weyl nodes have been found at -45.7 meV and -69.5 meV from the E_F, causing also a small bump of the AHC near that point. In addition to this pair, another three pairs of Weyl nodes have been also found 624 meV above the E_F (Figure 4B.12(d)). The band crossing that represents such Weyl nodes are plotted in Figures 4B.12 (e) & (f).
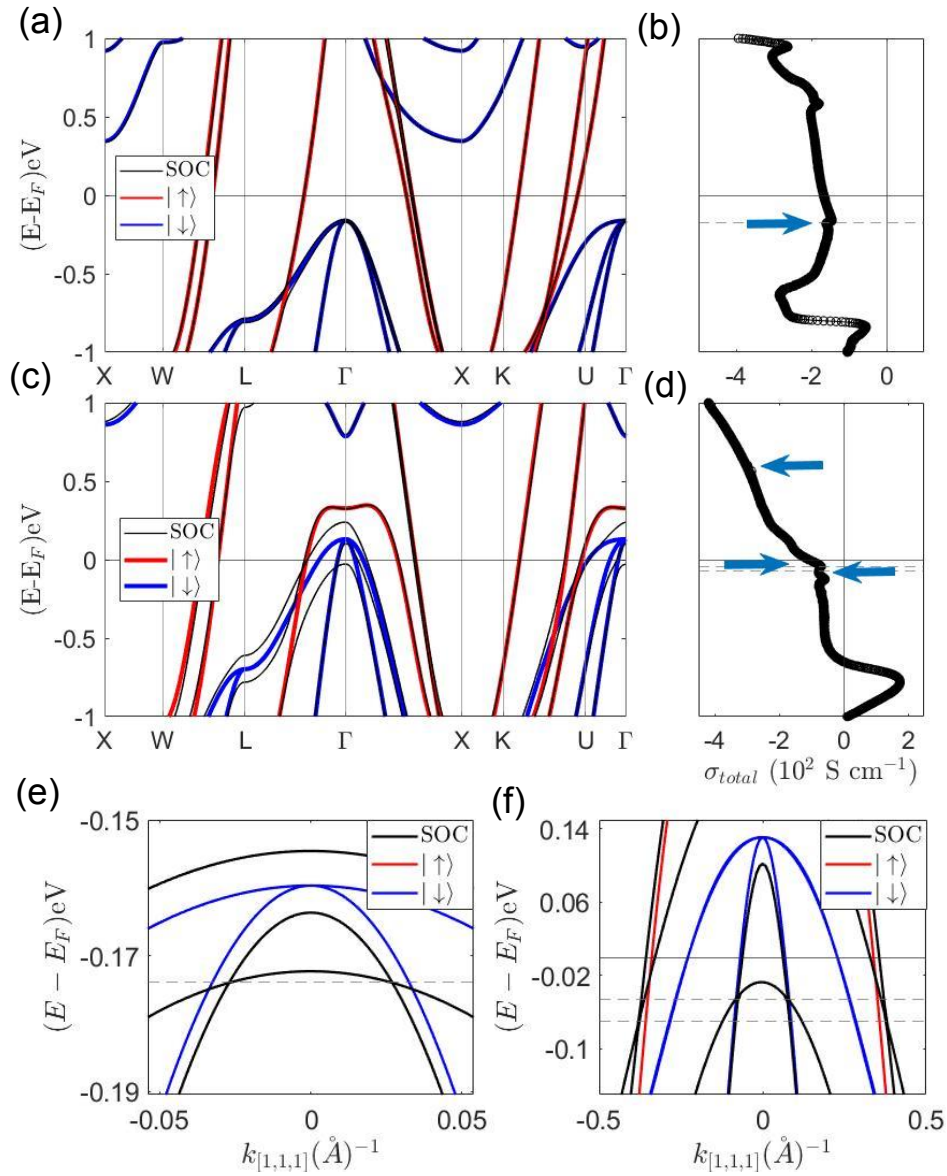
Figure 4B.12: Band structure and calculated AHC of NiMnSb and PtMnSb. (a) & **(c)** Electronic band structure of NiMnSb and PtMnSb, respectively with SOC included (black solid lines) and without SOC (spin-up in red solid lines; spin-down in blue solid lines). **(b)** & **(d)** Energy dependence of calculated intrinsic AHC. The bumps caused by Weyl nodes are indicated with blue arrows. **(e)** & **(f)** Band crossing of the Weyl nodes in each compound.

4B.6. Summary and outlook

In summary, electronic and magnetic transport properties as well as the band structure of well-known half metallic half Heusler ferromagnet NiMnSb and nearly half metallic PtMnSb have been investigated. Both intermetallic compounds exhibit extremely high T_C of 660 K and 560 K for NiMnSb and PtMnSb, respectively with a M_S of approximately 4 μ_B f.u.$^{-1}$ for both. NiMnSb shows AHC of 180 Ω^{-1}cm^{-1} measured at 2 K, wherein the intrinsic contribution is 135 Ω^{-1}cm^{-1}, and this value remains same for crystals grown by different techniques indicating that our estimated intrinsic contribution from BC is correct as AHC value does alter with crystal quality, if extrinsic mechanism is dominating. Even in calculated intrinsic AHC we have almost energy independent curve with a value of 180 Ω^{-1}cm^{-1} which explains why the AHC remains constant even if there is change in the E_F. While in case of PtMnSb, this is slightly different. The value of AHC reaches 2200 Ω^{-1}cm^{-1} at 2 K, while this drops to 450 Ω^{-1}cm^{-1} at 300 K, and the calculated intrinsic AHC is 100 Ω^{-1}cm^{-1} at the E_F, but if we move slight away from E_F we have a value of 300 Ω^{-1}cm^{-1} which is in good agreement with our experimental measured value.

5. Diamagnetism in topological semimetals

In this chapter, the primary focus has been on understanding the fundamental study underlying the large diamagnetism observed in topological semimetals that are non-magnetic. Experimentally, we determined that the value of diamagnetic susceptibility in topological semimetals is comparable to the magnitude of bismuth. In recent years, several theoretical studies have been proposed to gain a better understanding of enhancement of orbital magnetization in topological materials. Bismuth is one of the very well-known examples, which exhibits very large diamagnetic susceptibility, and this large diamagnetic susceptibility is a result of orbital magnetization. Diamagnetism was recently examined for a few topological semimetals [14-16], and it was revealed that the orbital diamagnetism caused by interband effects, enhances the diamagnetism in these topological materials. A new terminology "*valley magnetization*" is introduced as this magnetization corresponds to the valley in energy and the valley results in enhancement, thus this is often referred to as valley magnetization [25,206]. $ZrTe_5$ and $HfTe_5$ show one of the largest diamagnetic values among previously reported state-of-the-art topological semimetals with magnetic susceptibility, χ of 17.3×10^{-4} and 12.44×10^{-4} emu mol^{-1} Oe^{-1}, respectively. The field-dependent diamagnetic signal grows linearly with the field without any sign of saturation. Interestingly, the observed diamagnetism is anisotropic, depending on the anisotropy of FS, and is strongly related to the Fermi velocity, indicating the dominating contribution of orbital diamagnetism is induced by interband effects. With our findings, a new physical phenomenon to this topological family has been introduced, which could lead to plenty of new opportunities for research into topological materials. Through this research, we hope to gain a better understanding of the huge diamagnetic signal found in diverse topological semimetals.

The magnetic response of over 25 topologically non-trivial semimetals which are non-magnetic in nature has been studied, in order to understand the origin of diamagnetism from a fundamental perspective. The magnetic measurements were performed using a SQUID vibrating sample magnetometer (MPMS 3, Quantum Design) with a sensitivity of 10^{-7} emu. For minimizing the error in the measurements, the same quartz holder was used for every measurement with the same amount of adhesive tape to stick the sample to the quartz paddle, instead of using GE varnish. A background measurement was taken for the quartz paddle with adhesive tape and was subtracted from each measured sample. The field as well as temperature-dependent magnetization for all materials were measured over a magnetic field range of -7 to $+7$ T at various temperatures between 2 and 300 K with field along their principle crystallographic axes.

It's challenging to comprehend such a diverse group of materials because their band topologies differ from one another. The material's topological classification was the first clue to look for. Therefore, measured topological semimetals were divided into three well defined categories: Dirac, Weyl, and chiral (B20) compounds to understand the magnetic response separately and to have a better comparison. Bismuth and bismuth-antimony (Bi-Sb) compounds were also examined to provide a better comparison, as bismuth is widely known for its extremely high diamagnetic value. Figure 5.1 displays the field dependent magnetization of topological semimetals, majority of them follow a linear trend as the magnetic field is increased. While only a few of them depart from the linear trend, as given in section 5B.5. DSMs have the highest value of all the categories, even surpassing Bi-Sb compounds. Besides these high magnetization values, the diamagnetic signal also comprises quantum oscillations, which starts below 1 T proving the high quality of crystals. Figure 5.1(a) illustrates field dependent magnetization of DSMs $ZrTe_5$, $HfTe_5$, YPtBi, Cd_3As_2, $NbAs_2$, LaBi, LaSb, and $TaTe_2$. $ZrTe_5$ and $HfTe_5$ exhibit one order of magnitude higher than bismuth, Bi-Sb compounds and WSMs. Figure 5.1(b) shows field dependent magnetization of bismuth and Bi-Sb compounds, measured with magnetic field applied along crystallographic axis [111], while for Weyl semimetals are shown in Figure 5.1(c). In the class of WSMs, the first realized WSM has been measured; the family of TaAs which includes NbAs, TaP, and NbP. Type-II WSMs have also been measured, such as WTe_2 and $MoTe_2$, and found that all WSMs follow a linear field dependent magnetization trend. Field dependent magnetization of B20 compounds like RhSn, RhSi, $Rh_{0.94}Ni_{0.06}Si$, $Rh_{0.9}Ni_{0.1}Si$, PtGa, PdGa, and PtAl are shown in Figure 5.1(d). $ZrTe_5$ and $HfTe_5$ exhibit the highest values in the DSMs category, whereas WTe_2 shows the highest value in the WSMs category, and RhSn has the highest value among B20 compounds.
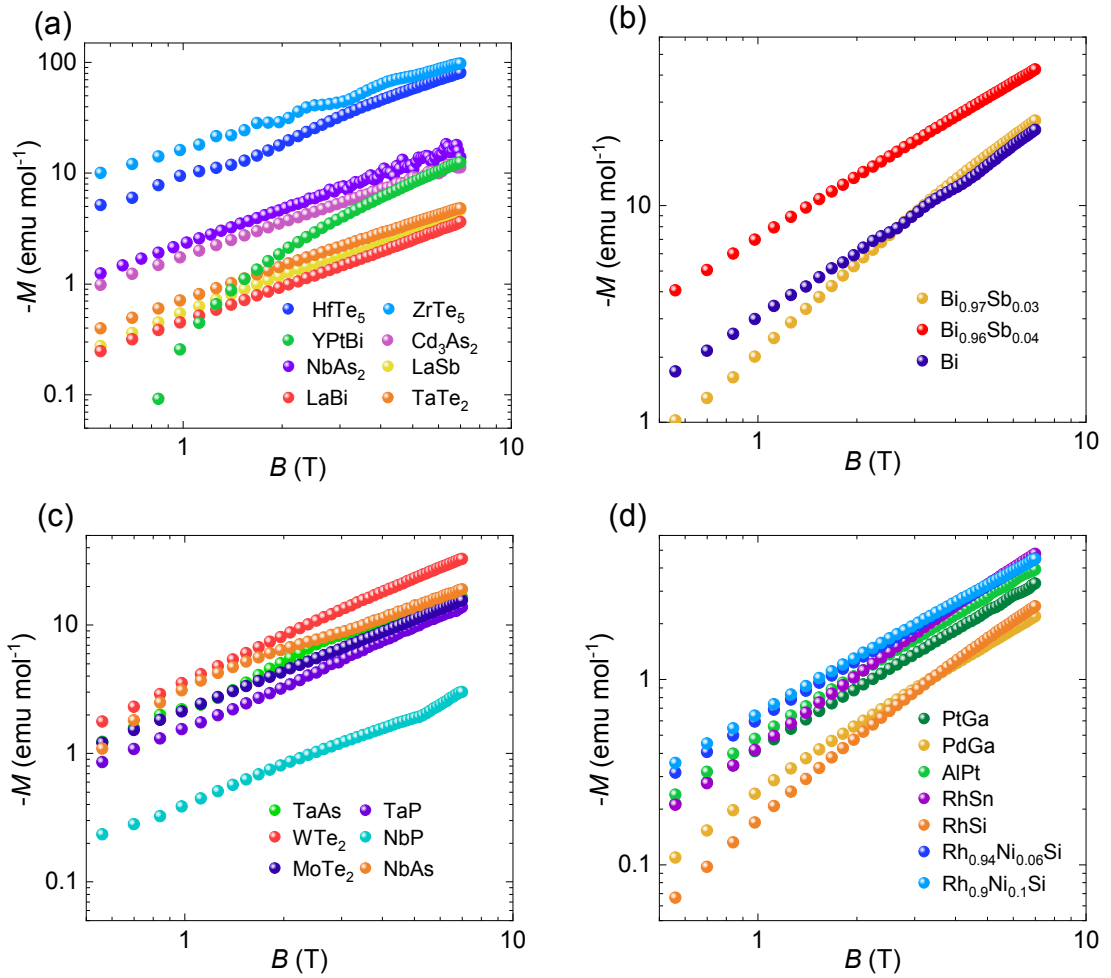
Figure 5.1: Field dependent magnetization of various topological semimetals. (a) DSMs measured at 2 K, **(b)** bismuth and antimony doped bismuth compounds measured at 2 K, **(c)** WSMs measured at 2 K, **(d)** chiral semimetals (B20 compounds) measured at 20 K.

Figure 5.2 illustrates the histogram of the magnetization values of a list of topological materials measured in an applied magnetic field of 7 T at 2 K. Among them, ZrTe$_5$ and HfTe$_5$ show largest values of 97.2 and 80.4 emu mol^{-1}, respectively, in the category of DSMs. WTe$_2$ has higher diamagnetic susceptibility after ZrTe$_5$ and HfTe$_5$, and is even greater than bismuth. The chiral semimetals show at least an order of magnitude smaller magnetic susceptibility compared to DSMs and WSMs.

To gain a better understanding behind such large diamagnetism or magnetic susceptibility found in these topological semimetals, several literatures have been explored. After reviewing several theoretical and experimental studies, it was realized that systems with a linear dispersion separated by a small band gap near the E_F can result in enhanced diamagnetism [121,123-126]. As discussed in chapter 2 section 2.5.3, Fermi velocity and the position of chemical potential inside the Dirac gap play a crucial role in the enhancement of orbital diamagnetism. This enhancement is in the orbital part as discussed in section 2.5.3. This enhanced diamagnetism is also referred to as *valley magnetization* since it is related to the valley present in the band structure.

In presence of very few bands at the E_F, it is much easier to distinguish the contribution of enhanced orbital magnetization, in which the position of chemical potential plays an important role. In all these topological materials, we realized that ZrTe$_5$ and HfTe$_5$ are the best candidates to understand the effect (section 2.5.3.) as they have only two bands at the E_F, forming a Dirac cone having a gap of around 10-20 meV [50,207,208]. Interestingly, both ZrTe$_5$ and HfTe$_5$ have also been known for their anomaly and the movement of chemical potential is clearly seen in spectroscopy tools e.g. ARPES [208-210]. Thus, we started this chapter to discuss ZrTe$_5$ and HfTe$_5$, (discussed in detail in section 5A) well known DSMs to create a better understanding of such large diamagnetism in the pool of topological semimetals experimentally.
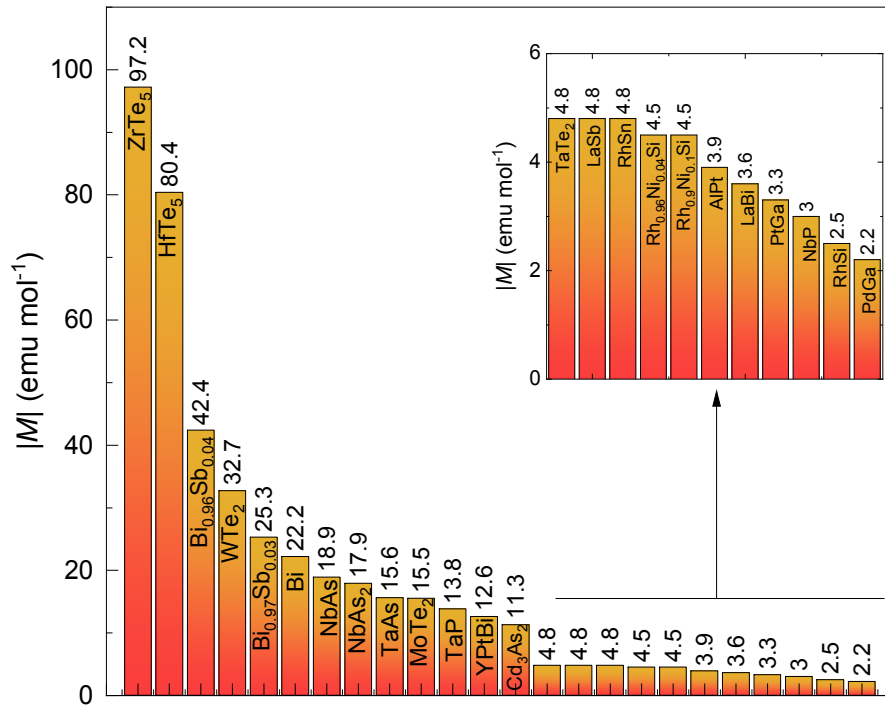
Figure 5.2: Histogram plot for various measured topological semimetals. List of all compounds measured, and their magnetization value measured at an applied magnetic field of 7 T at 2 K. The corresponding magnetization value is mentioned on the top.

5A. Anisotropic diamagnetism in ZrTe$_5$ and HfTe$_5$

5A.1. Preface

Transition-metal pentatellurides, namely ZrTe$_5$ and HfTe$_5$, are one of the most studied topological DSMs, and they behave as quasi-2D semimetals owing to the presence of van der Waals coupling between the layers. Such geometry can also drive to an anisotropic FS. These anisotropic properties can easily be tuned by applying strain or pressure, which is beneficial for tunable applications [211]. Moreover, both ZrTe$_5$ and HfTe$_5$ show an anomaly in the temperature-dependent resistivity namely known as the transition temperature T_p, at which the charge carrier type changes [208,210]. The most feasible explanation of this anomaly is the sweeping of chemical potential with temperature through the Dirac point [209]. Magnetization of these compounds has never been part of the investigation along with other physical properties, even though a controversial anomaly is seen in temperature dependence resistivity and thermopower. In this regard, we strongly believe that ZrTe$_5$ and HfTe$_5$ are the best suitable candidates and have only single band at E_F. The thermodynamic evidence through magnetization of such band can really be promising and the movement of chemical potential can easily be reflected on the measuring property. The SOC is one of the main tuning parameters, and is unavoidably present in the topological semimetals in which a large orbital diamagnetism can be expected. In this chapter, the large anisotropic diamagnetism and the anomaly in temperature dependence magnetization similar to resistivity and thermopower have been discussed, and also shown that how effective mass of charge carriers and position of chemical potential are correlated with the diamagnetism. The anomaly seen in temperature dependence magnetization is characteristics of nodal crossing at which interband scattering enhances.

The texts and figures are taken from the following publication-

5A.2. Growth and crystal structure

Crystal growth

ZrTe$_5$ and HfTe$_5$ single crystals used in this study were grown using CVT. During CVT crystal growth, iodine (I$_2$) was used as a transport agent. Zr (Hf) (powder 99.2 percent) and Te (powder, 5N) were mixed in the molar ratio Zr (Hf): Te 1: 5.5 and sealed in a quartz ampoule with I$_2$ (7 mg = ml). The ampoule was placed in a two-zone furnace. A typical temperature gradient of 480 °C to 400 °C was used. After two months, long ribbon-shaped single crystals were formed, as illustrated in Figures 5 A.1 (b) & (c).

Crystal structure

Both ZrTe$_5$ and HfTe$_5$ crystallize in orthorhombic crystal structure with space group (SG) *Cmcm* (63), as shown in Figure 5A.1(a). In this figure, we can see that van der Waals layers are stacked along the crystallographic *b*-axis, while the prismatic chain of transition metals surrounded by Te atoms run along the *a*-axis. These prismatic chains are linked by zigzag Te atoms along the *c*-axis, forming a 2D sheet of Zr/HfTe$_5$ in the *ac*-plane [62]. These atomic arrangements facilitate the crystal growth in a long plate-like shape as shown in Figures 5A.1(b) & (c). The length and cleaving planes are always along the *a*-axis and the *ac*-plane, respectively.
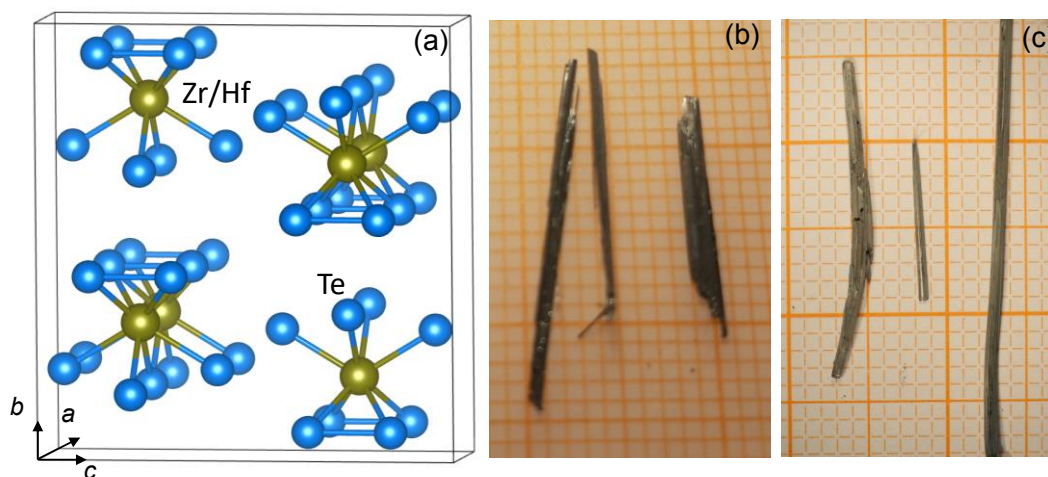
Figure 5A.1: **Crystal structure and image of Zr/HfTe₅. (a)** Orthorhombic crystal structure of Zr/HfTe$_5$, showing that the layers are stacked along the *b*-axis where van der Waals layers are present. Image of **(b)** ZrTe$_5$ and **(c)** HfTe$_5$ crystal grown using CVT technique.

5A.3. Anomaly in magnetization

The field as well as temperature-dependent magnetization for Zr/HfTe$_5$ were measured over the magnetic field range of −7 to +7 T at temperatures between 2 and 300 K with field along all three crystallographic axes. In this study, we investigated the diamagnetism and found it to be −17.33 × 10^{-4} emu mol^{-1} Oe^{-1} for ZrTe$_5$ and −12.49 × 10^{-4} emu mol^{-1} Oe^{-1} for HfTe$_5$ at T_p in 1 T, which are highest among the previously reported state-of-the-art topological semimetals [130-132]. An anomaly develops at T_p in temperature-dependent magnetization measurement, which was illusive and now adds an important experimental aspect characterizing nodal crossing. The highest diamagnetic signal appears at T_p. The measured diamagnetic signal is sensitive to the band structure and the position of chemical potential specifically when topological nodes are present near to the E_F.
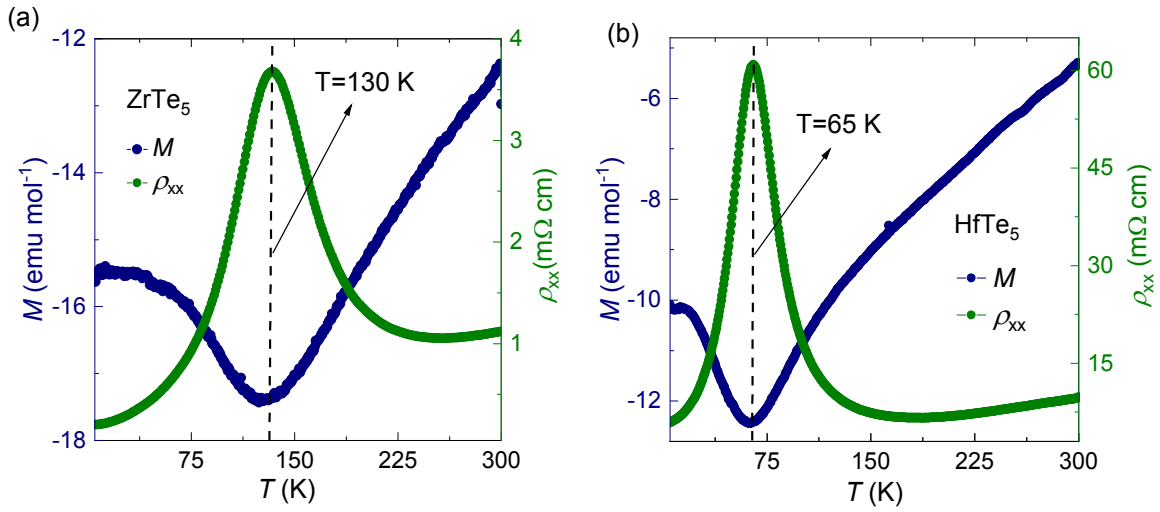
Figure 5A.2: Anomaly in magnetization and resistivity of Zr/HfTe$_5$. Temperature-dependent zero field longitudinal resistivity, ρ_{xx} along a-axis and magnetization, M along crystallographic b-axis measured at magnetic field, B of 1 T for **(a)** ZrTe$_5$ and **(b)** HfTe$_5$. The dotted lines correspond to the anomaly transition temperature, T_p.

It has been known that ZrTe$_5$ and HfTe$_5$ are electronically quasi-2D, and it is more interesting to see whether this behavior also retains when subjected to a magnetic field. To this end, we measured the temperature-dependent magnetization, M along different axes in various magnetic fields. Figures 5A.2(a) & (b) show the plots of magnetization along the b-axis in magnetic field of 1 T and the zero-field resistivity along the a-axis of ZrTe$_5$ and HfTe$_5$, respectively. Both the compounds exhibit diamagnetic signals over the entire temperature range. The magnitude of M continuously increases with temperature and shows a deep minimum at 130 and 65 K for ZrTe$_5$ and HfTe$_5$, respectively; as the temperature lowers further, the magnitude of M decreases. The above mentioned temperatures correspond to their respective temperature T_p at which anomaly appears in the resistivity

also, wherein charge carrier changes sign in Hall resistivity [58]. The minimum in the curve corresponds to the highest diamagnetic value of -17.33 and -12.44 emu mol^{-1} for ZrTe$_5$ and HfTe$_5$, respectively, in an applied magnetic field of 1 T. The resistivity anomaly peaks observed in Figures 5A.2(a) & (b) correspond to 3.7 and 60 mΩ cm at T_p in ZrTe$_5$ and HfTe$_5$, respectively; the anomaly peak in the temperature-dependent resistivity matches well with the minima observed in temperature-dependent magnetization. Such anomaly was also observed in the thermopower, wherein the Seebeck coefficient changes sign [58,209].

5A.4. Temperature dependent magnetization

Figure 5A.3 shows plots of the temperature-dependent magnetization for ZrTe$_5$ and HfTe$_5$ along all three crystallographic axes at various fields of 1, 3.5, 5, and 7 T. It can be seen that when the field is along the *a*- and *c*-axes, the magnetization is almost temperature independent throughout the measured temperature range at a fixed field. However, when the applied field is along the *b*-axis, the magnetization shows significant temperature dependence. We observe a linear decrease in magnetization with lowering temperature until T_p, above which the magnetization increases slightly while approaching the lowest temperature. Such temperature-dependent magnetization can be interpreted in terms of change in chemical potential through the Dirac point. In Figures 5A.3(c) & (d), the behavior of temperature dependent magnetization curve below from T_p is slightly different when the intensity of field is increased. The probable reason behind this is that in ZrTe$_5$, the FS spectral width is higher for electron pocket as paramagnetic signal and thus responsible for the upturn, decreasing the strength of diamagnetic signal while in case of HfTe$_5$ it is just opposite *i.e.* hole pocket spectral width is higher contributing in diamagnetic signal [208]. The small kink in the magnetizations around 50 K is rather known and is due to the presence of O$_2$ molecules in the instrument chamber.

In particular, for ZrTe$_5$, the value of M in 7 T along the *b*-axis is -0.81 emu cm^{-3} at 2 K, and it reaches the maximum value of -0.87 emu cm^{-3} at T_p (130 K). A further decrease in diamagnetism is observed at 300 K, with a value of -0.62 emu cm^{-3} at 300 K. The same trend is also observed for HfTe$_5$, with slightly lower diamagnetic values. For HfTe$_5$, the values of M along the *b*-axis in 7 T are -0.60, -0.68, and -0.29 emu cm^{-3} at 2 K, T_p (65 K), and 300 K, respectively.
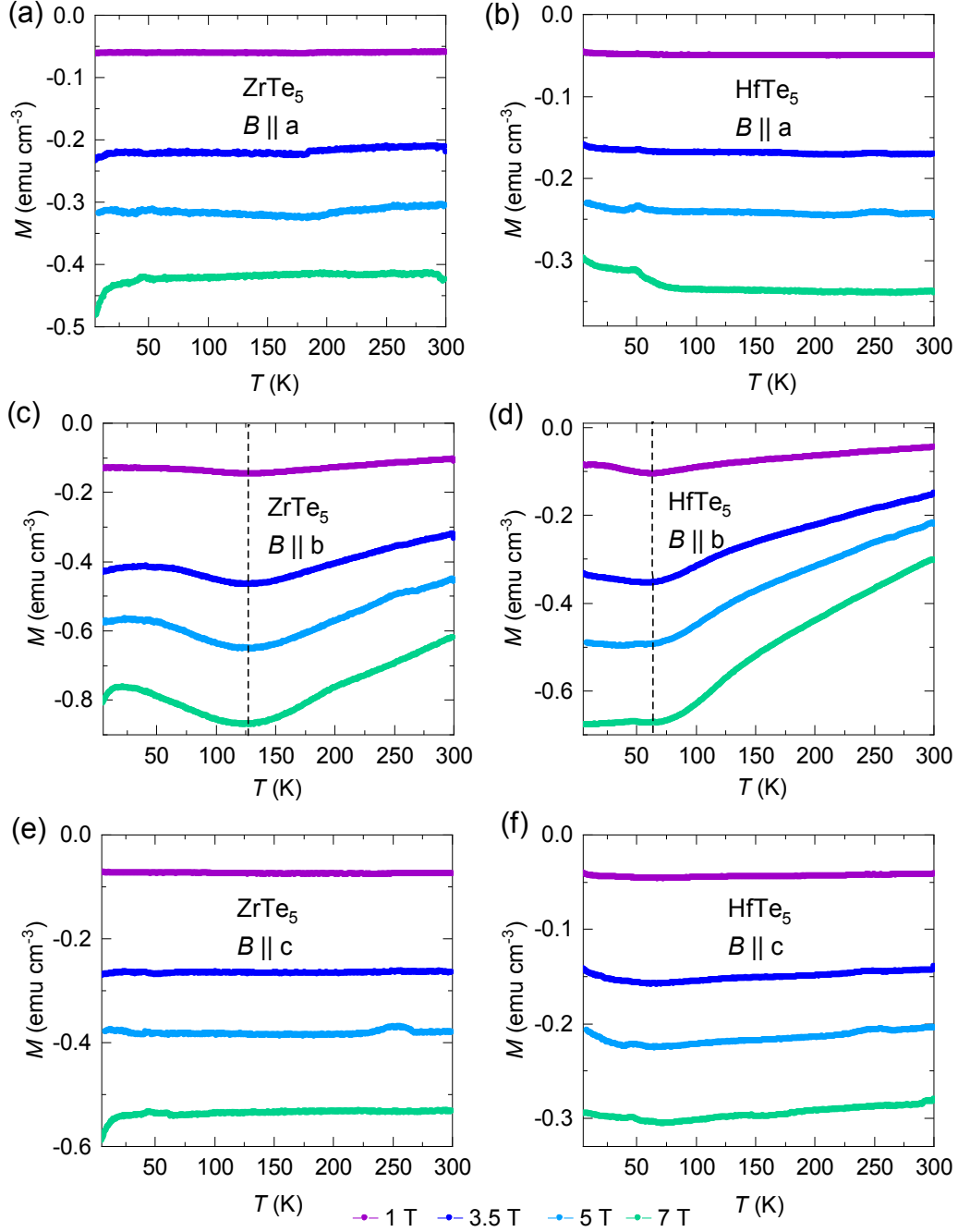
Figure 5A.3: Temperature dependent magnetization of Zr/HfTe$_5$. $M(T)$ curve at different applied magnetic fields along **(a)** a-, **(b)** b-, and **(c)** c-axes for ZrTe$_5$ and along **(d)** a-, **(e)** b-, and **(f)** c-axes for HfTe$_5$. In both (b) and (e) an anomaly is observed, similar to that observed in the resistivity and thermopower. The dotted line corresponds to T_p.

5A.5. Field dependent magnetization

Isothermal magnetization for ZrTe$_5$ and HfTe$_5$ at temperatures between 2 to 300 K have been measured. For better visualization for comparison of anisotropic magnetization along all three crystallographic axes, the magnetization measured at 2 K along all crystallographic axes is shown in Figures 5A.4(a) & (b). While the magnetization measured at different temperatures in different directions are shown in Figure 5A.5. The isothermal magnetization at 2 K and 7 T for ZrTe$_5$ along the a-, b-, and c-axes are −0.49, −0.81, and −0.60 emu cm^{-3}, respectively. In the same conditions, the magnetization of HfTe$_5$ when B is along the a-, b-, and c-axes is −0.29, −0.68, and −0.23 emu cm^{-3}, respectively. Besides these high magnetization values, the diamagnetic signal also comprises quantum oscillations, which start below 1 T proving the high quality of crystals. It is true that the quantum oscillations appear in magnetization only along b-axis, and other two axes do not show. However, these oscillations are present along all the axes in resistivity [14,15]. Usually, the sensitivity of the measurement types depends on the shape of FS, for example, magnetization is sensitive to asymmetrical FS while resistivity for symmetrical. If the FS is asymmetrical in a sense that extremal area normal to applied field varies with the direction of field, there will be torque on the crystal and therefore magnetic measurements are more sensitive for asymmetrical FS [112]. Different diamagnetic values are observed along different axes within the compound, indicating anisotropic behavior, which is relatively high in HfTe$_5$.
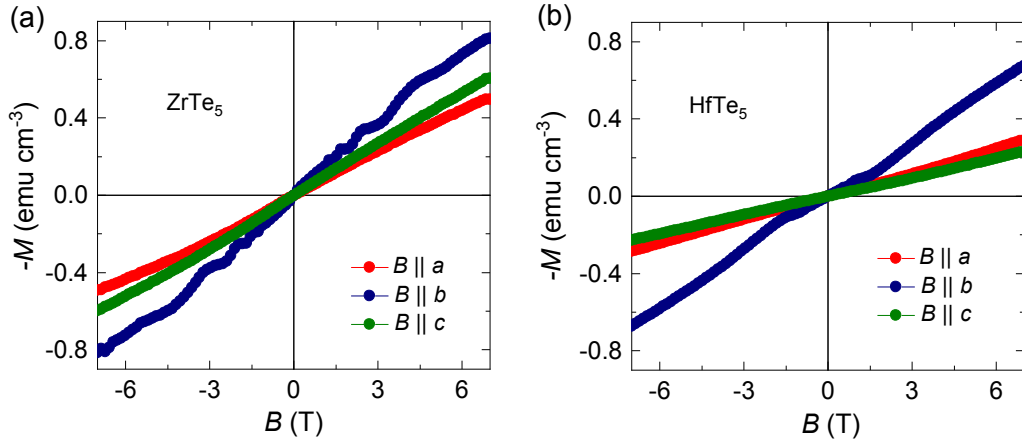
Figure 5A.4: Field-dependent isothermal magnetization of Zr/HfTe$_5$. M(H) curves are measured in range of +7 to −7 T at 2 K along all three crystallographic axes for **(a)** ZrTe$_5$ and **(b)** HfTe$_5$. The highest diamagnetization is reached along the b-axis.
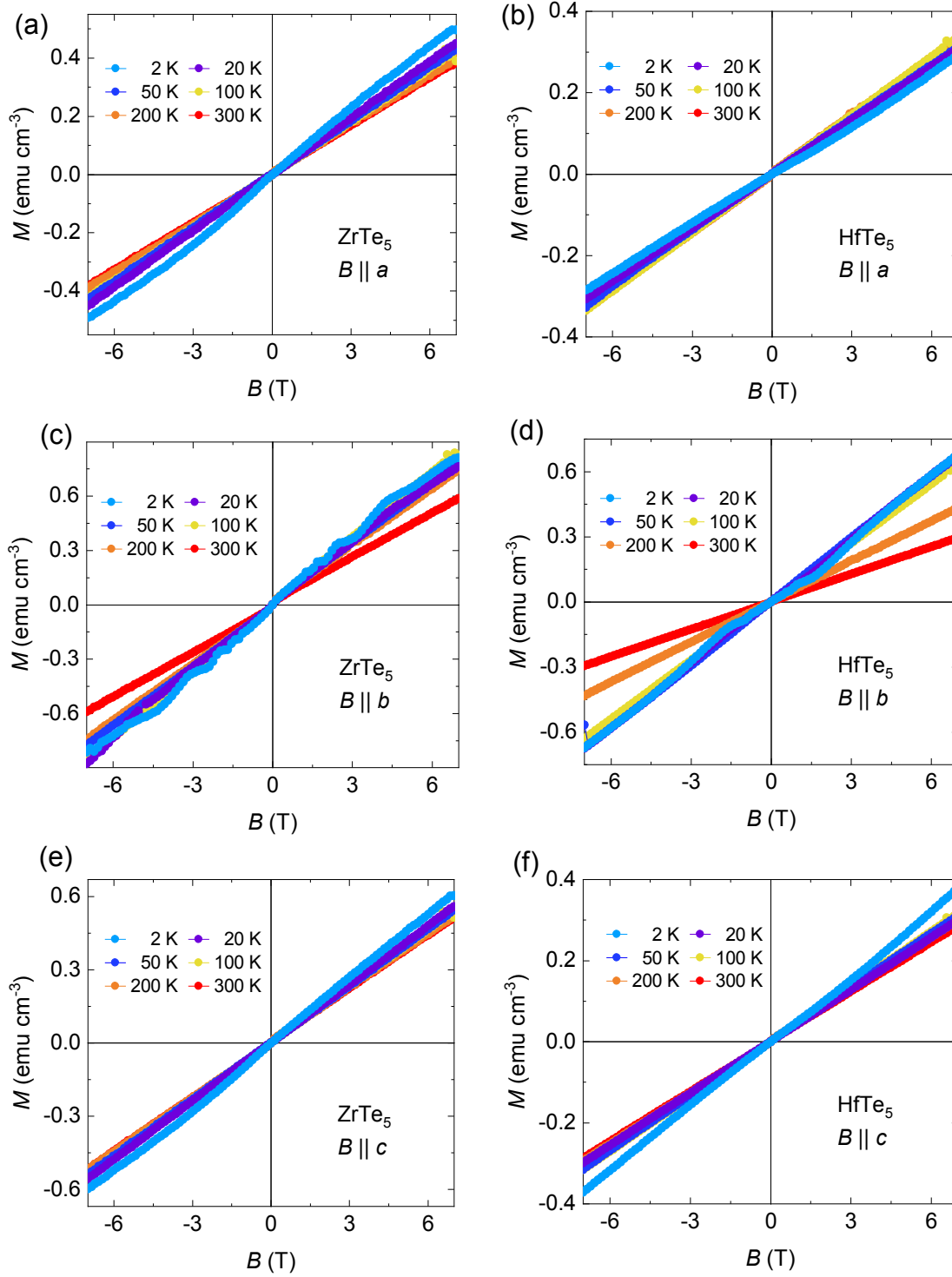
Figure 5A.5: Field dependent magnetization in all crystallographic directions of Zr/HfTe$_5$. *M*(H) curves measured with field along **(a)**, & **(b)** *a*-axis; **(c)**, & **(d)** *b*-axis and **(e)**, & **(f)** *c*-axis of ZrTe$_5$ and HfTe$_5$, respectively.

5A.6. Enhanced orbital magnetization

We correlated the observed anisotropic magnetization with the anisotropic effective mass. The anisotropic effective mass m^* for $ZrTe_5$ along the a-, b-, and c-axes is 0.26 m_0, 0.026 m_0, and 0.16 m_0, respectively, where m_0 is the bare mass of an electron, and the corresponding values for $HfTe_5$ are 0.117 m_0, 0.013 m_0, and 0.303 m_0, respectively [52,80]. Figure 5A.6 shows a plot of the magnetization as a function of the effective mass. From the Figure 5A.6, it can be seen that the smaller effective mass exhibits comparatively larger diamagnetism. This correlation can be attributed to the fact that the Landau diamagnetism (χ_{LD}) dominates over the Pauli spin paramagnetism (χ_{PP}) if the effective mass is very small as $\chi_{LD}/\chi_{PP} \sim (m_0/m^*)^2$ [120] which illustrates that the small effective mass enhances the orbital diamagnetic signal. The anisotropic effective mass ratio for $HfTe_5$ $(m_c^*/m_b^*)^2$ and $ZrTe_5$ $(m_a^*/m_b^*)^2$ is approximately 550 and 100, respectively, which explains the relatively larger anisotropy found in $HfTe_5$ compared to that in $ZrTe_5$. Here, we selected the effective mass along the a-axis instead of the c-axis for $ZrTe_5$ to show the highest anisotropy.
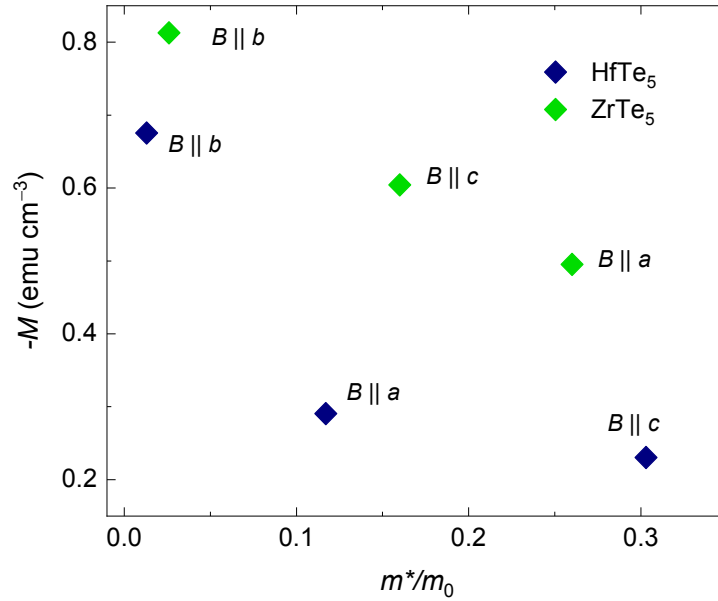
Figure 5A.6: Correlation between magnetization and effective mass for Zr/HfTe5. The diamagnetic signal decreases as effective mass increases and is highest along the b-axis wherein the effective mass is the lowest.

Recently, high orbital diamagnetism was observed in several topological semimetals with linear dispersion near the E_F, e.g., TaAs, Bi$_{0.92}$Sb$_{0.08}$, Bi$_{0.84}$Sb$_{0.16}$, and Sr$_3$PbO [84,114,130,132]. From Figure 5A.7, we can see that ZrTe$_5$ and HfTe$_5$ show one the largest magnetic susceptibility (M/H) among previously reported topological semimetals.
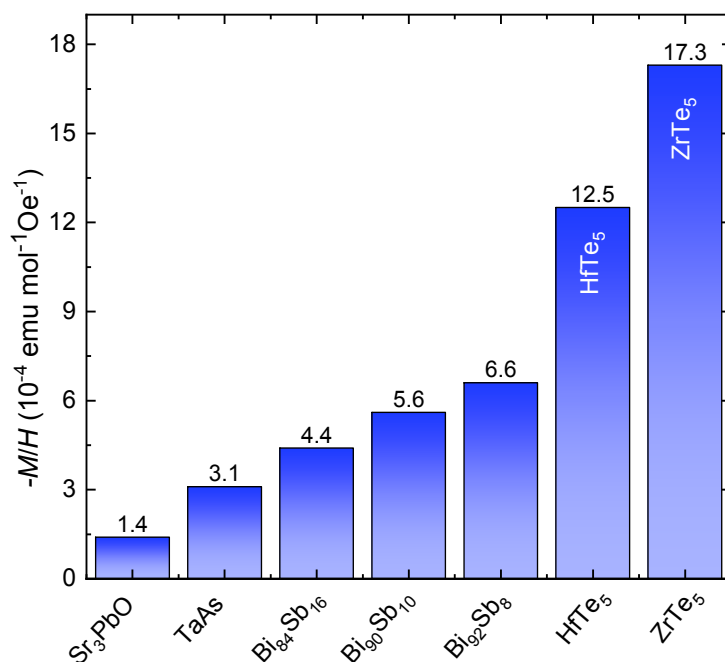
Figure 5A.7: Histogram plot of magnetic response for Zr/HfTe$_5$ along with other compounds. Histogram showing M/H values for previously reported topological semimetals together with ZrTe$_5$ and HfTe$_5$. Present work shows one of the largest values reported till yet [24,26,27,30].

Usually, the magnetization of 3D Fermi gas exhibits paramagnetic response known as Pauli-spin paramagnetism and diamagnetic response from Larmor diamagnetism and Landau diamagnetism, wherein the paramagnetic response dominates and is approximately three times larger than Landau diamagnetic response as discussed in chapter 2 section 2.5.3 [120]. However, Landau (orbital) diamagnetic response can dominate over paramagnetic response, depending on the origins. For example, when the interband effect dominates in the presence of strong SOC, orbital diamagnetism is enhanced [123] and a reasonably high value of diamagnetism was observed in bismuth [122]. The diamagnetism has recently been studied in various semimetals including topological semimetals like graphene, Bi, TaAs, Sr$_3$PbO, and Bi$_{(1-x)}$Sbx , where orbital diamagnetism is responsible for such large diamagnetism [84,121,128,130-132]. In nonmagnetic compounds such as ZrTe$_5$ and HfTe$_5$, magnetism mainly arises from the Pauli paramagnetism, and Landau diamagnetism. The former is induced by the spin of the free electrons, while the latter originates from the

orbital motion. In addition to these two, the Larmor diamagnetism also contributes in diamagnetism which originates from core ions, but its magnitude is normally very small. In particular case of ZrTe$_5$ and HfTe$_5$, the contribution from Larmor diamagnetism is found to be 8.0×10^{-5} emu mol^{-1}Oe^{-1} and 8.6×10^{-5} emu mol^{-1}Oe^{-1}, respectively [212]. While the experimentally observed value is of order 10^{-3} emu mol^{-1}Oe^{-1} which is two order of magnitude higher, clearly indicating a large contribution from the orbital diamagnetism. For any 3D isotropic Dirac system, the value of orbital magnetic susceptibility

$$\chi = \frac{e^2 \vartheta_f}{\pi^2 \hbar} \ln\left(\frac{2E_c}{\Delta}\right),$$

where e is the elementary charge, $\hbar$ is reduced Planck constant, E_c is cutoff energy, ϑ_f is Fermi velocity and Δ is gap [126]. The susceptibility depends on Fermi velocity ϑ_f and gap Δ, if interband effects are taken into consideration [125,126]. Interband transition is more feasible if the band gap is small, thus enhancing the orbital diamagnetism. After taking the naively values of $\Delta = 10$ meV [210], $\vartheta_{fa} = 1.7 \times 10^5$ m s^{-1}, $\vartheta_{fb} = 5.2 \times 10^5$ m s^{-1}, $\vartheta_{fc} = 2.2 \times 10^5$ m s^{-1} [80] for ZrTe$_5$; and $\Delta = 10$ meV [208], $\vartheta_{fa} = 1.7 \times 10^5$ m s^{-1}, $\vartheta_{fb} = 6.4 \times 10^5$ m s^{-1}, $\vartheta_{fc} = 0.8 \times 10^5$ m s^{-1} [52] for HfTe$_5$, considering the system isotropic and $E_c = 500$ meV in the above relation, the value of magnetization at 7 T for ZrTe$_5$ along a-, b- and c-axes is 0.14, 0.41 and 0.17 emu cm^{-3}, respectively, and for HfTe$_5$ along a, b and c-axes is 0.14, 0.51 and 0.06 emu cm^{-3}. The magnitude of magnetic susceptibility merely changes even if we change E_c by a large amount [124]. These values are of the order as measured values depicting a huge enhancement in diamagnetism from orbital diamagnetism.

Unusual large diamagnetism is observed along the b-axis, along which the diamagnetism is highly temperature-dependent, while along the other two axes, it is almost temperature-independent. In a previous study, large diamagnetism was observed in Bi wherein the interband scattering effect was considered, which enhances the orbital diamagnetism when E_F lies between the gap [121,123]. Similarly, in this study, it has been observed that the highest diamagnetic signal corresponding to T_p occurred when the chemical potential lied between the gap [213]. However, an additional factor also controls the diamagnetism. The most likely factor is the anisotropic effective mass according to Landau diamagnetism, as mentioned above. Among all the axes, the effective mass is smallest along the b-axis, where van der Waals coupling exists between the layers, and the diamagnetic signal is highest. For Dirac dispersion, the effective mass does not change with energy, in contrast to the case of parabolic dispersion. Considering the fact that ZrTe$_5$ and HfTe$_5$, the dispersion along the a- and c-axes are linear, while such linear dispersion is suppressed by a parabolic component along the b-axis [214,215]. We observed nearly temperature-independent diamagnetic signals along the a- and c-axes. However, the diamagnetic signal changes with temperature along the b-axis, along which the effective mass is expected to change. Therefore, the diamagnetic signal measured in this study are consistent with the anisotropic dispersion of the bulk Dirac cone, which results in an

anisotropic effective mass. Such a strong correlation between the effective mass and magnetization clearly indicates that the orbital contribution is dominant.

5A.7. Summary and outlook

One of the largest magnitudes of diamagnetism have been measured in ZrTe$_5$ and HfTe$_5$ among previously reported topological semimetals. The magnetization measured is anisotropic and temperature-independent along the *a*- and *c*-axes. Along the *b*-axis, they have anomalous behavior similar to that of the resistivity and thermopower observed in previous studies. The highest diamagnetic signal was observed at T_p, at which the chemical potential lies in the gap. Within the different axes, the *b*-axis shows the highest diamagnetism, which is in accordance with the lower effective mass compared to that in the other axes, indicating the dominant role of orbital diamagnetic contribution. This study adds another physical property as giant diamagnetism to other known physical properties in ZrTe$_5$ and HfTe$_5$, motivating others to look for topological semimetals resulting in such large diamagnetism. This work also provides a thermodynamic experimental platform to investigate nodal crossing.

5B.1. Magnetic response of non-magnetic topological semimetals

Table 5B.1 shows the list of measured topological materials along with their magnetic susceptibility M/H values at 5 K and 300 K, wherein most of the topological materials exhibit the magnetic susceptibility of the order of 10^{-4} emu mol^{-1} Oe^{-1}, while only a few of them are an order of magnitude smaller. As discussed in the previous section 5A, that the position of chemical potential and the Fermi velocity of charge carriers play a crucial role in enhancing the diamagnetism. It is important to note that interband effects can only be observed when the SOC is strong and the pair of conduction band and valence bands are segregated from the other bands. An example of ZrTe$_5$ and HfTe$_5$, helped us to gain a better understanding of enhanced diamagnetism. Here, the diamagnetism of other topological materials has been discussed.

5B.2. Magnetic response of Bi and Bi$_{1-x}$Sb$_x$

Figure 5B.1 illustrates the field and temperature dependent magnetization of bismuth and bismuth-antimony compounds measured in the range of +7 to −7 T at 2, 5, 20, 50 100, 200, 300 K. Figures 5B.1(a),& (b) illustrate M(H) and M(T) curve for bismuth with field applied along [111]. It is known that the bismuth-based materials have played an important role in topological physics due to strong SOC. The first experimental realization of a 3D TI was Bi$_{1-x}$Sb$_x$ compounds. Therefore, we also included these compounds in our diamagnetic study of topological materials. The field dependent magnetization shows linear behavior at higher temperature. The magnetization value reaches −22.2 emu mol^{-1} at 2 K in an applied field of 7 T, and the trend at low temperature is non linear due to the appearance of quantum oscillations. The quantum oscillations present at low temperature makes it more difficult to conclude about the actual behavior of the curves in field dependent magnetization. The temperature dependent magnetization measured at different fields 1, 3.5, 5, and 7 T shows a linear dependence on temperature, which is usually absent in many diamagnetic materials [106]. Magnetic susceptibility (M/H) measured at 300 K is −2.4× 10^{-4} emu mol^{-1} Oe^{-1} and this value reaches to −2.9× 10^{-4} emu mol^{-1} Oe^{-1} at 2 K with an applied field of 1 T. From the literature as well as from the previous section of Zr/HfTe$_5$, it is understable that the strong linear temperature dependence in magnetization curves reveals the movement of chemical potential across the Dirac or Weyl node. Antimony doped bismuth introduces the topological surface states, and it was realized that at 4% doping of antimony, a bulk Dirac node appears at E_F. With the aim to realize Dirac node in Bi$_{1-x}$Sb$_x$, Bi$_{0.96}$Sb$_{0.04}$ and Bi$_{0.97}$Sb$_{0.03}$ compositions were synthesized using a horizontal zone refinement furnace, for detials see appendix. The magnetization value is enhanced in addition of antimony in bismuth, probably due to introduction of topological surface states and gap near the E_F. The magnetization value reaches −25.3 and −42.4 emu mol^{-1} measured in an applied magnetic field of 7 T at 2 K for Bi$_{0.97}$Sb$_{0.03}$ and Bi$_{0.96}$Sb$_{0.04}$, respectively. The M/H measured at 300 K is −2.5 × 10^{-4} emu mol^{-1} Oe^{-1} in an applied field of 1 T and achieves a peak at 44 K value of −2.8 × 10^{-4} emu mol^{-1}Oe^{-1} around 50 K, reaches −2.1 × 10^{-4} emu mol^{-1} Oe^{-1} at

2 K for $Bi_{0.97}Sb_{0.03}$. In case of $Bi_{0.96}Sb_{0.04}$, M/H is -3.5×10^{-4} emu mol^{-1} Oe^{-1} measured at 300 K and it reaches -7×10^{-4} emu mol^{-1} Oe^{-1} at 2 K in 1 T.

Table 5B.1: Magnetic susceptibilities (M/H) for various topological semimetals measured at an applied field of 7 T at 2 K and 300 K. The highest value in red is for $ZrTe_5$

Material	M/H (5 K) emu mol^{-1}Oe^{-1}	M/H (300 K) emu mol^{-1}Oe^{-1}
Bi	-2.9×10^{-4}	-2.41×10^{-4}
$Bi_{0.97}Sb_{0.03}$	-2.4×10^{-4}	-2.1×10^{-4}
$Bi_{0.96}Sb_{0.04}$	-7.09×10^{-4}	-3.48×10^{-4}
$ZrTe_5$	-1.5×10^{-3}	-1.3×10^{-3}
$HfTe_5$	-1.0×10^{-3}	-5.34×10^{-4}
Cd_3As_2	-1.62×10^{-4}	-1.59×10^{-4}
YPtBi	-9.27×10^{-5}	-1.78×10^{-4}
$NbAs_2$	-2.36×10^{-4}	-2.30×10^{-4}
LaBi	-1.55×10^{-6}	-7.91×10^{-5}
LaSb	-4.90×10^{-6}	-7.55×10^{-5}
$TaTe_2$	-5.69×10^{-5}	-6.83×10^{-5}
TaAs	-2.29×10^{-4}	-1.54×10^{-4}
TaP	-1.99×10^{-4}	-1.51×10^{-4}
NbAs	-3.07×10^{-4}	-1.25×10^{-4}
NbP	-6.46×10^{-5}	-1.12×10^{-4}
WTe_2	-5.77×10^{-4}	-5.02×10^{-4}
$MoTe_2$	-2.16×10^{-4}	-1.98×10^{-4}
RhSn	-3.40×10^{-5}	-4.72×10^{-5}
RhSi	-3.61×10^{-5}	-5.06×10^{-5}
$Rh_{0.94}Ni_{0.06}Si$	-6.07×10^{-5}	-5.91×10^{-5}
$Rh_{0.9}Ni_{0.1}Si$	-5.56×10^{-5}	-5.49×10^{-5}
AlPt	-4.68×10^{-5}	-6.09×10^{-5}
PdGa	-2.64×10^{-5}	-4.52×10^{-5}
PtGa	-4.48×10^{-5}	-6.36×10^{-5}
CoSi	1.55×10^{-4}	-2.70×10^{-5}

Figure 5B.1: Field and temperature dependent magnetic response Bi and Bi$_{1-x}$Sb$_x$.
Field dependent magnetization and temperature dependent susceptibility; **(a)**, & **(b)** for bismuth; **(c)**, & **(d)** for and Bi$_{0.97}$Sb$_{0.03}$; and **(e)**, & **(f)** for Bi$_{0.94}$Sb$_{0.04}$ with applied magnetic field along [111].

5B.3. Magnetic response of type I Weyl semimetals

Figures 5B.2 and 5B.3 show field and temperature dependent magnetization of first experimetally realized WSMs in Ta family which includes TaAs, TaP, NbAs and NbP[71]. The magnetization value for TaAs measured at 2 K in applied field of 7 T is -15.6 emu mol^{-1}, and this is -13.6 emu mol^{-1} for TaP, while for NbAs magnetization value reaches -18.9 emu mol^{-1}. Due to small Fermi pockets, the majority of Fermi pockets enters their quantum limit below 7 T in all these compounds. The magnetic susceptibility measured at 300 K is -1.55×10^{-4} emu mol^{-1} Oe^{-1} which reaches -2.3×10^{-4} emu mol^{-1} Oe^{-1} at 2 K for TaAs, while for TaP this is -1.5×10^{-4} emu mol^{-1} Oe^{-1} and -1.7×10^{-4} emu mol^{-1} Oe^{-1} measured at 300 K and 2 K, respectively. We observe a peak in several M(T) curves which is characteristics of nodal crossing and depending on materials, the peak varies. For present TaAs family, it is in between 40-70 K and close to this range, charge carrier type also changes in this family of compounds. In NbAs, magnetic susceptibility (M/H) is -1.25×10^{-4} emu mol^{-1} Oe^{-1} measured at 300 K which reaches -3.1×10^{-4} emu mol^{-1} Oe^{-1} at 2 K. Quantum oscillations in NbP are huge which result the magnetization value is positive at low temperatures can be seen in M(H) curve in Figure 5B.3 and as the oscillations disappear at high temperature $i.e.$ above 50 K this value turns to be negative. All these materials show similar behavior except NbP as itshows huge quantum oscillations. Their temperature dependent curve at different fields also shows inverse temperature dependency above 60 K, which is not very clear.

Figure 5B.2: Field and temperature dependent magnetic response of TaAs and TaP. The field dependent magnetization and temperature dependent susceptibility of first discovered Ta family of Weyl semimetals; **(a)**, & **(b)** for TaAs and **(c)**, & **(d)** for TaP. The field is applied along [001] in the measurement.

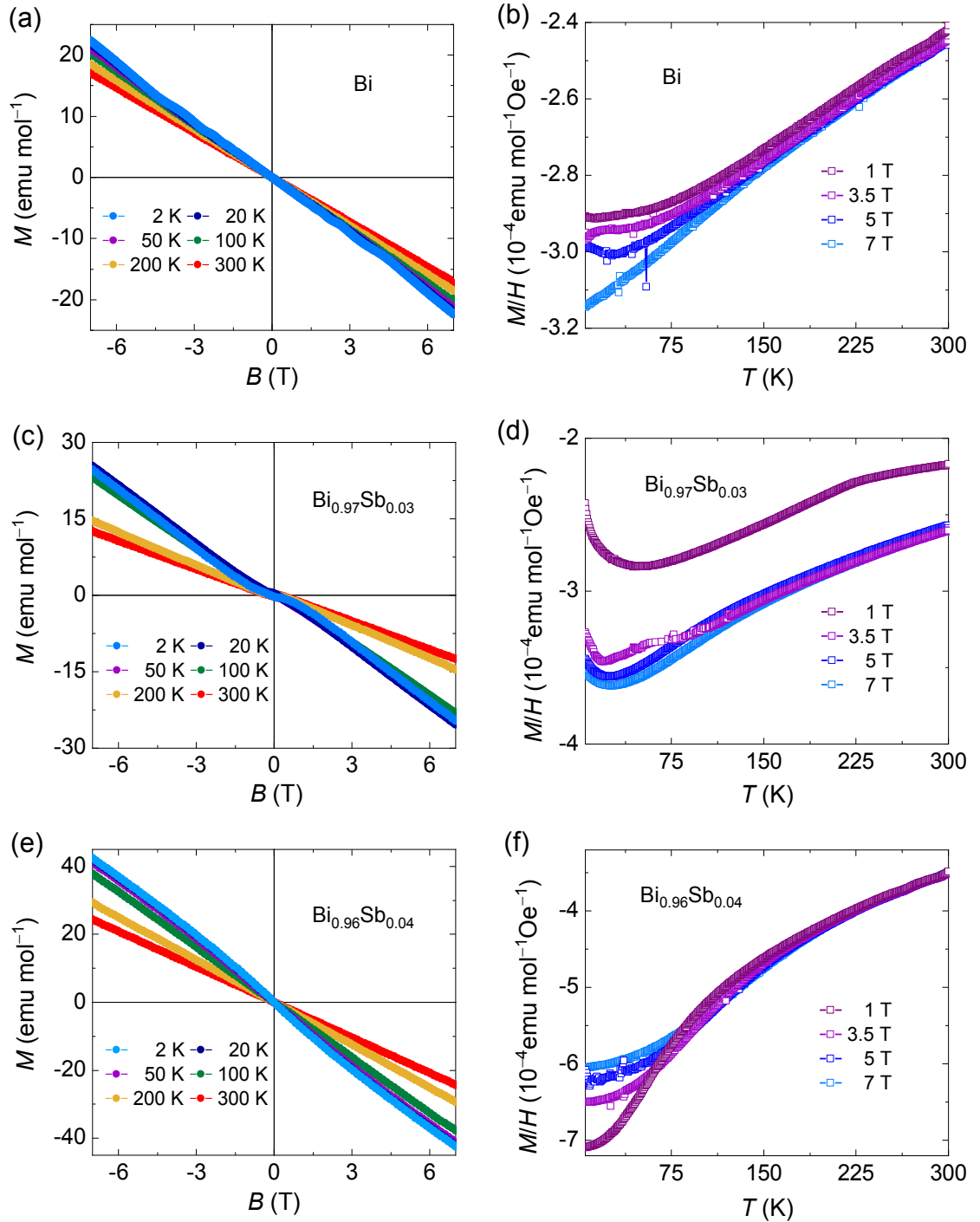**Figure 5B.3: Field and temperature dependent magnetic response of NbAs and NbP.** The field dependent magnetization and temperature dependent susceptibility of first discovered Nb family of Weyl semimetals; **(a)**, & **(b)** for NbAs and **(c)**, & **(d)** for NbP. The magnetic field is applied along [001].

5B.4. Magnetic response of type II Weyl semimetals

Type II Weyl semimetals like $MoTe_2$ and WTe_2 were also measured to study their magnetic response as shown in Figure 5B.4. It turns out that in case of WTe_2, the magnetization value surpasses the TaAs, NbAs, TaP and NbP and the value reaches -32.7 emu mol^{-1} measured at 2 K in applied magnetic field of 7 T along *ab*-plane, while when the applied magnetic field is along *c*- axis the value of magnetization measured is -32 emu mol^{-1}. In case of $MoTe_2$, magnetization value is -15 emu mol^{-1} at 2 K in 7 T along *b*-axis. Temperature dependent magnetization of type II WSMs does not show strong temperature dependence, as this can be understood from the fact that the bands are always present , relaying nearly constant density of states [74] and chemical potential does not alter effectively. Magnetic

susceptibility measured in an applied magnetic field of 1 T at 2 K is -2.2×10^{-4} emu mol^{-1} Oe^{-1} (along b-axis), and -5.8×10^{-4} emu mol^{-1} Oe^{-1} (along c-axis) for MoTe$_2$ and WTe$_2$, respectively. While in the case of WTe$_2$, when an applied field is along ab-plane, magnetic susceptibility measured at 2 K is -3.6×10^{-4} emu mol^{-1} Oe^{-1}. However, a non-linear behavior is seen in field dependent magnetization curve of WTe$_2$.

5B.5. Magnetic response of Dirac semimetals

Among the all categories, few DSMs show one of the largest negative magnetic susceptibility, one order of magnitude higher than other topological semimetals. ZrTe$_5$ and HfTe$_5$ show the largest values and it has been discussed earlier in section 5A because of their very interesting anomaly seen in magnetization and large diamagnetic values. M(H) and M(T) curves are illustrated in Figure 5B.5 and Figure 5B.6 for YPtBi, NbAs$_2$, Cd$_3$As$_2$, LaSb, LaBi, TaTe$_2$. DSMs NbAs$_2$, Cd$_3$As$_2$, and TaTe$_2$ have negative value in M(H) curve throughout the range of 0-9 T field, while in case of YPtBi, LaSb, LaBi they exhibit positive value at low field and as field is increased further the magnetization turns to be negative. The value of the M(H) curve does not vary much as the temperature rises, which is also reflected in M(T) curves, where no noticeable temperature dependence is observed. Quantum oscillations are visible in NbAs$_2$, Cd$_3$As$_2$, LaSb, and LaBi. Detailed analysis of dvHA oscillation is not performed as we are interested in understanding the diamagnetic behavior and the reason behind such large diamagnetic susceptibilities rather than understanding the FS topology which has been studied earlier. The magnetization value for measured DSMs at 2 K is -12.6, -17.9, -11.3, -4.8, -4.8, -3.6 emu mol^{-1} for YPtBi, NbAs$_2$, Cd$_3$As$_2$, TaTe$_2$, LaSb and LaBi, respectively, at an applied magnetic field of 7 T.

In M(T) curves, a strong temperature dependence is absent here in all DSMs measured except ZrTe$_5$ and HfTe$_5$. One of the possible reasons is the presence of other bands, which reduce the impact of interband effects introduced by Dirac bands separated by a small gap with strong SOC interaction. A small peak at around 50 K is because of O$_2$ present in the chamber of instrument. The charge density wave (CDW) transition in TaTe$_2$ [59] present at around 150 K is observed in M(T) curve as sudden drop (Figure 5B.6 (f)). A Curie tail is observed in LaBi, LaSb and YPtBi, which can be attributed to ferromagnetic impurities present. The magnetic susceptibilities of each compound measured at 2 and 300 K are given Table 5B.1.
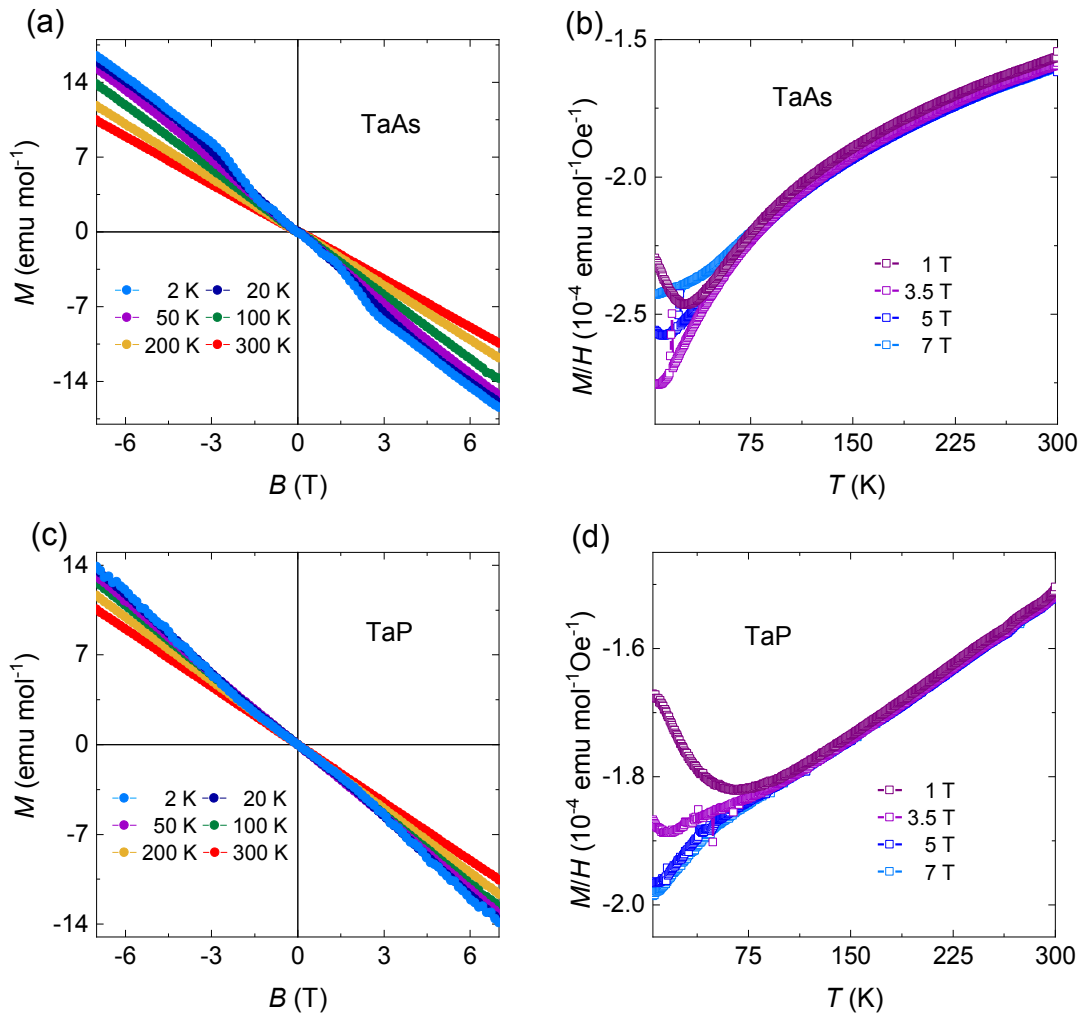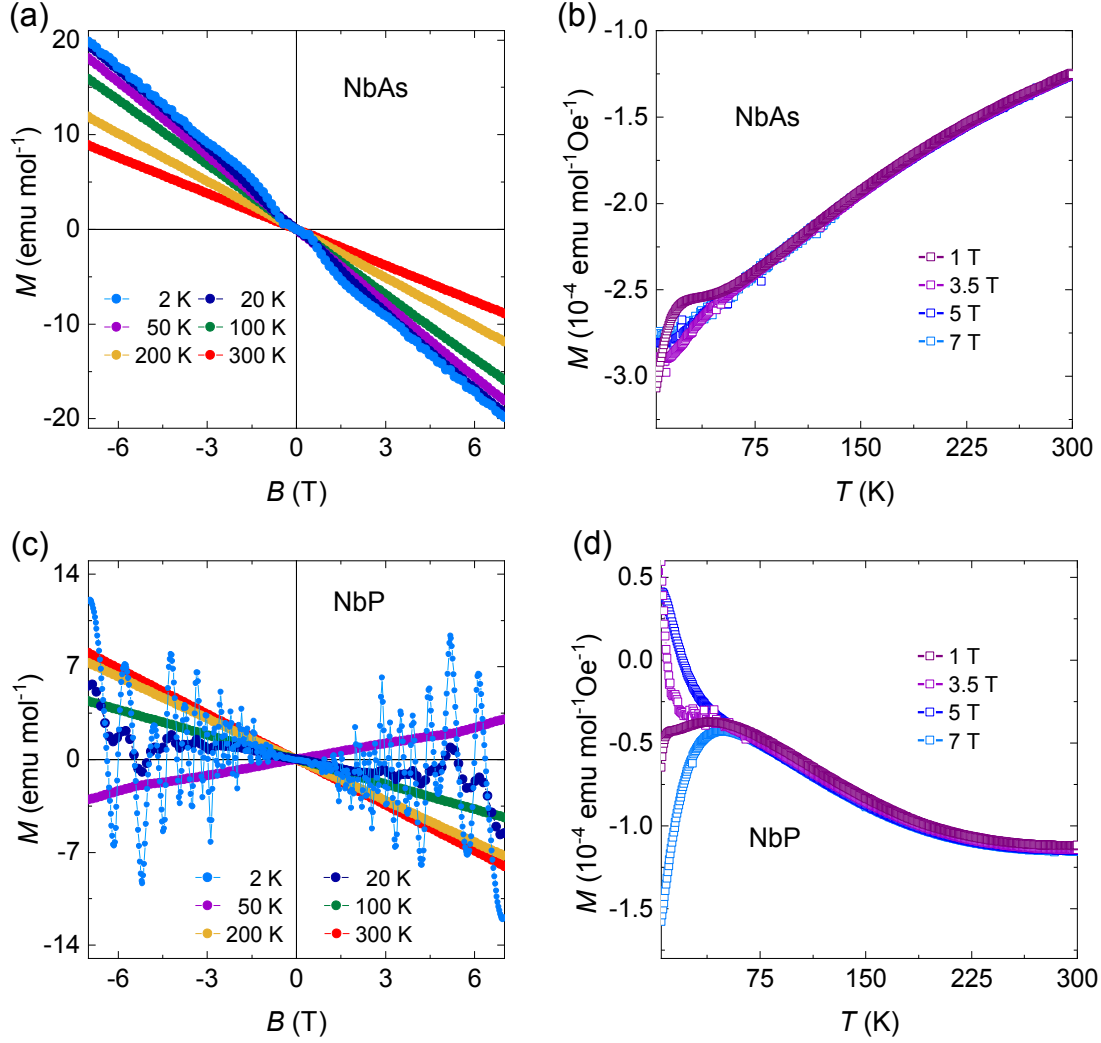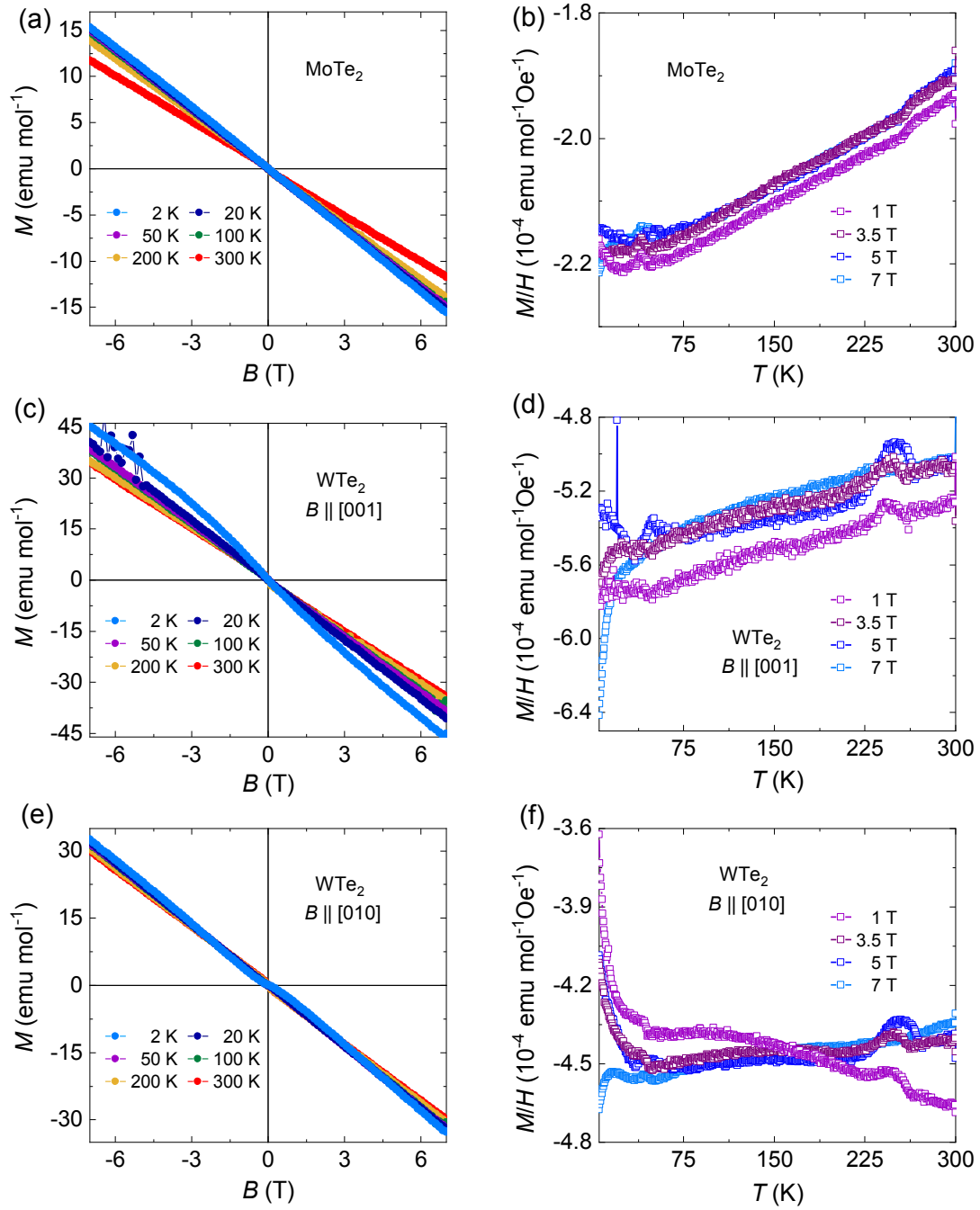
Figure 5B.4: Field and temperature dependent magnetic response of type II WSMs.
The field dependent magnetization and temperature dependent susceptibility of type II
WSMs; **(a)**, & **(b)** for MoTe$_2$ and **(c)**, **(d)**, & **(e)**, **(f)** for WTe$_2$ along c- axis and ac-plane,
respectively.

Figure 5B.5: Field and temperature dependent magnetic response of DSMs YPtBi, NbAs₂ and Cd₃As₂. The field dependent magnetization and temperature dependent susceptibility; **(a)**, & **(b)** for YPtBi; **(c)**, & **(d)** for NbAs$_2$ and **(e)**, & **(f)** for Cd$_3$As$_2$.
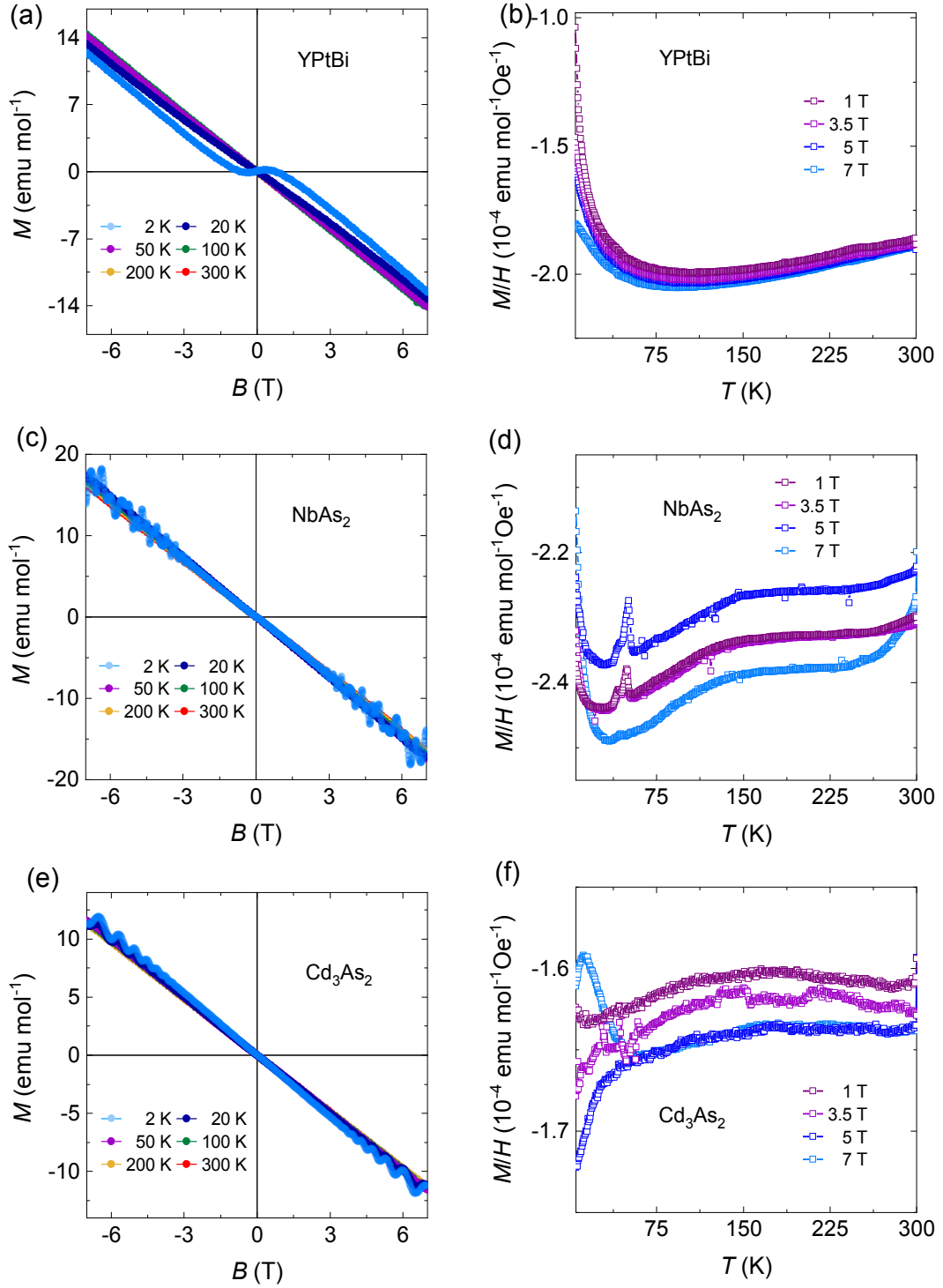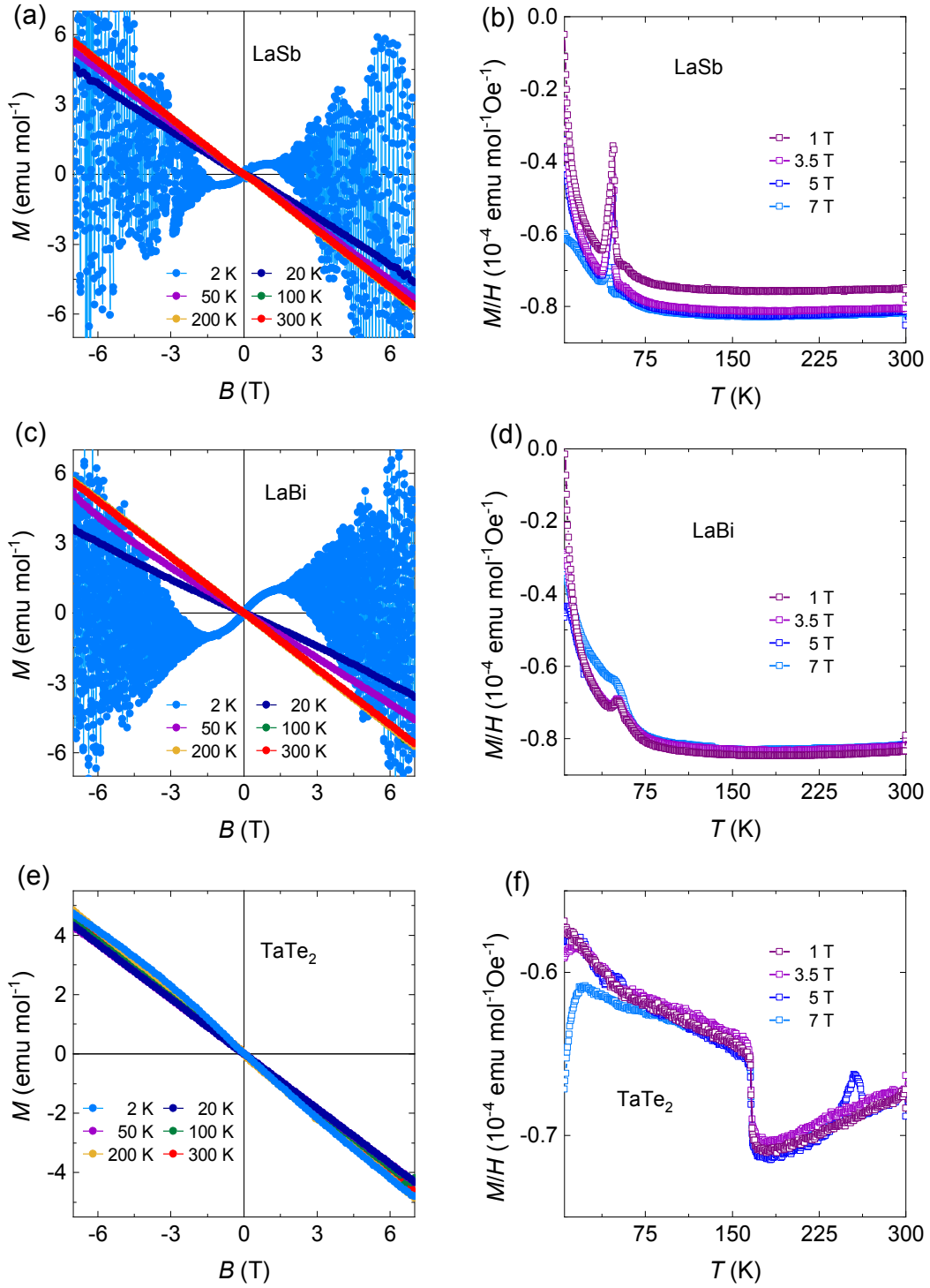
Figure 5B.6: Field and temperature dependent magnetic response of DSMs LaSb, LaBi and TaTe₂. The field dependent magnetization and temperature dependent susceptibility; **(a)**, & **(b)** for LaSb; **(c)**, & **(d)** for LaBi and **(e)**, & **(f)** for TaTe₂.

5B.6. Magnetic response of chiral semimetals (B20 compounds)

Chiral semimetals like CoSi, RhSi, PdGa, and PtGa have recently been studied because of their chirality and the existence of multifold Fermions. The compounds including CoSi, RhSn, RhSi, PtGa, PdGa, AlPt, Ni doped RhSi were investigated to study their magnetic response. However, it turns out that the majority of B20 compounds (excluding CoSi) are diamagnetic and display a negative magnetization in the range of 0 to 7 T. Pt and Pd based B20 compounds such as PtAl, PtGa and PdGa show quantum oscillations below 7 T. Family of Ni doped RhSi shows large values after RhSn. The magnetization value measured at 2 K at an applied field of 7 T is −4.75, −2.5, −4.5, −4.5, −3.3, −2.2, −3.9 emu mol^{-1} for RhSn, RhSi, $Rh_{0.96}Ni_{0.04}Si$, $Rh_{0.9}Ni_{0.1}Si$, PtGa, PdGa and PtAl, respectively. We observe a paramagnetic response, *i.e.*, small positive magnetization in the range of 0 to 7 T magnetic field, in the M(H) and M(T) curves for CoSi as shown in the Figure 5B.10. We believe that this behavior is probably due to Co impurities, but there might be another cause for the positive magnetic susceptibility, which are not now very clear. Some study says that this is due to existence of local magnetic moments, while other says it is signature of chirality-induced spin selective (CISS) transport [216]. At 2 K, CoSi has a magnetization of 7 emu mol^{-1}, measured at magnetic applied field of 7 T. As the temperature increases, the magnetization turns negative, and at 300 K, it is −1.5 emu mol^{-1}.

According to chapter 2 section 2.5.3, the orbital magnetization is directly proportional to the Fermi velocity, thus we can explain the lower magnitude of diamagnetic response for B20 compounds because their effective mass (Fermi velocity) is larger (smaller). Furthermore, the contributions from the interband effects are hampered by the large number of bands present at E_F.

Figure 5B.7: Field and temperature dependent magnetic response of chiral compounds PdGa, PtGa and PtAl. The field dependent magnetization and temperature dependent susceptibility; **(a)**, & **(b)** for PdGa; **(c)**, & **(d)** for PtGa; and **(e)**, & **(f)** for PtAl.

Figure 5B.8: Field and temperature dependent magnetic response of chiral compounds RhSi and Ni doped RhSi. The field dependent magnetization and temperature dependent susceptibility; **(a)**, & **(b)** for RhSi; **(c)**, & **(d)** for $Rh_{0.96}Ni_{0.04}Si$ and **(e)**, & **(f)** for $Rh_{0.9}Ni_{0.1}Si$.

Figure 5B.9: Field and temperature dependent magnetic response of chiral compounds RhSn. The field dependent magnetization **(a)**, & **(b)** the temperature dependent susceptibility of chiral WSM RhSn.
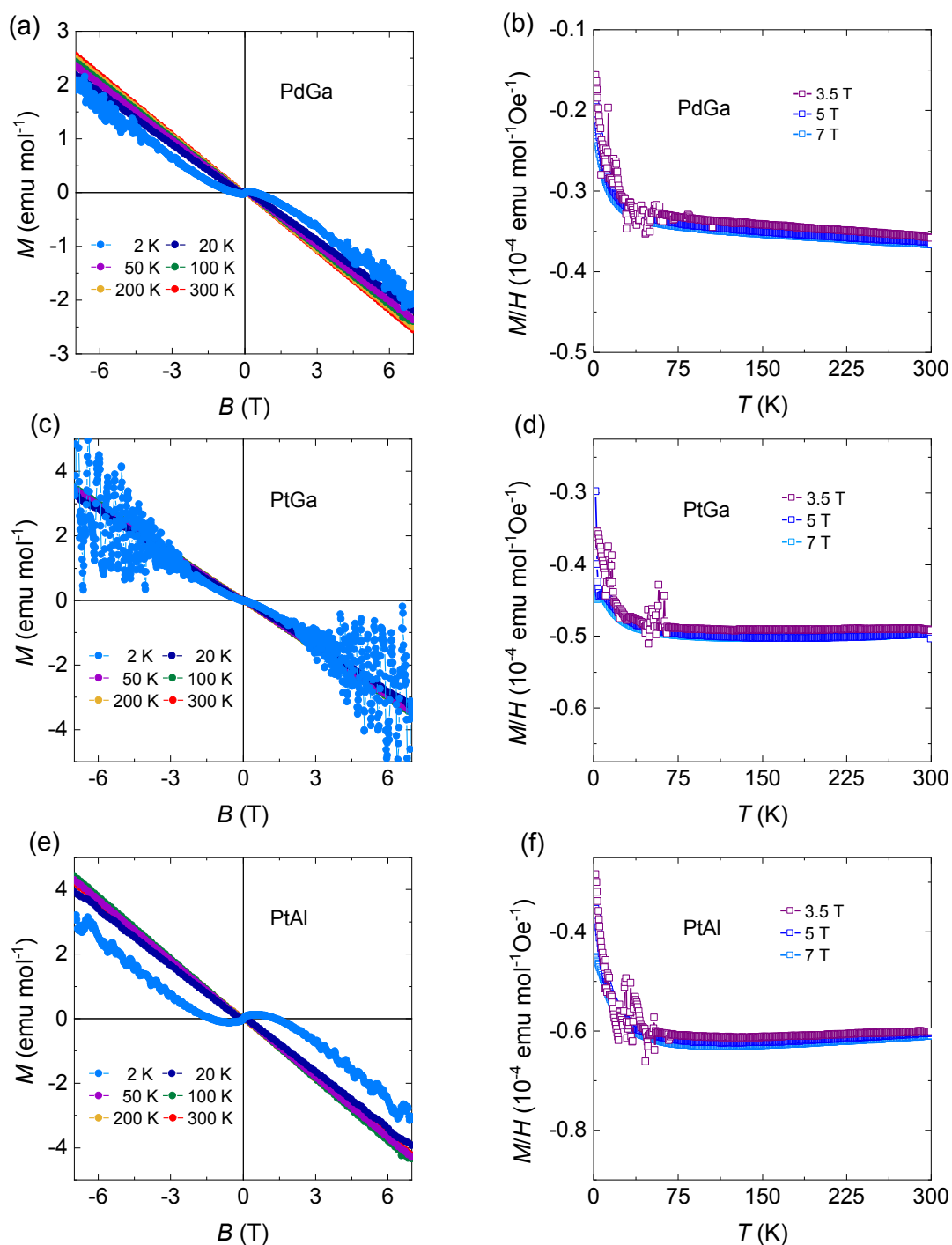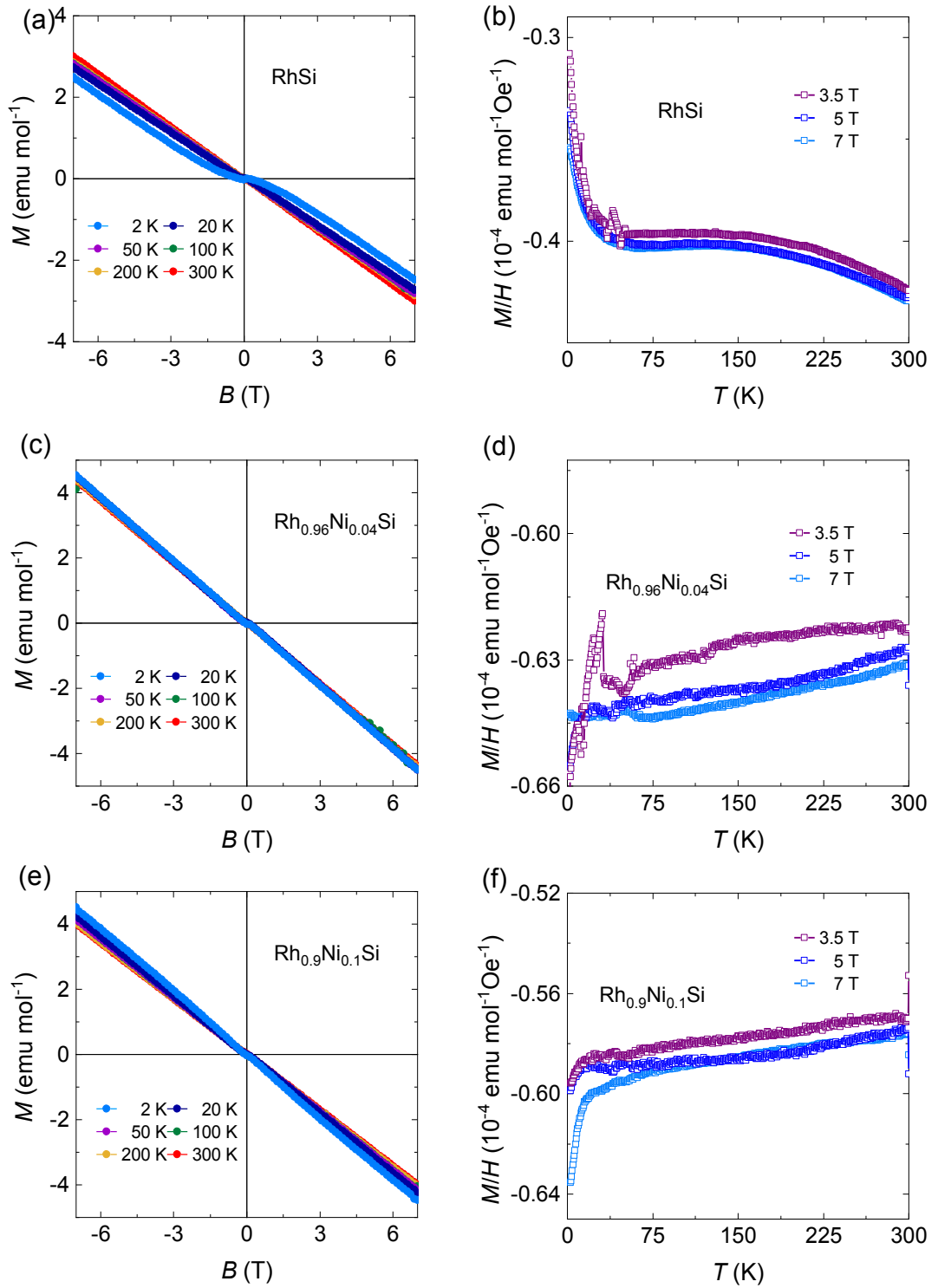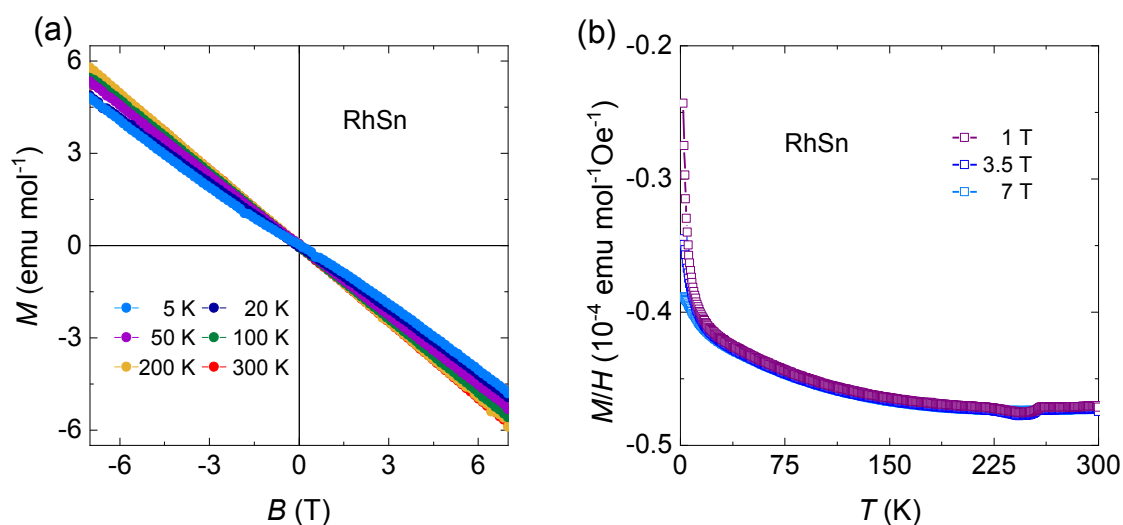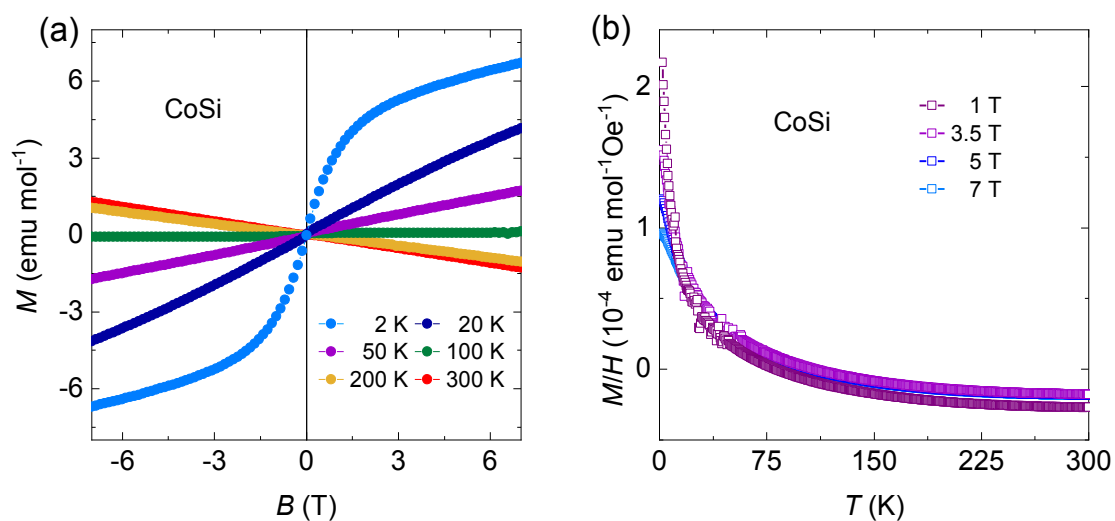

Figure 5B.10: Field and temperature dependent magnetic response of chiral compound CoSi. (a) The field dependent magnetization and **(b)** the temperature dependent susceptibility of chiral WSM CoSi.

From the theoretical understanding in section 2.5.3, that the total magnetic susceptibility has a major contribution from orbital magnetic susceptibility, which depends on two parameters: one of them is Fermi velocity or effective mass and second parameter is position of Dirac/Weyl point from the E_F. The best suitable material would be $ZrTe_5$ and $HfTe_5$ to realize the interband effect since there is no other bands present at E_F. We have discussed $ZrTe_5$ and $HfTe_5$ in particular in detail in section 5A. In all other topological materials, we cannot separate out the contributions of such interband effect as we have many other bands present at E_F, which interfere the interband effects. Thus, one to one relation between magnetization with Fermi velocity and the position of Dirac/Weyl nodes cannot be expected. Therefore, the correlation of these two factors with magnetization has been shown separately in Figure 5B.11. And it has been observed that these parameters for nearest Dirac/Weyl nodes to E_F, they all lie in a region close to the axes. Figure 5B.11 illustrates the plot of magnetization with parameters affecting the orbital diamagnetic susceptibility effective mass m^* and position of Dirac/Weyl point Δ. The lines are drawn corresponding to proportionality relation of χ_{LD} and, χ_{orb} which is shown in Figure 5B.12. For more details, a hyperbola line is drawn on magnetization (M/H) and effective mass m^* plot since χ_{LD} is proportional to $(m_0/m^*)^2$ and a logarithmic decrease line is done on the plot magnetization (M/H) with position of Dirac/Weyl point Δ, as χ_{orb} is proportional to ln $(1/\Delta)$. These lines are done to show that there is a correlation between magnetization and topological parameters Fermi velocity (ϑ_F), effective mass (m^*) and position of Dirac/Weyl point (Δ) from the E_F or not. However, we see a strong deviation from the drawn line as discussed above that in these topological semimetals, the band structure has many bands present at E_F, interfering the interband effect. Thus, no one to one correlation can be concluded.
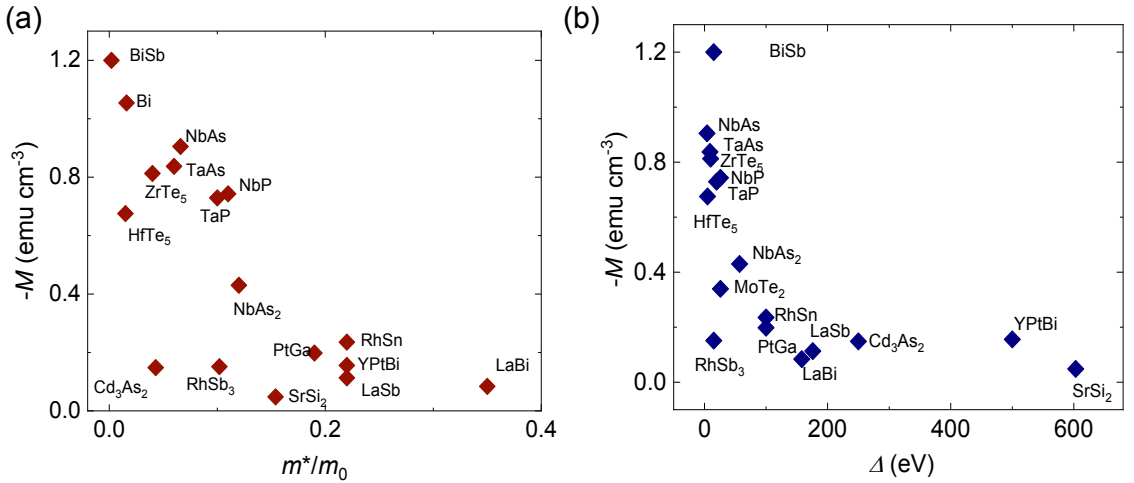
Figure 5B.11: Dependent of magnetic response with effective mass and position of Dirac/Weyl point. The plot of magnetization with parameters affecting the orbital diamagnetic susceptibility of topological semimetals **(a)** magnetization, M and their effective mass m^*, **(b)** magnetization, M with position of Dirac/Weyl point, Δ from the E_F.
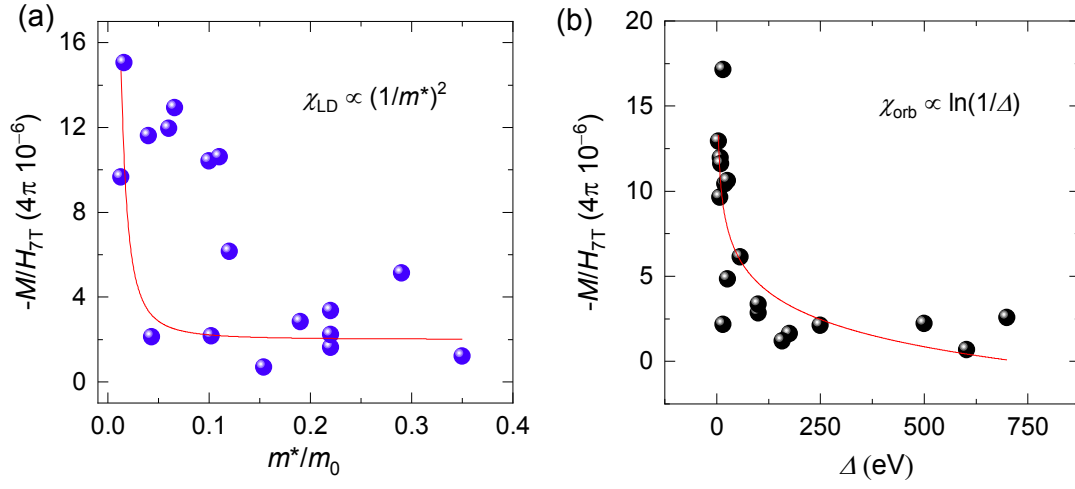
Figure 5B.12: Magnetic susceptibility response on scale of effective mass and position of Dirac/Weyl points. The plot of magnetic susceptibility with **(a)** effective mass m^*, **(b)** position of Dirac/Weyl point. The line indicating **(a)** χ_{LD} is proportional to $(m_0/m^*)^2$, **(b)** χ_{orb} is proportional to $\ln(1/\Delta)$.

5B.7. Summary and outlook

In this chapter, we aimed to explore the underlying mechanism that causes topological semimetals to exhibit such large diamagnetism. We found a strong temperature dependency of the magnetization in various topological semimetals, which can be a hallmark of nodal crossing. $ZrTe_5$ and $HfTe_5$ were found to have the largest diamagnetic signal because of the clear interband effect. There appears to be a considerable correlation between magnetization and effective mass and Dirac mass gap and thus we believe that the enhancement in the diamagnetism we have observed is due to enhanced orbital magnetization. We need a strong theoretical foundation to explain the orbital magnetization better in topological semimetals, which could be the focus of future research. Giant diamagnetism is a new physical phenomenon that we discovered in topological semimetals, and this might inspire other researchers to search for topological semimetals with such huge diamagnetism.

6. Extremely large magnetoresistance and mobility

6.1. Preface

DSMs and WSMs exhibit various exciting properties due to their linearly dispersed bands owning Dirac and Weyl points close to E_F. And, since the valence band and conduction band are in close proximity, charge carriers do not require significant energy to move. Therefore, topological semimetals, in general, are very sensitive to even small perturbations, which further lead to change in their physical properties. Topological materials including TIs and topological semimetals are topologically protected, and this nontrivial topological nature guarantees the existence of exotic surface states [35,63,68,71,147,217-223]. Due to linearly dispersed band near the E_F these semimetals are accompanied with low effective mass charge carriers expecting in high mobility [32,34,36,37,107,224]. This low effective mass results in a high mobility; thus, the material reaches the quantum limit in a moderate magnetic field. In this condition, the resistivity of materials varies linearly with the applied magnetic field, resulting in a linear MR, which is known as quantum MR [36,76,110,225,226]. Topological materials exhibiting linear MR is comparatively low [109]. Generally, MR deviates from linearity in a majority of the compounds and exhibits parabolic behavior due to the charge carrier compensation [29,31,33,103,107,227-233]. An excellent example of materials to show parabolic MR is type-II WSMs, in which unavoidably Fermi level possesses through the tilted Weyl cone and simultaneously creates electron and hole bands. The MR and the mobility are highly pronounced in these topological semimetals, and it has been expected that there is strong correlation between MR and mobility. This chapter focuses on the substantial MR and mobility observed in DSMs and WSMs as well as PtGa$_5$, a new material that expected to be topological semimetal. We found MR is strongly correlated with mobility and follows a right turn path with mobility. PtGa$_5$ was previously discussed only for its crystal structure [234]. Interestingly, PtGa$_5$ shows extremely large MR in addition to extremely large mobility as compared to DSMs and WSMs, which bring it in line of well know topological semimetals. Crystal growth and magneto-electrical transport properties will be covered in this chapter. Due to time restraints, a full examination of the FS of PtGa$_5$ was not completed, however this can be investigated further.

The texts and figures are taken from the following publication-

Sukriti Singh, Vicky Süβ, Marcus Schmidt, Claudia Felser, and Chandra Shekhar, **Strong correlation between mobility and magnetoresistance in Weyl and Dirac semimetals**, *J. Phys. Mater.*, **3**, 024003 (2020).

6.2. Magnetoresistance of Weyl semimetals

Resistivity measurements were performed in PPMS using the AC-transport option. Crystals were cut into bar-shapes using wire saw keeping long direction parallel to the crystallographic a-axis. The physical dimensions (length × width × thickness) are $3.1 \times 1.6 \times 0.56$ mm^3 for NbP, $1.1 \times 0.42 \times 0.16$ mm^3 for TaP, $0.93 \times 0.83 \times 0.17$ mm^3 for NbAs and $1.5 \times 0.42 \times 0.28$ mm^3 for TaAs. Resistivity and Hall resistivity measurements were done in four and five-probe geometries, respectively, in constant current source of 3-4 mA.

Resistivity, ρ_{xx} of all crystals at zero field decreases with decreasing temperature as expected from metallic compound. Their low residual resistivity and high residual resistivity ratio values reflect high quality of the crystals [235,236]. Besides well-established Weyl property, these compounds are also well known for producing ultrahigh mobility and MR. We now focus on the MR measurements. The MR is calculated using equation 2.5. The measured MR of NbP, TaP, NbAs and TaAs at selected temperatures are shown in Figure 6.1 and its remarkable features are: (I) Positive and unsaturation MR that shows systematic variations with temperature and field. (ii) MR is almost constant up to 50 K while it decreases sharply above 50 K. (iii) The more striking feature in MR is that all compounds show SdH oscillations below 20 K, reflecting the high quality of the crystals. The detailed analysis of SdH oscillations and their fermiology can be found elsewhere [235,236]. Among the four compounds, NbP exhibits highest MR of 8.5×10^5 % at 1.85 K in a field of 9 T and interestingly, it does not show any sign of saturation under ultrahigh fields of 62 T at 1.5 K [235]. This value is five times larger than the value that reported for the same field in WTe$_2$ [31], another WSM. The MR of NbP is as high as 250% even at room temperature and 9 T (inset of Figure 6.1(a)). Moreover, the other members of this series also exhibit similar order of MR like NbP at all temperatures and field ranges [35,237]. In presence of the magnetic fields, a nonzero transverse current will experience a Lorentz force in the inverse-longitudinal direction. Such a back flow of carriers eventually increases the apparent longitudinal resistance, resulting the extremely high MR. From above measurements, we can say that these materials have unique property of high and never saturating MR.
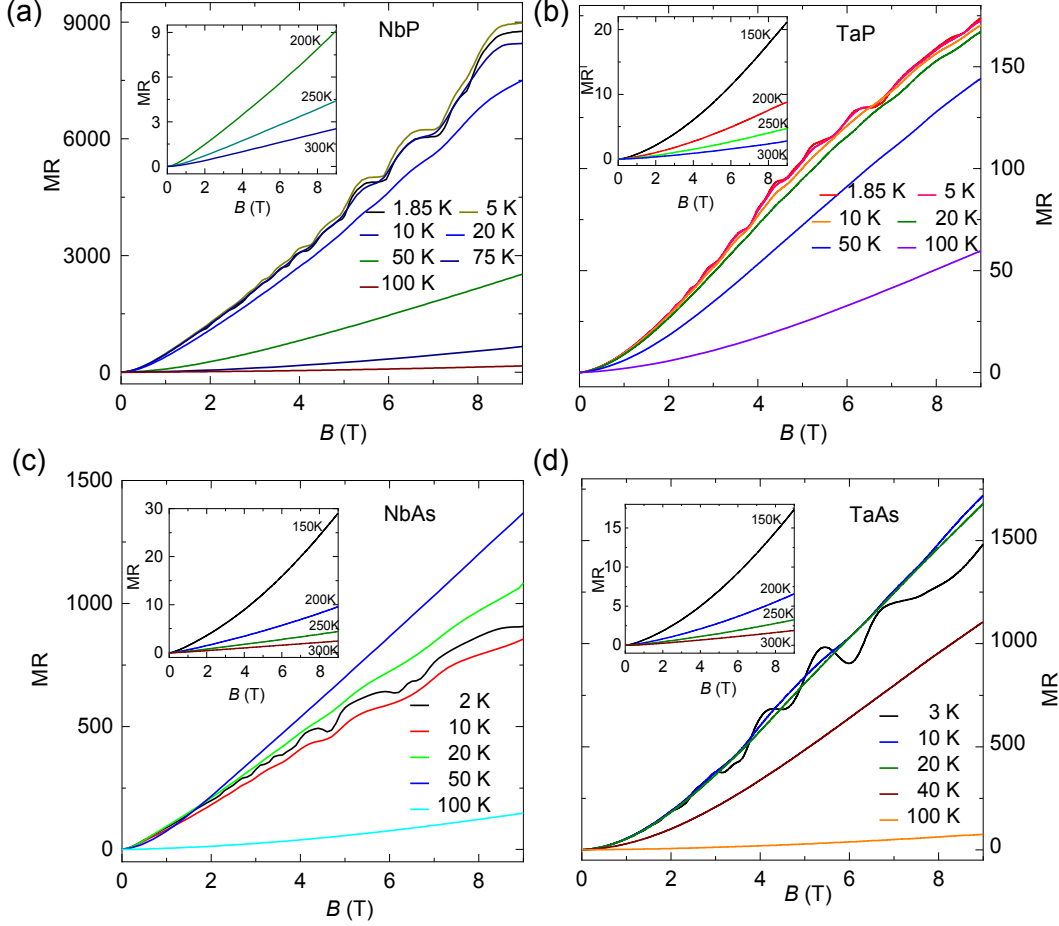
Figure 6.1: MR of NbP, TaP, NbAs & TaAs. Estimated transverse magnetoresistance (MR) at different temperatures from the field dependent resistivity for **(a)** NbP, **(b)** TaP, **(c)** NbAs, and **(d)** TaAs. Insets show their respective magnetoresistance at high temperature ≥ 150 K.

6.3. Mobility of Weyl semimetals

The Hall measurements is performed in positive and negative field directions to improve the accuracy of data. For the sake of simplicity, we used the single-carrier Drude model, $\mu_{avg}(T) = R_H(T)/\rho_{xx}(T)$, where $\mu_{avg}(T)$ is the average mobility and $R_H(T)$ is the Hall coefficient calculated from the linear slope of the $\rho_{xy}(T)$ at high field. However, there is a change in the sign of Hall coefficient from negative to positive between 125-170 K depending on the material e.g. this temperature is about 125 K for Nb-compounds and 170 K for Ta-compounds [235,236]. The charge carrier density lies between 10^{18}-10^{20} cm^{-3} in the temperature range 2-300 K. The observed small carrier density at low temperature and its huge change on increasing the temperature are a typical semimetallic nature. A large MR is usually associated with high mobility and it plays a major role in the charge transport in a material and consequently determines the efficiency of devices. Average mobility is calculated and plotted against the temperature in Figure

6.2. NbP shows the highest mobility 5×10^6 cm^{2}V^{-1}s^{-1} and the lowest residual resistivity 0.63 $\mu\Omega$ cm at 2 K. These values are very close to that of Cd$_3$As$_2$ [238]. The mobilities of others members are 3×10^5 cm^{2}V^{-1}s^{-1} for TaP, 5×10^5 cm^{2}V^{-1}s^{-1} for NbAs and 4×10^5 cm^{2}V^{-1}s^{-1} for TaAs at 2 K and their residual resistivities are 3.2 $\mu\Omega$ cm for TaP, 6.2 $\mu\Omega$ cm for NbAs and 4.2 $\mu\Omega$ cm for TaAs. It is worthy to note here, the estimated mobility from a single-carrier model only slightly differs from mobility obtained from the two-carrier model, and consequently overall its temperature dependent behavior remains almost the same. From the above values of mobility and residual resistivity, it is clear that the anomalously low residual resistivity can be achieved in a clean system where the mobility attains ultrahigh value. When the magnetic field turns on, low temperature resistivity steeply increases, resulting in the extremely large MR [31,235,236]. To examine the role of the mobility on the MR, we have calculated the slope of the MR around 9 T and the mobility at different temperatures for NbP, TaP, NbAs, and TaAs. The slope $\partial MR/\partial B$ is plotted on right axis and the carrier mobility on the left axis as a function of temperature as shown in Figure 6.2. $\partial MR/\partial B$ and the μ_{avg} show identical variation with temperature indicating that the MR is governed by the mobility at least in these four compounds. A slight deviation of mobility graph in the range 100-200 K belongs to the region where the majority type of charge carrier switches from electron to hole. We find that the average mobility and MR very well correlate for all the four compounds.
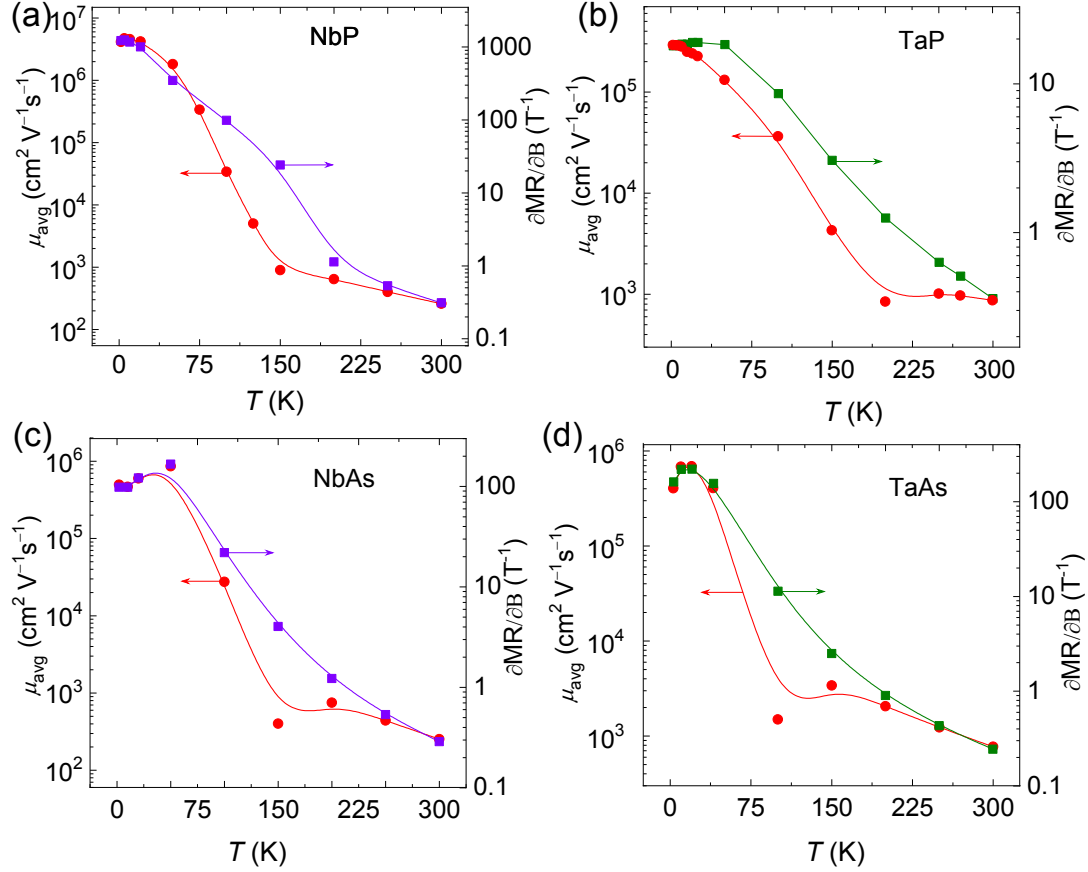
Figure 6.2: Mobility and first order derivative of MR. Temperature dependent average mobility, μ_{avg} (left axis) from single carrier model and slope of magnetoresistance (right axis) around 9 T field for **(a)** NbP, **(b)** TaP, **(c)** NbAs, and **(d)** TaAs. From the two-carrier model, the obtained mobility is similar as single-carrier model, and therefore its temperature dependent does not alter much.

6.4. Correlation between magnetoresistance and mobility

These findings were generalized in broader range of WSMs and DSMs and it is very striking to examine how the MR varies with the mobility in these compounds. We gathered these two quantities from various compounds at ~2 K and 9 T from the literatures [29,31,103,228,233,238-249]. Since MR varies with field therefore taking the slope of MR with field is more valid presentation rather than taking the value of MR at a fix field. However, we plotted both MR and its slope around 9 T against the mobility at 2 K in Figure 6.3(a) & (b), respectively. Behavior of both the graphs is very much alike and both show an intriguing relation between MR and mobility. The MR first increases sharply with mobility and then begins to saturate after reaching the value of 10^3, forming the shape like *right turn* symbol. Nevertheless, this relation confirms that high mobility compounds possess high MR. Noticeably, in presence of the magnetic fields, a high mobile carrier experience stronger Lorentz force, and exhibits high MR. However, it seems that this is not

the only reason and some other factors are also accountable along the Lorentz force, otherwise MR would be in a linear relationship with mobility.
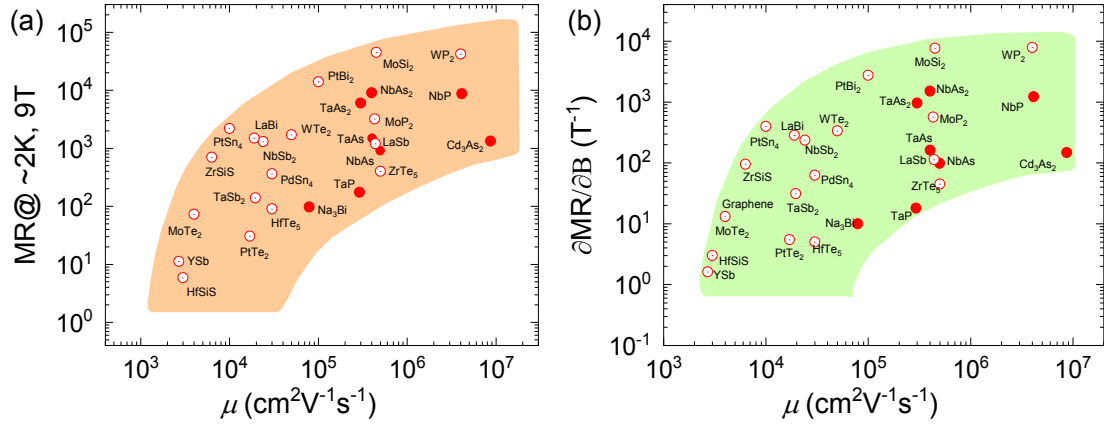
Figure 6.3: MR and mobility of various well-known Weyl and Dirac semimetals. (a) MR at ~2 K and in 9 T versus mobility. **(b)** Slope of MR around 9 T at ~2 K versus mobility. The compounds with filled circle show linear MR. The data were taken from the references [29,31,103,228,233,238-249].

6.5. Extremely large magnetoresistance and mobility in PtGa$_5$

After getting intriguing results for the DSMs and WSMs, we were continuously searching such more compounds that show high MR and high mobility. Our main and starting recipes are to look first electronic band structure of interested materials, and then to search its physical existence in term of reactivity. For an experimentalist, low density of states semimetal is a point of interest, in which valence and conduction bands occur close to the E_F. In such scenario, the probability of overlapping of these bands is high enough, and consequently the appearance of topology near to E_F. After an extensive effort, it was found that PtGa$_5$ would be interesting to investigate in this regard.

6.5.1. Growth and crystal structure

Crystal growth

Gallium-rich phases with platinum were created by reacting the respective precursors into 1:5 ratio with excess of Ga at various temperatures (160-360 °C), and then eliminating the flux by high-temperature centrifugation.

The elements Pt and Ga were taken in a 1:10 ratio. Because gallium has a low melting point (30 °C) and platinum melts at 1768 °C, alloying is done in simple and inexpensive traditional furnace for producing gallium-rich phase. Both elements were mixed and put in alumina crucibles which was further sealed under argon (~5 mbar) inside a quartz tube, with nominal compositions of about 10 and 90 at. % of Pt and Ga, respectively. The alumina crucible was held at 600 °C in the box furnace. The sample was allowed to cool slowly to 300 °C at a rate of 2 °C h^{-1} for crystallization after being maintained at this temperature for 12 hours for homogenization. The surplus of unreacted gallium was removed at the end of the reaction by centrifugation through silica wool. Figure 6.4(b) shows crystals formed using the self-flux approach that are 1-2 mm in size.

Chemical characterization and crystal structure

PtGa$_5$ crystallizes in a monoclinic structure with space group (SG) $P2_1/m$ (11). Single crystal X-ray analyses demonstrated the lattice parameters are found to be $a = 8.8396$ Å, $b = 15.9126$ Å, $c = 12.7442$Å and $\beta = 110.2346°$. In the structure, each antiprism shares atoms with five neighboring polyhedra, creating a 3D network along b-axis, which is the thickness of crystal (Figure. 6.4(b)), while the length of the crystal is along a-axis. The structure has two independent platinum atoms, each surrounding with nine-gallium atoms polyhedron. Pt-Ga distances range from 2.538 Å to 2.713 Å. Ga$_9$ polyhedra are distorted antiprisms which capped on larger square face.
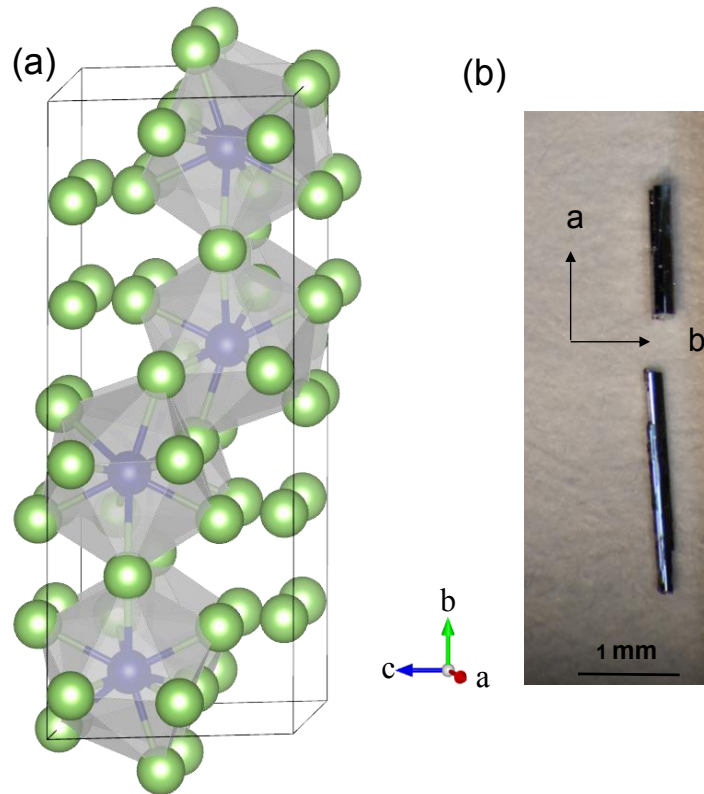
Figure 6.4: Crystal structure of PtGa₅ and optical image of as grown crystals. (a) Crystal structure of PtGa₅ where blue atoms are Pt; while Ga atoms are green. **(b)** Optical image of as grown crystals is shown along with scale of mm to illustrate their size.
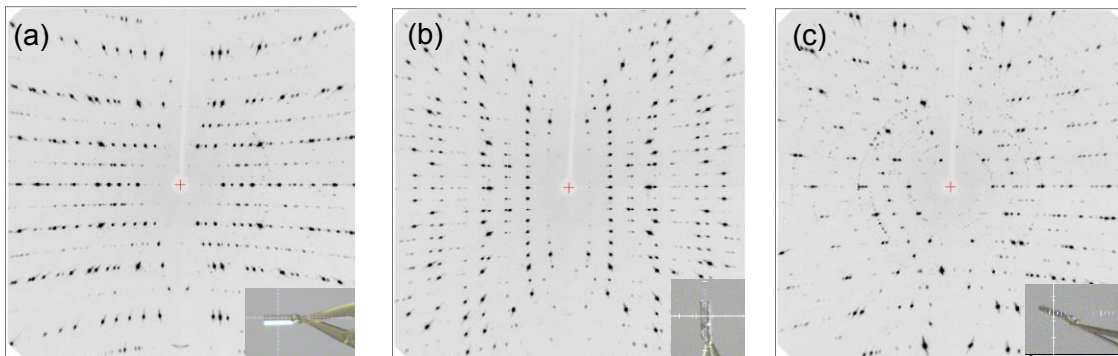
Figure 6.5: Single crystal X-ray diffraction patterns of PtGa₅. Single crystal X-ray diffraction patterns along **(a)** *a*-axis, **(a)** *b*-axis, **(c)** *c*-axis. Respective insets show the image of the crystal in oriented directions.

The collected single crystal diffraction patterns can be described on the basis of two reticular twinned domains that possess a primitive monoclinic unit cell. Despite the fact that mirror planes are only permitted along the one unique axis in monoclinic crystal structures, which in this case is *b*-axis (Figure 6.5 (b)), it has clearly been observed in single

crystal X-ray diffraction that mirror symmetry is also present along *a*-axis (Figure 6.5(a)). After the careful investigations, we found that the structure of PtGa$_5$ is twined, which is in consistent with what has been discussed in previous reference [234].

6.5.2. Electro-magnetic transports of PtGa$_5$

Temperature-dependent resistivity

As mentioned earlier, PtGa$_5$ has been studied before for its crystal structure only and it is now interesting to study beyond this. Figure 6.6(a) depicts the zero-field temperature dependent resistivity measured in the range of 2-300 K. The ρ_{xx} value at 300 K is 75.2 $\mu\Omega$ cm, which drops to 0.129 $\mu\Omega$ cm at 2 K, resulting in RRR of 576. This large value indicates very high purity of the crystal. We further analyzed the resistivity at high temperature and low temperature seperately to understand the scattering mechanism dominanting in this system. At low temperature, resistivity was fitted using relation the $\rho(T) = \rho_0 + aT^2 + bT^5 + c\sqrt{T}$, shown in Figure 6.6(b), where dependece can be accounted for electron-electron scatering (*e-e*, T^2), electron-phonon scattering (*e-ph*, T^5) mechanism and weak localization term ($\sqrt{T}$); *a*, *b* and *c* are contants . The weak localization term describes the coherent backscattering of charge carriers, and it is directly proportional to the system's randomness [250]. The green solid line illustrates the fit without including $c\sqrt{T}$, wherein the fit deviates largely at low temperature. However, the red solid line illustrates fit after including c$\sqrt{T}$ term, which improves the fit. It seems, the twinnings present in the crystal stucture are responsible for increasing randomness, and consiquently increases the scattering probability.
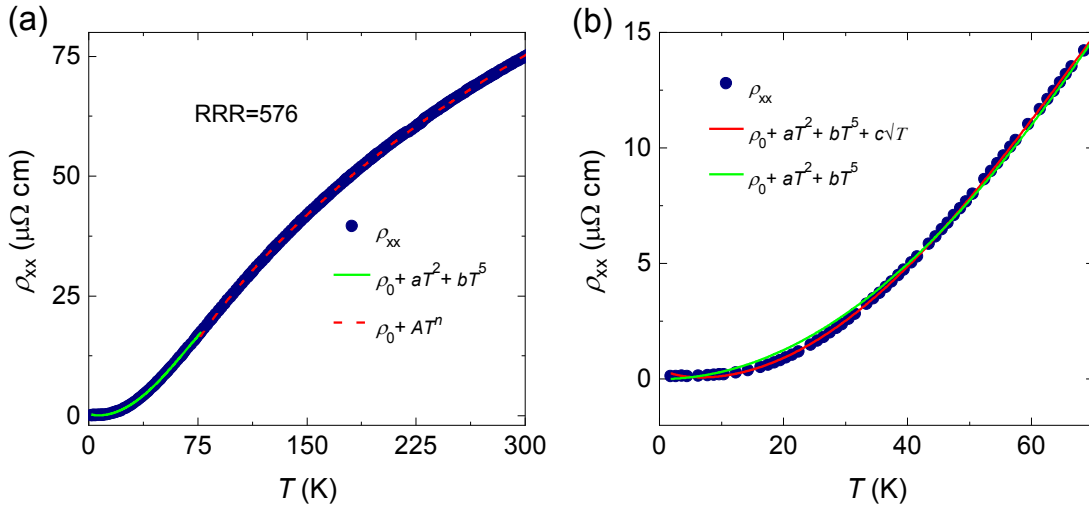
Figure 6.6: Temperature dependent longitudinal resistivity of PtGa$_5$ in zero-field. (a) Resistivity, ρ_{xx} measured in the range of 2 - 300 K, **(b)** The low temperature ρ_{xx} fit with *e-e* scattering term, *e-ph* scattering term and weak localization term.

Effect of magnetic field on resistivity

Figures 6.7 illustrate the temperature dependent resistivity measured at various field with field perpendicular to *ab*-plane (out of plane) and along *b*-axis (in plane), while the current along is applied along *a*-axis. We can see, there is small change in resistivity when field is out of plane (Figure 6.7(a)), and this changes drastically when field is in plane (Figure 6.7(b)). The Lorentz force acts maximum on charge carriers when a magnetic field is applied perpendicular to an electric field, resulting in positive MR. It is because of this that we detect a change in resistivity when the field is applied. The field dependency of the resistivity is almost negligible above 75 K. We observe an upturn below 30 K for fields above 1 T, which is characteristic of many semimetals [29]. To explain this transition, multi band approach is taken into consideration. It is believed that such transition is linked to the magnetic field induced excitonic insulator transition [31]. However, this is not very much clear, thus more research is needed to explore the cause of this effect. This upturn in more pronounce while field is in-plane and such anisotropic behavior is related to anisotropic FS, which we will discuss further in more details.
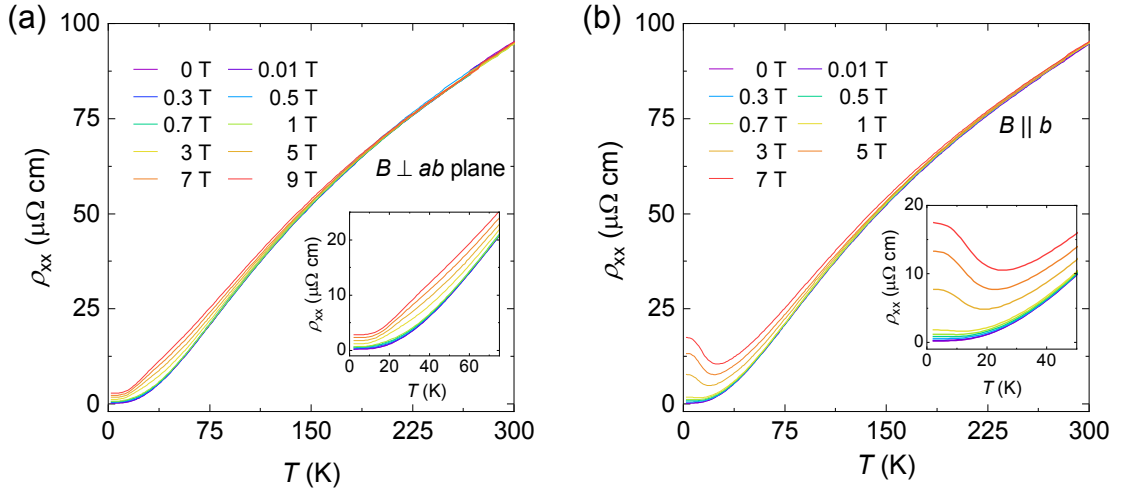
Figure 6.7: Temperature dependent resistivity of PtGa₅ at various fields. Resistivity, $\rho_{xx}(T)$ measured at various fields in a temperature range of 2 - 300 K with current along *a*-axis for **(a)** magnetic field perpendicular to *ab*-plane and **(b)** magnetic field parallel to *b*-axis.
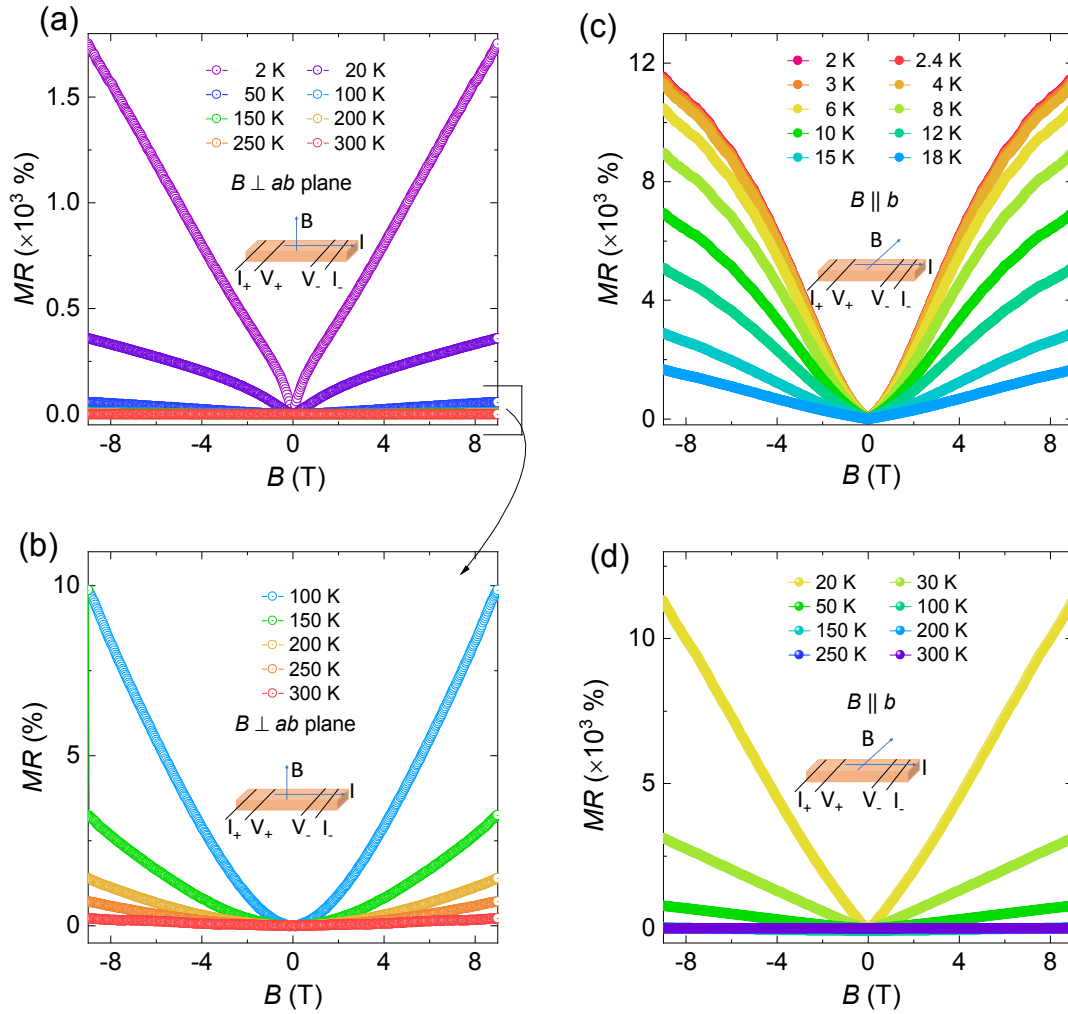
Figure 6.8: MR of PtGa₅ at various temperatures. (a), & **(b)** Magnetic field perpendicular to *ab*-plane measured at low temperature and high temperature, respectively. **(c)**, & **(d)** Magnetic field parallel to *b*-axis measured at low temperature and high temperature, respectively.

Both in-plane and out-of-plane field dependent resistivity were measured, then MR has been calculated using equation 2.5. At 2 K in 9 T, PtGa₅ exhibits a transverse MR of 1.75×10^3 %, as shown in Figure 6.8(a), however there is there is huge drop in MR at higher temperatures, and it is 0.2 % at 300 K in 9 T. MR reaches to 1.13×10^4 % when applied magnetic field is along *b*-axis shown in Figure 6.8(c). In the same orientation MR at higher temperatures are shown in Figure 6.8(d) for a better representation. Noticeably, we observed highest MR when field is applied *b*-axis. There is huge drop in MR either field is *b*-axis or out-of-plane. Interestingly, when the field is *b*-axis, MR shows ups and downs below 10 K in high field region, this behavior in resistivity is known as SdH oscillations and further details are given in the separate section of SdH oscillations in PtGa₅. The Hall conductivity, σ_{xy} and transverse conductivity, σ_{xx} are estimated from the relations 2.3 and they are shown

in Figure 6.9. At low temperatures, the magneto conductivity steeply goes down around low field, indicating a typical behavior of anti-localization of charge carriers. Normally, compounds with high spin-orbit coupling (SOC) tend to exhibit such behavior and Pt might be responsible for this [28].

Hall effect measurements

We used 4-probe geometry as described earlier in the chapter 4 to perform Hall measurements at various temperatures on the crystals of PtGa$_5$ with field perpendicular to *ab*-plane and current along the *a*-axis. We observed linear field dependent Hall resistivity, ρ_{yx} shown in Figure 6.10(a) with positive slope, indicating that majority charge carriers are holes. The value of ρ_{yx} measured at 2 K at an applied magnetic field of 7 T is 1.8 $\mu\Omega$ cm. From this measurement, the temperature dependent mobility and charge carrier concentration evaluated using the relations $R_H = \rho_{yx}/B$, $\mu = R_H/\rho_{xx}$ and $n = 1/eR_H$. The temperature dependent estimated mobility and carrier density are plotted in Figure 6.10(b). The mobility at 2 K is 1.3×10^4 cm^2 V^{-1}s^{-1}, which is extremely large and this has not been reported earlier in this compound. This value drops sharply with increase in temperature. The carrier concentration in PtGa$_5$ is the order of magnitude of 10^{21}cm^{-3}, which increases slowly with temperature.
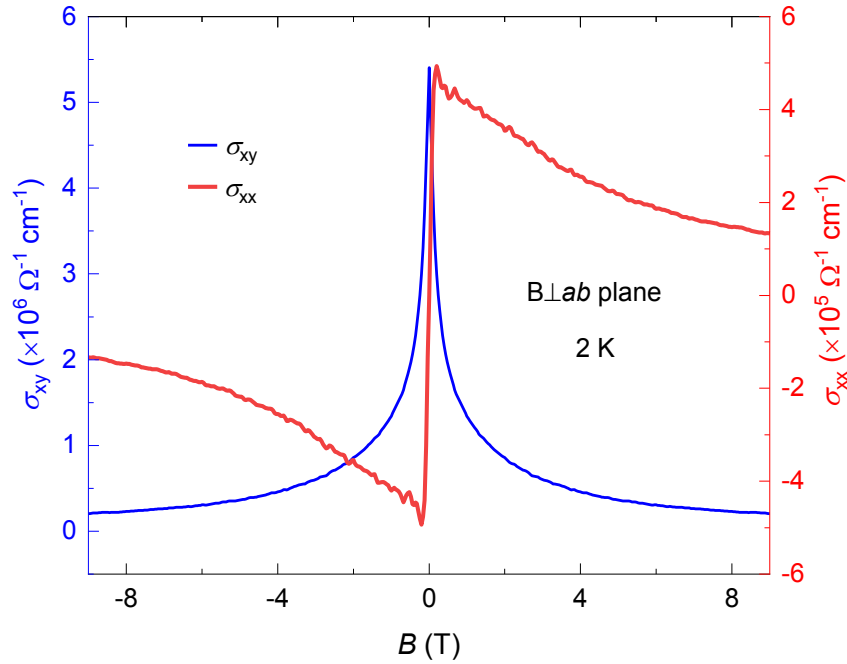
Figure 6.9: Field dependent Hall and transverse conductivities of PtGa$_5$. Estimated field dependent Hall conductivity and transverse conductivity at 2 K.
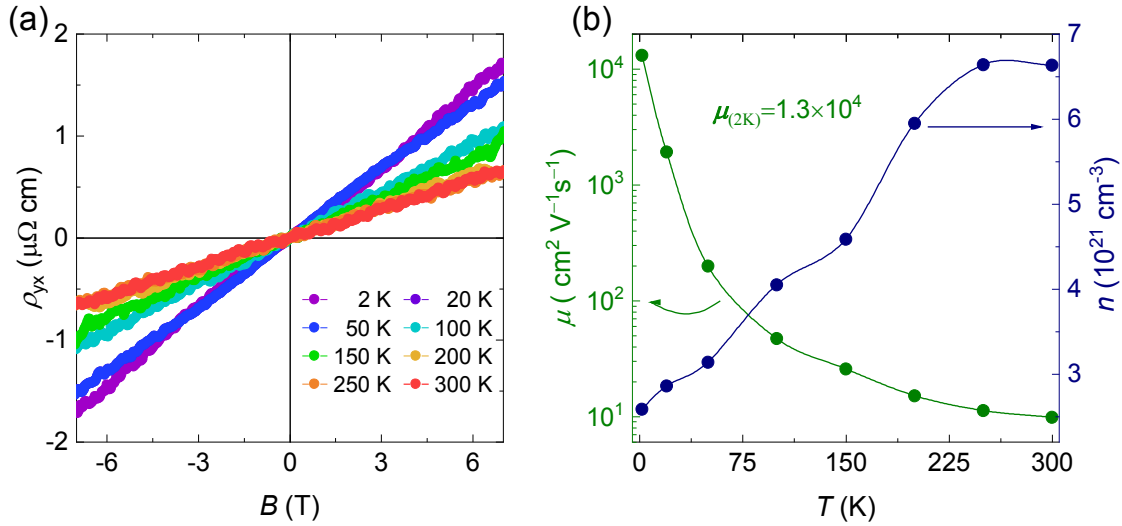
Figure 6.10: Hall resistivity, mobility & carrier concentration of PtGa₅. (a) Measured Hall resistivity, ρ_{yx} at various temperatures. **(b)** Temperature dependent mobility, μ and charge carrier concentration n, evaluated from the Hall resistivity data.

Magnetoresistance at different angles

Field dependence of MR measured at 2 K in the range of magnetic field of +9 T to −9 T at various field orientations is shown in Figure 6.11. 0° orientation means when field is out-of-plane (perpendicular to *ab*-plane) and 90° means field is in-plane (along *b*-axis). With the rotation of magnetic field, we see how MR changes and it reaches maximum value when magnetic field is in plane. The change in MR is a direct indication of anisotropy in FS topology. The quantum oscillations start to visible as soon as orientation of magnetic field reaches 30°, and this continues till magnetic field is along *b*-axis.
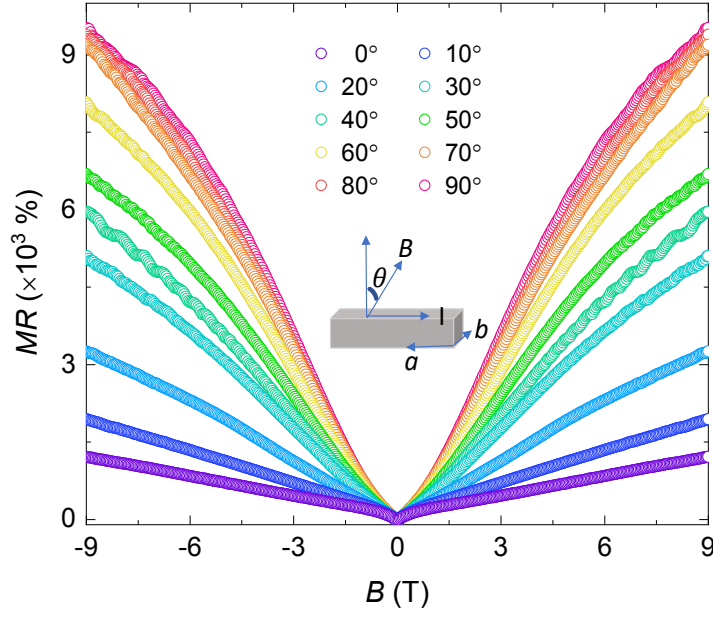
Figure 6.11: Angle dependent MR of PtGa₅. MR at different angles, where angle, θ measures from out-of-plane to the b-axis.

Analyses of SdH oscillation in PtGa₅

From the Topological Materials Database [23], PtGa₅ is a topological insulator with topological indices $Z_{2w},1 = 1$, $Z_{2w},2 = 0$, $Z_{2w},3 = 0$, $Z_4 = 3$. The electronic band structure shown Figure 6.12(a) has many electron and hole Fermi pockets at the E_F. Figure 6.12 (b) illustrates the 3D FS calculation, where 16 bands cross at E_F. Such large number of bands at E_F is also detected in the equivalent analysis of SdH oscillations.

We have now analyzed SdH quantum oscillations observed when applied magnetic field is along b-axis. The external cross section area of the FS perpendicular to applied magnetic field is directly related to the frequency of quantum oscillations. To determine the topology of FS, we have subtracted the background from field dependent MR data. Figure 6.8(c) shows the MR measured at different temperatures between 2 K to 18 K. SdH oscillations are extracted by subtracting the quadratic polynomial background from MR data. The extracted amplitudes of SdH oscillations as a function of inverse field at various temperatures are shown in Figure 6.13(a). The FFT of SdH oscillations are shown in Figure 6.13(b), wherein various frequencies are visible. We have evaluated the effective mass corresponding to two most intense peaks F_1 (8.9 T) and F_2 (31.3 T).
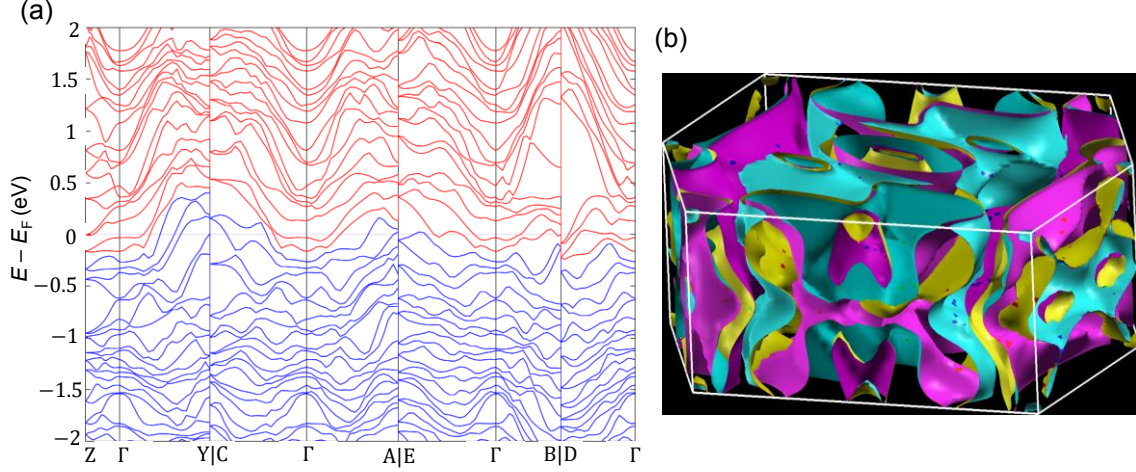
Figure 6.12: Electronic band structure of PtGa₅. (a) Electronic band structure of PtGa$_5$ strongly suggests that system is a strong topological insulator with non-zero topological index. **(b)** Calculated 3D Fermi sufrace shows that 16 bands crossing at E_F, including electron and hole pockets.
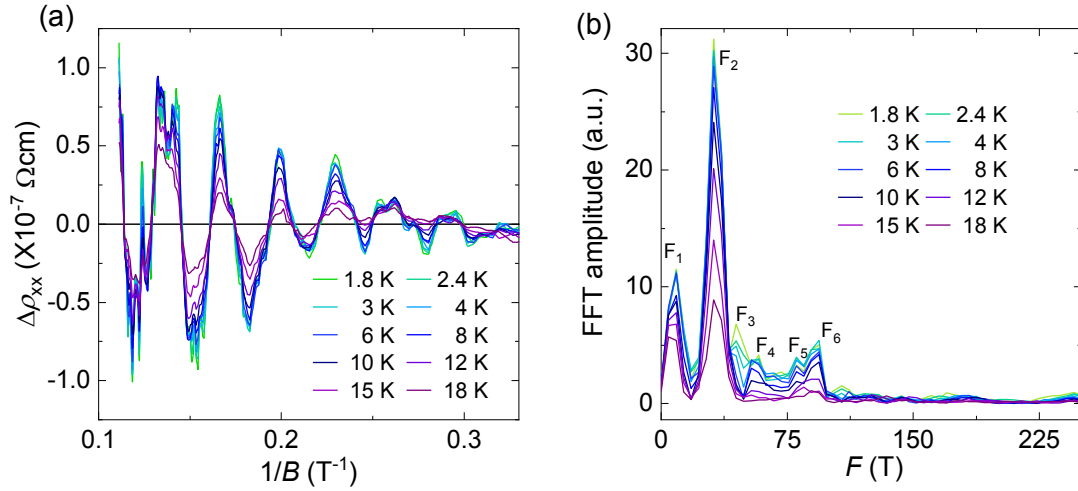
Figure 6.13: Quantum oscillations and effective mass of PtGa₅. (a) SdH oscillation amplitudes obtained by subtracting the background from the resistivity with field in plane $(B \parallel b)$, **(b)** Fast Fourier transform (FFT) of SdH amplitude at mentioned temperatures, showing peaks corresponding to Fermi pockets present at E_F.

We calculated effective mass (m^*) of Fermi pockets corresponding the frequencies F_1 and F_2, using Lifshitz Kosevich (LK) formula $\Delta R = X/\sinh X$, where $X = 14.69 m^* T/B$, and B is average field. The fittings are shown in Figure 6.14. The effective mass for F_1 is 0.038 m_0, while for F_2 is 0.045m_0, where m_0 is the bare mass of electron. Considering the cross section of FS to be circular for simplicity, we evaluated the enclosed area of the Fermi

pockets corresponding to each frequency, shown in table 6.1. Fermi area, A_F, was calculated by Onsager relation as discussed in section 2.5.2 of the chapter 2.

Table 6.1: Oscillation frequency, F, extremal enclosed area, A_F, Fermi wave vector, k_F, effective mass, m^*, Fermi wave velocity, v_F.

	F (T)	A_F (m^2)	k_F (m^{-1})	m^* (m$_0$)	v_F ($10^5 \times$ m s^{-1})
F_0	3	2.86×10^{16}	9.54×10^7	0.045	2.42
F_1	8.9	9.53×10^{16}	1.74×10^8	0.038	5.30
F_2	31.3	2.95×10^{17}	3.06×10^8		
F_3	55	5.24×10^{17}	4.08×10^8		
F_4	68	6.48×10^{17}	4.54×10^8		
F_5	79	7.53×10^{17}	4.89×10^8		
F_6	93	8.87×10^{17}	5.31×10^8		
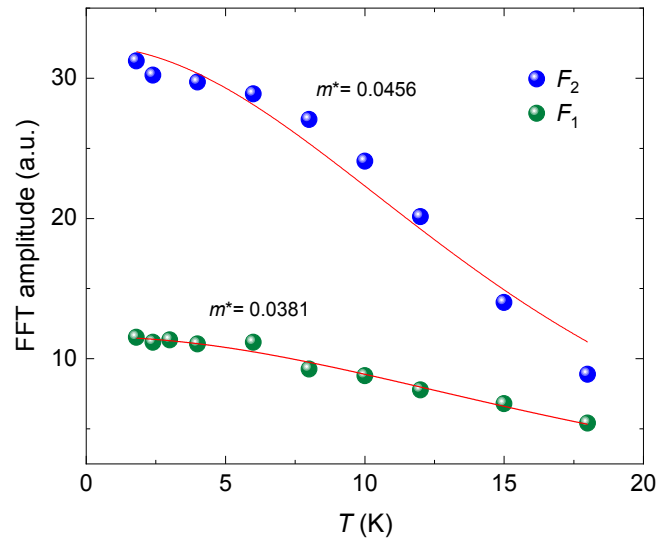
Figure 6.14: Effective mass for PtGa$_5$. Fitting of FFT amplitude vs temperature plot using LK formula to estimate effective mass corresponding to F_1 and F_2.

6.6. Summary and outlook

In conclusion, it has been shown that how MR and mobility depend on temperature by taking the examples of transition metal-monopnictides. Weyl semimetals and a similar dependency may exist in other compounds. The plots between the MR or slope of MR versus mobility of most popular Weyl and Dirac semimetals show like a right turn symbol *i.e*. MR increases sharply and then undergoes toward saturation after reaching10^3. These analyses reveal that the MR highly depends on mobility, and high MR can be expected in high carrier mobility compounds. Similar to topological semimetals, extremely large MR and mobility is overserved in PtGa$_5$.

PtGa$_5$ is binary metallic compound, which crystallizes in monoclinic structure, with twinning. Despite of twin structure, we see extremely large MR and mobility in the order of 10^4. PtGa$_5$ is electronically strong topological insulator from the topological index, but at the same time it has very complex band structure with many Fermi pockets at the E_F. In such system, it is quite fascinating to observe quantum oscillations starting from 2 T, even though PtGa$_5$ has many Fermi pockets at E_F. All these interesting properties in a material-known earlier only for its structural twinning but weren't explored, pave a path to look for materials exhibiting extremely large MR and mobility. The complex band structure and the time limitations do not allow to explore deep analyses of FS, but it would be quite interesting to search for new material as well exhibiting such large MR and mobility.

7. Anomalous Hall effect in AFM MnPt₂Sn₃

7.1. Preface

Solid state research in general and material science in particular are driven by the hunt for novel materials with potential applications. Re-examination of previously known phases with undiscovered topological transport was described in the preceding chapters. On the other hand, the results presented in this chapter focus on the search for novel materials with novel topological properties. However, new materials are still interesting because they haven't been explored, and it is also critical to revisit previously studied materials in order to gain a better understanding. Introduction of topology into material science led to an understanding of various new unusual properties, and as a result, it is important to study materials that have been studied in the past. As a result of topology's introduction into material science, it is virtue to investigate new materials that have not been examined previously.

Mn-Pt-Sn based compounds have been studied due to their unique magnetic structure, wherein $Mn_{1.4}PtSn$ hosts antiskyrmions. In this series, $MnPt_2Sn_3$ is a new compound, which crystallizes in cubic structure and is AFM in nature. Being an AFM with transition temperature, T_N at 114 K, a non-linear magnetization is observed which results in non-linear Hall conductivity. This non-linear Hall conductivity can be attributed to BC induced AHC. In AFM systems, usually AHC is not expected due to formation of opposite magnetic domains, but recently it was found that BC induces non-zero AHC in AFM as well, even though it lacks magnetization. Magnetic structure of $MnPt_2Sn_3$ seems to be quite interesting and there is possibility of complex magnetic structure present below T_N. As ICSD database lack information on this composition, this chapter is mainly focused on its electrical transport, and magnetic transport.

7.2. Growth and chemical characterization

Crystal growth

Single crystals of MnPt$_2$Sn$_3$ were grown by the flux-growth method using Tin (Sn) as a flux. Highly purified Mn (99.999%), Pt (99.999%), Sb (99.99%), and Sn (99.99%) were cut into small pieces and weighed in a 1:1:1:20 molar ratio, resulting in a total weight of 15 g. This stoichiometric amount was placed in an alumina crucible altogether. The alumina crucible was then sealed in a quartz tube at argon pressure of 3 mbar. The quartz ampule was placed in box furnace and heated to 800 °C at a rate of 100 °C h^{-1}. For homogeneity, the content was kept at this temperature for 24 hours. The furnace temperature was slowly cooled to 400 °C, at a rate of 2 °C h^{-1}, for the crystal growth. At 400 °C, the extra tin flux was removed by centrifugation. From this procedure, two silvery single crystals with 5-8 mm sizes were obtained. One of the crystals was cut into smaller pieces for further characterizations. The composition of MnPt$_2$Sn$_3$ crystals was determined using SEM and an EDXS analyzer.

Chemical characterization

In order to do elemental analysis to check composition, the EDXS analyzer was used and it have been discovered that the compounds have a 1:2:3 composition. A slice of a large crystal cut with a wire saw was handed to Mr. Ulrich Burkhard of the Chemical Metal Science section so that he could conduct more research and confirm the purity of the phase as this composition was not available in the ICSD database. Figure 7.1(a) shows that the sample is first polished by our colleague Ms. Sylvia Kostmann to prepare it for back scattering EDXS analysis. The images in Figure 7.1(a) & (b) were taken from a polarized optical microscope of single crystal slice depicts two contrasts, indicating the presence of two phases (one is highlighted in red circle, which was analyzed in detail). According to comprehensive study through SEM, the lighter contrast is the major phase, which is MnPt$_2$Sn$_3$ (Figure 7.1(d) & (e)), whereas the dark grey contrast is only flux Sn (Figure 7.1(f)). To be certain about the major phase, an EDXS elemental analysis was performed at 10 sites. Figure 7.2 shows a SEM picture of a slice of MnPt$_2$Sn$_3$ with labeled points indicating where EDXS analysis was performed. Elemental analysis for these compounds was averaged at 10 locations, which concludes that Mn:Pt:Sn is in atomic ratio of 17:32:51, confirming that the composition of the compounds was close to 1:2:3, as indicated in Table 7.1.

Before measuring structure and direction-dependent physical properties, the directions of the crystals were analyzed by the Laue diffraction method. The single crystallinity of the as-grown crystal was evaluated by white-beam backscattering Laue X-ray diffraction.
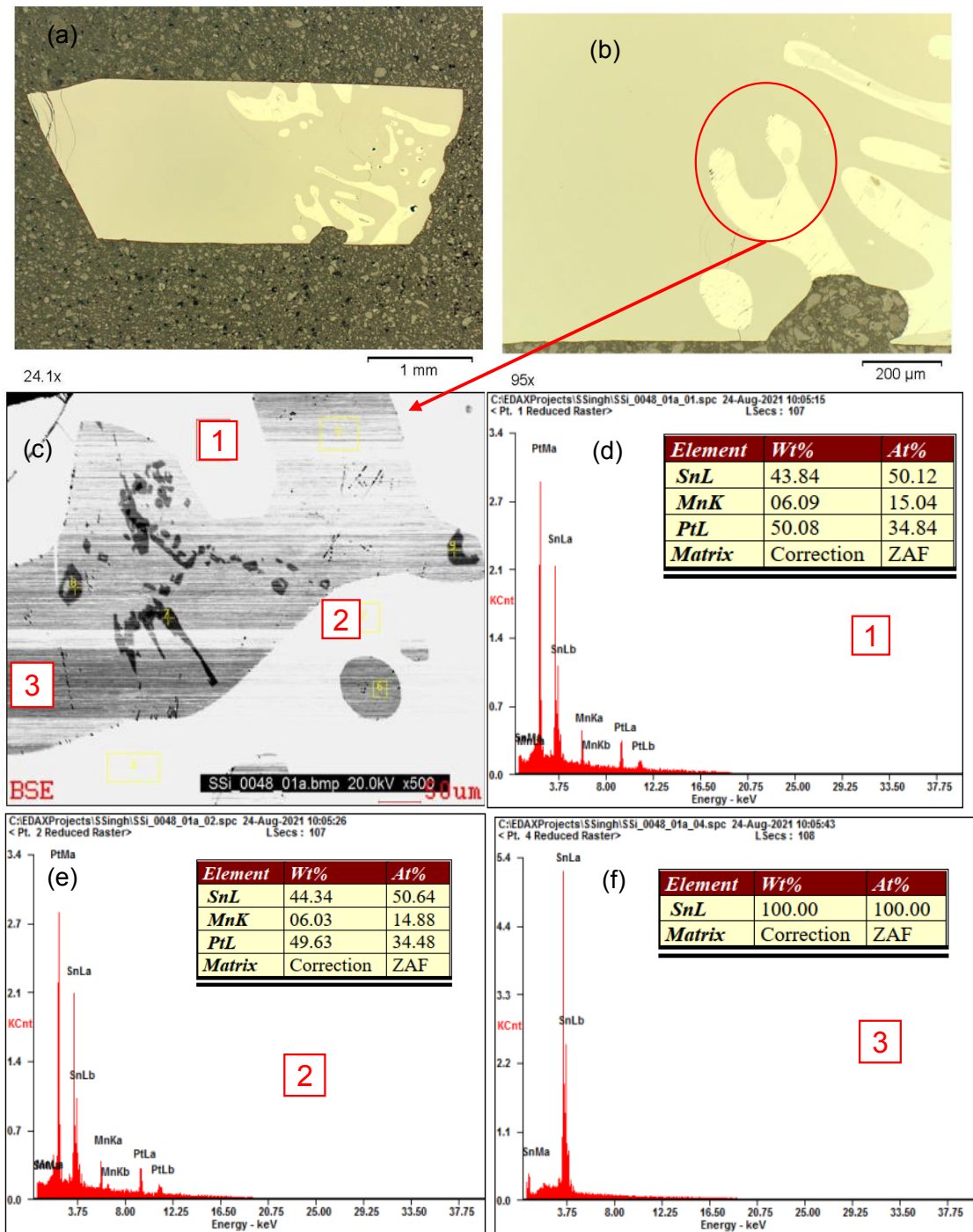
Figure 7.1 EDXS spectrum of MnPt$_2$Sn$_3$. **(a)** Slice of polished single crystal of MnPt$_2$Sn$_3$ under polarized light microscope. **(b)** Zoomed in picture of (a), where different contrast corresponds to different phase. **(c)** Highlighted portion zoomed in for detailed analysis of two different phases. **(d)**, **(e)**, and **(f)** EDXS spectrum along with elemental composition (insets) for highlighted sections 1, 2 and 3, respectively.
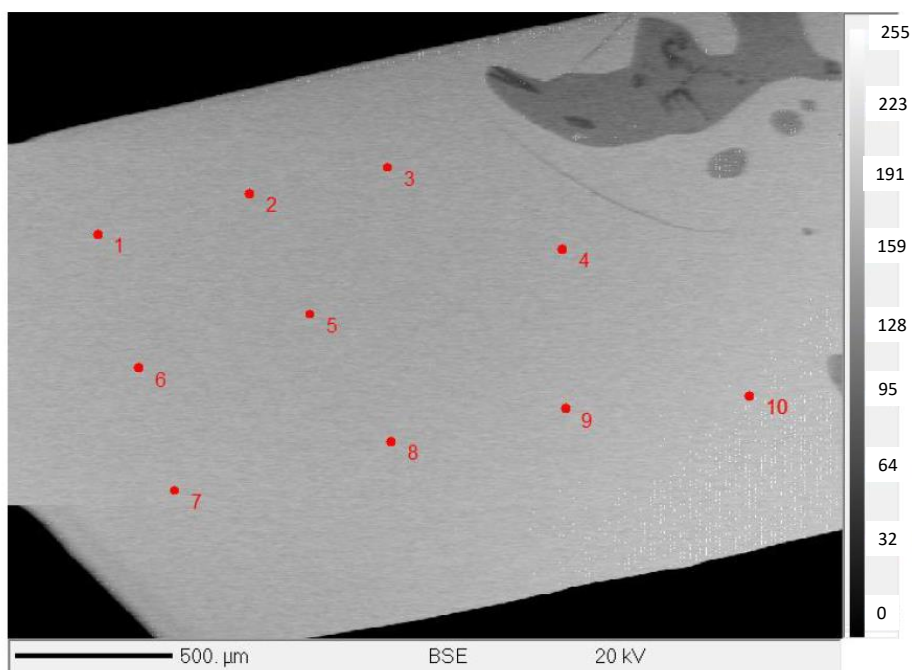
Figure 7.2: Microstructure image of MnPt$_2$Sn$_3$. SEM image of slice of MnPt$_2$Sn$_3$ wherein labeled points show the points taken into consideration for EDXS elemental composition analysis.

Table 7.1: Average on 10 points of EDXS analysis for elements Mn, Pt, Sn.

Elements	Mn	Pt	Sn
1	16.65	32.10	51.25
2	16.70	32.01	51.29
3	16.68	32.15	51.17
4	16.66	32.17	51.27
5	16.68	32.03	51.28
6	16.73	32.12	51.15
7	16.79	32.04	51.17
8	16.66	32.20	51.14
9	16.70	32.01	51.28
10	16.67	32.10	51.23
Average	16.69	32.08	51.22

7.3. Magnetic property

Temperature and field dependent magnetization of MnPt$_2$Sn$_3$ is shown in Figure 7.3(a), suggesting an anti-ferromagnetic (AFM) transition, T_N at 114 K. In conventional AFMs magnetization decreases after the kink, but we see a rise in magnetization here. Usually, such rise after the kink is usually absent in AFM state, which presumably comes from complex magnetic structure. Here we don't observe any second transition below T_N, like Mn$_{1.4}$PtSn [251].

In field dependent magnetization we observe a non-linear trend, and magnetization do not saturate till an applied magnetic field of 7 T, depicting high saturation beyond this field (Figure 7.3(b). Magnetization reaches 12.5 emu g^{-1} measured at 2 K at an applied magnetic field of 7 T, which is equivalent to 1.8 μ_B f.u.$^{-1}$, which decreases to 6.5 emu g^{-1} (0.93 μ_B f.u.$^{-1}$) at 150 K.
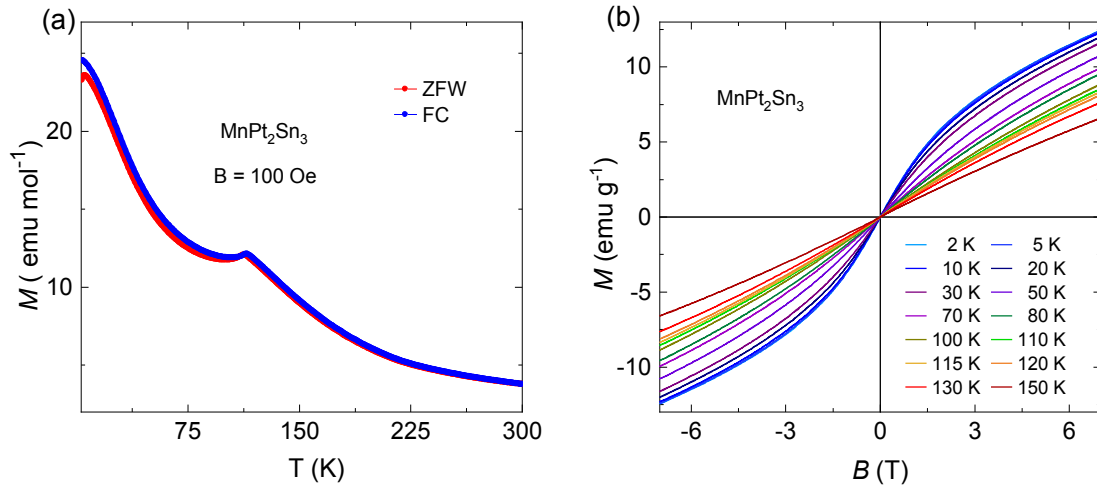
Figure 7.3: Magnetic property of MnPt$_2$Sn$_3$. (a) Temperature dependent magnetization with applied field of 100 Oe in zero-field-warming (ZFW) and field-cooled (FC) conditions, **(b)** Field dependent magnetization of MnPt$_2$Sn$_3$.

7.4. Magneto-transport in MnPt$_2$Sn$_3$

Temperature-dependent resistivity

Temperature dependent resistivity measured at zero field shown in Figure 7.4 follows linear behavior above transition temperature, $T_N \sim 114$ K, which means that electron-phonon scattering dominates, while below T_N, we observe a bump, which is related to presence of AFM state. The longitudinal resistivity measured at 2 K in zero-field is 81.7 $\mu\Omega$ cm, which reached 88.4 $\mu\Omega$ cm at 300 K, resulting in RRR value of 1.08. With application of field, there is small change in resistivity, at an application of 9 T magnetic field longitudinal

resistivity reached 78 μΩ cm at 2 K. Noticeably, T_N does not change with field, which is rather unusual.
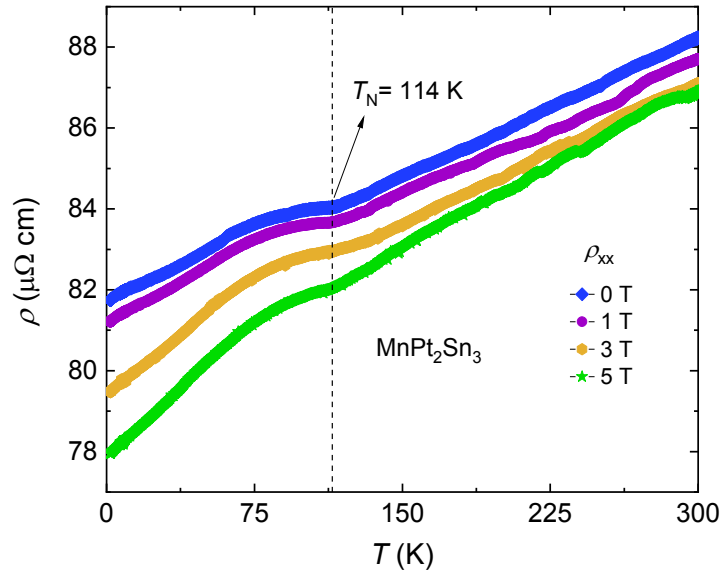
Figure 7.4: Temperature dependent resistivity of MnPt$_2$Sn$_3$ at various fields. Temperature dependent longitudinal resistivity measured at various fields, showing magnetic transition at 114 K.
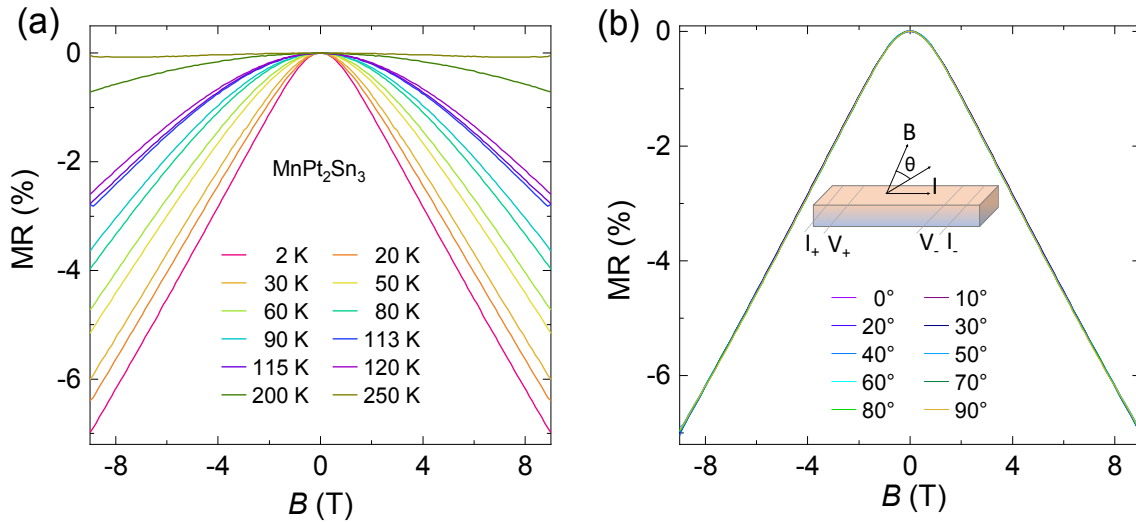
Figure 7.5: MR of MnPt$_2$Sn$_3$. Magnetoresistance measured at **(a)** different temperature, where magnetic field is out of plane **(b)** different orientation of field at 2 K in the range of an applied magnetic field of +9 to −9 T.

Figure 7.5(a) shows field-dependent MR at various temperatures in the range of +9 to −9 T applied magnetic field. For every field and temperature measured, the MR (calculated using equation 2.5) is negative. The MR measured at 2 K with 9 T applied magnetic field reaches −7%, which is owing to the suppression of spin disorder scattering by magnetic field. Measurements of MR are shown in Figure 7.5(b) in various orientations of the applied magnetic field. Field orientation is shown in the inset of the Figure 7.5(b). It is very interesting to see that when MR is measured in different directions, there is almost no change. This is probably due to spherical FS.

Hall effect measurements

Four probe geometry was used to perform Hall measurements, where current and applied magnetic field were in perpendicular geometry as discussed in chapter 4A. A non-linear Hall resistivity was observed, which scales perfectly with magnetization measurement as shown in Figure 7.6, which clearly indicates the presence of AHE. The positive slope of ρ_{yx} indicates that holes are the primary charge carriers. Field dependent ρ_{yx} (σ_{xy}) measured (calculated using equation-2.3) at various temperatures is shown in Figures 7.7(a), & (b). Hall resistivity, ρ_{yx} measured at 2 K at an applied magnetic field of 9 T is 0.79 $\mu\Omega$ cm, and σ_{xy} is 129 Ω^{-1}cm^{-1}. We also measured ρ_{yx} in different orientation (Figure 7.7(b)) when applied magnetic field is out of plane and changing to in plane orientation shown in the inset of Figure 7.7 (d). The orientation of field is in such a way that 0° represent when applied field is out of plane, while 90° represents when field is in plane and perpendicular to current *i.e.* some other principle axis. When field is in-plane, we observe almost negligible ρ_{yx}. When applied field is perpendicular to applied current, Lorentz force acts on charge carrier and thus Hall voltage measures a highest value, while it is minimum in-plane field due to the absence of Lorentz force.
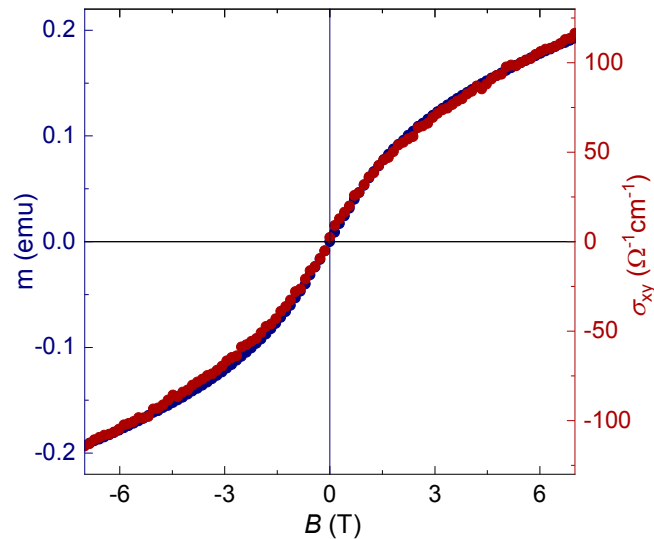
Figure 7.6: Field dependent magnetization and Hall conductivity MnPt$_2$Sn$_3$. Both field dependent magnetization and Hall conductivity follows the same trend.
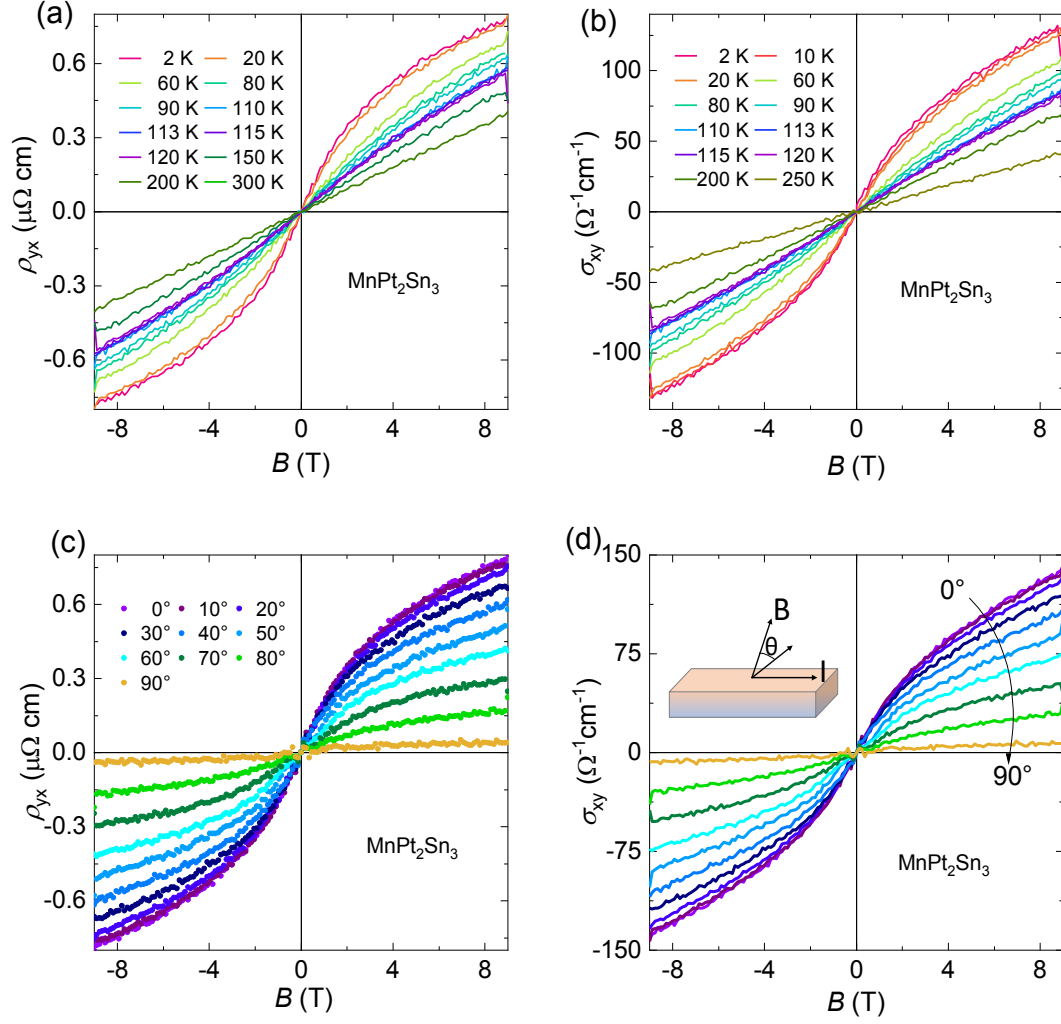
Figure 7.7: Hall resistivity and Hall conductivity of MnPt$_2$Sn$_3$. Hall resistivity measured at **(a)** various temperatures and **(c)** various angles. The corresponding calculated Hall conductivity in **(b)**, **(d)**.

Figure 7.8(a) depicts field dependent AHC, which is deduced by subtracting the linear fit at high magnetic field. AHC measured at 2K at an applied magnetic field of 9 T is 53 Ω^{-1}cm^{-1}, and this decreases to 12 Ω^{-1}cm^{-1} measured at 110 K, which is just below the transition temperature T_N, *i.e.* 114 K. As magnetic materials lose their magnetic characteristics approaching T_N, a drop in AHC is evident as shown in Figure 7.8(b). From previous knowledge, it is clear that AHC in AFM is evident due to presence of BC (intrinsic) contribution, and now is clear indication of topological states present in the system. Our presumable assumption is that the BC also plays a dominating role in source of AHC in MnPt$_2$Sn$_3$.
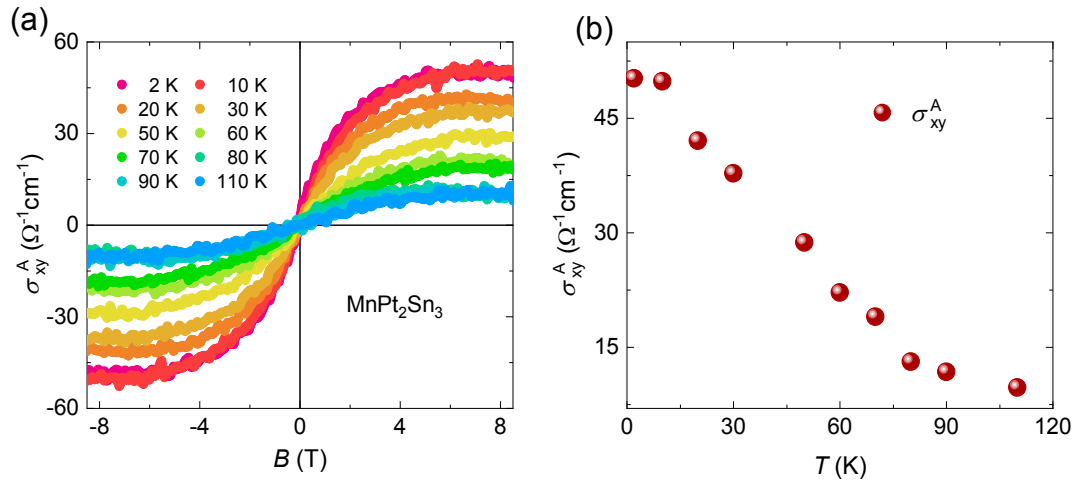
Figure 7.8: AHC of MnPt$_2$Sn$_3$. (a) Field dependent AHC at various temperatures. **(b)** Temperature dependent AHC estimated from (a).

7.5 Summary and outlook

Search of new topological material is always challenging and experimental realization of these new materials are even more challenging. When it comes to quantum applications, the discovery of new topological materials could be quite valuable. In this chapter, a new topological material MnPt$_2$Sn$_3$ is explored, which is AFM in nature with $T_N \sim 114$ K. MnPt$_2$Sn$_3$ exhibits AHE, and magnetization scales perfectly with the Hall resistivity, which is most likely a result of BC. We believe that topological states are present which results in BC induced AHE in such AFM material, while more detail investigations need to be done in this regard.

8. Conclusion

The aim of the thesis was to investigate the electrical and magnetic properties of topological semimetals by growing high quality single crystals and study their responses. All the investigated topological materials have been sought out for their intriguing low energy consumable applications such as spintronics, thermoelectrics, catalysis, photovoltaics, and many more because they host unique physical phenomena. For the particular, this thesis also provides to develop a fundamental knowledge of the phenomenon of diamagnetism in non-magnetic topological materials. Such study simplifies the selection rules of materials to grasp them on the basics of their strange physical properties. There is no better illustration of these than the introduction of topology, which has precisely been implemented for the previously accessible class of materials. Preparing the high-quality single crystals is essential and has been done successfully, which was one of the goals of this thesis. Subsequently, we examined transport properties by in-depth using various experimental probes, which provided the proof of presence of topological states, and aided the valuable contributions to the fields. Anomalous Hall effect, which is unique to magnetic materials, has been studied in depth along with other aspects such as MR, mobility, and diamagnetism in the non-magnetic topological materials.

Chapter 2 explained the fundamentals of a handful of topics for the classifications of different topological materials. From the given discussion of different topological phases present, anyone can simply learn the classification of topological semimetals. Furthermore, an overview of expecting physical phenomena of magnetic and non-magnetic topological materials was really correlated to their characteristics like anomalous Hall effect, extremely large MR, mobility, and diamagnetism. The details of experimental techniques mentioned in chapter 3 including the growth and the characterization techniques are precisely convenient. From these techniques, the various high quality of crystals from the different family have been obtained and their physical properties have been measured.

As mentioned above, the introduction of topology in the field of condensed matter physics opened doors for investigation of a large class of materials to create better understanding of many physical phenomena. Thus, the chapter 4 provided the study of anomalous electro-magnetic transport behavior for transition metal pnictides family and half- Heusler family provided. Section 4A of this chapter summarized the electrical transports and magnetic properties of ZrMnP and HfMnP. The presented investigations unveiled that the presence of the Dirac nodal lines at the E_F leads to BC induced very large AHC. These values were found to be one of the largest in the family of nodal line

semimetals. The Dirac nodal lines are protected by mirror planes, revealing from the first principle calculations. While section 4B dealt the structural and transport study of the half Heusler's NiMnSb and PtMnSb. These compounds are a room temperature ferromagnets and they possess the multiple Weyl nodes near the E_F as confirmed from the first principle calculations. The room temperature ferromagnetism of NiMnSb is known earlier but its topological features are new. This study here not only shows that they exhibit Weyl nodes, but also shows the anomalous transport, originating from the topological features. NiMnSb is the first half metallic half-Heusler ferromagnet to exhibit Weyl nodes leading to BC driven AHC. Similarly, PtMnSb also exhibits Weyl nodes, which are away from the E_F, consequently, its large value of AHC is dominated by the extrinsic mechanism. The findings of this chapter emphasize the anomalous Hall transport and the presence of topological features in the magnetic systems are unique and interesting, which can applicable further in the selection of magnetic materials having a plenty of mirror planes and half metallicity.

The subsequent chapter 5 demonstrated the diamagnetism responses of well know non-magnetic topological materials, which were extensively investigated in respect of various topological phenomena. The majority of these topological semimetals were found to exhibit the large diamagnetism which was never the part of discussion before. The diamagnetism was studied for over more than 25 topological semimetals from different classes including Dirac, Weyl and chiral semimetals. The materials $ZrTe_5$ and $HfTe_5$ from the Dirac class were found to exhibit one of the largest diamagnetic signals in previously reported state-of-art-topological semimetals. Such a large diamagnetism is due to enhanced orbital magnetism from interband scattering effects of the Dirac bands. Moreover, the large diamagnetism is correlated with the position of Dirac/Weyl nodes and the effective mass of the respective bands. These findings also added magnetization as a tool to investigate where the chemical potential crosses a nodal point. Therefore, such study opens the windows for researchers to look more materials and to find theoretical explanations for large diamagnetic susceptibility.

The chapter 6 discussed an additional relation that can be observed at least in topological materials. Topological semimetals are known for their extremely large MR and mobility, and it is caused by the massless charge carriers that results from the linear dispersion. There is the strong correlation between MR and mobility that has been found in well-known Dirac and Weyl semimetals. The gained experiences played the critical role for finding the binary metallic compound $PtGa_5$, which shows the extraordinarily high MR and the high mobility, reaching an order of magnitude of 10^4. For $PtGa_5$, only the crystal structure was known. Despite having twinning in crystal structure and the plenty of Fermi pockets, the material demonstrates such high mobility and MR. Noticeably, the quantum oscillations starting from 3 T quite surprising and interesting. This chapter paves the way for future research into topological materials with high mobility, which gives the mandate to have extremely large MR. Additionally, the twinning free crystals of $PtGa_5$ needs to be grown in order to conduct an in-depth study of the FS topology.

The final chapter 7 focused on the completely new magnetic compound $MnPt_2Sn_3$, which belongs to the Mn-Pt-Sn family, which is famous for its first antiskyrmions discovery. The magnetic measurements revealed that $MnPt_2Sn_3$ is antiferromagnet (AFM) below 114 K. The observations of electro-magnetic transports suggest the presence of AHC, which is likely to be the result of BC as no net magnetism is present. A comprehensive analysis for the crystal and magnetic structures is required further because this information is lacking in the ICSD database.

Appendix

Growth of various topological materials used in measurement of diamagnetic study

TaAs, TaP, NbAs, NbP (grown by Marcus Schmidt and Vicky Süß)

Single crystals of NbP, TaP, NbAs, and TaAs were grown via chemical vapour transport [30, 31]. As a first step for polycrystalline material, stoichiometric amounts of Nb, Ta (Alfa Aesar, 99.99 % P (Alfa Aesar, 99.999 %), and As (Chempur, 99.9999 %) were accurately weighed in a quartz ampoule. After that, they were flushed with argon and sealed under a vacuum. For 24 hours, the sealed quart tube was heated to 600 °C and then 800 °C. In the next step, the microcrystalline powders were used from step one and added 7–8 mg ml^{-1} of iodine before putting the powders in a quartz tube. This helped the crystals grow. The crystal grew in a two-zone furnace for 2–4 weeks at temperatures between 900 °C and 1050 °C. Here, I$_2$ acts as a transport agent. The temperature gradient is one of the most important factors in making high-quality crystals, and it depends on the material. It was found the best temperature gradient for each of the materials mentioned in this study. For NbP and TaP, it is 900 °C (source) to 1000 °C (sink), and for NbAs and TaAs, it is 900 °C (source) to 1050 °C (sink).

Bi$_{1-x}$Sb$_x$ (grown by myself)

Single crystals of antimony doped bismuth were grown using horizontal zone refinement furnace. Bi and Sb pieces were taken in the desired stoichiometric ratio and was melted in the induction meting almost 100 times to ensure the homogeneity of the required phase. And then this melt was sealed in a dry quartz ampoule under 3 mbar partial pressure of argon, and further kept in the very narrow heating zone of horizontal zone refinement furnace at 295 °C where it was pulled from one side at the rate of 1.8 mm h^{-1}.

YPtBi (grown by myself)

Single crystals of YPtBi were grown by a solution growth method from Bi flux. Freshly polished pieces of Y, Pt and Bi, each of purity >99.99%, in the stoichiometric ratio (with significant excess Bi, i.e., Y: Pt: Bi = 1:1:9) were placed in a tantalum crucible and sealed in a dry quartz ampoule under 3.0 mbar partial pressure of argon. The ampoule was heated at a rate of 100 °C h^{-1} up to 1150 °C and left for 12 h at this temperature. For the crystal growth, the temperature was slowly reduced at a rate of 2 °C h^{-1} to 500 °C and the extra Bi flux was removed by decanting from the ampoule at 500 °C.

RhSn (grown by myself)

Single crystals of RhSn were grown by self-flux growth method using Sn as flux. Freshly cut pieces of Rh and Sn each of purity greater than 99.99 %, in the stoichiometric ratio of 45:55 (Rh:Sn), where excess of Sn as flux was placed in a alumina crucible and sealed in a dry quartz ampoule under vacuum. The ampoule was heated at a rate of 100 °C h^{-1} up to 1100 °C and left there for 12 hours at this temperature. The temperature of the furnace was slowly cooled down to 1000 °C at a rate of 2 °C h^{-1} for growth of single crystal and the extra Sn flux was removed by centrifuging from the ampoule at 500 °C.

ZrTe$_5$ (grown by myself) (see section 5A.2)

HfTe$_5$ (grown by myself) (see section 5A.2)

CoSi (grown by Dr. Kaustuv Manna)

Single crystals of CoSi were grown using a CVT technique. First of all, a polycrystalline sample of CoSi was prepared using arc-melting furnace by melting equal amounts of Co slices and Si pieces. The ingot prepared from arc melting was crushed and ground further into powder. The powdered sample was then put in an empty silica tube with a concentration of about 0.25 mg cm^{-3} of iodine. For two weeks, the transport reaction took place at a temperature gradient from 1000 °C (source) to 1100 °C (sink).

PtGa (grown by Dr. Kaustuv Manna)

PtGa single crystals were grown from the melt using the self-flux technique. Firstly, a polycrystalline ingot prepared by arc melting, using stoichiometric amounts of constituent metals with 99.99% purity in an argon atmosphere. The single-phase ingot was crushed, and placed in an alumina crucible, and further sealed in a quartz tube. The quartz ampoule was then kept in commercial box-type furnace at 1150 °C and maintained at that temperature for 10 h for homogeneity of the melt. The ampoule was then slowly cooled to 1050 °C at a rate of 1 °C h^{-1} followed by further cooling to 850 °C at a rate of 50 °C h^{-1}. Finally, the sample was annealed at 850 °C for 120 h prior to being cooled to 500 °C at a rate of 5 °C h^{-1}.

RhSi (grown by Dr. Kaustuv Manna)

Vertical Bridgman method was used to grow the single crystals of RhSi. In particular, little extra Si was added than was needed to make sure that the flux type growth takes place inside the Bridgman ampoule. After growth, the extra amount of Si was segregated on top of the ingot due to density different between RhSi and Si First, a polycrystalline ingot was made by using an arc furnace to melt the highly pure parts in an argon atmosphere. The crushed powder was put into an alumina tube with a sharp bottom edge that is especially made to initiate the crystal seeding in the tinny region. The tube was then sealed inside a tantalum tube with an argon atmosphere. The sample was heated to 1550 °C and then slowly pulled down to the cold zone at a rate of 0.8 mm h^{-1}. Single crystals were on average about to 15 mm long and 6 mm wide.

LaBi (grown by Dr. Nitesh Kumar)

In a glove box filled with argon, high-purity La and Bi metals were weighed and put into an alumina crucible with the following composition: $La_{0.33}Bi_{0.67}$ (15 g). To prevent the La attack on the quartz tube, the crucible was enclosed in a quartz vessel under 3-mbar Ar pressure. At a rate of 100 °C h^{-1}, the contents were heated to 1250 °C. It was then cooled to 1200 °C at a pace of 100 °C h^{-1} while being kept at this temperature for one hour afterward. After that, the material was cooled down to 1050 °C for crystal formation at a rate of 1°C h^{-1}. Extra Bi flux was decanted out at this temperature, and the contents were quickly cooled to room temperature.

WTe₂ (grown by Dr. Nitesh Kumar)

WTe$_2$ single crystals were synthesized by self-flux method using Te flux. Pieces of W (99.5% Chempur) and Te (99.99999% Alfa Aesar) were weighed in accordance with the stoichiometric ratio of $W_{1.8}Te_{98.2}$ (5 g) and maintained in a quartz crucible for the synthesis. Vacuum sealed crucible in a quartz tube is kept in a programmable muffle furnace. Content in the vacuum sealed crucible was heated to 1050 °C at a rate of 100 °C h^{-1}. After maintaining this temperature for 10 hours to achieve a uniform molten phase, it was gradually decreased to 750 °C at a rate of 1 °C h^{-1}. By centrifuging surplus molten flux at this temperature, lustrous plate-like single crystals of WTe$_2$ were obtained.

Abbreviation

1D	One-dimensional
2D	Two-dimensional
3D	Three-dimensional
AHA	Anomalous Hall angle
AHC	Anomalous Hall conductivity
AHE	Anomalous Hall effect
AFM	Anti-ferromagnet
ANC	Anomalous Nernst conductivity
ANE	Anomalous Nernst effect
BC	Berry curvature
BZ	Brillouin zone
CCD	Charge-coupled device
CDW	Charge density wave
CISS	Chirality induced spin selective
CMSM	Chiral multifold semimetal
CVT	Chemical vapor Transport
DFT	Density functional theory
dHvA	de Haas van Alphen
DSM	Dirac semimetal
EDXS	Energy dispersive X-ray spectroscopy
E_F	Fermi energy
ETO	Electrical transport option
FC	Field cooled
fcc	Face centered cubic
FFT	Fast Fourier transform
FM	Ferromagnetic
FS	Fermi surface
ICP-OES	Inductively coupled plasma optical emission spectroscopy
ICSD	Inorganic crystal structure database
IS	Inversion symmetry
LFZ	Laser floating zone
LK	Lifshitz Kosevich

MR	Magnetoresistance
NLSM	Nodal line semimetal
QHE	Quantum Hall effect
RRR	Residual resistivity ratio
SdH	Shubnikov-de Haas
SEM	Scanning electron microscope
SG	Space group
SOC	Spin-orbit coupling
SQUID	Superconducting quantum interference device
TI	Topological insulator
TRS	Time-reversal symmetry
VASP	Vienna ab initio simulation package
WDXS	Wavelength-dispersive X-ray spectroscopy
WSM	Weyl semimetal
XRD	X-ray diffraction
ZFW	Zero field warming
B, H	Magnetic field
c	Speed of light
Δ	Dirac/Weyl bode from E_F
$\hbar$	Planck constant
m^*	Effective mass
m	Mass
μ_k	Chemical penitential
μ	Mobility
M	Magnetization
M_S	Saturation magnetization
μ_B	Bohr magneton
p	Momentum
ρ	Resistivity
ρ_{xy}	Hall resistivity
ρ_{xy}^A	Anomalous Hall resistivity
σ_{xy}	Hall conductivity
σ_{xy}^A	Anomalous Hall conductivity
σ	Pauli spin matrix

T_C	Curie temperature
T_N	Neel temperature
τ	Scattering time
v_f	Fermi velocity
ω_c	Cyclotron frequency
χ	Susceptibility
χ_c	Chirality

References

[1]   G. E. Moore, Electronics **38**, 114 (1965).

[2]   E. Gibney, Nature **560**, 151 (2018).

[3]   N. Kumar, S. N. Guin, K. Manna, C. Shekhar, and C. Felser, Chem. Rev. **121**, 2780 (2020).

[4]   K. v. Klitzing, G. Dorda, and M. Pepper, Phys. Rev. Lett. **45**, 494 (1980).

[5]   D. J. Thouless, M. Kohmoto, M. P. Nightingale, and M. den Nijs, Phys. Rev. Lett. **49**, 405 (1982).

[6]   D. J. Thouless, J. Math. Phys. **35**, 5362 (1994).

[7]   C. L. Kane, and E. J. Mele, Phys. Rev. Lett. **95**, 226801 (2005).

[8]   L. Fu, and C. L. Kane, Phys. Rev. B **74**, 195312 (2006).

[9]   M. König, S. Wiedmann, C. Brüne, A. Roth, H. Buhmann, L. W. Molenkamp, X. L. Qi, and S. C. Zhang, Science **318**, 766 (2007).

[10]   S. Murakami, N. Nagaosa, and S.C. Zhang, Phys. Rev. Lett. **93**, 156804 (2004).

[11]   J. E. Moore, and R. Moessner, *Topological Phases of Matter*, (Cambridge University Press, Cambridge, 2021), pp. 218.

[12]   J. E. Moore, Nature **464**, 194 (2010).

[13]   M. Z. Hasan, and C. L. Kane, Rev. Mod. Phys. **82**, 3045 (2010).

[14]   M. Shuichi, New J. Phys. **9**, 356 (2007).

[15]   H. Zhang, C. X. Liu, X. L. Qi, X. Dai, Z. Fang, and S. C. Zhang, Nat. Phys. **5**, 438 (2009).

[16]   D. Hsieh *et al.*, Science **323**, 919 (2009).

[17]   D. Hsieh, D. Qian, L. Wray, Y. Xia, Y. S. Hor, R. J. Cava, and M. Z. Hasan, Nature **452**, 970 (2008).

[18]   D. Vanderbilt , *Berry Phases in Electronic Structure Theory: Electric Polarization, Orbital Magnetization and Topological Insulators*, (Cambridge University Press, Cambridge, 2018), pp. 201.

[19]   B. Yan, and C. Felser, Annu. Rev. Condens. Matter Phys. **8**, 337 (2017).

[20]   C. Fang, H. Weng, X. Dai, and Z. Fang, Chin. Phys. B **25**, 117106 (2016).

[21]   A. A. Burkov, M. D. Hook, and L. Balents, Phys. Rev. B **84**, 235126 (2011).

[22]   M. G. Vergniory, L. Elcoro, C. Felser, N. Regnault, B. A. Bernevig, and Z. Wang, Nature **566**, 480 (2019).

[23]   B. Bradlyn, L. Elcoro, J. Cano, M. G. Vergniory, Z. Wang, C. Felser, M. I. Aroyo, and B. A. Bernevig, Nature **547**, 298 (2017).

[24]   M. G. Vergniory, B. J. Wieder, L. Elcoro, S. S. P. Parkin, C. Felser, B. A. Bernevig, and N. Regnault, Science **376**, eabg9094 (2022).

[25]   V. Vargiamidis, P. Vasilopoulos, M. Tahir, and N. Neophytou, Phys. Rev. B **102**, 235426 (2020).

[26]   D. Xiao, M. C. Chang, and Q. Niu, Rev. Mod. Phys. **82**, 1959 (2010).

[27]   O. Stejskal, M. Veis, and J. Hamrle, Sci. Rep. **12**, 97 (2022).

[28]   N. Kumar *et al.*, Nat. Commun. **10**, 2475 (2019).

[29]   N. Kumar *et al.*, Nat. Commun. **8**, 1642 (2017).

[30]   N. Kumar, C. Shekhar, M. Wang, Y. Chen, H. Borrmann, and C. Felser, Phys. Rev. B **95**, 155128 (2017).

[31]   M. N. Ali *et al.*, Nature **514**, 205 (2014).

[32]   C. Shekhar *et al.*, Nat. Phys. **11**, 645 (2015).

[33]   W. Gao *et al.*, Phys. Rev. Lett. **118**, 256601 (2017).

[34]   Y. Yan, L. X. Wang, D. P. Yu, and Z.-M. Liao, Appl. Phys. Lett. **103**, 033106 (2013).

[35]   N. J. Ghimire, Y. Luo, M. Neupane, D. J. Williams, E. D. Bauer, and F. Ronning, J. Phys. Condens. Matter **27**, 152201 (2015).

[36]   T. Liang, Q. Gibson, M. N. Ali, M. Liu, R. J. Cava, and N. P. Ong, Nat. Mater. **14**, 280 (2015).

[37]   H. Wang *et al.*, Phys. Rev. B **93**, 165127 (2016).

[38] S. Singh, V. Süβ, M. Schmidt, C. Felser, and C. Shekhar, J. Phys. Materials **3**, 024003 (2020).

[39] H. Yang *et al.*, Phys. Rev. Mater. **4**, 024202 (2020).

[40] P. Li *et al.*, Nat. Commun. **11**, 3476 (2020).

[41] A. A. Burkov, Phys. Rev. Lett. **113**, 187202 (2014).

[42] K. Manna, Y. Sun, L. Muechler, J. Kübler, and C. Felser, Nat. Rev. Mater. **3**, 244 (2018).

[43] Y. Liu *et al.*, Phys. Rev. B **103**, L201110 (2021).

[44] S. Singh, J. Noky, S. Bhattacharya, P. Vir, Y. Sun, N. Kumar, C. Felser, and C. Shekhar, Adv. Mater. **33**, 2104126 (2021).

[45] O. Pavlosiuk, P. Fałat, D. Kaczorowski, and P. Wiśniewski, APL Materials **8**, 111107 (2020).

[46] B. Ernst *et al.*, Phys. Rev. B **100**, 054445 (2019).

[47] C. Shekhar *et al.*, Proc. Natl Acad. Sci. **115**, 9140 (2018).

[48] K. Manna *et al.*, Phys. Rev. X **8**, 041045 (2018).

[49] J. Noky, Y. Zhang, J. Gooth, C. Felser, and Y. Sun, npj Comput. Mater. **6**, 77 (2020).

[50] S. Galeski *et al.*, Nat. Commun. **12**, 3197 (2021).

[51] F. Tang *et al.*, Nature **569**, 537 (2019).

[52] S. Galeski *et al.*, Nat. Commun. **11**, 5926 (2020).

[53] S. N. Guin *et al.*, NPG Asia Mater. **11**, 16 (2019).

[54] I. Samathrakis, T. Long, Z. Zhang, H. K. Singh, and H. Zhang, J. Phys. D: Appl. Phys. **55**, 074003 (2021).

[55] F. Mende *et al.*, Adv. Sci. **8**, 2100782 (2021).

[56] T. Chen *et al.*, Sci. Adv. **8**, eabk1480 (2022).

[57] J. Xu, W. A. Phelan, and C. L. Chien, Nano Lett. **19**, 8250 (2019).

[58] P. Shahi *et al.*, Phys. Rev. X **8**, 021055 (2018).

[59] H. Chen, Z. Li, L. Guo, and X. Chen, Europhys. Lett. **117**, 27009 (2017).

[60] D. Chen *et al.*, Phys. Rev. B **105**, L201109 (2022).

[61] D. X. Qu, Y. S. Hor, J. Xiong, R. J. Cava, and N. P. Ong, Science **329**, 821 (2010).

[62]   P. Yang, W. Wang, X. Zhang, K. Wang, L. He, W. Liu, and Y. Xu, Sci. Rep. **9**, 3558 (2019).

[63]   J. Hu, S. Y. Xu, N. Ni, and Z. Mao, Annu. Rev. Mater. Res. **49**, 207 (2019).

[64]   B. A. Bernevig, T. L. Hughes, and S. C. Zhang, Science **314**, 1757 (2006).

[65]   Y. Xia *et al.*, Nat. Phys. **5**, 398 (2009).

[66]   Y. L. Chen *et al.*, Science **325**, 178 (2009).

[67]   N. P. Armitage, E. J. Mele, and A. Vishwanath, Rev. Mod. Phys. **90**, 015001 (2018).

[68]   M. Z. Hasan, S.Y. Xu, I. Belopolski, and S. M. Huang, Annu. Rev. Condens. Matter Phys. **8**, 289 (2017).

[69]   C. Herring, Phys. Rev. **52**, 365 (1937).

[70]   H. Weyl, Z. Phys. **56**, 330 (1929).

[71]   C. C. Lee *et al.*, Phys. Rev. B **92**, 235104 (2015).

[72]   E. Liu *et al.*, Nat. Phys. **14**, 1125 (2018).

[73]   Y. Zhang, Y. Yin, G. Dubuis, T. Butler, N. V. Medhekar, and S. Granville, npj Quantum Mater. **6**, 17 (2021).

[74]   J. Jiang *et al.*, Nat. Commun. **8**, 13973 (2017).

[75]   H. Xiong *et al.*, Phys. Rev. B **95**, 195119 (2017).

[76]   J. Xiong, S. Kushwaha, J. Krizan, T. Liang, R. J. Cava, and N. P. Ong, Europhys.Lett. **114**, 27002 (2016).

[77]   M. Neupane *et al.*, Nat. Commun. **5**, 3786 (2014).

[78]   J. Xiong, S. K. Kushwaha, T. Liang, J. W. Krizan, M. Hirschberger, W. Wang, R. J. Cava, and N. P. Ong, Science **350**, 413 (2015).

[79]   X. Yuan *et al.*, NPG Asia Mater. **8**, e325 (2016).

[80]   Y. Liu *et al.*, Nat. Commun. **7**, 12516 (2016).

[81]   I. Crassee, R. Sankar, W. L. Lee, A. Akrap, and M. Orlita, Phys. Rev. Mater. **2**, 120302 (2018).

[82]   L. N. Oveshnikov, A. B. Davydov, A. V. Suslov, A. I. Ril', S. F. Marenkin, A. L. Vasiliev, and B. A. Aronzon, Sci. Rep. **10**, 4601 (2020).

[83]   Z. Wang, H. Weng, Q. Wu, X. Dai, and Z. Fang, Phys. Rev. B **88**, 125427 (2013).

[84]   Y. Watanabe, M. Kumazaki, H. Ezure, T. Sasagawa, R. Cava, M. Itoh, and Y. Shimizu, J. Phys. Soc. Japan **90**, 053701 (2021).

[85]   Z. Chi, Y. C. Lau, X. Xu, T. Ohkubo, K. Hono, and M. Hayashi, Sci. Adv. **6**, eaay2324 (2020).

[86]   Y. H. Chan, C. K. Chiu, M. Y. Chou, and A. P. Schnyder, Phys. Rev. B **93**, 205132 (2016).

[87]   Y. H. Kwan, P. Reiss, Y. Han, M. Bristow, D. Prabhakaran, D. Graf, A. McCollam, S. A. Parameswaran, and A. I. Coldea, Phys. Rev. Res. **2**, 012055 (2020).

[88]   G. Bian *et al.*, Phys. Rev. B **93**, 121113 (2016).

[89]   C. Shekhar, Nat. Mater. **17**, 953 (2018).

[90]   G. Chang *et al.*, Nat. Mater. **17**, 978 (2018).

[91]   Z. Rao *et al.*, Nature **567**, 496 (2019).

[92]   B. Xu *et al.*, Proc. Natl Acad. Sci. **117**, 27104 (2020).

[93]   D. Rees, K. Manna, B. Lu, T. Morimoto, H. Borrmann, C. Felser, J. E. Moore, D. H. Torchinsky, and J. Orenstein, Sci. Adv. **6**, eaba0509 (2020).

[94]   Z. Ni *et al.*, npj Quantum Mater. **5**, 96 (2020).

[95]   N. B. M. Schröter *et al.*, Nat. Phys. **15**, 759 (2019).

[96]   G. Gong, L. Xu, Y. Bai, Y. Wang, S. Yuan, Y. Liu, and Z. Tian, Phys. Rev. Mater. **5**, 034405 (2021).

[97]   P. Li *et al.*, Nano Lett. **21**, 84 (2021).

[98]   J. Gooth *et al.*, Nature **547**, 324 (2017).

[99]   M. Stone, Phys. Rev. B **85**, 184503 (2012).

[100] Q. Li *et al.*, Nat. Phys. **12**, 550 (2016).

[101] N. Nagaosa, J. Sinova, S. Onoda, A. H. MacDonald, and N. P. Ong, Rev. Mod. Phys. **82**, 1539 (2010).

[102] N. Nagaosa, J. Phys. Soc. Japan **75**, 042001 (2006).

[103] I. A. Leahy, Y.P. Lin, P. E. Siegfried, A. C. Treglia, J. C. W. Song, R. M. Nandkishore, and M. Lee, Proc. Natl Acad. Sci. **115**, 10570 (2018).

[104] B.D. Culity and C.D. Graham, *Introduction to Magnetic Materials* (John Wiley & Sons, Limited, 2008), pp. 241.

[105] C. Kittel and P. McEuen, *Introduction to Solid State Physics* (John Wiley & Sons, Limited, 2018).

[106] J. M. D. Coey, *Magnetism and Magnetic Materials* (Cambridge University Press, Cambridge, 2010).

[107] M. N. Ali, L. M. Schoop, C. Garg, J. M. Lippmann, E. Lara, B. Lotsch, and S. S. P. Parkin, Sci. Adv. **2**, e1601742 (2016).

[108] W. Wang *et al.*, Sci. Rep. **3**, 2181 (2013).

[109] L. K. Zeng *et al.*, Phys. Rev. Lett. **117**, 127204 (2016).

[110] Z. Yuan, H. Lu, Y. Liu, J. Wang, and S. Jia, Phys. Rev. B **93**, 184405 (2016).

[111] N. W. Ashcroft, and N. D. Mermin, *Solid State Physics* (Saunders College Publishing, 1976).p563

[112] D. Shoenberg, *Magnetic Oscillations in Metals* (Cambridge University Press, Cambridge, 1984)

[113] L. S. Lerner, Phys. Rev. **127**, 1480 (1962).

[114] D. Shoenberg, M. Z. Uddin, and E. Rutherford, Proc. R. Soc. Lond. A Math. Phys. Sci. **156**, 701 (1936).

[115] D. Shoenberg, Nature **170**, 569 (1952).

[116] D. Shoenberg and P. L. Kapitza, Proc. R. Soc. Lond. A Math. Phys. Sci. **170**, 341 (1939).

[117] M. V. Kartsovnik, Chem. Rev. **104**, 5737 (2004).

[118] D. G. Seiler, (Springer Berlin , Heidelberg, 1989), pp. 578.

[119] W. Biberacher, *Encyclopedia of Condensed Matter Physics*, (Elsevier, Oxford, 2005), pp. 360.

[120] N. W. Ashcroft, and N. D. Mermin, *Solid State Physics* (Saunders College Publishing, 1976)., p. 666.

[121] Y. Fuseya, M. Ogata, and H. Fukuyama, J. Phys. Soc. Japan **84**, 012001 (2014).

[122] S. Otake, M. Momiuchi, and N. Matsuno, J. Phys. Soc. Japan **49**, 1824 (1980).

[123] H. Fukuyama, and R. Kubo, J. Phys. Soc. Japan **28**, 570 (1970).

[124] Y. Fuseya, M. Ogata, and H. Fukuyama, J. Phys. Soc. Japan **83**, 074702 (2014).

[125] Y. Fuseya, M. Ogata, and H. Fukuyama, J. Phys. Soc. Japan **81**, 093704 (2012).

[126] M. Koshino, and T. Ando, Phys. Rev. B **81**, 195431 (2010).

[127] M. Koshino and I. F. Hizbullah, Phys. Rev. B **93**, 045201 (2016).

[128] Z. Li, L. Chen, S. Meng, L. Guo, J. Huang, Y. Liu, W. Wang, and X. Chen, Phys. Rev. B **91**, 094429 (2015).

[129] D. Shoenberg, M. Z. Uddin, and E. Rutherford, Proc. R. Soc. Lond. A Math. Phys. Sci. **156**, 687 (1936).

[130] Y. Liu, Z. Li, L. Guo, X. Chen, Y. Yuan, F. Liu, S. Prucnal, M. Helm, and S. Zhou, J. Magn. Magn. Mater. **408**, 73 (2016).

[131] C. L. Zhang *et al.*, Nat. Commun. **10**, 1028 (2019).

[132] S. Suetsugu, K. Kitagawa, T. Kariyado, A. W. Rost, J. Nuss, C. Mühle, M. Ogata, and H. Takagi, Phys. Rev. B **103**, 115117 (2021).

[133] D. T. J. Hurle, *Fundamentals, Thermodynamics and Kinetics, Handbook of Crystal Growth* (Elsevier, Amsterdam, 1993), p. ii.

[134] W. T. Read and W. Shockley, Phys. Rev. **78**, 275 (1950).

[135] D. M. Duffy, J. Phys. C Solid State Phys. **19**, 4393 (1986).

[136] J. Paglione, N. P. Butch, and E. Rodriguez, *Fundamentals of Quantum Materials: A Practical Guide to Synthesis and Exploration* (World Scientific, 2020).

[137] R. A. Laudise, *Changes of State*, (Springer US, Boston, MA, 1975), pp. 407.

[138] V. I. Voronkova, V. K. Yanovskii, I. V. Vodolazskaya & E. S. Shubentsova, Growth of Crystals. Growth of Crystals, **19** (Springer, Boston, MA, 1993).

[139] Z. Fisk and J. P. Remeika, *Handbook on the Physics and Chemistry of Rare Earths* (Elsevier, 1989), pp. 53.

[140] P. C. Canfield and Z. Fisk, Philosophical Magazine B **65**, 1117 (1992).

[141] T. Zilber, S. Cohen, D. Fuks, and Y. Gelbstein J. Alloys Compd, **781**, 1132-1138 (2019).

[142] M. G. Kanatzidis, R. Pöttgen, and W. Jeitschko, Angew. Chem. Int. Ed. **44**, 6996 (2005).

[143] M. Binnewies, R. Glaum, M. Schmidt, and P. Schmidt, Z. Anorg. Allg. Chem. **639**, 219 (2013).

[144] M. Binnewies, M. Schmidt, and P. Schmidt, Z. Anorg. Allg. Chem. **643**, 1295 (2017).

[145] R. Heinemann and P. Schmidt, Cryst. Growth Des. **20**, 5986 (2020).

[146] A. Ubaldini and E. Giannini, J. Cryst. Growth **401**, 878 (2014).

[147] K. A. Modic, T. Meng, F. Ronning, E. D. Bauer, P. J. W. Moll, and B. J. Ramshaw, Sci. Rep. **9**, 2095 (2019).

[148] I. Maskery, C. W. Burrows, M. Walker, R. P. Singh, G. Balakrishnan, J. A. Duffy, and G. R. Bell, J. Vac. Sci. Technol. B **34**, 041219 (2016).

[149] P. S. Dutta, *Comprehensive Semiconductor Science and Technology*, (Elsevier, Amsterdam, 2011), pp. 36.

[150] T. Duffar and L. Sylla, *Crystal Growth Processes Based on Capillarity,* 2010, pp. 355.

[151] P. Rudolph and F. M. Kiessling, Cryst. Res. Technol. **23**, 1207 (1988).

[152] P. Rudolph *Handbook of Crystal Growth* (Elsevier, Boston, 2015), pp. 281.

[153] H. Riemann and A. Luedge, *Crystal Growth of Si for Solar Cells*, (Springer Berlin Heidelberg, Berlin, Heidelberg, 2009), pp. 41.

[154] Y. A. Tatarchenko, *Shaped Crystal Growth* (Springer Netherlands, Dordrecht, 1993), pp. 187.

[155] H. A. Dabkowska and A. B. Dabkowski, *Handbook of Crystal Growth*, (Springer Berlin Heidelberg, Berlin, Heidelberg, 2010), pp. 367.

[156] A. Lüdge, H. Riemann, M. Wünscher, G. Behr, W. Löser, A. Muiznieks, and A. Cröll, in *Crystal Growth Processes Based on Capillarity*2010), pp. 203.

[157] Levitation Meting Facility KTS, SCIDRE Scientific Instrunents Dresden GmbH, https://scidre.de/index.php?id=13.

[158] K. Takagi, and M. Ishii, J. Cryst. Growth **40**, 1 (1977).

[159] T. Berry, S. Bernier, G. Auffermann, T. M. McQueen, and W. Adam Phelan, J. Cryst. Growth **583**, 126518 (2022).

[160] W. L. Ritzert Frank, https://ntrs.nasa.gov/citations/19960017267 (2013).

[161] T. Ogawa, Y. Urata, S. Wada, K. Onodera, H. Machida, H. Sagae, M. Higuchi, and K. Kodaira, Opt. Lett. **28**, 2333 (2003).

[162] F. Rey García, R. Ibáñez, L. A. Angurel, F. M. Costa, and G. F. de la Fuente, Crystals **11**, 38 (2021).

[163] laser floatoing zone schematic https://www.tf.unikiel.de/matwis/amat/elmat_en/kap_6/advanced/t6_1_3.html#_dum_2.

[164] Laser-heated floating zone crystal growth furnace LKZ, https://scidre.de/index.php?id=44.

[165] *International Tables for Crystallography, Volume B* (Springer Dordrecht, 2 edn., International Tables for Crystallography.

[166] B.D. Culity and C.D. Graham, *Introduction to Magnetic Materials* (John Wiley & Sons, Limited, 2008), pp. 23.

[167] J. M. Luttinger, Phys. Rev. **112**, 739 (1958).

[168] R. Wang, J. Z. Zhao, Y. J. Jin, Y. P. Du, Y. X. Zhao, H. Xu, and S. Y. Tong, Phys. Rev. B **97**, 241111 (2018).

[169] M. M. Hosen *et al.*, Sci. Rep. **8**, 13283 (2018).

[170] G. Chang *et al.*, Sci. Rep. **6**, 38839 (2016).

[171] T. Bzdušek, Q. Wu, A. Rüegg, M. Sigrist, and A. A. Soluyanov, Nature **538**, 75 (2016).

[172] R. Bi, Z. Yan, L. Lu, and Z. Wang, Phys. Rev. B **96**, 201305 (2017).

[173] K. Manna *et al.*, Phys. Rev. X **8**, 041045 (2018).

[174] S. Nakatsuji, N. Kiyohara, and T. Higo, Nature **527**, 212 (2015).

[175] A. K. Nayak *et al.*, Sci. Adv. **2**, e1501870 (2016).

[176] E. Liu *et al.*, Nat. Phys. **14**, 1125 (2018).

[177] A. Sakai *et al.*, Nat. Phys. **14**, 1119 (2018).

[178] S. N. Guin *et al.*, Adv. Mater. **33**, 2006301 (2021).

[179] I. Belopolski *et al.*, Science **365**, 1278 (2019).

[180] T. N. Lamichhane, V. Taufour, M. W. Masters, D. S. Parker, U. S. Kaluarachchi, S. Thimmaiah, S. L. Bud'ko, and P. C. Canfield, Appl. Phys. Lett. **109**, 092402 (2016).

[181] K. Kim *et al.*, Nat. Mater. **17**, 794 (2018).

[182] L. Ye, Y. Tian, X. Jin, and D. Xiao, Phys. Rev. B **85**, 220403 (2012).

[183] G. Kresse, and J. Furthmüller, Phys. Rev. B **54**, 11169 (1996).

[184] J. P. Perdew, K. Burke, and M. Ernzerhof, Phys. Rev. Lett. **77**, 3865 (1996).

[185] A. A. Mostofi, J. R. Yates, Y. S. Lee, I. Souza, D. Vanderbilt, and N. Marzari, Comput. Phys. Commun. **178**, 685 (2008).

[186] T. Suzuki, R. Chisnell, A. Devarakonda, Y. T. Liu, W. Feng, D. Xiao, J. W. Lynn, and J. G. Checkelsky, Nat. Phys. **12**, 1119 (2016).

[187] V. An Dinh, K. Sato, and H. KatayamaYoshida, J. Phys. Soc. Japan **77**, 014705 (2008).

[188] A. Szytuła, A. T. Pędziwiatr, Z. Tomkowicz, and W. Bażela, J. Magn. Magn. Mater. **25**, 176 (1981).

[189] Y.Y. Zhao *et al.*, J. Am. Chem. Soc. **137**, 1746 (2015).

[190] H. Fjellvåg, and A. F. Andresen, J. Magn. Magn. Mater. **50**, 291 (1985).

[191] S. Ohta, T. Kaneko, H. Yoshida, T. Kanomata, and H. Yamauchi, J. Magn. Magn. Mater. **150**, 157 (1995).

[192] H. Rozale, A. Amar, A. Lakdja, A. Moukadem, and A. Chahed, J. Magn. Magn. Mater. **336**, 83 (2013).

[193] H. Nakamura, M. Y. P. Akbar, T. Tomita, A. A. Nugroho, and S. Nakatsuji, *Proceedings of J-Physics 2019: International Conference on Multipole Physics and Related Phenomena* (Journal of the Physical Society of Japan, 2020).

[194] M. J. Otto, R. A. M. v. Woerden, P. J. v. d. Valk, J. Wijngaard, C. F. v. Bruggen, C. Haas, and K. H. J. Buschow, J. Phys. Condens. Matter **1**, 2341 (1989).

[195] I. Galanakis, E. Şaşıoğlu, and K. Özdoğan, Phys. Rev. B **77**, 214417 (2008).

[196] C. Hordequin, J. Pierre, and R. Currat, J. Magn. Magn. Mater. **162**, 75 (1996).

[197] S. J. Youn, and B. I. Min, Phys. Rev. B **51**, 10436 (1995).

[198] Z. Wen, T. Kubota, T. Yamamoto, and K. Takanashi, Sci. Rep. **5**, 18387 (2015).

[199] K. E. H. M. Hanssen, P. E. Mijnarends, L. P. L. M. Rabou, and K. H. J. Buschow, Phys. Rev. B **42**, 1533 (1990).

[200] C. Ciccarelli *et al.*, Nat. Phys. **12**, 855 (2016).

[201] S. Gardelis, J. Androulakis, P. Migiakis, J. Giapintzakis, S. K. Clowes, Y. Bugoslavsky, W. R. Branford, Y. Miyoshi, and L. F. Cohen, J. Appl.Phys. **95**, 8063 (2004).

[202] P. Dürrenfeld *et al.*, Phys. Rev. B **92**, 214424 (2015).

[203] R. A. de Groot, F. M. Mueller, P. G. v. Engen, and K. H. J. Buschow, Phys. Rev. Lett. **50**, 2024 (1983).

[204] P. G. v. Engen, K. H. J. Buschow, R. Jongebreur, and M. Erman, Appl. Phys. Lett. **42**, 202 (1983).

[205] Z. Wen *et al.*, Sci. Adv. **5**, eaaw9337 (2019).

[206] D. Xiao, W. Yao, and Q. Niu, Phys. Rev. Lett. **99**, 236809 (2007).

[207] Z.G. Chen *et al.*, Proc. Natl. Acad. Sci. **114**, 816 (2017).

[208] Y. Zhang *et al.*, Sci. Bull. **62**, 950 (2017).

[209] B. Fu, H. W. Wang, and S. Q. Shen, Phys. Rev. Lett. **125**, 256601 (2020).

[210] Y. Zhang *et al.*, Nat. Commun. **8**, 15512 (2017).

[211] J. Mutch, W. C. Chen, P. Went, T. Qian, I. Z. Wilson, A. Andreev, C. C. Chen, and J. H. Chu, Sci. Adv. **5**, eaav9771 (2019).

[212] G. A. Bain and J. F. Berry, J. Chem. Edu. **85**, 532 (2008).

[213] Y. Tian, N. Ghassemi, and J. H. Ross, Phys. Rev. B **100**, 165149 (2019).

[214] Y. Jiang *et al.*, Phys. Rev. Lett. **125**, 046403 (2020).

[215] E. Martino *et al.*, Phys. Rev. Lett. **122**, 217402 (2019).

[216] S. M. Stishov, A. E. Petrova, V. A. Sidorov, and D. Menzel, Phys. Rev. B **86**, 064433 (2012).

[217] H. Weng, C. Fang, Z. Fang, B. A. Bernevig, and X. Dai, Phys. Rev. X **5**, 011029 (2015).

[218] S. Jia, S. Y. Xu, and M. Z. Hasan, Nat. Mater. **15**, 1140 (2016).

[219] Z. K. Liu *et al.*, Nat. Mater. **15**, 27 (2016).

[220] B. Q. Lv *et al.*, Phys. Rev. X **5**, 031013 (2015).

[221] S. M. Huang *et al.*, Proc. Natl. Acad. Sci. **113**, 1180 (2016).

[222] G. S. Saini, L. D. Calvert, and J. B. Taylor, Can. J. Chem. **42**, 630 (1964).

[223] L. X. Yang *et al.*, Nat. Phys. **11**, 728 (2015).

[224] S. Lei *et al.*, Sci. Adv. **6**, eaay6407 (2020).

[225] A. A. Abrikosov, Phys. Rev. B **58**, 2788 (1998).

[226] B. Bradlyn, J. Cano, Z. Wang, M. G. Vergniory, C. Felser, R. J. Cava, and B. A. Bernevig, Science **353**, aaf5037 (2016).

[227] D. H. Keum *et al.*, Nat. Phys. **11**, 482 (2015).

[228] N. Kumar, C. Shekhar, S. C. Wu, I. Leermakers, O. Young, U. Zeitler, B. Yan, and C. Felser, Phys. Rev. B **93**, 241106 (2016).

[229] E. Mun, H. Ko, G. J. Miller, G. D. Samolyuk, S. L. Bud'ko, and P. C. Canfield, Phys. Rev. B **85**, 035135 (2012).

[230] O. Pavlosiuk, P. Swatek, D. Kaczorowski, and P. Wiśniewski, Phys. Rev. B **97**, 235132 (2018).

[231] N. H. Jo *et al.*, Phys. Rev. B **96**, 165145 (2017).

[232] M. Matin, R. Mondal, N. Barman, A. Thamizhavel, and S. K. Dhar, Phys. Rev. B **97**, 205130 (2018).

[233] O. Pavlosiuk and D. Kaczorowski, Sci. Rep. **8**, 11297 (2018).

[234] M. Tillard and C. Belin, Intermetallics **19**, 518 (2011).

[235] C. Shekhar *et al.*, Nat. Phys. **11**, 645 (2015).

[236] F. Arnold *et al.*, Nat. Commun. **7**, 11615 (2016).

[237] X. Huang *et al.*, Phys. Rev. X **5**, 031023 (2015).

[238] T. Liang, Q. Gibson, M. N. Ali, M. Liu, R. J. Cava, and N. P. Ong, Nat. Mater. **14**, 280 (2015).

[239] E. Mun, H. Ko, G. J. Miller, G. D. Samolyuk, S. L. Bud'ko, and P. C. Canfield, Phys. Rev. B **85**, 035135 (2012).

[240] D. H. Keum *et al.*, Nat. Phys. **11**, 482 (2015).

[241] F. F. Tafti, Q. D. Gibson, S. K. Kushwaha, N. Haldolaarachchige, and R. J. Cava, Nat. Phys. **12**, 272 (2015).

[242] Z. Yuan, H. Lu, Y. Liu, J. Wang, and S. Jia, Phys. Rev. B **93**, 184405 (2016).

[243] M. N. Ali, L. M. Schoop, C. Garg, J. M. Lippmann, E. Lara, B. Lotsch, and S. Parkin, Sci. Adv. **2**, e1601742 (2016).

[244] J. Xiong, S. Kushwaha, J. Krizan, T. Liang, R. J. Cava, and N. P. Ong, Europhys. Lett. **114**, 27002 (2016).

[245] O. Pavlosiuk, P. Swatek, and P. Wiśniewski, Sci. Rep. **6**, 38691 (2016).

[246] N. H. Jo *et al.*, Phys. Rev. B **96**, 165145 (2017).

[247] W. Gao *et al.*, Phys. Rev. Lett. **118**, 256601 (2017).

[248] N. Kumar, K. Manna, Y. Qi, S.C. Wu, L. Wang, B. Yan, C. Felser, and C. Shekhar, Phys. Rev. B **95**, 121109 (2017).

[249] M. Matin, R. Mondal, N. Barman, A. Thamizhavel, and S. K. Dhar, Phys. Rev. B **97**, 205130 (2018).

[250] S. Chaudhuri, P. A. Bhobe, and A. K. Nigam, J. Phys. Condens. Matter **30**, 015703 (2017).

[251] P. Vir, N. Kumar, H. Borrmann, B. Jamijansuren, G. Kreiner, C. Shekhar, and C. Felser, Chem. Mater. **31**, 5876 (2019).

Versicherung

Hiermit versichere ich, dass ich die vorliegende Arbeit mit dem title "Investigation of electronic and magnetic response in topological semimetals" ohne unzulässige Hilfe Dritter und ohne Benutzung anderer als der angegebenen Hilfsmittel angefertigt habe. Die aus fremden Quellen direkt oder indirekt übernommenen Gedanken sind als solche kenntlich gemacht. Die Arbeit wurde bisher weder im Inland noch im Ausland in gleicher der ähnlicher Form einer anderen Prüfungsbehörde vorgelegt. Die vorliegende Dissertation wurde am *Max-Planck-Institut für Chemische Physik fester Stoffe* unter der wissenschaftlichen Betreuung von *Frau Prof. Dr. Claudia Felser*.

_____   _____

Datum   Unterschrift